DANIELA BLESSENT

INTEGRATION OF 3D GEOLOGICAL AND NUMERICAL MODELS BASED ON TETRAHEDRAL MESHES FOR HYDROGEOLOGICAL SIMULATIONS IN FRACTURED POROUS MEDIA

Thèse présentée
à la Faculté des études supérieures de l'Université Laval
dans le cadre du programme de doctorat en Sciences de la Terre
pour l'obtention du grade de Philosophiae Doctor (Ph.D.)

DÉPARTEMENT DE GÉOLOGIE ET DE GÉNIE GÉOLOGIQUE
FACULTÉ DES SCIENCES ET DE GÉNIE
UNIVERSITÉ LAVAL
QUÉBEC

2009

Abstract

A new modeling approach for fractured geological media represented by a deterministic discretely-fractured conceptual model is presented in this thesis. The main objective of this study is to reproduce the heterogeneity and the complexity typical of fractured media in a three-dimensional geometrical model required to execute numerical simulations, with the objective to improve numerical modeling capabilities in hydrogeology. This objective is accomplished with the coupling between a geological modeling platform (GOCAD) and a numerical code (HydroGeoSphere). The main challenges to overcome are the geometrical representation of the network of fractures, the selection of a suitable mesh for the spatial discretization of the simulation domain, and the adaptation of the numerical code to this mesh.

The new approach consists of three phases (1) 3D geological modeling (2) generation of a 3D tetrahedral mesh and (3) numerical simulation of saturated groundwater flow and contaminant transport. Tetrahedral meshes are generally more suitable than block or prism based-meshes to discretize complex geometries, such as the fractured media considered here. Moreover, an alternative definition of the dual grid, which is essential to apply the Finite Element – Control Volume numerical method used by HydroGeoSphere, is discussed and implemented in the numerical code.

The enhanced numerical code is initially verified with simple analytical and numerical simulation scenarios whose solutions are known. Then, the complexity of the simulation scenarios is gradually increased. The modeling approach is finally applied to the site of Olkiluoto (Finland), where an underground rock characterisation facility is being built to evaluate the feasibility of a deep geological repository for high-level nuclear waste. The selected geological modeling techniques allow for a straightforward geometrical modeling of the fractures identified through in situ geological characterization. Moreover, the numerical model is shown to be adequate for the simulation of groundwater flow and solute transport at this complex site.

This research presents a contribution to the development of the techniques of hydrogeological modeling for fractured geological media.

Résumé

Une nouvelle approche de modélisation des milieux géologiques fracturés représentés par un modèle conceptuel de fractures discrètes et déterministes est présentée dans cette thèse. L'objectif principal de l'étude est de reproduire l'hétérogénéité et la complexité des milieux poreux fracturés dans un modèle géométrique tridimensionnel afin d'effectuer des simulations numériques dans le but d'améliorer les capacités de modélisation en hydrogéologie. Ceci est réalisé à travers le couplage entre une plateforme de modélisation géologique (GOCAD) et un code numérique (HydroGeoSphere). Les principaux défis à relever sont: la représentation géométrique du réseau de fractures, la sélection d'un maillage approprié pour la discrétisation spatiale du domaine de simulation et l'adaptation du code numérique à ce maillage.

La nouvelle approche est basée sur une première phase de modélisation géologique 3D, suivie par la génération d'un maillage tétraédrique 3D et par la simulation numérique de l'écoulement souterrain en conditions saturées et du transport de solutés. En général, le maillage tétraédrique s'avère plus adéquat que les maillages de blocs ou de prismes pour discrétiser les géométries complexes telles que les milieux fracturés. De plus, une définition alternative du maillage "dual", qui est essentiel pour appliquer la méthode numérique élément finis - volume de contrôle utilisée par HydroGeoSphere, est analysée et intégrée dans le code numérique.

Le code numérique proposé est d'abord vérifié par l'intermédiaire de simples scénarios de simulation dont les solutions, analytiques et numériques, sont déjà connues. La complexité des simulations est augmentée de façon graduelle. L'approche de modélisation est finalement appliquée au site Olkiluoto (Finlande) où un laboratoire de recherche souterrain est en construction afin d'évaluer la faisabilité du stockage géologique profond de déchets nucléaires à haute activité. Les techniques de modélisation géologique mises au point permettent de modéliser facilement la géométrie des fractures identifiées à travers la caractérisation géologique in situ. De plus, le modèle numérique s'avère adéquat pour la simulation de l'écoulement et du transport de solutés dans ce site complexe.
Ce travail de recherche présente une contribution au développement des techniques de modélisation hydrogéologique des milieux fracturés.

Avant-propos

Ce travail de recherche a été réalisé avec le soutien financier du réseau GEOIDE dans le cadre du projet GeoTopo3D.

Je tiens à remercier mon directeur de thèse, René Therrien, qui m'a offert la possibilité de travailler sur un projet très intéressant et d'orienter la recherche selon mes intérêts. Merci pour tous ses précieux conseils et pour m'avoir donné la possibilité de participer à plusieurs conférences internationales. Je souhaite aussi remercier Kerry MacQuarrie pour avoir accepté la codirection de cette thèse et pour ses conseils.

Un gros merci aussi à Carl Gable pour la permission d'utiliser le logiciel LaGriT et pour m'avoir invitée à Los Alamos National Laboratory. Ses explications, ses réponses rapides et toujours exhaustives à mes nombreuses questions ont fait de ce stage une étape essentielle pour l'avancement de mon projet.

Merci à Pierre Therrien pour son aide dans l'utilisation des outils informatiques. Merci aussi à tous mes collègues de bureau, passés et présents. En particulier, un gros merci à Daniel Lemaire et à Jasmin Raymond pour leur amitié et leurs conseils.

Un merci tout particulier à ma chère amie Judith Nyiraneza et à son adorable famille pour tous les moments agréables passés ensemble. Merci à tous mes amis, en Italie et au Québec, qui ont été à mes côtés pendant ces dernières années.

Des remerciements spéciaux à mon père et à mon frère qui ont été toujours présents et intéressés par mon projet, malgré les grandes distances géographiques qui nous séparent. En particulier, je tiens à remercier mon frère, Luca, pour son aide dans la correction de cette thèse. Un grand merci à mon époux, César, pour m'avoir encouragée à entreprendre un doctorat et pour ses irremplaçables conseils. Je lui suis très reconnaissante pour son soutien quotidien.

À tous les autres que je ne peux pas citer ici, mais qui m'ont encouragée et aidée tout au long de cette thèse, j'adresse un grand merci.

Contents

List of tables

List of figures

Chapter 1

Introduction

1.1 Problem definition

Geological modeling is an area that has experienced a great expansion in recent years thanks to new tools and techniques designed to build and visualize a computerized representation of subsurface geological structures, such as layers, faults, folds, and fracture networks. This representation is based on discrete models that approximate the real geometry of geological structures. This discrete representation, with spatial mesh, is also required for numerical modeling in hydrogeology. In fact, hydrogeological modeling is based on the numerical solution of governing equations, such as groundwater flow and contaminant transport, on a spatial mesh that covers the simulation domain. Therefore, the two disciplines, geological modeling and hydrogeological modeling converge into the discrete representation of geological systems. This representation is called Geomodel by Mallet (2002). The terms "Geomodel" and "geological model" are used interchangeably in this thesis. A larger and better exploitation of Geomodels can significantly increase the capabilities in hydrogeological modeling, which is often affected by limitations on the discretization of complex domain geometries. In fact, it is a

key challenge to generate a discretized Geomodel that incorporates the structural complexity of the geology while maintaining model sizes that are practical for flow simulations (Prevost et al., 2004). More specifically, integration between Geomodels and numerical models can be considered for studies in fractured geological media, which are generally characterized by a geometry that is difficult to capture.

Computational simulations of physical phenomena and processes start with the acquisition of boundary data, which may be in the form of output from a Computer-Aided Design (CAD) system. These data are used to give a geometric configuration to the simulation domain. A geometry definition is suitable if it provides the appropriate level of detail, and sufficient fidelity to the "real" geometry to make solution effects due to geometry inaccuracy small compared to the overall accuracy of the analysis (Thompson et al., 1999). For geological applications, a new breed of CAD especially dedicated to the modeling of natural objects, such as those encountered in geology, has been developed (Mallet, 2002). Contrary to classical CAD methods, this new generation of tools is designed to address the complexity and the enormous quantity of available geoscientific data and to perform spatial analysis. Moreover, CAD-Systems and hydrogeological models have been increasingly combined to study fractured rocks because of their capabilities to represent and visualize complex 3D geological objects, such as fractures.

Once the boundary of the simulation domain is defined, it must be discretized, such that a specific numerical code can be used to simulate physical processes. Therefore, a mesh generation phase, representing the connection between geological and numerical models, is necessary to discretize the 3D Geomodel. More precisely, the simulation of groundwater flow and contaminant transport in geological formations requires three steps: (1) characterizing the geology and developing conceptual models of the hydrogeology and hydrologic material properties, (2) building the computational grid and prescribing initial and boundary conditions and (3) applying numerical models for fluid flow, energy transport, and/or chemical transport (Gable et al., 1996b).

This research addresses fractured geological media. From a hydrogeological point of view, fractured rocks are complex and are characterized by a porous rock mass dissected by various

types of discontinuities. A distinctive feature of these discontinuities is that they cover a wide scale range from millimetric fissures to long faults of hundreds of kilometers (Adler and Thovert, 1999). The general term "fractures" may refer to cracks, fissures, joints and faults. In the context of modeling groundwater flow and transport, a finer distinction is not usually necessary (Berkowitz, 2002). Permeability of fractures may be reduced by mineral deposition, brecciation, cataclasis, such as mentioned by Gleeson and Novakowski (2009) who reinterpreted lineaments as watershed-scale hydraulic barriers, in contrast to previous interpretations as fractured conduits that focus recharge and flow. In this thesis only relevant conductors of groundwater flow are considered and it will be referred to as fractures. The rock mass typically has a low permeability and high storage capacity, while hydraulically-active fractures have high permeability but lower storage capacity because of their lower contribution to the total porosity of the rock mass. Because they are permeable, fractures can therefore be preferential pathways for contaminants. Transport processes in fractured rocks include molecular diffusion, mechanical dispersion and advection. In the rock matrix, molecular diffusion usually dominates over advection, in such a way that the porous rock mass may attenuate and retard the advective propagation of contaminants along fractures (Tang et al., 1981; Therrien and Sudicky, 1996). Depending on the investigation scale and on the fracture properties, two main conceptual models exist to represent fractured media: the equivalent continuum model, where fractures in the rock mass are not explicitly represented, and the discrete fracture model, where discontinuities are discretized. This investigation addresses the discrete fracture representation and focuses on the discretization of individual fractures.

Interest for fractured rock can be found in the discontinuities, which play a major role in the formation of ore deposits, in the exploitation of petroleum, gas, and geothermal reservoirs. Moreover, fractured aquifers and fracture zones in bedrock terrains are also important as a source of groundwater to wells and flow through permeable fractures is also of interest to mining and geotechnical engineers (Neuman, 2005). Finally, the interest for low permeability fractured rocks has mainly increased in recent years because of their potential suitability as deep geological repositories for high level nuclear waste (IAEA, 1999; OECD, 1999; ANDRA, 2005; NWMO, 2005). Of the various disposal options examined, deep geologic disposal is potentially the most appropriate means of long-term management. According to OECD (1999), it conforms to ethical concerns, it is technically feasible, and it has been found to

provide a high degree of public safety, security from malicious intervention, and protection of the environment both in the short and long term. No matter what is the interest for fractured rocks, 3D hydrogeological modeling is the tool required to characterize and predict the future behavior of these geological systems. Thus, all work that contributes to improve modeling capabilities of groundwater flow and contaminant transport is of great interest in different geoscientific applications.

1.2 Prior study on fractured geological media

The simplest conceptual model adopted to study fractured media is based on the equivalent continuum approach, as mentioned in Section 1.1. Historically, this approach has been the first one used for modeling flow and transport in fractured media (Bodin et al., 2003). It should be theoretically valid only if a representative elementary volume, REV, exists. The definition of REV (Bear, 1988) is based on average properties of the geological medium. Nevertheless, it is often difficult or an extreme simplification to attribute hydraulic properties that represent the average behavior of both fractures and porous rock matrix. The equivalent porous model may be applied to finely and highly fractured media, which may behave as an equivalent porous formation. Some authors have developed a different approach based on two continuums, which are used to make a distinction between the roles played by the fractures and the rock matrix in groundwater flow problems (Barenblatt et al., 1960; Warren and Root, 1963). According to this approach, two REVs are defined and two different sets of average properties are attributed to the fractures and the rock matrix, respectively. However, the precise location and properties of single fractures is overlooked, such that the geometry of the network of fractures is disregarded.

If discrete modeling of fractured media is considered, an important distinction should be made between fracture network models, where the surrounding porous rock matrix contribution is neglected, and discretely-fractured porous media, where fluid flows simultaneously along fractures and through the porous rock matrix surrounding fractures (Berkowitz, 2002). A fracture network is generally defined as a set of individual fractures which may or may not intersect (Adler and Thovert, 1999). Investigations focused on the transport of contaminants

should be conducted using the discretely-fractured porous media model. In fact, molecular diffusion, mechanical dispersion and advection contribute in a different way to the whole transport process, depending on the presence of fractures or porous rock matrix (Tang et al., 1981; Therrien and Sudicky, 1996). Representation of all fluid flow and transport processes is required to realistically simulate the hydrogeological behavior of fractured rocks. Thus, an exhaustive conceptual model should include both the fractures and the surrounding rock matrix. While with the continuum approach fractures are not explicitly discretized, with the discrete approach it is possible to model every fracture with its own geometry, giving a much more detailed representation of geological systems. Andersson and Dverstorp (1987) affirmed that field investigations of flow in fractured rock clearly demonstrated that modeling the rock as a homogeneous continuum might be an oversimplification. Likewise, Neuman (2005) stated that all evidence suggests that rarely can one model flow and transport in a fractured rock consistently by treating it as a uniform or mildly nonuniform isotropic continuum. Although the discrete approach may appear more intuitive and logical than the continuum one because transport mechanisms in each fracture are explicitly taken into account, it requires much more difficult calculations and field measurements (Bodin et al., 2003). As summarized by Neuman (2005), three main ways of modeling fractured rocks can be considered: one way is to depict the rock as a network of discrete fractures, with permeable or impermeable matrix, another as a nonumiform continuum, which can be single, dual or multiple, and finally a third way is to combine these into a hybrid model of a nonuniform continuum containing a relatively small number of discrete dominant features. In either case the description can be deterministic or stochastic. No matter which approach is used, modeling groundwater flow in fractured rocks is relatively complex because fractures can be as difficult to observe and characterize as they are to represent in a numerical model (Selroos et al., 2002).

In the discretely-fractured porous media conceptual models, a distinction should be made between networks of fractures that are randomly located in space and those where the location of the discrete fractures is deterministic. The Discrete Fracture Network approach, DFN, coupled with the generation of stochastic fractures has been largely studied (Andersson and Dverstorp, 1987; Cacas et al., 1990; Nordqvist et al., 1992; Bogdanov et al., 2007). Random populations of fractures and statistical estimates of fracture size, orientation, and density are usually generated. Fractures are represented by planar circular discs randomly and

independently distributed in space (Andersson and Dverstorp, 1987; Nordqvist et al., 1992), by regular polygons, rectangles, and ellipses (Bogdanov et al., 2007) or by a network of interconnected pipes (Cacas et al., 1990). This last representation originates from the evidence of channeling in fractured media, as field observations suggest that fracture surfaces are uneven and mineralized, with flow and contaminants distributed non-uniformly across the fracture plane in preferential paths, or channels (Selroos et al., 2002). In contrast, other studies are focused on the representation of deterministic fractures, which are identified after geological investigations. In this case, there is no need for random generation of fractures because their location is identified by in situ geological characterization. The interest is focused only on major conductors of groundwater flow, such that smaller fractures are not discretized, but rather their presence is incorporated in the properties of the porous rock matrix. Moreover, deterministic fractures can be explicitly represented by the user using geomodeling tools, which allow the management of geological spatial data. Thus, fractures may be represented by irregular surfaces whose location and shape depends on available field data.

Specific studies have already been conducted to use geomodeling tools in combination with numerical models and they constitute the main background of this thesis. Mancini (2004) combined a geometrical model created in GOCAD[1] with the Finite Element Modeling package Rockflow[2]. A geometrical model of a hypothetical nuclear repository system in crystalline rock was created. The 3D mesh was generated using the *Solid* GOCAD object, which allows connecting nodes into tetrahedra. The tetrahedral mesh was obtained from closed surfaces and a few attempts were required to find an optimal densification rate. The utilization of the *Solid* tool was possible because of the simple geometry of the simulation domain and the lack of fractures, since a homogeneous crystalline rock was considered.

More complex geometries have been considered by Taniguchi and Fillion (1996). They considered a domain with multiple planar fractures and they also took into account their intersection. The simulation domain was characterized by convex subdomains bounded by fracture planes. These subdomains were discretized with tetrahedra using Delaunay triangulation and handling fracture polygons between adjacent subdomains. Then, tetrahedra

[1] http://www.gocad.org/www/
[2] http://www.rockflow.de

were transformed to distorted hexahedra for computational reasons. The drawback of this method is that severe constraints exist on the geometry of fractures, as they are planar and they must define closed and convex subdomains.

Andenmatten-Berthoud and Kohl (2003) built a complex structural model with GOCAD, where different irregular surfaces describing stratigraphic horizons, faults, and topography. Boreholes were also included in the Geomodel. The discretization was performed with the TGridlab GOCAD plug-in, which generates tetrahedra. As in Taniguchi and Fillion (1996), closed subdomains are required to make the TGridlab application possible. Thus, stratigraphic horizons and faults constitute internal boundaries, which must define closed volumes. The authors stated that the utilization of the plug-in is not as straightforward as it may seem and some tests were necessary to verify its capabilities, resulting in a time-consuming phase of the project.

Prevost et al. (2004) developed a sophisticated gridding framework called Soft Frame Model. Their data structure enables the construction of grids that conform to geometrically complex 3D surfaces and honor complex surface intersections and topology constraints. Moreover, the framework creates higher mesh resolution in regions of special interest. Complex geometries including horizons and faults were discretized by a Delaunay tetrahedral mesh. However, the tetrahedralization required the definition of bounded volume regions inside the simulation domain, as in Taniguchi and Fillion (1996) and Andenmatten-Berthoud and Kohl (2003).

Kalbacher et al. (2005) proposed an interface between GOCAD and the numerical software Rockflow for fractured network models. They considered a 2.5D fractured rock network, consisting of planar surfaces in the 3D space, and represented it as a triangular mesh in GOCAD. Although they did not consider the rock matrix, they increased the mesh density of fractures around drill holes to enable a more accurate numerical representation of the system. They used the GMSH meshing software[3] to generate a suitable mesh for the numerical model. They noted that generating and transforming the mesh within GOCAD can lead to numerical errors, which are difficult to locate, correct, and remove once the mesh is generated.

---

[3] http://www.geuz.org/gmsh/

Numerical methods are widely used to simulate groundwater flow and mass transport in fractured geological media. A review of numerical methods and codes employed was presented by Diodato (1994). In his review, he stated that for the spatial derivatives, integral methods have enjoyed more widespread use than the differential approach of the Finite Difference (FD) method, partly because they are amenable to irregular domain geometries. Integral methods used in fracture flow modeling include the Finite-Element (FE) method and the Boundary-Element method (BE). Additionally, Control Volume Finite Element (CVFE) methods have been presented and applied. Besides, Diodato (1994) presented numerical codes available at that time with respect to their capabilities and limitations. In conclusion, he stated that to select an appropriate flow code, one should carefully consider the geology, physics, and, if appropriate, chemistry of the problem to be solved. Careful consideration of the conceptual model of fluid flow in a fractured rock setting is critical to successful fracture flow modeling.

In the previous cited work, simplifications were made, such as neglecting either the fractures (Mancini, 2004) or the rock matrix (Kalbacher et al., 2005), or assuming planar fractures (Taniguchi and Fillion, 1996; Kalbacher et al., 2005). Furthermore, the fact of considering the Geomodel as an ensemble of volume bounded regions (Taniguchi and Fillion, 1996; Andenmatten-Berthoud and Kohl, 2003; Prevost et al., 2004) imposed a constraint on the geometry that can be represented. To overcome these limitations, a more flexible modeling approach is proposed.

1.3 Contribution of this study

This research is part of the GEOIDE project called GeoTopo3D ("Development of a 3D predictive modeling platform for exploration, assessment and management of mineral, petroleum and groundwater resources", Kirkwood, Pouliot, Therrien, MacQuarrie, Li, and Mostafavi). Since 1998, GEOIDE has been a federal-funded Network of Centers of Excellence administrated by the business center GEOIDE inc. based at Laval University. This "network of networks" brings together skills, technology and people from different communities of practice, in order to develop and consolidate the Canadian competences in geomatics. GEOIDE wants to change the way geomatics research and development is carried

out, to ensure increased circulation of knowledge across disciplines, regions, and between researchers, industry and government users to establish a permanent legacy of cooperation (http://www.geoide.ulaval.ca).

GeoTopo3D is organized into three principal scientific areas: Geomodels, 3D GIS and 3D Numerical Modeling. The general purpose of the project is to enable a more efficient use of and integration of geoscientific data and, consequently, to increase the knowledge of natural systems and their resources. Specific goals are to facilitate user access to Geomodels, to help modelers to build Geomodels, and allow for a better and larger exploitation of Geomodels, especially taking advantage of their link with 3D GIS and numerical models.

The work of this thesis is focused on the integration between Geomodels and numerical models. The expression "numerical model" refers both to the mathematical scheme used to solve the partial differential equations that describe the physical phenomenon simulated and to the software built to solve these equations, depending on the context. More specifically, this research addresses the need to increase the numerical modeling capabilities in hydrogeology, applied to investigations in fractured geological media. The primary goal is to create an efficient link between Geomodels and numerical models, such that the latter benefits from the knowledge gained in constructing Geomodels (Kirkwood et al., 2003). The key problem is how to provide the connection between GOCAD and the numerical model HydroGeoSphere (Therrien et al., 2007), which have been selected for this work. These two software tools have been combined with the intermediate use of LaGriT[4], which is a mesh generation software. Thus, a workflow for numerical modeling of groundwater flow and contaminant transport in fractured geological media adapted to the geological modeling platform GOCAD is created. The application of this workflow leads to a new modeling approach. With this approach it is possible to build realistic and detailed models for fractured media and ensure an appropriate 3D spatial discretization, especially for complex geometries. In fact, hydrogeological modeling on complex geometries is now possible thanks to the combination of three different tools: GOCAD is used to build the Geomodel, LaGriT to discretize it and HydroGeoSphere to solve equations of groundwater flow and mass transport over this spatially discretized Geomodel. Thus, one of the main contributions of this work is the enhanced version HydroGeoSphere,

[4] http://lagrit.lanl.gov/

coupled with LaGriT. The whole procedure, which combines the three software tools, is summarized in Figure 1.1.

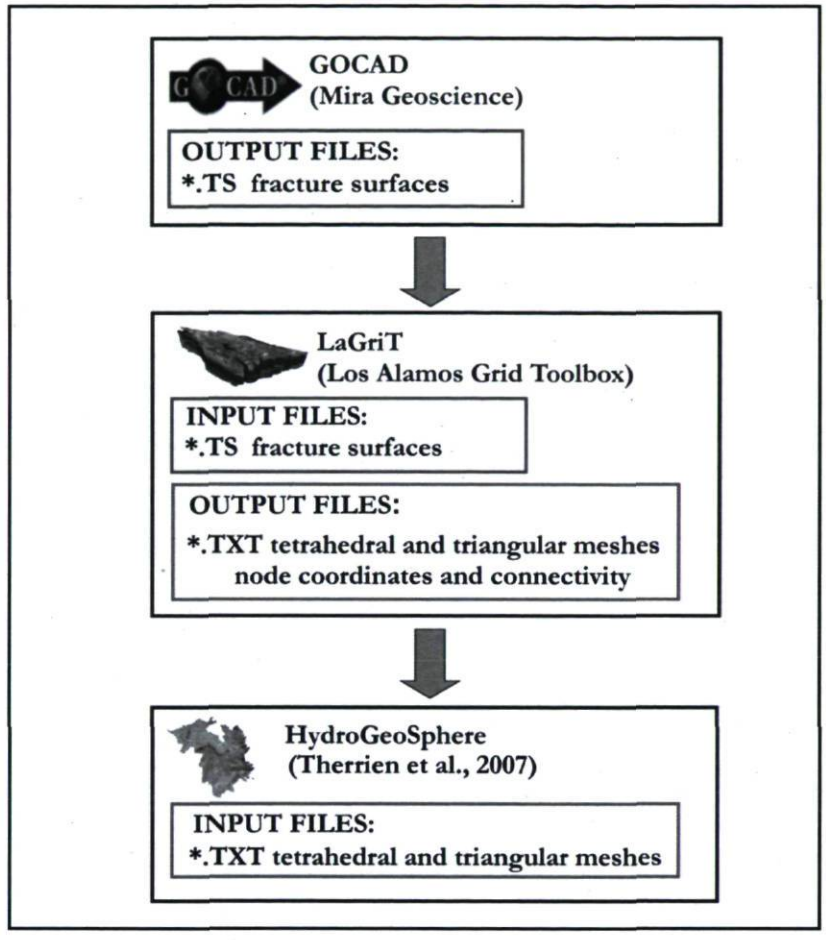

Figure 1.1 - Flowchart of the modeling approach developed

A second objective is to improve the representation and discretization of fractures. In this study, deterministic fractures, which have been identified through field investigations, are represented as surfaces with GOCAD. Spatial data coming from in situ geological characterization are used to give the fractures an irregular shape that conforms to the observations of fractures (see Section 2.1.2.2). Moreover, an appropriate representation of intersections between boreholes and fractures is provided and the axis of inclined boreholes is now represented as it is in reality, avoiding the limitation whereby the spatial discretization affects its shape (see Section 3.3.3). The use of an unstructured tetrahedral mesh allows for

easy local refinement, for example near fractures and around wells (see Section 2.2.1.2). These aspects represent a big challenge of the Geomodel discretization, as it is required to both preserve the model geometry and guarantee an accurate numerical solution. The simultaneous discretization of irregular fractures, inclined wells, and porous rock matrix with a refined tetrahedral mesh, represents the novelty of this work. The combination of modeling tools proposed here leads to the representation and investigation of more complex domain geometries, which constitutes the new research direction of this thesis.

The third main objective is the application of the approach developed to a test site, to show its capabilities by analyzing a specific and real hydrogeological context. Thus, this thesis also provides a real case study (see Chapter 5). The site chosen is on Olkiluoto Island, located on the coast of Finland. The site is characterized by granitic bedrock containing major fracture zones and it has been selected for the construction of a deep geological repository for high-level nuclear waste.

An additional development area focuses on the Control Volume Finite Element numerical method used by HydroGeoSphere to solve the governing equations. An analysis of the fluid conductance matrix has led to the application of the Orthogonal Subdomain Collocation method, OSC, (Putti and Cordes, 1998) as an alternative to the standard Galerkin method to evaluate the fluid conductance matrix (see Section 3.2.2). The OSC method leads to a different evaluation of the matrix coefficients, whose expression is now based on the geometry of the Delaunay and Voronoi meshes used to discretize the simulation domain. The OSC method is implemented in the HydroGeoSphere numerical code and its advantage of ensuring the generation of a fluid conductance matrix with desirable characteristics for iterative solvers is highlighted through illustrative examples.

1.4 Organization of the thesis

This thesis is organized in six chapters, including this Introduction. Chapter 2 contains a background on Geomodeling and mesh generation. Moreover, geomodeling and mesh generation tools used in this work are presented. Chapter 3 covers numerical modeling theory. It presents the HydroGeoSphere model and its new aspects introduced during this work. Chapter 4 presents test cases especially designed to verify and illustrate the modeling approach developed. The complexity of test cases gradually increases from very simple to more complex examples. Nevertheless, they remain far from the complexity characterizing real sites. Thus, Chapter 5 shows the application of the new modeling method to the test site of Olkiluoto, Finland. Finally, Chapter 6 contains conclusions and insights from the application of the modeling approach and future research directions.

Some results of this work are also presented in the following papers:

Blessent D, Therrien R, MacQuarrie K. Coupling geological and numerical models to simulate groundwater flow and mass transport in fractured media. Computers and Geosciences 35(9): 1897-1906. doi:10.1016/j.cageo.2008.12.008.

Blessent D, Hashemi Beni L, Therrien R. 3D Modeling for hydrogeological simulations in fractured geological media. Proceedings of the 19th IASTED International Conference Modelling and simulation (MS 2008), May 26-28, 2008. Quebec City, Canada.

Chapter 2

Geological model and mesh generation

The implementation of numerical methods involving geometrical description of geosystems with the application of numerical meshes is of vital importance for investigation and modeling of various physical processes (Kalbacher et al., 2005). The geometrical description is here called a Geomodel. Meshes represent the spatial discretization of Geomodels and they are required for numerically solving the partial differential equations describing specific processes, such as groundwater flow and contaminant transport. To better capture the geometry of the simulation domain, fine meshes may be employed, increasing the resolution of the model. The main challenge is to understand the tradeoff between a high-resolution model that represents geological structures with a high degree of fidelity and a lower resolution model that is perhaps better suited for intensive computations (Bower et al., 2005).

The first section of this chapter covers general topics on geomodeling. Then, the specific geomodeling tools used to build a Geomodel for discretely-fractured geological media are presented. The second section of the chapter gives an overview of mesh generation issues which is followed by the description of the mesh generation procedure adopted in this work.

2.1 Geomodeling

A Geomodel is the 3D representation of subsurface geological structures, such as horizons, faults, and folds. The definition of geomodeling is given by Mallet (2002), who states that it consists of the set of all mathematical methods allowing modeling in a unified way the topology, the geometry and the physical properties of geological objects while taking into account any type of data related to these objects. A Geomodel allows visualizing subsurface geological structures, which are neither directly accessible nor wholly known. It is built by field data obtained by in situ investigations. Although there are generally few data available and they are usually scattered and not evenly distributed, specific geomodeling tools allow using them to build a Geomodel. Thus, Geomodels offer a possible 3D representation and contribute to increase the knowledge of subsurface geological structures. However, it is clear that quality and availability of field data will directly influence Geomodel accuracy.

A distinction should be made between surface and volume models. A geological model, or Geomodel, is the structural representation of the domain of interest. It can contain a collection of horizons, faults, or fractures, such as done in this work. No matter what type of geological structure is considered, it is usually represented by a triangulated surface. An ensemble of distinct surfaces constitutes the surface model (Figure 2.1a). Nevertheless, this representation is not enough if physical processes must be simulated in the rock matrix that surrounds those surfaces. In this case, a volume of interest is defined to delineate the external boundary of the model. Then, this volume is filled with 3D elements, like hexahedra, prisms or tetrahedra. Conforming topological relations must be ensured between these 3D elements and the 2D triangles that discretize the internal surfaces. When the Geomodel is discretized with 3D elements, it represents a volume model (Figure 2.1b). The mesh generation described in Section 2.2.1.2 is the process through which the Geomodel is discretized with 3D elements. This process is not as straightforward as it may seem because the 3D discretization is constrained by the presence of fracture surfaces inside the volume.

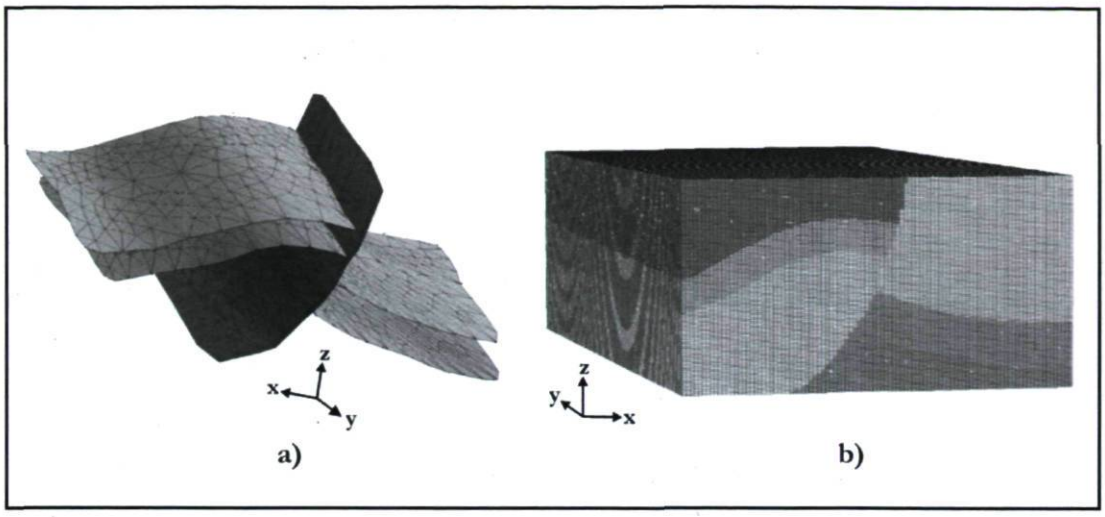

Figure 2.1 - Two horizons cut by a reverse fault: a) surface model and b) volume model

To build the surfaces that represent the deterministic fractures, information about fracture location and extension is required. Fracture characterization may come from observation of outcrops, aerial photographs, core samples, and various geophysical techniques. Hydraulic and tracer tests can yield information on hydraulic conductivity and flow rates of single fractures. In general, fractures are not measured directly but, rather, a response to the presence of fractures is measured. Therefore, a fundamental problem in terms of fracture characterization arises in the distinction between what is measured and what is determined indirectly (Berkowitz, 2002). Thus, data coming from field investigations should be carefully analyzed, eventually discarding those of low reliability. Moreover, the inherent complexity of fractured formations, both structural and hydraulic, severely limits the type and quality of data that can be obtained from field measurements. As a result, geological modeling must largely rely on extrapolation and subjective considerations (Berkowitz, 2002). Different interpretations about the geometry of fractures can be examined before attributing a specific structure to the fracture network.

2.1.1 The GOCAD geological modeling platform

The acronym GOCAD means "Geological Object Computer Aided Design". GOCAD is an integrated 3D geological object modeling and visualization software. It has been developed by the GOCAD consortium[5] in 1989 at the National School of Geology in Nancy, France. With GOCAD it is possible to edit, manage and interpolate spatial field data obtained from in situ geological characterization, such that a realistic Geomodel of the physical system is built in a straightforward manner. Different GOCAD modules are available: base module for geometrical modeling, geological structural modeling, seismic interpretation, velocity modeling, and reservoir modeling. For the purposes of this work, only the base module is considered.

2.1.1.1 GOCAD base module tools

Specific geometric tools are available to build the 3D representation of geological systems. Among geometric objects available in the base module (Earth Decision Science, 2006), the following are considered in this work:

1. *PointsSets* (*.vs files)
   A PointSet is a set of points or atoms that are not connected in any way.

2. *Curves* (*.pl files)
   A Curve consists of connected (and/or disconnected) segments, which can be closed or open. Each segment connects two atoms or points (Figure 2.2a).

3. *Surfaces* (*.ts files)
   A Surface is made of connected (and/or disconnected) triangles; each triangle is made up of three atoms, one on each corner (Figure 2.2b). When creating a surface GOCAD uses a Delaunay triangulation algorithm to triangulate the atoms.

[5] http://www.gocad.org/www/consortium/index.xhtml

4. *Gridded Surfaces or 2D-Grids* (*.grs files)

   A 2D-Grid object, also called a gridded surface, is a surface defined by an origin point, a delta-x, a delta-y, and a series of z-values regularly spaced on the grid itself. Thus, it is similar to a surface, except that points are distributed in a regular grid pattern made of cells (Figure 2.2c). These cells are arranged along grid lines parallel to two axes, which do not have to be orthogonal.

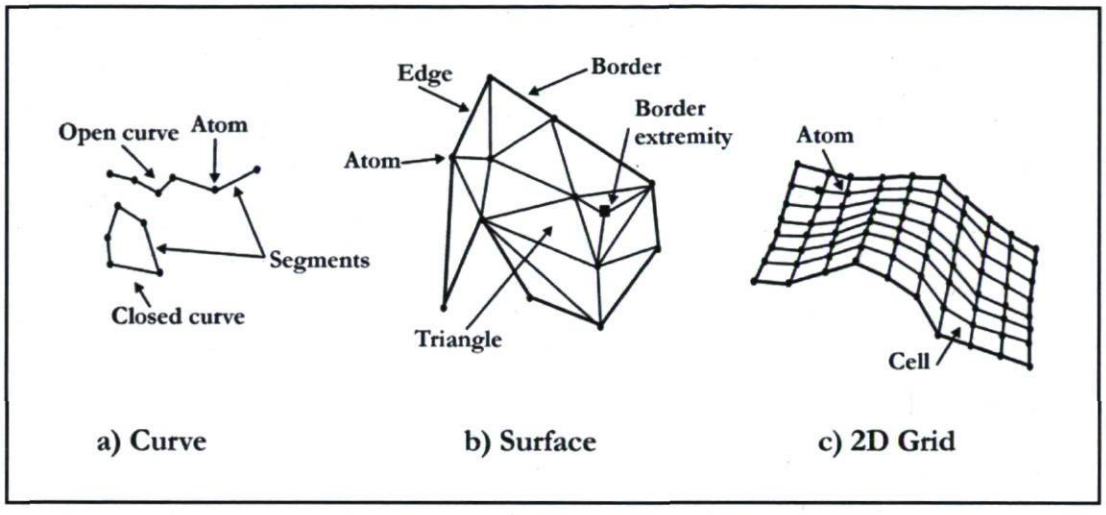

Figure 2.2 - GOCAD geometric objects used in this work
(adapted from Earth Decision Science, 2006)

The most important geometric object in the context of this work is the *Surface*. A surface is used to represent a deterministic fracture identified after geological characterization. Any desired surface can be built, because different actions can locally or globally modify its shape. It is possible to edit surfaces to improve their shape. For example, atoms can be added, deleted, or dragged by mouse, while triangles can be switched, split, merged or deleted. Therefore, the user gives the fractures the shape he considers the most appropriate according to available field data and knowledge on specific geological sites. The advantage of using the GOCAD geological modeling platform is that 2D triangulated fracture surfaces are directly modeled by the user and they are easily visualized before building the volume model through the mesh generation phase.

2.1.1.2 Geomodel building

Geomodel building consists of creating a 3D representation of the fracture network characterizing the geological site of investigation. Fractures can be built from *PointsSets*, which represent local observations of specific fracture zones, or imported into GOCAD from previously created compatible format surface files, like DXF files. No matter which approach is used, at the beginning of the modeling phase, surfaces are generally represented by coarse and heterogeneous triangular meshes (Figure 2.3a). Although this mesh provides a discretization, it is not appropriate for numerical solutions, and therefore further amending is required. *2D-Grids* are used to improve the triangular mesh. A *2D-Grid* is built from a surface characterized by coarse and heterogeneous triangulation. The vertices of the coarse triangulation are used to define the shape and the extent of the *2D-Grid*, such that it will have the same shape as the original surface (Figure 2.3a), but will be discretized by a regular and finer square grid (Figure 2.3b). The resolution of the *2D-Grid* is chosen by the modeler according to the desired edge length in the final triangulated surface. In a further step, the new triangulated surface is created by splitting each square of the 2D-Grid into two triangles and by switching triangles to improve the quality of the final triangular mesh (Figure 2.3c). In addition, triangles may be recursively split until the desired edge length is obtained.

Fracture surfaces considered here are not planar, but they are instead fitted to specific *PointsSets*, which correspond to observations of specific fracture zones. These observations come from core samples, optical borehole images, seismic and borehole radar measurements. Moreover, the continuity of fracture zones can be assessed on the basis of geological properties, hydraulic responses, seismic measurements, and galvanic charged potential measurements (Vaittinen et al., 2003). An example is shown in Figure 2.4, where the same fracture is represented by a planar surface and by an irregular surface fitted to field data. Figures 2.4a and 2.4d show two distinct views of the same planar fracture, while in Figures 2.4b and 2.4e the fracture surface has been fitted to the *PointSet* representing field data. The *PointSet* is clearly visible in Figure 2.4e. The difference between planar and irregular fracture surfaces is better illustrated in Figure 2.4c, where both configurations are shown.

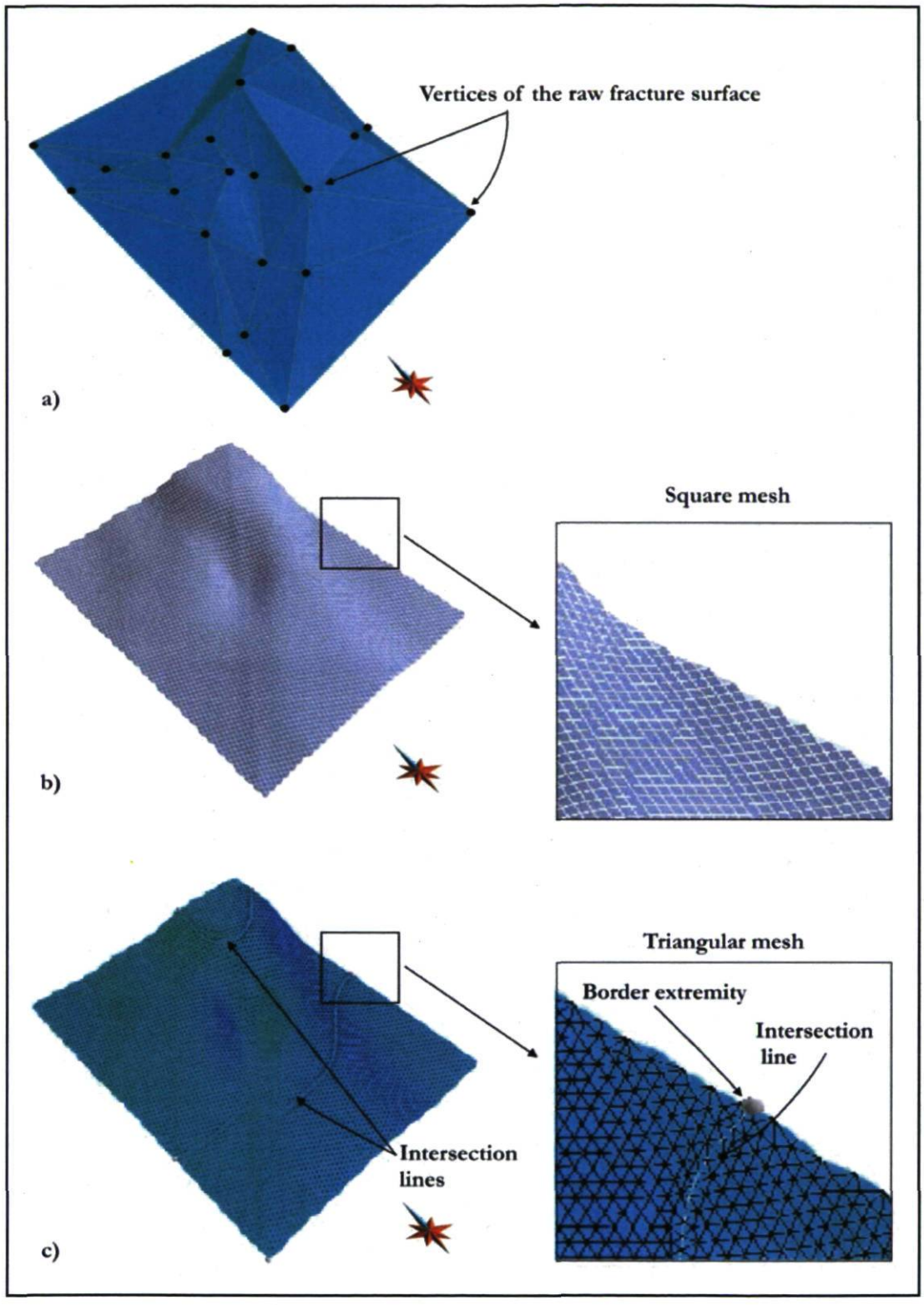

Figure 2.3 - Modeling of fracture surfaces: a) raw triangulation, b) *2D-Grid* regular square mesh and c) final triangular mesh, with two lines of intersecting fractures

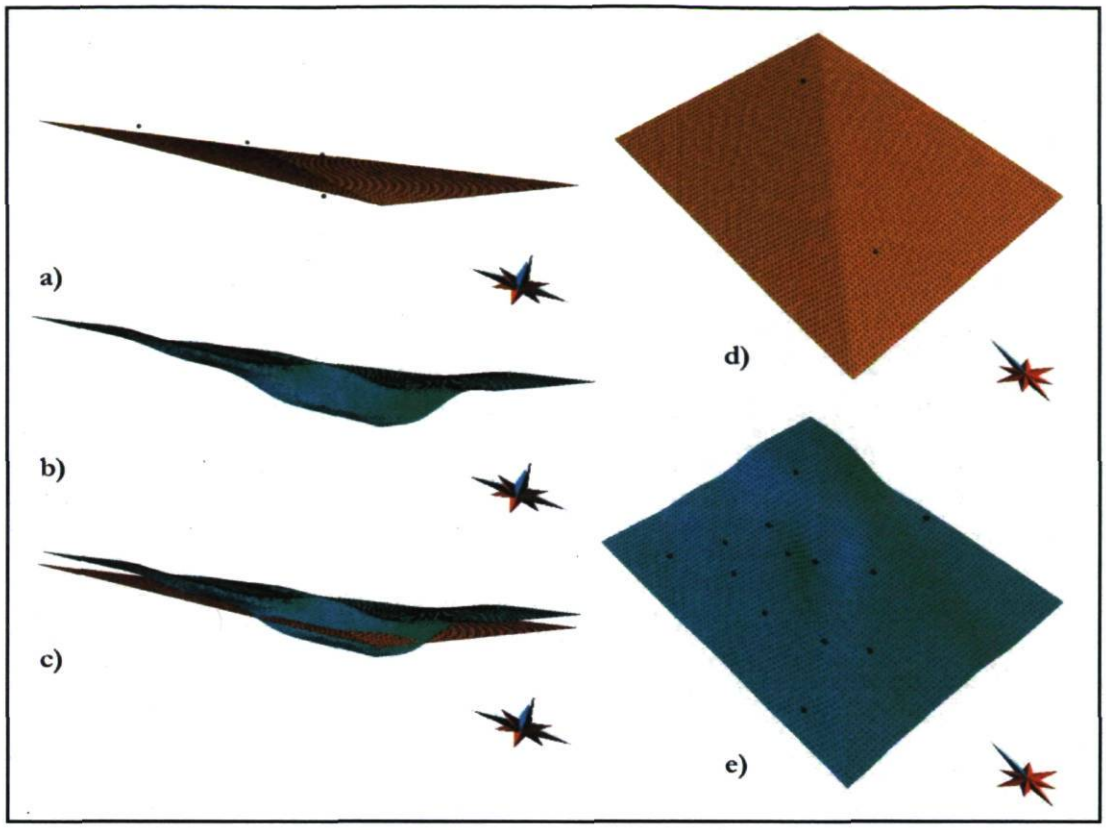

Figure 2.4 - Modeling of fracture surfaces: a) and d) planar surface, b) and e) surface fitted to point set and c) both planar and fitted surfaces

If boreholes are included in the Geomodel, coordinates of their axes are imported into GOCAD as *Curves*, such that each borehole is represented by a set of connected segments. If boreholes intersect fracture surfaces, these can be refined around the intersection. GOCAD tools allow defining regions. A region is a portion, or subset, of an object (Earth Decision, 2006). If a fracture surface is considered, a region can be defined by drawing a curve over it. Quasi-circular regions are defined around each intersecting borehole on fracture surfaces. Then, local refinement is executed exclusively in these regions by splitting triangles that are within them (Figure 2.5). The size of these regions and the number of splitting phases are chosen according to the desired mesh resolution for each specific modeling scenario.

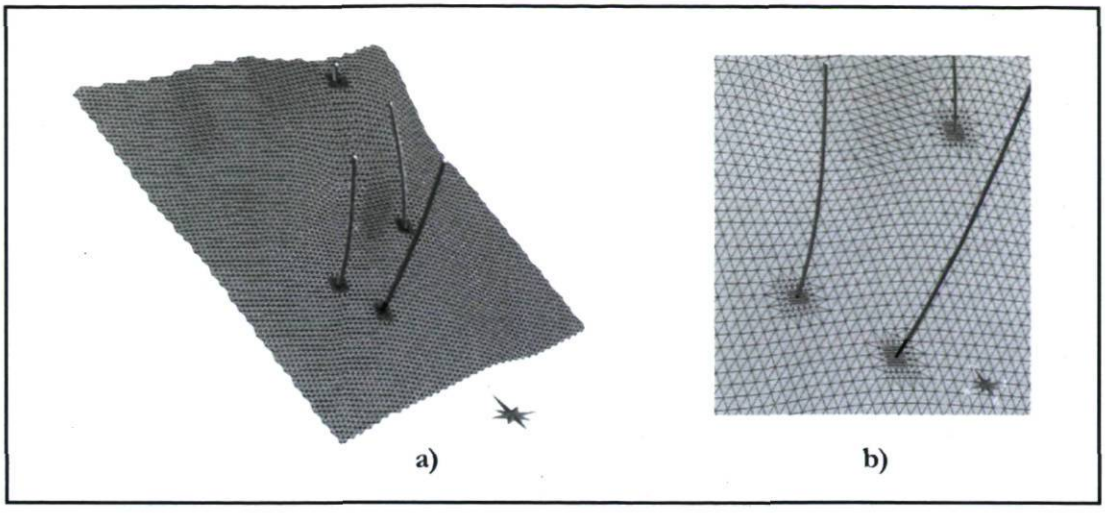

Figure 2.5 - Refinement around boreholes: a) whole fracture surface and b) close-up

Once fractures are all properly refined, their mutual intersections have to be accurately reproduced to obtain a network of connected fractures. The connectivity between fractures is one of the most important aspects that should be considered in Geomodel building. In fact, the connectivity in fracture networks is of primary importance for flow and contaminant transport properties (Bogdanov et al., 2007). The computation of intersection lines, where triangular elements are shared between the intersecting surfaces, is not as simple as it may seem. Two intersecting fractures (Figure 2.6a) have independent and disjoint triangular meshes before their intersection is performed: there are no common nodes at the intersection line (Figure 2.6b). Using the *Mutual cut* GOCAD tool, the intersection between the surfaces is computed. The resulting intersection line holds concurrently the mesh of both intersecting surfaces, but one side effect is that long and skinny triangles are created (Euler et al., 1999), as shown in Figure 2.6c. These badly-shaped elements should be removed or improved to obtain a suitable representation of fracture intersections. The GOCAD *Beautify* algorithm is used to perform this task. The aim of the *Beautify* algorithm is to minimize the number of nodes, to optimize the size of the segments and to obtain the best fitting line (Euler et al., 1999). This algorithm is based on a topological analysis of the adjoining borders, which share the same topological and geometrical information, in order to compute the number of representative nodes to obtain equilateral triangles. After applying the *Beautify* tool, a conforming triangular mesh is obtained at the intersection line. Moreover, this line becomes a *Border* and it has *Border*

extremities, which are represented, respectively, by the white line and the two spherical points shown in Figure 2.6d. *Borders* represent the boundary of surfaces in GOCAD. *Border extremities* are set when *Borders* share the same boundary. Thus, after intersecting fracture surfaces, new boundaries appear.

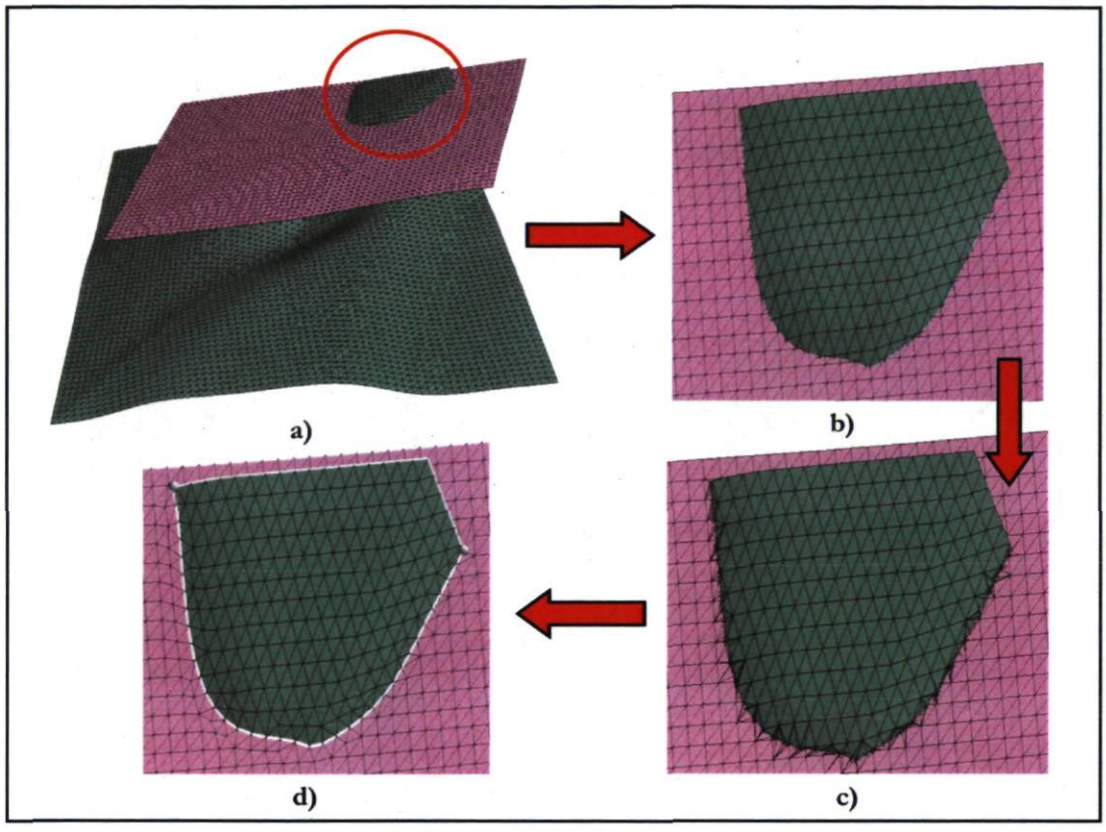

Figure 2.6 - Triangular mesh enhancement at the intersection line between two fractures surfaces: a) and b) initial surfaces, c) after execution of a mutual cut, and d) final triangular conforming mesh at intersection line

The surface model representing a geological fractured medium is now complete. All relations between boreholes and fractures are easily visualized in the 3D space and any modification of their geometry can be done here, before the volume model, or the 3D discretized Geomodel, is generated. In fact, the volume model is created in a further step by using 3D tetrahedra to fill up the volume around fracture surfaces and boreholes curves (see Section 2.2.1). The process of building surface and volume models one at a time is one of the advantages of the

proposed workflow. In fact, the fracture-fracture and fracture-borehole intersections, which are crucial features of the Geomodel, are more easily edited in the geological modeling platform than in the final tetrahedral volume model. The representation of these intersections is fundamental, especially in the case of a low permeability porous rock matrix, where the majority of groundwater flow takes place along borehole axes and fracture surfaces, which are characterized by higher hydraulic conductivity. Thus, the connectivity between these elements must be accurately represented because it strongly influences groundwater flow and determines preferential pathways for contaminants. In addition, it should be noticed that, in general, the triangular discretization of fractures generated in GOCAD, will be preserved as is in the final tetrahedral mesh. In case of fractures with small intersection angles, few triangles change their connectivity once the Geomodel is discretized with tetrahedra. However, this change does not affect the average representation of the fracture network. In conclusion, the geological modeling platform is useful to visualize and understand the geometry and the topological relations between the most important features of the hydrogeological model, like fractures and boreholes. Without using a geological modeling platform like GOCAD, this visualization is possible only after the 3D mesh is built, precluding an accurate geometrical modeling of the simulation domain.

2.2 Tetrahedral meshes

Many forms of geoscientific analysis seek to collect data about spatial objects and domains such as features of the solid earth (aquifers), oceans (currents) or atmosphere (weather fronts), which fill or enclose a 3D space. A complete geometric representation of these domains requires the definition of each known location in a x,y,z coordinate system (Lattuada and Raper, 1996). After collecting data about the geometry of a simulation domain, its discretization is required to apply numerical methods used to solve specific governing equations. In fact, numerical methods for the solution of partial differential equations are irreplaceable means of simulating a wide variety of physical phenomena in scientific computing and they represent the most challenging application of mesh generation (Shewchuk, 1999). The terms grid and mesh are used interchangeably, with identical meaning, throughout this thesis, according to Thompson et al. (1999).

A mesh consists of nodes at specific locations in space that are connected to form elements. These elements can be triangles or quadrilaterals in 2D models and tetrahedra, hexahedra, prisms, or pyramids in 3D models (Gable, 2000). Two main types of meshes exist, structured and unstructured. The fundamental difference between structured and unstructured meshes is the ordering of the nodes to form the elements, or cells, within the grid (Thompson et al., 1999). In other words, this difference usually extends to the shape of the elements: structured meshes typically use quadrilaterals or hexahedra, while unstructured meshes use triangles or tetrahedra (Bern and Plassmann, 1999). Structured meshes have a simpler geometry and they are characterized by a foreseeable rule that describes nodal connectivity and that can be used to find the neighbors to any node in the mesh. In contrast, unstructured mesh connectivity needs to be explicitly stored, because there is not a repeatable pattern describing nodal connectivity, as the index of neighbor nodes changes all over the domain. However, structured meshes lack the flexibility in fitting a domain with a complicated shape, while unstructured meshes can provide multiscale resolution and conformity to complex geometries (Shewchuck, 1999). Thus, unstructured meshes are usually preferred to discretize complex domains. In general, simply fitting the domain is not enough, because a finite element mesh must also use elements of appropriate size and shape, and these quantities may vary over the mesh (Bern and Eppstein, 1995). Well-studied geometric constructions such as Delaunay triangulation are central to unstructured mesh generation (Bern and Plassman, 1999).

The Delaunay approach is a popular technique to build unstructured meshes. It had been presented in 1934 by Boris Delaunay, who developed its theory for triangles in 2D. The basis of the Delaunay triangulation is a geometrical concept: circumcircles of triangles enclose no nodes in its interior, but the three vertices of each triangle. The Delaunay triangulation is related to the Voronoi diagram, which is its dual representation. Given a set of nodes, the Voronoi diagram subdivides the space into tessellations, in which each tile is the space closer to a particular node than any other node. Voronoi diagrams are named after Georgy Fedoseevich Voronoi, who defined and studied the general n-dimensional case in 1908. Nevertheless, a systematic approach to the problem of connecting a set of points dates back to 1850 and is due to Dirichlet, who proposed a way to subdivide a given domain into a set of convex polygons (Lattuada and Raper, 1996). The duality between the Delaunay triangulation and the Voronoi diagram is represented by the fact that the circle circumscribed about a

Delaunay triangle has its center at the vertex of a Voronoi polygon. The extension of the triangulation to 3D leads to the definition of circumspheres and tetrahedra, such that the circumsphere through each tetrahedron contains no points other than the tetrahedron vertices. Then, the boundary that forms a face of a Voronoi polyhedron in 3D (Figure 2.7) is equidistant between the two points it separates and it is perpendicular to the segment joining these two points (Thompson et al., 1999). A complete and clear summary of all aspects of Delaunay triangulation and algorithms is presented by Shewchuk (2005).

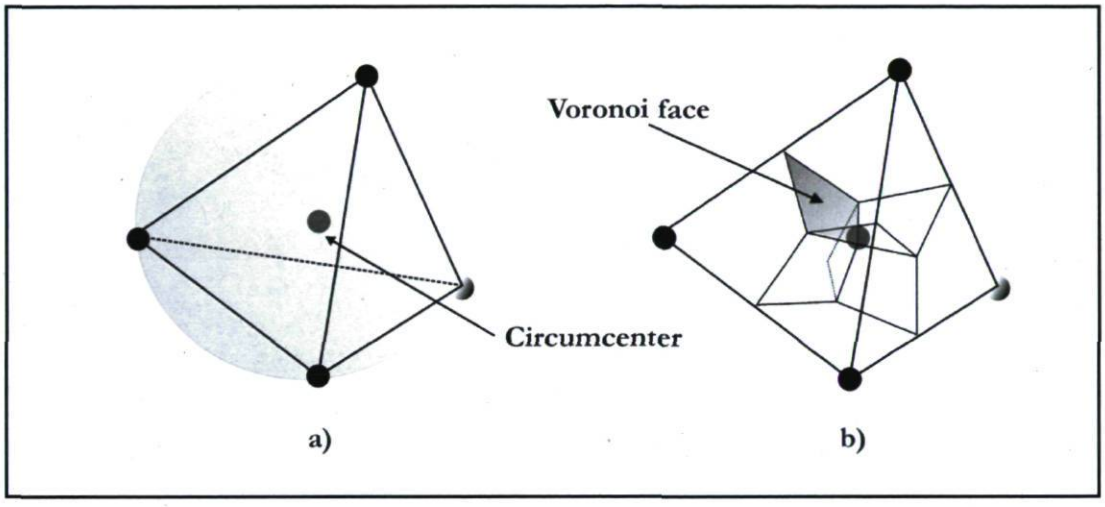

Figure 2.7 - a) Tetrahedron and circumscribed sphere and b) tetrahedron and Voronoi faces

The Delaunay triangulation and the Voronoi diagram are suitable for numerical methods based on the Control Volume Finite Element method (see Chapter 3), which requires the definition of a finite element mesh and a control volume mesh. Thus, the Delaunay triangulation allows for building the tetrahedral finite element mesh, while the Voronoi diagram is used for the definition of the control volumes associated to each node in the mesh. A tetrahedral Delaunay mesh is chosen for the purpose of this work for two main raisons. First, it is more flexible than structured meshes, which generate difficulties when attempting to model a general 3D domain with fractures (Taniguchi and Fillion, 1996). Since the modeling approach developed here is intended for investigations in complex fractured geological media, an unstructured tetrahedral mesh is preferred. In addition, a tetrahedral mesh can be easily used in combination with the Control Volume Finite Element method, which is the numerical method implemented in

HydroGeoSphere. Moreover, to increase the accuracy of numerical results, meshes can be refined. Mesh refinement involves the addition of points into regions where adaptation is required, providing additional resolution at the expense of increasing the number of points in the computation (Thompson et al., 1999). Thus, although high resolution meshes offer the best geometrical representation of real geological systems and the most accurate solutions, they contain a larger number of elements and they require more computer memory and computational time. Therefore, a compromise is necessary to find the optimal resolution according to the goals of modeling tasks. An unstructured tetrahedral mesh, as used here, is the best choice to create an adaptive mesh refinement, which does not propagate to the mesh boundaries.

2.2.1 The LaGriT mesh generation software

The tetrahedral mesh is generated with the LaGriT software, developed in the 1990s at Los Alamos National Laboratory (LANL, New Mexico). LaGriT is a collaborative product of the Applied Physics, Theoretical, Earth and Environmental Science, and Computing, Information, and Communications Divisions at Los Alamos. LaGriT is a library of user callable tools that provide mesh generation for a variety of applications, such as geology. There is no GUI interface. Thus, meshes are in general visualized with the General Mesh Viewer (GMV) software, also developed at Los Alamos National Laboratory. In addition, LaGriT writes files to be read by the Tecplot graphics package, which is also used for the visualization of simulation output files generated by the HydroGeoSphere numerical code. Although software like LaGriT helps automate complex meshing operations, generating successful meshes still relies on a series of judgment calls by an expert, who must weigh many tradeoffs (Gable, 2000). Among possible mesh generators investigated, LaGriT has been chosen for this work because it offers the greatest number of advantages. The main advantage is its module designed to import GOCAD surface files. Moreover, LaGriT maintains the geometric integrity of the geologic framework and produces optimal Delaunay tetrahedral grids (Cherry et al., 1996).

2.2.1.1 LaGriT tools

When working with LaGriT, data structures called Mesh Objects must be defined. A Mesh Object, or simply MO, contains all the information necessary to define a mesh, such as the number of nodes, elements, edges, faces and other default attributes. Attributes can also be added by the user. Mesh Objects can be made of tetrahedra, hexahedra, prisms, pyramids, triangles, squares or lines. Hybrid meshes can also be built with LaGriT. In general, a MO is defined by an enclosing volume and, eventually, interior surfaces. Nodes are distributed within the volume and then connected into elements. It should be noted that several Mesh Objects can be handled in the same LaGriT work session. Moreover, nodes can be copied from one MO to another, even if they are already connected into elements, because nodes can be selected separately from elements.

Among all LaGriT commands used to build a tetrahedral mesh suitable for the applications envisaged in this work, some of them should be mentioned for their essential role in the mesh generation procedure. More specifically, they are:

1. *Read:* this command and its options for reading the supported file formats *gocad* (*.ts) and *avs* (*.avs) are used to import into LaGriT triangulated fracture surfaces and borehole curves, respectively.

2. *Refine:* this command, with its *octree* refine option, is used to refine hexahedral meshes. An octree is a tree data structure in which each internal node has up to eight children. Thus, the octree refinement algorithm applied to 8-nodes hexahedra will create eight smaller hexahedral elements (Figure 2.8).

3. *Compute:* this command computes various attributes and functions based on one or more Mesh Objects. It is applied here to compute the *distance_field* (*dfield* attribute) between a source Mesh Object, MO_source, and a sink Mesh Object, MO_sink. The terms MO_source and MO_sink are simply introduced to make a distinction between the two Mesh Objects considered for the distance computation. The command evaluates the minimum distance from any node in MO_source to every node in

MO_sink and creates a *dfield* attribute in the MO_sink. If the tetrahedral mesh is the MO_sink, the *dfield* attribute is used to identify and select the tetrahedral elements that are within a user defined distance from fractures and boreholes, which represent, respectively, the triangular and linear MO_source.

4. *Connect:* this command connects nodes into a Delaunay tetrahedral mesh. It is based on the criterion that the circumsphere defined by each tetrahedron contains no mesh nodes in its interior. A volume test is also performed by the algorithm to look for near zero-volume tetrahedra.

5. *Extract:* this command produces a 2D MO from a 3D MO by picking up all nodes and 2D faces lying on a user defined interface. Fracture surfaces are considered here as the interfaces. Thus, the command is used to get the triangular mesh representing each fracture incorporated in the 3D tetrahedral mesh.

6. *Interpolate*: this command interpolates attribute values from nodes or elements of a MO_source to node or element attributes of a MO_sink. The interpolation option considered here is called *voronoi*. For each node in MO_sink, it finds the closest node in MO_source and it assigns the attribute value from MO_source to MO_sink. In this work, the MO_source is represented by the tetrahedral mesh, while the MO_sink are boreholes and fractures, respectively. Thus, this command finds the global (tetrahedral) nodal numbering of fractures and boreholes integrated in the 3D tetrahedral mesh.

7. *Dump*: this command produces output files from a specific MO. It is used here to create ASCII files with nodal coordinates and mesh connectivity. Moreover, it generates compatible files for graphic packages supported by LaGriT, like GMV and Tecplot.

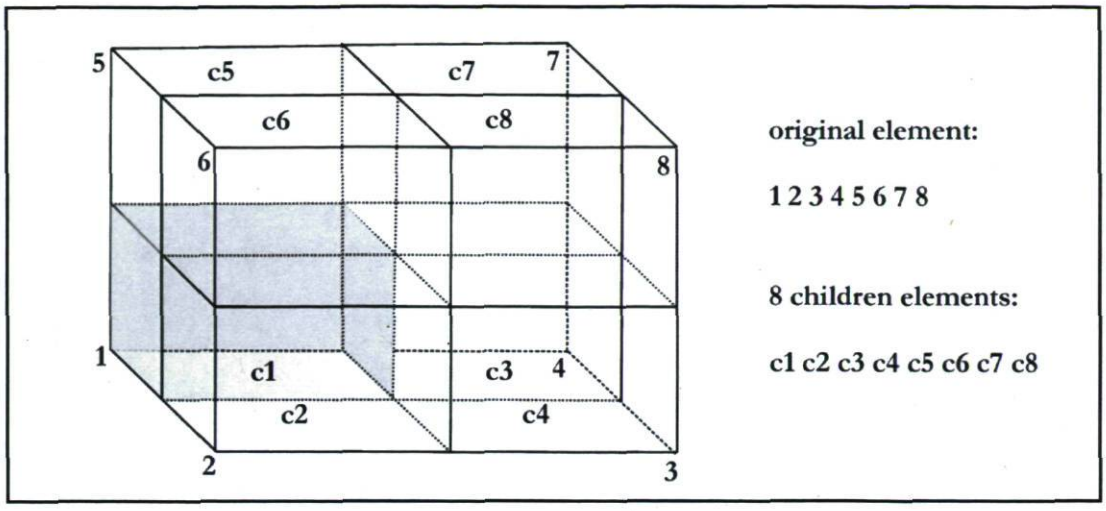

Figure 2.8 - Octree refinement: block c1 is highlighted in grey

2.2.1.2 Mesh generation with LaGriT

The procedure adopted here to generate the mesh for a fractured geological medium uses the current LaGriT capabilities. The mesh generation procedure is implemented by executing several LaGriT input files, which contain a sequence of required commands. An example is presented in Appendix A. The procedure is summarized by the seven following steps:

1) Import into LaGriT the files containing fractures and boreholes information

The first step in the mesh generation process is the application of the LaGriT module capable of reading the GOCAD TSurf files (*.ts). Hence, fracture surfaces built in GOCAD are imported into LaGriT as sheets, which are topologically 2D, but geometrically 3D objects constituted by a collection of connected triangles. The edge length of triangles defines the smallest tetrahedral edge near the fractures, to obtain a well-graded mesh where the size of tetrahedral elements gradually increases away from fractures. Boreholes, represented by open curves, are also included in the mesh generation process. Spatial coordinates of borehole axes are imported into LaGriT through AVS (*.avs) files, such that a curve of regularly spaced nodes will represent each borehole. In analogy to fractures, the nodal spacing along a borehole axis defines the smallest tetrahedral edge around it.

2) Create a hexahedral mesh covering the domain of interest

The strategy for building the tetrahedral mesh is based on this step, whose goal is to generate a hexahedral nodal distribution to be concatenated with the nodes of the GOCAD triangulated surfaces and the borehole curves. Nodes of the hexahedral mesh actually represent the porous rock matrix. The basic idea is to create an appropriate distribution of nodes, which will be later connected into a tetrahedral mesh. A regular nodal distribution is actually preferred to a random nodal distribution. In fact, in a randomly distributed set of nodes the distance between nodes varies significantly and consequently the generated tetrahedra will not have a homogeneous size, which is actually a suitable property of the final computational mesh (Lepage and Mallet, 2001). That is why the hexahedral mesh is built: it is used to sample the simulation domain with a regular nodal distribution. This mesh represents the background mesh that characterizes the nodal spacing far from the regions of interest.

3) Refine the hexahedral elements that are close to fractures and boreholes

The *octree* refinement algorithm is applied to refine the background hexahedral mesh built in the previous step. The idea is to develop a suitable nodal distribution, where a high density of nodes is created near fractures and boreholes, while low density is kept far from them. To select the zones to be refined, the *compute* command is applied. The hexahedral elements within the distance entered by the user are selected for refinement (Figure 2.9). This distance should be carefully chosen in order to avoid generating an excessively refined mesh, which will increase the computation effort and memory requirements. In fact, the number of elements increases after each refinement step, as each hexahedron is subdivided into 8 smaller elements. Hexahedra are split up recursively until the mesh reaches the desired level of resolution. With a few consecutive refinement steps, it is possible to obtain a gradual and local variation in element size, just where needed (Figure 2.10). The number of refinement steps clearly depends on the desired resolution for the final computational mesh, which varies according to the hydrogeological modeling goals.

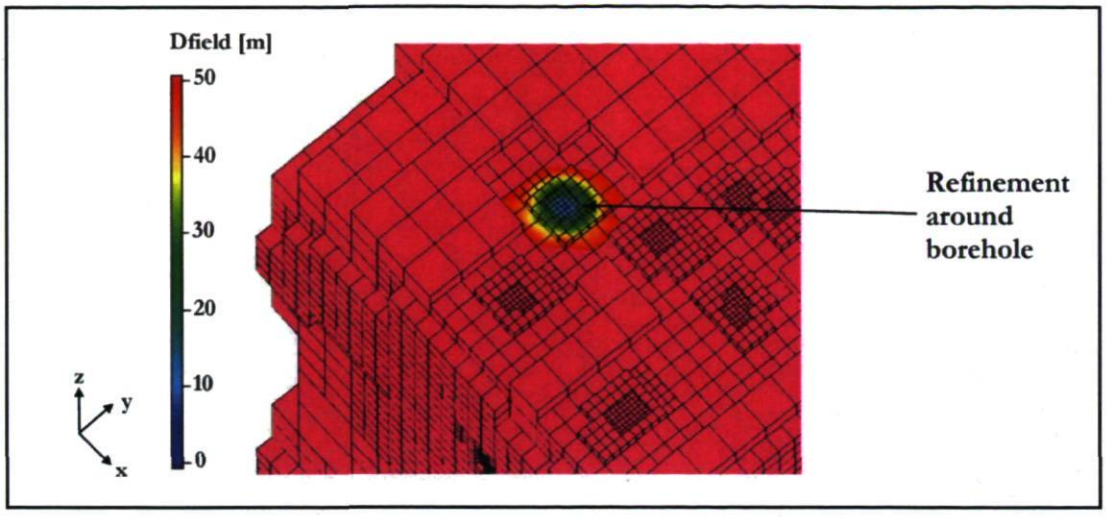

Figure 2.9 - *Dfield* element attribute and refinement around a borehole

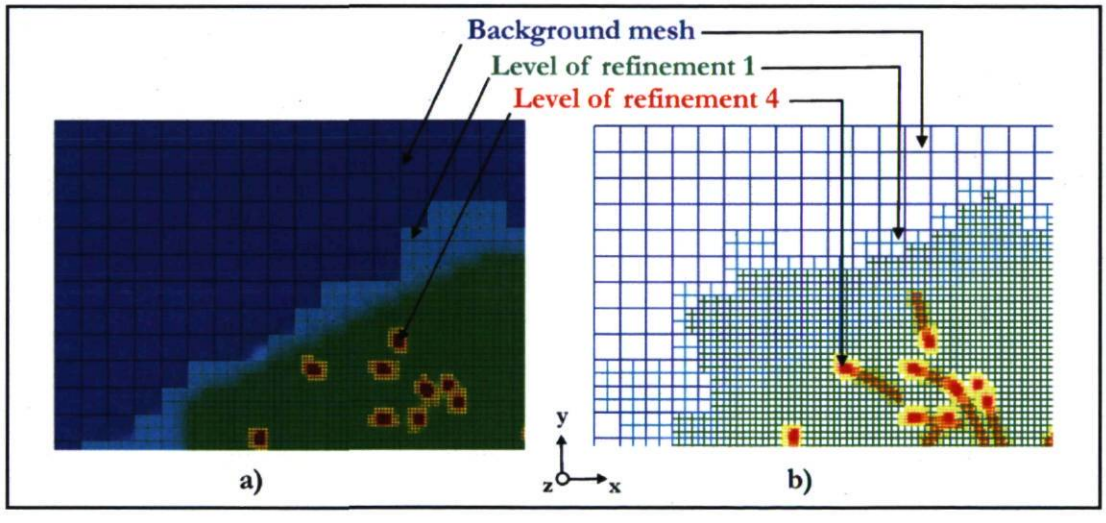

Figure 2.10 - Visualization of a refined hexahedral mesh: a) faces and edges and b) only edges

4) Remove hexahedral elements close to fractures and boreholes

The hexahedral mesh built and refined in the previous steps covers the whole simulation domain. Thus, it is clear that some hexahedral elements overlap fracture triangular elements and borehole linear segments. As the objective is to concatenate all nodes together, it is necessary to remove from the hexahedral mesh the nodes, as well as the elements, that are too close to fractures and boreholes. Elements and nodes within a specific distance from fractures

and boreholes are selected for removal. Then, these elements and nodes are deleted from the hexahedral mesh, such that a hole is created (Figure 2.11). It is obvious that the distance for removal depends on the mesh resolution. In general, this distance should be at least equal to the minimum tetrahedral edge length desired for that specific location in the mesh.

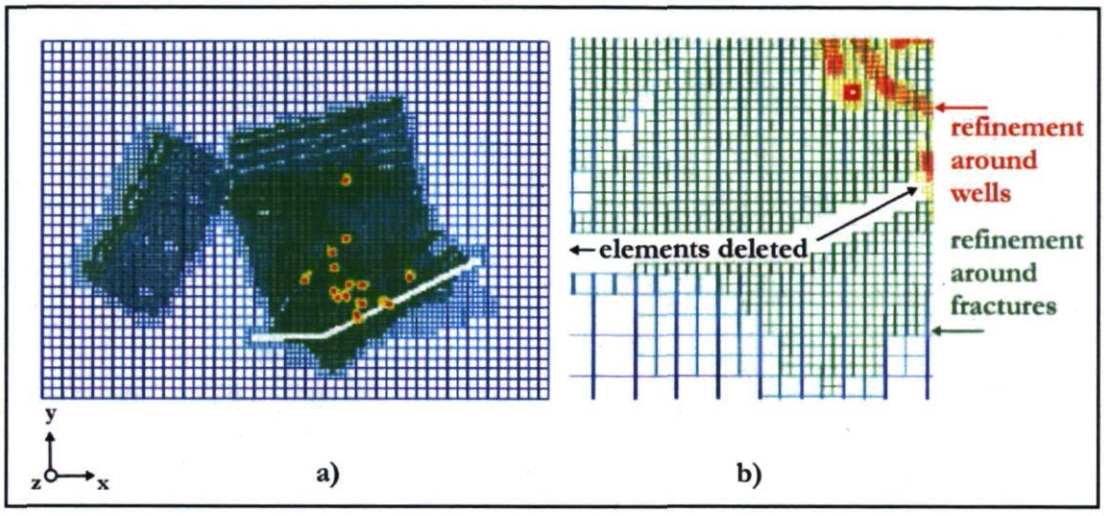

Figure 2.11 - Refined hexahedral mesh with hole around a fracture: a) overview of the whole mesh and b) close-up

5) Connect all nodes into tetrahedra

A tetrahedral Mesh Object must be created. When it is created, it is still empty, because it does not contain any nodes. Then, nodes from other MOs are copied into this new tetrahedral MO (Figure 2.12). Nodes come from three different meshes: hexahedral, triangular, and linear. These meshes are all Mesh Objects in the same LaGriT session and they represent, respectively, the porous rock matrix, the fractures, and the boreholes. The tetrahedral mesh just created is the fourth mesh type in the same LaGriT session. All nodes copied to the tetrahedral mesh are now connected using the Delaunay algorithm available in LaGriT (Figure 2.13). Previous steps have generated an optimal distribution of nodes, such that the execution of the Delaunay algorithm will not run into connection problems causing the circumsphere criterion to fail (see Section 2.2.1.1). This mesh generation procedure ensures that each triangle on the fracture surfaces corresponds to only one face of the surrounding tetrahedra. It is clear

that the quality of the triangulated surfaces becomes an important factor influencing the final 3D tetrahedral mesh generation. If the quality of these surfaces is very low, respecting their triangulation will automatically create tetrahedra with a low aspect ratio (Lepage and Mallet, 2001).

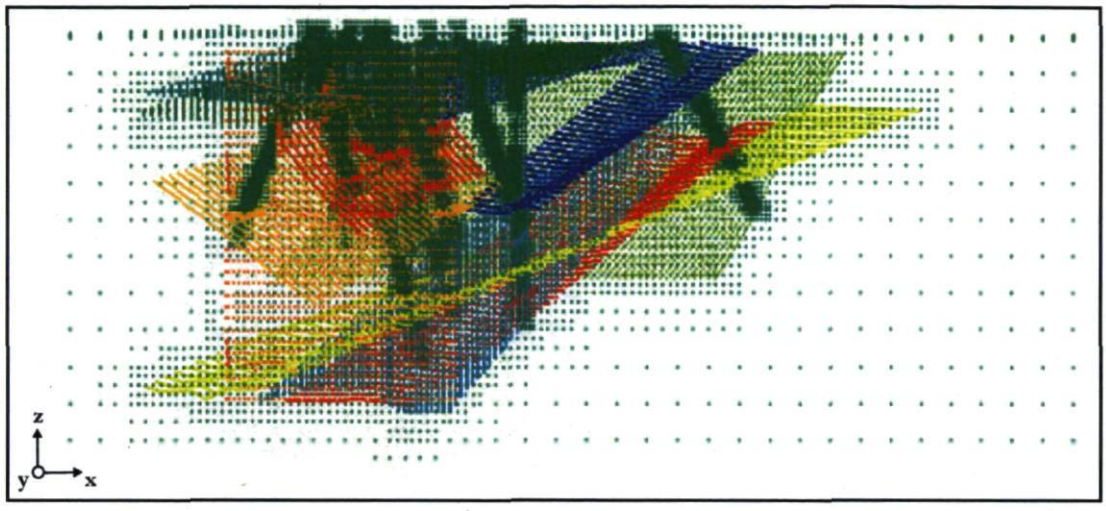

Figure 2.12 - Nodes in a tetrahedral Mesh Object

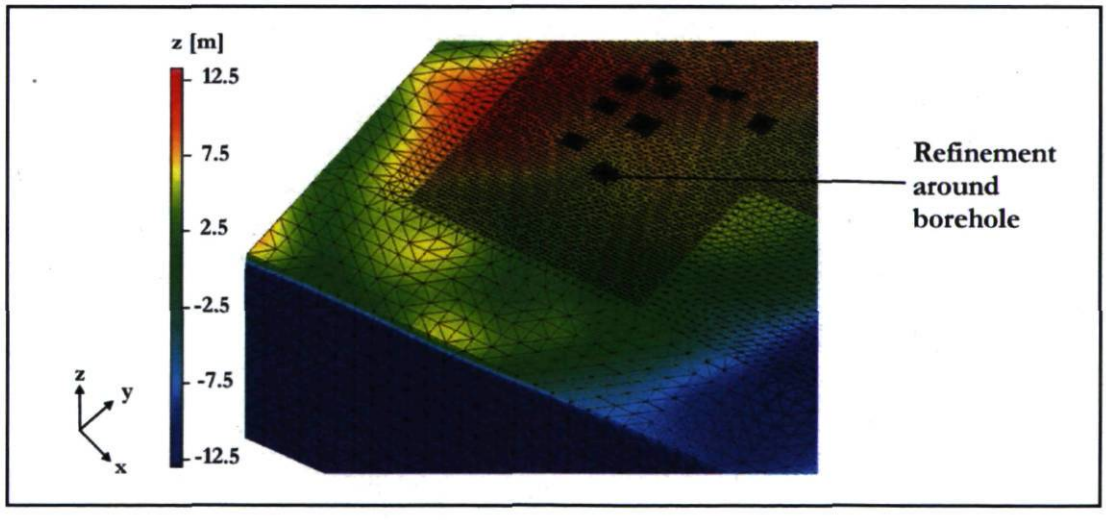

Figure 2.13 - Portion of a tetrahedral mesh

6) Extract 2D triangulated surfaces from 3D tetrahedral mesh

The *extract* command requires the definition of two geometric regions around each fracture, such that the fracture surface corresponds to the interface between these regions (see Section 2.2.1.1). This geometric definition is done by using existing LaGriT operators, which are based on the notion of surface inward-pointing normal and surface outward-pointing normal. As a result, the 3D space containing the inward-pointing normal and the 3D space containing the outward-pointing normal are defined as two distinct regions separated by the fracture (Figure 2.14). This geometric definition works both for bounded and unbounded regions. In fact, even if the fracture does not extend to the external domain boundary, which can have any kind of shape, fracture borders are automatically projected to this boundary, as shown by the dashed lines in Figure 2.14. Then, the *extract* LaGriT command is executed and the tetrahedral faces lying on the fracture surface are identified. Although a 2D triangular Mesh Object representing the discrete fractures is obtained, its nodal numbering is independent from the 3D tetrahedral MO. The "extracted" surface has its own local nodal numbering, although it is necessary to find the global numbering, which is represented by the nodal numbering of the tetrahedral mesh. In fact, the global numbering is used to identify faces of tetrahedra that should act as fractures during simulations. By applying the *interpolate/voronoi* LaGriT command, the global numbering of fractures and boreholes is printed out.

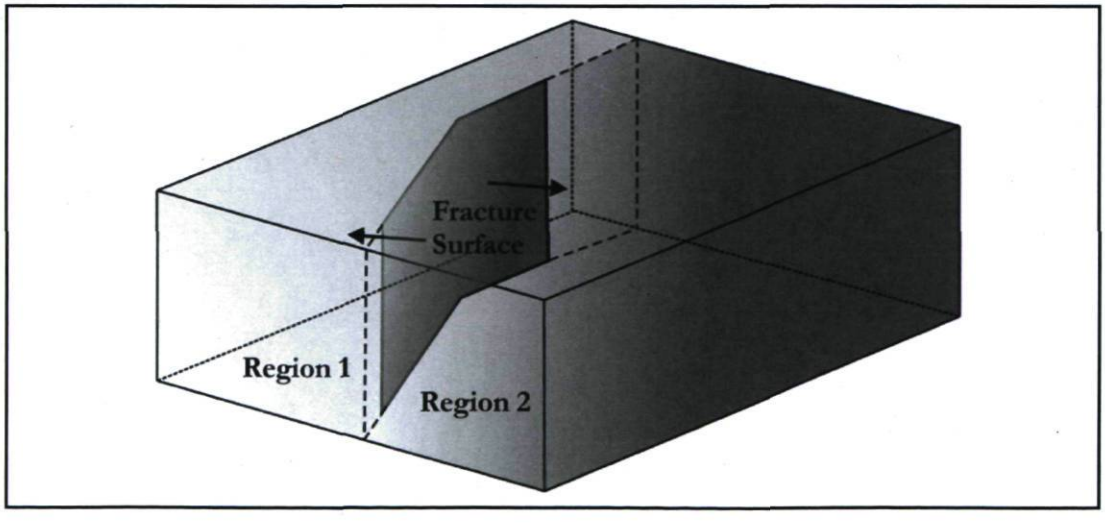

Figure 2.14 - Regions defined through a surface fracture

7) Create output files for every mesh

Several *.txt files are generated, one for each mesh. One file contains the nodal spatial coordinates and the connectivity of the tetrahedral mesh. Moreover, one file is created for the triangular mesh of each discrete fracture included in the model. Finally, each borehole is represented by a file containing the index of nodes describing its axis.

The seven-step procedure just described creates a suitable mesh that captures the complexity of a fractured geological medium with discrete fractures and boreholes. It should be mentioned that the topography of the simulation domain, as well as any other surface, like horizons separating different stratigraphic units, can also be included in the Geomodel and in the tetrahedral mesh generation using exactly the same method described for fracture surfaces. Once all seven steps are completed, the HydroGeoSphere numerical code can be executed. Output text files generated by LaGriT become input files for the pre-processor of the numerical code, which has been modified to handle such LaGriT input files.

Chapter 3

Numerical model

To model complex physical processes, mathematical tools and computer simulations are required. To solve the partial differential equations describing specific physical phenomena, numerical techniques are generally used. Mathematical equations are translated into a specific numerical code by computer programming. The code is then executed to simulate physical phenomena, such as groundwater flow and contaminant transport, on a spatially discretized domain.

The purpose of this chapter is to present the enhanced numerical code version developed during this research. The code HydroGeoSphere (Therrien et al., 2007) is used here and it is presented in Section 3.1. Then, a detailed description and analysis of two different ways to evaluate the fluid conductance matrix are presented in Section 3.2. Finally, the most important elements integrated in the numerical code are listed and described in Section 3.3. Two test cases are also presented at the end of the chapter to verify the right evaluation of the fluid conductance matrix for tetrahedral meshes.

3.1 HydroGeoSphere

The choice of a specific numerical code depends on the physical processes that have to be simulated and on the conceptual model selected for the study. The numerical model chosen here is called HydroGeoSphere (Therrien et al., 2007), which is a numerical simulator specifically developed for supporting water resource and engineering projects pertaining to hydrologic systems with surface and subsurface flow and contaminant transport components. HydroGeoSphere has been developed from the FRAC3DVS code. The Control Volume-Finite Element method, CVFE, constitutes the basis of the numerical solution. In this method, a finite volume subgrid is constructed as a complement to the finite element grid (Geiger et al., 2004). The Control Volume technique produces discretized equations by applying physical conservation laws to control volumes surrounding mesh nodes. The discretized equation for a given node consists of a term describing the change in fluid mass storage for the control volume associated with that node. This term is balanced by the divergence of the fluid mass flux in the same volume. In addition, the Finite Element technique allows for the representation of complex geometrical domains with ease and efficiency. Thus, the CVFE method combines advantages from both techniques. The CVFE method applied to numerical modeling in hydrogeology is discussed in Forsyth (1991) and Letniowski and Forsyth (1991). Its implementation in HydroGeoSphere is presented in Therrien and Sudicky (1996) and Therrien et al. (2007). HydroGeoSphere solves fully or variably saturated subsurface flow and surface flow equations, as well as solute transport and heat equations. Solution options also include density-dependent flow and 1D hydromechanical coupling. The matrix equations arising from the discretization of governing equations are solved by a preconditioned iterative solver. Newton-Raphson or Picard linearization methods are applied if equations are non linear. Depending on the problem to be solved, 3D finite elements are used to discretize governing equations for porous-media and dual continua, 2D finite elements for discrete fractures and surface flow, 1D linear elements for wells, channels and drains. The current implementation of HydroGeoSphere assumes that the subsurface flow equation in the porous medium is always solved during a simulation.

In the specific context of this thesis, fully-saturated conditions are always considered. Simulations are focused on the solution of subsurface flow and solute transport equations

through porous media, discrete fractures and wells. The fluid is assumed to be essentially incompressible and the porous medium and fractures non-deformable.

3.1.1 Governing equations

The governing equation for 3D transient subsurface flow in fully-saturated porous media characterized by hydraulic conductivity K and specific storage S_s is:

$$\nabla\left(K_{ij}\nabla h\right)\pm\Gamma = S_s\frac{\partial h}{\partial t} \tag{3.1}$$

where Γ is a volumetric flux representing a source (positive) or a sink (negative) to the porous medium system. The first term on the left hand side of Eq.(3.1) represents the divergence of the fluid flux. According to the Gauss's theorem, a triple integral over a closed bounded region (volume) can be transformed into a surface integral over the boundary surface of the same region. Therefore, it is possible to interpret physically the divergence term applied to the control volume as the fluid flux mass balance orthogonal to the control volume surface. Eq.(3.1) describes the equivalence between the change in fluid storage and the mass balance over a control volume. The analogous 2D equation for fully-saturated flow in a discrete fracture of aperture 2b is:

$$\nabla(2b)\left(K_{f_{ij}}\nabla h\right)+q_{n|I^+}+q_{n|I^-}\pm\Gamma = (2b)S_{sf}\frac{\partial h}{\partial t} \tag{3.2}$$

Eqs.(3.1) and (3.2) are linked via the fluid leakage fluxes $q_{n|I^+}$ and $q_{n|I^-}$ across the two surfaces I^+ and I^-, respectively, of a fracture. Because in HydroGeoSphere, the finite elements representing fractures are generated such that they correspond to sides of three-dimensional finite elements, the nodes comprising fracture elements are common to nodes comprising porous matrix elements (Therrien and Sudicky, 1996). The commonality of these nodes ensures the continuity of hydraulic head at fracture-matrix interfaces. Also, by superimposing the contributions at each node from both fracture and porous medium, there is no need to explicitly calculate fluid leakage terms appearing in Eq.(3.2).

The CVFE method and the standard Galerkin technique are used in HydroGeoSphere to discretize the governing equations (Therrien and Sudicky, 1996; Therrien et al., 2007). According to the CVFE approach, a volume of influence is assigned to each node in the mesh which is referred to as a control volume. The Galerkin method requires defining basis functions, which depend on the element type and on the order of approximation chosen (linear, quadratic or cubic functions). In this context basis functions are linear and satisfy the following properties:

$$\begin{aligned} N_i &= 1 \quad \text{at node } i \\ N_i &= 0 \quad \text{at all other nodes} \\ \sum_j N_j &= 1 \quad \text{everywhere in the domain} \end{aligned} \tag{3.3}$$

The function N is used to approximate the unknown, for example the hydraulic head h:

$$h(x,t) \cong \hat{h} = \sum_j N_j(x) h_j(t) \tag{3.4}$$

where $h_j(t)$ are nodal values of hydraulic head at time t. By replacing the exact value h by its approximation $\hat{h}$ in Eq.(3.1), multiplying by the weighting function N_i, and forcing to zero the integral over the volume of interest V, it is possible to write:

$$\int_V \left[S_s \frac{\partial \hat{h}}{\partial t} - \nabla\left(K_{ij} \nabla \hat{h} \right) \right] N_i dV = 0 \tag{3.5}$$

where the source/sink term Γ is neglected for the sake of clarity. Eq.(3.5) is now considered applied to node i and its nodal control volume v. If a finite difference approximation is used, it is possible to write the time derivative as:

$$\int_v \left[S_s \frac{\partial \hat{h}}{\partial t} \right] N_i dv = S_s \frac{h^{t+1} - h^t}{\Delta t} \int_v N_i \, dv \tag{3.6}$$

where the integral of the weighting function N_i corresponds to the control volume associated to node i:

$$\int_v N_i \, dv = v_i \tag{3.7}$$

By using the divergence theorem, the flux term is written as:

$$\int_v -\nabla\left(K \nabla \hat{h} \right) N_i dv = \int_v \nabla N_i K \nabla \hat{h} \, dv - \int_B q^* N_i dB \tag{3.8}$$

The last term on the right-hand side of Eq.(3.8) is the integral of the fluid flux normal to the boundary B of control volume v and it is assumed to be zero (Therrien et al., 2007). From Eq.(3.3), the following relations can be defined:

$$N_i = 1 - \sum_{j \neq i} N_j$$
$$\nabla N_i = -\nabla \sum_{j \neq i} N_j \tag{3.9}$$

After a few mathematical steps (Therrien et al., 2007), it is possible to express the flux term as a function of the hydraulic head difference between node i and its neighbor nodes:

$$\int_v \nabla N_i \cdot K \cdot \nabla \left(\sum_{j \neq i} N_j \right) \left(h_j - h_i \right) dv = \sum_{j \in \eta_i} \int_v \nabla N_i \cdot K \cdot \nabla N_j \left(h_j - h_i \right) dv \tag{3.10}$$

By defining:

$$\gamma_{ij} = \int_v \nabla N_i K \nabla N_j dv \tag{3.11}$$

the discretized porous medium subsurface flow equation finally becomes:

$$\sum_{j \in \eta_i} \gamma_{ij} \left(h_j^{t+1} - h_i^{t+1} \right) = S_s \left(h_i^{t+1} - h_i^t \right) \frac{v_i}{\Delta t} \tag{3.12}$$

where η_i is the set of nodes connected to node i. It is obvious that the nodes not included in η_i will not contribute to the change in storage or fluid flow at node i. The term γ_{ij} contains the integral of the standard finite element basis functions and it is sometimes referred to as the transmissibility (for example, Forsyth, 1991; Letniowski and Forsyth, 1991; Gable et al., 1996b). It is possible to observe that the sign of γ_{ij} in Eq.(3.12) determines the direction of fluid flow: if γ_{ij} is negative, flow from the node with lower hydraulic head toward the node with higher hydraulic head can be numerically simulated, even if this is physically unrealistic. Further details on the definition of transmissibilities are given in Section 3.2. Equations for discrete fractures are analogous, but the volume v_i is replaced by fracture area a_i and basis functions to evaluate $\gamma_{f_{ij}}$ are now defined on 2D triangular finite elements. Therefore, the subsurface flow discretized equation for a fracture with aperture $2b$ is:

$$S_{s_f} \left(h_{f_i}^{t+\Delta t} - h_{f_i}^t \right) \frac{a_i \cdot 2b}{\Delta t} = \sum_{j \in \eta_{f_i}} \gamma_{f_{ij}} \left(h_{f_j}^{t+\Delta t} - h_{f_i}^{t+\Delta t} \right) \tag{3.13}$$

where η_{f_i} is the set of nodes connected to fracture node i through 2D fracture elements.

To describe solute transport in discretely-fractured porous media, two equations are required. These equations are similar to those presented for subsurface flow problem. The propagation of a solute characterized by relative concentration c through a 3D porous medium is described by the following equation:

$$\theta\frac{\partial c}{\partial t}+\frac{q_i}{R}\nabla c-\nabla\left(\frac{\theta D_{ij}}{R}\nabla c\right)+\theta\lambda c=0 \qquad i,j=1,2,3 \qquad (3.14)$$

where q_i is the Darcy flux computed during the flow simulation, θ is the porosity of the porous medium, D_{ij} is the hydrodynamic dispersion coefficient, R is the retardation factor if solute is adsorbed onto solid porous medium particles, and λ is the decay coefficient for radioactive or biodegradable solutes. In Eq.(3.14) it is possible to identify, from left to right, the transient term, which represents the accumulation of solute in a control volume, the advection term, which describes the movement of solute due to the existence of a velocity field, and the hydrodynamic dispersion term, which describes both molecular diffusion and mechanical dispersion transport processes. Similarly to transport in 3D porous media, the 2D transport equation in discrete fractures is:

$$\theta\frac{\partial c_f}{\partial t}+\frac{q_{f_i}}{R_f}\nabla c_f-\nabla\left(\frac{\theta D_{f_{ij}}}{R_f}\nabla c_f\right)+\theta\lambda c=0 \qquad i,j=1,2 \qquad (3.15)$$

Molecular diffusion is a physical process that causes solutes to move from regions of higher concentration to regions of lower concentration, by random molecular motion. This physical phenomenon is mathematically described by Fick's first law, which expresses the diffusive flux by:

$$J_d=-\theta D_d\nabla c \qquad (3.16)$$

where D_d is the molecular diffusion coefficient, which depends on the free-diffusion solute coefficient D_0 and on the tortuosity τ of the porous medium. Tortuosity is a parameter describing the ratio between straight line and real flow path-lines. As flow path-lines in porous media are sinuous, the tortuosity is smaller than 1. The diffusion coefficient is therefore expressed by:

$$D_d=D_0\tau \qquad (3.17)$$

Mechanical dispersion is related to velocity deviations from the average groundwater velocity. These deviations are caused by varying pore sizes, roughness of pore channels, and pore

connectivity. As a result, flow path-lines are sinuous and velocity varies both in magnitude and direction across any pore cross-section. These effects are represented by the dispersivity, which is indicated by the parameter α. Mechanical dispersion is also modeled as a Fickian process. Field and laboratory experience shows that the rate of mixing is greater in the direction of flow than transverse to this direction, and the dispersion coefficient is proportional to the flow rate (Charbeneau, 2000). Various empirical equations exist to evaluate dispersivity values (Neuman, 1990; Gelhar et al., 1992; Xu and Eckstein, 1995). Molecular diffusion and mechanical dispersion are combined into a single hydrodynamic dispersion coefficient, which is defined as (Bear, 2007):

$$D_{ij} = \alpha_T q \delta_{ij} + (\alpha_L - \alpha_T)\frac{q_i q_j}{q} + \tau D_o \delta_{ij} \tag{3.18}$$

where δ_{ij} is the Kronecker delta and subscripts L and T indicate longitudinal and transversal dispersivity, respectively. For Cartesian coordinates and velocity vector q with components q_x, q_y, and q_z, it is possible to obtain:

$$D_{xx} = \alpha_T |q| + (\alpha_L - \alpha_T)\frac{q_x^2}{|q|}$$

$$D_{yy} = \alpha_T |q| + (\alpha_L - \alpha_T)\frac{q_y^2}{|q|} \tag{3.19}$$

$$D_{zz} = \alpha_{TV} |q| + (\alpha_L - \alpha_T)\frac{q_z^2}{|q|}$$

The discretization scheme for the transport equations is identical to that used for the subsurface flow problem, such that the solute equation in a 3D porous medium becomes:

$$\left(c_i^{t+\Delta t} - c_i^t\right)\frac{v_i}{\Delta t} = \sum_{j\in\eta_i} c_{(ij+1/2)}^{t+\Delta t} q_{(ij+1/2)}^{t+\Delta t} + \sum_{j\in\eta_i} \chi_{ij}\left(c_j^{t+\Delta t} - c_i^{t+\Delta t}\right) + R\lambda c_i v_i \tag{3.20}$$

The term $q_{(ij+1/2)}^{t+\Delta t} = \gamma_{ij}\left(h_j^{t+\Delta t} - h_i^{t+\Delta t}\right)$ represents the fluid flux at the interface between nodes i and j and is obtained from the flow solution. The term $c_{(ij+1/2)}$ depends on the type of advective weighting used. If upstream weighting is used, as in the majority of simulations presented in Chapters 4 and 5, the concentration will be:

$$c_{(ij+1/2)} = c_{ups} = c_j \quad \text{if} \quad \gamma_{ij}\left(h_j - h_i\right) > 0 \tag{3.21a}$$

$$c_{(ij+1/2)} = c_{ups} = c_i \quad \text{if} \quad \gamma_{ij}\left(h_j - h_i\right) < 0 \tag{3.21b}$$

The term χ_{ij} in Eq.(3.20) is the transmissibility associated with the segment joining nodes i and j. Its expression is analogous to Eq.(3.11) used for subsurface flow equation, but here the hydraulic conductivity is replaced by the hydrodynamic dispersion coefficient D_{ij}:

$$\chi_{ij} = \int_v \nabla N_i D_{ij} \nabla N_j dv \tag{3.22}$$

Similarly to Eq.(3.20), the discretized solute transport equation for a fracture of aperture $2b$ is:

$$\left(c_{f_i}^{t+\Delta t} - c_{f_i}^{t}\right)\frac{2b \cdot a_i}{\Delta t} = (2b) \cdot \sum_{j \in \eta_{f_i}} c_{f(ij+1/2)}^{t+\Delta t} q_{(ij+1/2)}^{t+\Delta t} + \sum_{j \in \eta_{f_i}} \chi_{f_{ij}} \left(c_{f_j}^{t+\Delta t} - c_{f_i}^{t+\Delta t}\right) + R\lambda c_i a_i \tag{3.23}$$

where all parameters have already been defined.

3.1.2 Numerical solution

As specific details of the numerical solution in HydroGeoSphere are presented in Therrien et al. (2007), only the features relevant to this work are mentioned here. The discretized equations form a matrix system, which is solved through iterative schemes and, eventually, linearization techniques. When subsurface flow is fully-saturated and density-independent, the equations are linear and a direct solution of the matrix system is possible. The steady-state groundwater field is always computed at the beginning of a simulation, while transient flow and transport simulations are performed only if required. In this case, adaptive time-steps are usually applied to provide suitable results. In fact, time-step size is determined according to the change of the solution unknown. The maximum rate of change for time-step, $X_{\max}$, is entered by the user. The following expression is used to evaluate the maximum time-step between time levels L and L+1:

$$\Delta t^{L+1} = \frac{X_{\max}}{\max\left|X_i^{L+1} - X_i^{L}\right|} \Delta t^{L} \tag{3.24}$$

Implementation of Eq.(3.24) allows using larger time-steps when variables do not show severe changes in time, while smaller time-steps are selected when changes are bigger, to properly capture variable variations, such as hydraulic head or concentration in the context of this work. Moreover, for each time-step, mass entering or leaving the domain through boundaries or

internal sources or sinks and mass change are computed and printed in output files. These values provide useful information to check simulation results.

Important issues about numerical schemes suitable to solve the advection-dispersion transport equation should be mentioned. The mathematical nature of this equation changes according to the predominance of advection or dispersion. If advection is neglected, the partial differential equation becomes parabolic, while purely advective transport is described by a hyperbolic type equation. The hyperbolic equation requires special attention in numerical solutions (Rausch et al., 2005). Three well known options for time discretization are available in HydroGeoSphere: explicit, central (Crank-Nicolson formulation) or fully implicit transport time weighting. The latter one is not prone to exhibit oscillations but more prone to numerical smearing than central-time weighting. Oscillations can be either overshoot, which is a concentration greater than the maximum possible, or undershoot, which is a negative concentration (Charbeneau, 2000). Instead, numerical smearing, or numerical dispersion, manifests by spreading sharp concentration fronts (Figure 3.1).

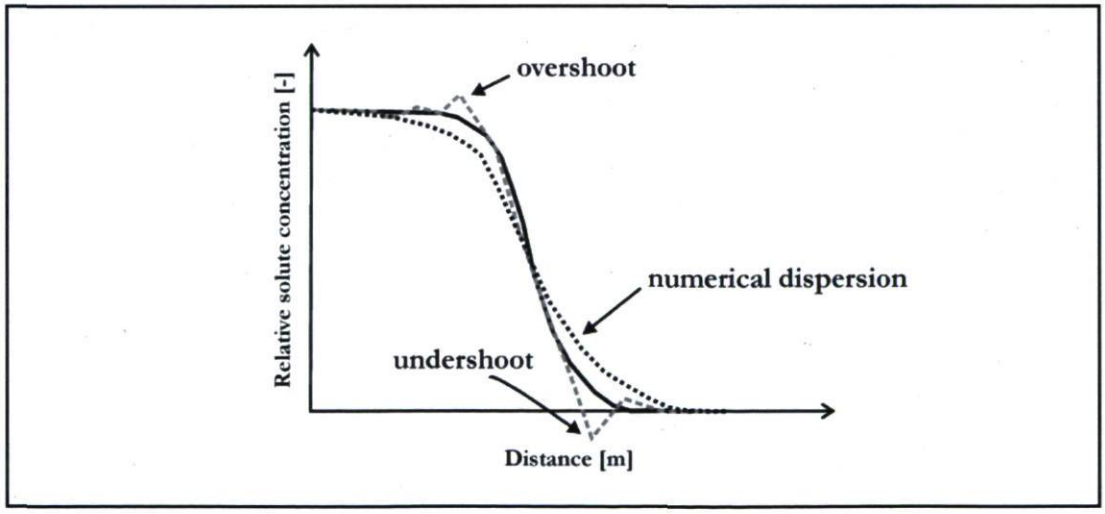

Figure 3.1 - Computational problems with numerical simulation of the transport equation (adapted from Charbeneau, 2000)

Numerical dispersion depends on grid and therefore finite element dimensions should be chosen small enough to ensure physical dispersion dominates numerical dispersion size

(Neuman, 1981; Rausch et al., 2005). As a general rule, numerical dispersion and oscillations can be avoided if implicit transport time weighing is used in combination with a Peclet number smaller than 2 (Rausch et al., 2005). The Peclet number is the ratio between advective and dispersive transport. Thus, high Peclet numbers indicate that advection dominates over dispersion. For flow characterized by velocity v_x along the x-axis, the Peclet number is expressed by:

$$Pe = \frac{\Delta x \cdot v_x}{D_x} = \frac{\Delta x}{\alpha_L} \tag{3.25}$$

where Δx is the mesh size along the x direction. As Eq.(3.25) depends on element dimensions, mesh generation becomes a crucial step in the modeling process. Refinement may contribute to ensuring small element sizes where transport processes take place and the velocity is higher. In simulations presented in Chapters 4 and 5 implicit transport time weighting is employed and the mesh size is selected to obtain small Peclet numbers.

The numerical solution in discretely-fractured media is based on the evaluation of elemental matrices for 3D and 2D finite elements, which discretize the porous medium and fractures, respectively. These matrices are assembled into a global symmetric matrix. For unstructured meshes, which is the case considered here, the global matrix is a sparse matrix with a large bandwidth. The lack of rules for assigning nodes numbers makes it impossible to obtain a uniformly banded matrix. As matrix storage and execution time are proportional to the bandwidth, a special technique is employed to speed up the numerical solution. This technique stores only non-zero matrix coefficients. However, it is necessary to maintain their original position in the matrix, as matrix structure reflects mesh connectivity. In fact, mesh connectivity can be thought in terms of a matrix, where row and column indices correspond to node indices in the mesh. As a result, each diagonal coefficient corresponds to a node in the mesh and coefficients in the same row are non-zero if the node in that column is connected to the node in the diagonal position. Thus, each matrix entry (i, j) represents the stiffness coefficient or, as it is called in this context, transmissibility γ_{ij} of the segment joining nodes i and j (see Section 3.2). For example, the matrix corresponding to a mesh composed of 6 tetrahedra is shown in Figure 3.2.

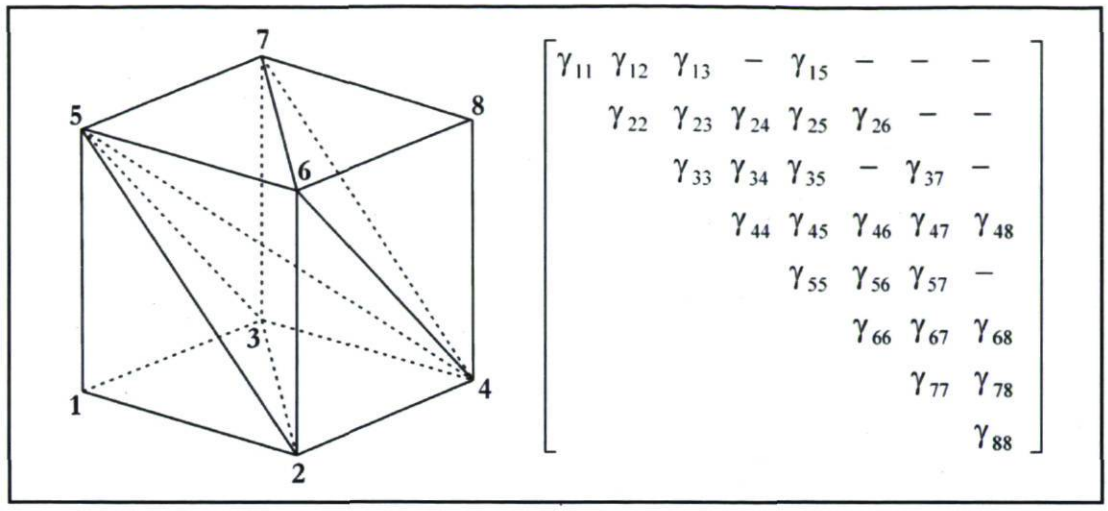

Figure 3.2 - Eight nodes mesh and corresponding global matrix

Non-zero coefficients are indicated by γ_{ij}, where i and j vary from 1 to 8, which is the number of nodes in the mesh. For example, matrix entry γ_{24} means that node 4, which corresponds to the column index, is connected to node 2, which corresponds to row index and to the diagonal position. In fact, tetrahedra 1 and 5 have segment $\overline{24}$ as edge. The matrix is symmetric, such that only the upper half matrix is presented, for the sake of clarity. The mesh connectivity list is shown in Table 3.1.

Table 3.1 - Mesh connectivity

Tetrahedron	Node 1	Node 2	Node 3	Node 4
1	3	5	4	2
2	7	6	8	4
3	5	6	7	4
4	3	5	7	4
5	5	6	4	2
6	1	5	3	2

In HydroGeoSphere, the global matrix is stored using three distinct arrays *a*, *ia*, and *ja*. This storage scheme has the objective to represent only the non-zero elements and to be able to

perform common matrix operations (Saad, 1996). Array *a* contains the non-zero coefficients, while arrays *ja* and *ia* contain, respectively, row and column indices of non-zero coefficient positions. Arrays *a* and *ja* are sized according to the parameter *nja,* while array *ia* to the parameter *nn*, which is the total number of nodes in the mesh. The parameter *nja* is the product between *nn* and *nbtetra*, which is the maximum number of segments connected to a single node in the tetrahedral mesh, which will be described in Section 3.3.1. For example, the three arrays associated with the matrix shown in Figure 3.2 are presented in Figure 3.3. Only first elements of arrays are shown.

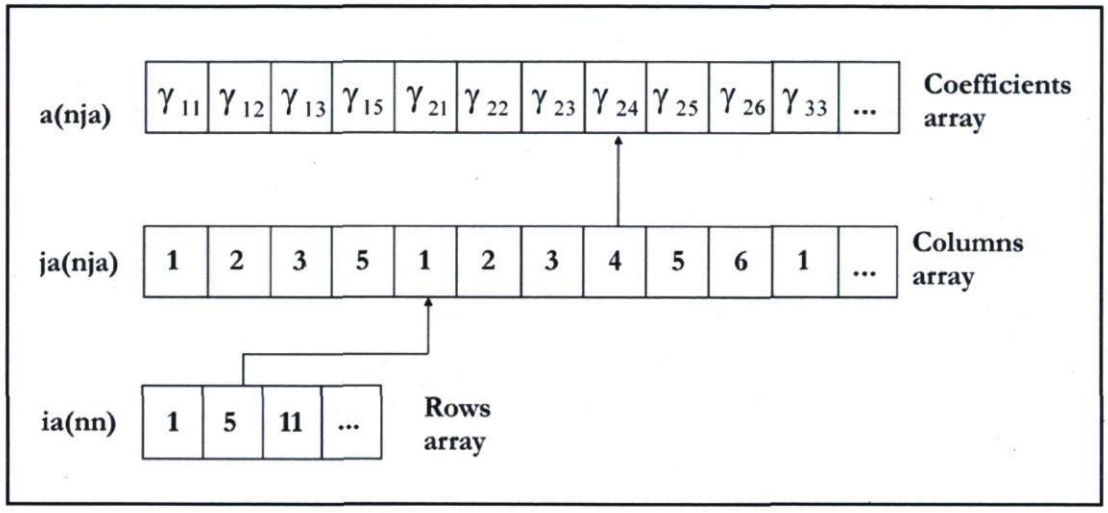

Figure 3.3 - Global matrix storage technique (adapted from Aagaard, 2000)

The coefficient γ_{24}, in row 2 and column 4, is considered to illustrate how matrix coefficients are memorized in these arrays. By looking up in the Rows array where the second row starts, the index 5 is found. Then, starting from the fifth element in the Columns array, a search is performed until the index 4, which corresponds to the fourth column, is found. This index indicates the position of the desired coefficient γ_{24} in the Coefficients array. In HydroGeoSphere, for computational reasons, further re-ordering of *ja* array is performed to move the diagonal element to the first column. These arrays contain information about neighbor nodes and their connectivity, as row and column indices correspond to nodes in the mesh. In unstructured tetrahedral meshes, neighbor node indices vary without a foreseeable rule. Thus, it is clear that these arrays are affected by the use of tetrahedral meshes. In fact, the

analysis of this technique used to store matrix coefficients has been the starting point to solve the discretized governing equations on a tetrahedral mesh. Code modifications have been made on the subroutine which properly sets up these arrays.

3.2 Evaluation of transmissibilities

Numerical solutions lead to a general system of equations $Ax = b$ that approximates the partial differential equation describing specific physical phenomena. By restricting the attention to a Control Volume setting, a minimal requirement for a Delaunay mesh to be suitable for numerical computation is that matrix A be an M-matrix (Murphy and Gable, 1998). As a result, solution techniques can exploit special properties of this class of matrix to obtain fast, accurate, and stable performance. M-matrices are real, square, nonsingular matrices, whose off-diagonal elements are either zero or negative and whose diagonal elements are strictly positive. This section illustrates the difference between two distinct approaches to evaluate the coefficients of matrix A.

The discretization of governing equations is often carried out by means of the well-known Galerkin method. Although it is widely used, the Galerkin method applied to 3D tetrahedral meshes does not lead to an M-matrix, which is suitable when iterative techniques are used to solve the system of linear equations (Saad, 1996). In contrast, the Orthogonal Subdomain Collocation method (OSC) leads to a matrix of type M. M-matrices lead to advantages in accuracy, stability, and running time over iterative solution techniques and convergence behavior (Forsyth, 1991; Letniowski and Forsyth, 1991; Murphy and Gable, 1998).

In the context of this thesis, coefficients of matrix A are called transmissibilities, as mentioned in Section 3.1.1. As different notations for transmissibilities are found in the literature, an overview of the main references is provided before presenting the notation used here. The basic concept related to the importance of transmissibilities is that their sign ensures that the discrete flux between two nodes corresponds to the physical direction. This concept is summarized by the positive transmissibility (PT) condition defined by Forsyth (1991): the PT condition must be satisfied to simulate down gradient flow. This condition is a prerequisite for

the existence of an M-matrix and ensures that nonphysical local extrema are not present in the solution (Putti and Cordes, 1998; Kosik et al., 2000). Some authors defined transmissibility in Eq.(3.11) with a negative sign and stated that the negative transmissibilities cause a nonphysical discrete flux (Forsyth, 1991; Letniowski and Forsyth, 1991; Letniowski, 1992; Cherry et al., 1996; Gable et al., 1996a; Gable et al., 1996b). In contrast, other authors (Putti and Cordes, 1998; Kosik et al., 2000; Cordes and Putti, 2001) defined the integral of basis functions with a positive sign, as done in Eq.(3.11), and affirmed that γ_{ij} must be negative to make A an M-matrix. To better understand and to clarify the definition of transmissibilities, the following formulation for the subsurface flow equation is considered:

$$\left(\frac{\Delta Mass}{\Delta t}\right)_i + Q_{ij} = S_s\left(h_i^{t+1} - h_i^t\right)\frac{V_i}{\Delta t} + \sum_{\eta_i}\gamma_{ij}\left(h_j^{t+1} - h_i^{t+1}\right) = 0 \tag{3.26}$$

where Q_{ij} is the volumetric flux between neighbor nodes. If flow goes from node i to node j, the mass variation in the control volume associated with node i is negative. Then, to satisfy Eq.(3.26), which should be equal to zero, Q_{ij} must be positive. As $Q_{ij} = \gamma_{ij}\left(h_j - h_i\right)$ and $h_i > h_j$, γ_{ij} should be negative, which represents the off-diagonal coefficient of the M-matrix associated to the problem considered.

Depending on the sign of γ_{ij} in Eq.(3.11), positive or negative transmissibilities are those to avoid, respectively. According to Letniowski and Forsyth (1991) even in cases where the discrete solution does not demonstrate non-physical behavior, negative transmissibilities may cause poor convergence behavior of the Newton iteration if non linear equations must be solved. Therefore, they declared that to satisfy the PT condition, it should be $\gamma_{ij} \geq 0$. Moreover, Letniowski (1992) stated that 3D Delaunay triangulation does not, in general, produce positive transmissibilities when a standard Galerkin finite element approximation is applied. However, it is possible to seek a triangulation that minimizes the number and size of the negative transmissibilities (Letniowski and Forsyth, 1991).

In contrast, Putti and Cordes (1998) affirmed that the PT condition is a prerequisite for the existence of an M-matrix, where $\gamma_{ij} \leq 0$. Likewise, Kosik et al. (2000) analyzed a transport problem and stated that to satisfy the PT condition and to ensure that physical flow is directed

from higher to lower concentration, γ_{ij} should be negative. In general, the violation of the PT condition can be detected by the emergence of negative concentrations and spurious oscillations in numerical results. In this thesis, transmissibilities are defined in reference to Eqs.(3.11) and (3.26), such that they must be negative to obtain an M-matrix associated with the mesh discretizing the domain of interest (Murphy and Gable, 1998; Putti and Cordes, 1998; Kosik et al., 2000; Cordes and Putti, 2001).

3.2.1 Standard Galerkin method

The Galerkin method was already implemented in the original version of HydroGeoSphere to evaluate the coefficients of the stiffness matrix for tetrahedra. If the CVFE technique is applied, matrix coefficients of the traditional finite element method can be interpreted as a linear function of the area through which the fluid passes traveling from one node i to its neighbor j (Bower et al., 2005). If the area is indicated with F_{ij} and the distance between nodes with r_{ij}, it is possible to write the volumetric flux Q_{ij} as:

$$Q_{ij} = \frac{F_{ij}}{r_{ij}} K \left(h_j - h_i \right) \tag{3.27}$$

where $F_{ij} / r_{ij} = \gamma_{ij}$. From Eq.(3.11), transmissibility γ_{ij} can be written as:

$$\gamma_{ij} = \int_v \frac{\partial N_i}{\partial x} K \frac{\partial N_j}{\partial x} dv + \int_v \frac{\partial N_i}{\partial y} K \frac{\partial N_j}{\partial y} dv + \int_v \frac{\partial N_i}{\partial z} K \frac{\partial N_j}{\partial z} dv \tag{3.28}$$

Instead of numerically solving integrals in Eq.(3.28), the influence coefficient technique proposed by Huyakorn et al. (1984) is used. This technique was first developed for linear rectangular elements and then applied to 3D blocks and prism elements (Huyakorn et al., 1986; Huyakorn et al., 1987; Beinhorn and Kolditz, 2003) and it provides a rapid and simple evaluation of matrix coefficients, without requiring numerical integration phases and therefore reducing the computation effort (Huyakorn et al., 1984; Beinhorn and Kolditz, 2003). It should be mentioned that Huyakorn et al. (1984; 1986) considered only simple blocks and prisms. Otherwise, if elements are too distorted, errors are introduced by substituting the numerical integration with the influence coefficient technique.

Basis functions in Eq.(3.28) can also be defined on simplex tetrahedra, which have linear sides and linear polynomials as the interpolation function. For a tetrahedron whose vertices are *i*, *j*, *k* and *l*, the following shape functions are used (Allaire, 1985):

$$N = \frac{1}{6V}\{1, x, y, z\}\begin{vmatrix} a_i & a_j & a_k & a_l \\ b_i & b_j & b_k & b_l \\ c_i & c_j & c_k & c_l \\ d_i & d_j & d_k & d_l \end{vmatrix} \tag{3.29}$$

where *a*, *b*, *c*, and *d* are the coefficients of the shape functions and they are calculated as:

$$\begin{bmatrix} a_i & a_j & a_k & a_l \\ b_i & b_j & b_k & b_l \\ c_i & c_j & c_k & c_l \\ d_i & d_j & d_k & d \end{bmatrix} = 6V \begin{bmatrix} 1 & x_i & y & z_i \\ 1 & x_j & y_j & z_j \\ 1 & x_k & y_k & z_k \\ 1 & x_l & y_l & z_l \end{bmatrix}^{-1} \tag{3.30}$$

The tetrahedron volume V is calculated from the determinant of the matrix containing the tetrahedral node coordinates:

$$V = \frac{1}{6}\begin{vmatrix} 1 & x_i & y & z_i \\ 1 & x_j & y_j & z_j \\ 1 & x_k & y_k & z_k \\ 1 & x_l & y_l & z_l \end{vmatrix} \tag{3.31}$$

The Jacobian matrix J or element derivative matrix is calculated as:

$$J = \begin{bmatrix} \frac{\partial N_i}{\partial x} & \frac{\partial N_j}{\partial x} & \frac{\partial N_k}{\partial x} & \frac{\partial N_l}{\partial x} \\ \frac{\partial N_i}{\partial y} & \frac{\partial N_j}{\partial y} & \frac{\partial N_k}{\partial y} & \frac{\partial N_l}{\partial y} \\ \frac{\partial N_i}{\partial z} & \frac{\partial N_j}{\partial z} & \frac{\partial N_k}{\partial z} & \frac{\partial N_l}{\partial z} \end{bmatrix} = \begin{bmatrix} b_i & b_j & b_k & b_l \\ c_i & c_j & c_k & c_l \\ d_i & d_j & d_k & d_l \end{bmatrix} \tag{3.32}$$

After evaluating the Jacobian matrix, the elemental stiffness matrix A is calculated by summing the contributions in the three spatial directions:

$$\left[A \right]^e_{Galerkin} = K_{xx}\left[A_{xx} \right] + K_{yy}\left[A_{yy} \right] + K_{zz}\left[A_{zz} \right] \tag{3.33}$$

where, for example, $\left[A_{xx} \right]$ is equal to:

$$\frac{1}{36V}\begin{bmatrix} b_ib_i & b_ib_j & b_ib_k & b_ib_l \\ & b_jb_j & b_jb_k & b_jb_l \\ & & b_kb_k & b_kb_l \\ & & & b_lb_l \end{bmatrix} \tag{3.34}$$

where only the half-upper part is shown because the matrix is symmetric. Matrices $\left[A_{yy} \right]$ and $\left[A_{zz} \right]$ are evaluated in an analogous way, but the derivatives along the y and z directions are used, respectively. Diagonal coefficients are evaluated as the sum of other entries in the same row. Matrix A is called the stiffness matrix, even if this term is usually used in the context of solid mechanics. For fluid mechanics, it might be more appropriate to call it the fluidity matrix or fluid conductance matrix as in Allaire (1985) and Beinhorn and Kolditz (2003). The global matrix contains all elemental contributions and it is obtained after the assembly phase. For example, transmissibility associated with segment r_{ij} is:

$$\gamma_{ij}^{Global} = \sum_e \left(\frac{K_{xx}}{36V} b_i b_j + \frac{K_{yy}}{36V} c_i c_j + \frac{K_{zz}}{36V} d_i d_j \right) \tag{3.35}$$

where the summation is carried out over all tetrahedral elements having segment r_{ij} as edge. Similarly, for the transport equation:

$$\gamma_{ij}^{Global} = \sum_e \left(\frac{D_{xx}}{36V} b_i b_j + \frac{D_{yy}}{36V} c_i c_j + \frac{D_{zz}}{36V} d_i d_j \right) \tag{3.36}$$

where the hydraulic conductivity has been replaced by the hydrodynamic dispersion coefficient.

3.2.2 Orthogonal Subdomain Collocation method

This alternative approach is presented by Putti and Cordes (1998) and Cordes and Putti (2001). The Orthogonal Subdomain Collocation (OSC) approach is based on a geometrical analysis of the control volume mesh and on the need to obtain an M-matrix associated with the mesh. As already stated, matrix structure is related to mesh connectivity. Therefore, if mesh geometry and topology follow specific requirements, an M-matrix is obtained. Moreover, if the CVFE numerical method is applied, the matrix diagonal elements are the sum of absolute values of

other entries in the same row, causing the matrix to be diagonally dominant. Let A be an M-matrix with coefficients γ_{ij}, where i and j are the row and column indices, respectively. Then, the M-matrix properties can be summarized as follows (Kosik et al., 2000):

$$\gamma_{ij} \le 0 \quad \gamma_{ii} \ge -\sum_{j} \gamma_{ij} \qquad \forall i \ne j$$
$$A^{-1} \ge 0 \tag{3.37}$$

M-matrices are desirable for iterative sparse matrix solvers. The existence of an M-matrix guarantees that the discrete flux between two nodes is in the opposite direction of the dependent variable gradient (Cordes and Putti, 2001). Otherwise, unrealistic results could be obtained, such as flux in the direction of increasing hydraulic heads. Thus, the importance of M-matrices lies in the fact that simulated numerical fluxes are consistent with the physics. Otherwise, a positive off-diagonal coefficient γ_{ij} means that a head decrease from node i toward node j induces a flux from j toward i, which is clearly unphysical (Putti and Cordes, 1998).

The Delaunay algorithm is commonly applied to discretize space with triangles or tetrahedra. In 2D, the Delaunay algorithm ensures the generation of an M-matrix associated with the mesh (Putti and Cordes, 1998; Cordes and Putti, 2001). This is possible because of the equivalence of the positive transmissibility condition and a Delaunay triangulation (Putti and Cordes, 1998). In fact, in 2D, it can be demonstrated that a transmissibility calculation based on the standard Galerkin method is equivalent to the calculation based on the OSC method, which ensures the existence of an M-matrix. According to the OSC method, transmissibilities are defined in 2D by the ratio between Voronoi segments and Delaunay triangular edges. For example, in reference to Figure 3.4, the transmissibility associated with triangular edge r_{ij} is calculated by:

$$\gamma_{ij} = \frac{\overline{CM}}{r_{ij}} = \frac{\sqrt{R^2 - \frac{r_{ij}^2}{4}}}{r_{ij}} \tag{3.38}$$

where the Voronoi edge $\overline{CM}$ is orthogonal to triangular edge r_{ij}.

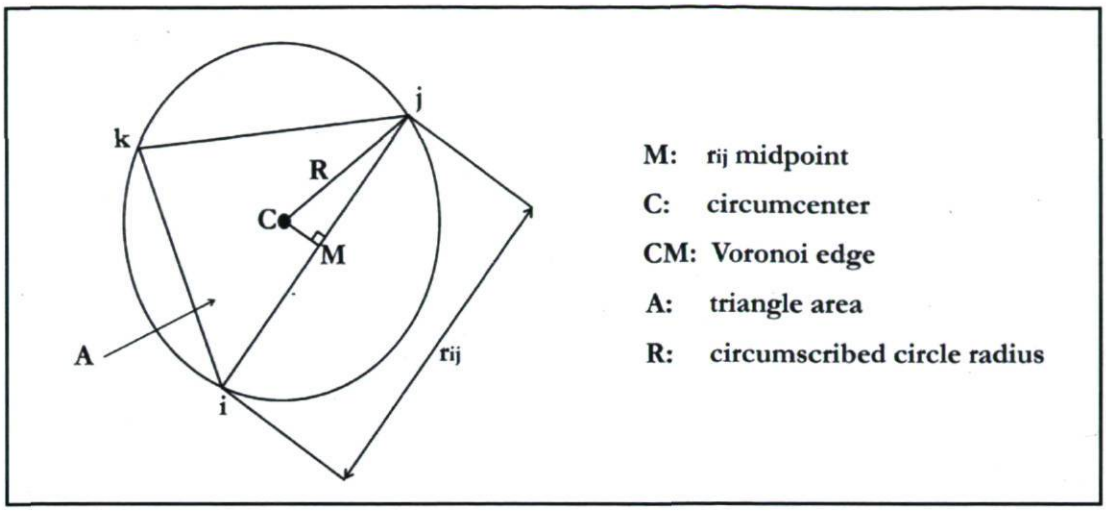

Figure 3.4 - Relation between Voronoi and Delaunay meshes in 2D

The radius of the circumscribed circle can be expressed by:

$$R = \frac{r_{ij} \cdot r_{jk} \cdot r_{ki}}{4A} \tag{3.39}$$

After a few mathematical steps, the following expression for transmissibility is derived:

$$\gamma_{ij} = \frac{(y_j - y_k)(y_k - y_i) + (x_k - x_j)(x_i - x_k)}{4A} \tag{3.40}$$

Eq.(3.40) corresponds to the expressions presented by Huyakorn et al. (1984) and Beihnorn and Kolditz (2003), who applied the Galerkin method and the influence coefficient technique. Eq.(3.40) is also used in HydroGeoSphere to compute matrix coefficients for triangular finite elements representing fractures. Thus, in 2D, transmissibilities calculated with Eq.(3.40) coincide with those obtained by applying the Galerkin method.

In 3D, the Galerkin method does not lead to an M-matrix if tetrahedral meshes are used (Letniowski, 1992; Putti and Cordes, 1998; Kosik et al., 2000; Cordes and Putti, 2001). Therefore, it is interesting to analyze the Orthogonal Subdomain Collocation method proposed by Putti and Cordes (1998). In 3D Delaunay meshes, if the standard Galerkin method is applied, control volumes are not represented by Voronoi cells, but rather by a median mesh. Voronoi and median meshes are both dual meshes, where tetrahedral nodes become new cell centers for control volumes. These control volumes are centered on

circumcenters or on barycenters of tetrahedra, depending on which dual mesh is used: circumcenters are used with Voronoi mesh, while barycenters with median mesh. The circumcenter is the intersection of the orthogonal bisectors, while the barycenter, or gravity center, is the point where the four medians meet. In 3D, an orthogonal bisector is a plane that crosses an edge at the midpoint and that it is perpendicular to it, while a median is a plane that joins an edge of a tetrahedron to the midpoint of opposite edge. Barycenters and circumcenters coincide only in regular tetrahedra, but it is impossible to discretize complex domains using exclusively regular tetrahedra, which are characterized by four equilateral triangular faces. The OSC method is based on the Voronoi mesh as a dual mesh, such that the circumcenters of tetrahedra are considered as vertices of control volumes. The orthogonality of the control volume faces to the tetrahedral edges and the interpretation of the nodal Voronoi subdomains as nodal control volumes give rise to the name Orthogonal Subdomain Collocation method (Putti and Cordes, 1998). It should be also noted that the physical interpretation of γ_{ij} as a flux requires that the control volume face, F_{ij}, be orthogonal to edge r_{ij}. This interpretation is related to the Gauss theorem applied to the divergence of flux, as mentioned in Section 3.3.1. Therefore, Voronoi control volumes, which are orthogonal to tetrahedra, should be considered. Otherwise, the orthogonality between tetrahedral edges and control volume faces will not be respected. As a result, the application of the OSC method, which is based on the Voronoi dual mesh, becomes significant for numerical solution and more appropriate than the Galerkin method.

According to the OSC method, the elemental stiffness coefficients are obtained as the negative ratio between the area of the Voronoi cell face and the length of the corresponding tetrahedral edge (Putti and Cordes, 1998):

$$\gamma_{ij}^{OSC} = -\frac{F_{ij}}{|r_{ij}|} \tag{3.41}$$

where hydraulic conductivity is omitted, for clarity. The Voronoi face F_{ij} is the orthogonal bisector of the tetrahedron. An orthogonal bisector crosses an edge at the midpoint and is perpendicular to it. Any three of these bisectors that have a vertex in common meet at the circumcenter of the tetrahedron (Figure 3.5a).

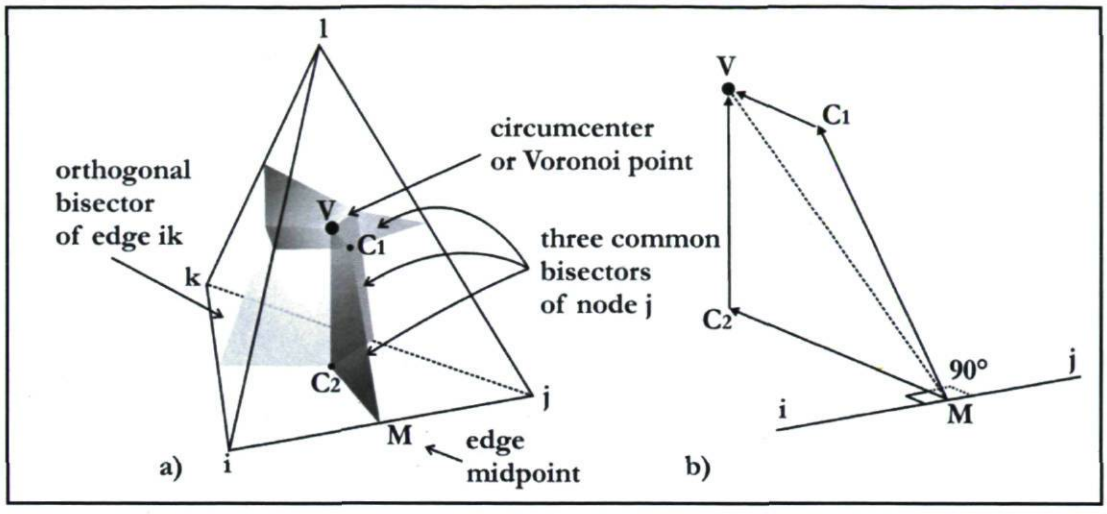

Figure 3.5 - Relation between Voronoi (shaded faces) and Delaunay (tetrahedron) meshes in 3D

The area of each Voronoi face is calculated by the cross product between the vectors defining the face. More specifically, if the segment of extremes i and j is considered, its corresponding Voronoi face is shown in Figure 3.5b. This face is defined by the circumcenter of the tetrahedron, or Voronoi point V, the edge midpoint M, the circumcenter C_1 of tetrahedral face *ijl*, and the circumcenter C_2 of tetrahedral face *ijk*. The cross product between two vectors results in another vector that is perpendicular to the plane containing the two input vectors. Moreover, the magnitude of the resulting vector is equal to the area of the parallelogram that the vectors span. The area of the Voronoi face can be thought of as the sum of triangles MC_2V and MC_1V (Figure 3.5b). Each triangle area is actually half of the parallelogram area. Therefore, the Voronoi face area is given by:

$$F_{ij} = \frac{1}{2}\left(r_{MC_2} \times r_{C_2V} + r_{C_1V} \times r_{MC_1}\right) \tag{3.42}$$

The result of Eq.(3.42) is a vector. Thus, to obtain the scalar value of the Voronoi face area a further step is necessary. As the vector resulting from the cross product is parallel to segment r_{ij}, a dot product with the unit vector in the direction of r_{ij} is performed to find the value of the Voronoi face area F_{ij} (Putti and Cordes, 1998):

$$F_{ij} = \frac{1}{2}\left(r_{MC_2} \times r_{C_2V} + r_{C_1V} \times r_{MC_1}\right)\frac{r_{ij}}{\left|r_{ij}\right|} \tag{3.43}$$

By other geometrical considerations, which are not repeated here, and by inserting Eq.(3.43) into Eq.(3.41), final expressions for transmissibilities are found (Putti and Cordes, 1998; Cordes and Putti, 2001). They can be applied to isotropic porous media characterized by hydraulic conductivity K:

$$\gamma_{ij} = -\frac{K}{48V}\left[2\left(r_{ik}\cdot r_{jk}\right)\cdot\left(r_{il}\cdot r_{jl}\right) + A_k A_l \cdot \left(\frac{\left(r_{ik}\cdot r_{jk}\right)^2}{A_l A_l} + \frac{\left(r_{il}\cdot r_{jl}\right)^2}{A_k A_k}\right)\right]$$

$$\gamma_{ik} = -\frac{K}{48V}\left[2\left(r_{ij}\cdot r_{kj}\right)\cdot\left(r_{il}\cdot r_{kl}\right) + A_j A_l \cdot \left(\frac{\left(r_{ij}\cdot r_{kj}\right)^2}{A_l A_l} + \frac{\left(r_{il}\cdot r_{kl}\right)^2}{A_j A_j}\right)\right]$$

$$\gamma_{il} = -\frac{K}{48V}\left[2\left(r_{ij}\cdot r_{lj}\right)\cdot\left(r_{ik}\cdot r_{lk}\right) + A_j A_k \cdot \left(\frac{\left(r_{ij}\cdot r_{lj}\right)^2}{A_k A_k} + \frac{\left(r_{ik}\cdot r_{lk}\right)^2}{A_j A_j}\right)\right] \qquad (3.44)$$

$$\gamma_{jk} = -\frac{K}{48V}\left[2\left(r_{ji}\cdot r_{ki}\right)\cdot\left(r_{jl}\cdot r_{kl}\right) + A_i A_l \cdot \left(\frac{\left(r_{ji}\cdot r_{ki}\right)^2}{A_l A_l} + \frac{\left(r_{jl}\cdot r_{kl}\right)^2}{A_i A_i}\right)\right]$$

$$\gamma_{jl} = -\frac{K}{48V}\left[2\left(r_{ji}\cdot r_{li}\right)\cdot\left(r_{jk}\cdot r_{lk}\right) + A_i A_k \cdot \left(\frac{\left(r_{ji}\cdot r_{li}\right)^2}{A_k A_k} + \frac{\left(r_{jk}\cdot r_{lk}\right)^2}{A_i A_i}\right)\right]$$

$$\gamma_{kl} = -\frac{K}{48V}\left[2\left(r_{ki}\cdot r_{li}\right)\cdot\left(r_{kj}\cdot r_{lj}\right) + A_i A_j \cdot \left(\frac{\left(r_{ki}\cdot r_{li}\right)^2}{A_j A_j} + \frac{\left(r_{kj}\cdot r_{lj}\right)^2}{A_i A_i}\right)\right]$$

where V is the tetrahedron volume, r_{ij} is the tetrahedral edge of extremes i and j, and A_i is the vector area orthogonal to face *jkl* and having an absolute value $|A_i|$ equal to the area of triangle *jkl*. The expressions presented above are used to evaluate the [4×4] matrix associated with each tetrahedron in the mesh. As the matrix is symmetric, calculations are required only for six elements. Moreover, diagonal elements are determined by using the property that matrix coefficients have a zero row sum:

$$\gamma_{ii} = -\gamma_{ij} - \gamma_{ik} - \gamma_{il} \qquad (3.45)$$

The elemental matrix will look like:

$$\left[A \right]^{e}_{OSC} = \begin{bmatrix} \gamma_{ii} & \gamma_{ij} & \gamma_{ik} & \gamma_{il} \\ \gamma_{ji} & \gamma_{jj} & \gamma_{jk} & \gamma_{jl} \\ \gamma_{ki} & \gamma_{kj} & \gamma_{kk} & \gamma_{kl} \\ \gamma_{li} & \gamma_{lj} & \gamma_{lk} & \gamma_{ll} \end{bmatrix} \tag{3.46}$$

Eq.(3.46) is analogous to Eq.(3.34), which is used to calculate $[A]^{e}_{Galerkin}$. However, Eq.(3.46) cannot be used as presented for solving the subsurface flow equation in anisotropic media and nor for the transport equation. When the Galerkin method is applied, the fluid conductance matrix can be split into three distinct components $[A_{xx}]$, $[A_{yy}]$, and $[A_{zz}]$, which are then multiplied by corresponding hydraulic conductivity values K_{xx}, K_{yy}, and K_{zz}. In contrast, Eq.(3.46) gives the whole elemental matrix and cannot be used to account for different hydraulic conductivity values or hydrodynamic dispersion coefficients. Further development is thus required, as will be described in Section 3.3.5.

3.3 Numerical code development

The development of an enhanced HydroGeoSphere version was motivated by the objective to reach a seamless combination between geological and numerical models. The numerical code can now solve the governing equations of flow and mass transport in saturated conditions on a fully 3D tetrahedral mesh created by the LaGriT mesh generator. Therefore, this new code version contributes to increased applications and modeling capabilities. In fact, without these enhancements, irregular grids were restricted to 3D block or prism meshes built by stacking 2D slices composed of triangular or quadrilateral elements, which are generated by compatible mesh generators (GRID BUILDER, GMS, FRACTRAN). The resulting 3D mesh is a layered system where 2D slices are replicated vertically, making it difficult to discretize complex 3D domain geometries. In contrast, the mesh generation technique proposed here allows building a fully 3D mesh covering the simulation domain, whose geometry is built with specific geomodeling tools. The current enhanced version works for groundwater flow and mass transport in saturated conditions, with discrete fractures and wells.

The HydroGeoSphere numerical code has pre-processor and post-processor tools, called GROK and HSPLOT, respectively. While the first is used to generate input data files for HydroGeoSphere, the latter is used to convert raw HydroGeoSphere output files into TECPLOT or GMS compatible input files. The use of a new mesh type has required modifications not only in HydroGeoSphere, but also in both the pre-processor and post-processor. The main and basic innovation is a new GROK subroutine that reads in nodal coordinates and connectivity of tetrahedral and triangular meshes. In fact, in the HydroGeoSphere version described in Therrien et al. (2007), available elements to solve the 3D porous medium equations are either hexahedral blocks or triangular prisms (Figure 3.6a), while tetrahedral elements are introduced here (Figure 3.6b). The original code version allows for subdivision of blocks into tetrahedra, but faces that can be designated as fracture elements are restricted to the original block elements. New code versions that may allow tetrahedral element faces to be designated as fractures were mentioned as an example of future code development in Therrien et al. (2007). Thus, this work takes that research direction, as one of the main outcomes is the designation of tetrahedral faces as fracture elements. Moreover, adaptation of output files to a tetrahedral mesh has involved a careful analysis of format files required by Tecplot and GMS.

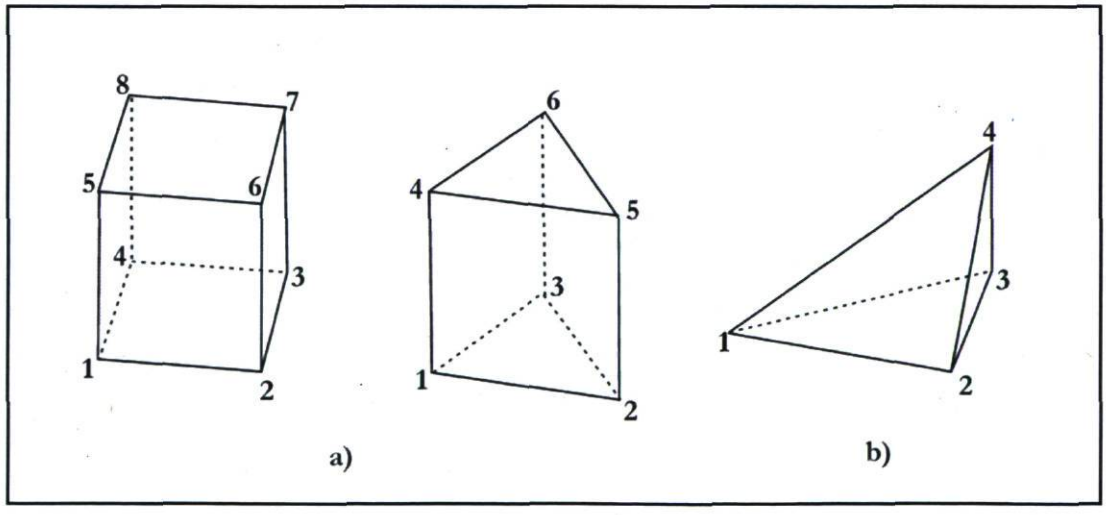

Figure 3.6 - Available 3D finite elements to discretize a porous medium: a) block and prism and b) tetrahedron

With the discretely-fractured medium representation, each fracture is explicitly represented by specifying its own geometry, areal extent, dimensions and position in 3D space. The numerical approach is based on continuity of hydraulic head and concentration at the fracture/matrix interface, which corresponds to instantaneous equilibrium between the two domains. This method is also called the common node approach and it is essentially based on superposition of 2D fracture elements onto the elements of the porous matrix (Therrien and Sudicky, 1996; Therrien et al., 2007). Thus, nodes at fracture locations are common nodes that receive contributions from both the rock matrix elements and the fracture faces. Representing irregular and non planar fractures is more complex than representing regular fractures. HydroGeoSphere has been enhanced by Graf (2005) and Graf and Therrien (2008) to represent nonuniform inclined discrete fractures by identifying triangular and quadrilateral internal faces in 3D elements (Figures 3.7a and 3.7b). The work of Graf (2005) constitutes the basis for the development presented which is used to compare numerical results and verify the approach proposed here. This approach is based on a new relationship, incorporated into HydroGeoSphere, between 2D triangular and 3D tetrahedral elements (Figure 3.7c) representing, respectively, the fractures and the porous rock matrix. This new relationship avoids looking for internal faces of 3D finite elements, because fracture elements are restricted to the four external faces of a tetrahedron. Moreover, as tetrahedra can have any orientation in the space, this relation offers more flexibility on the representation of fractures.

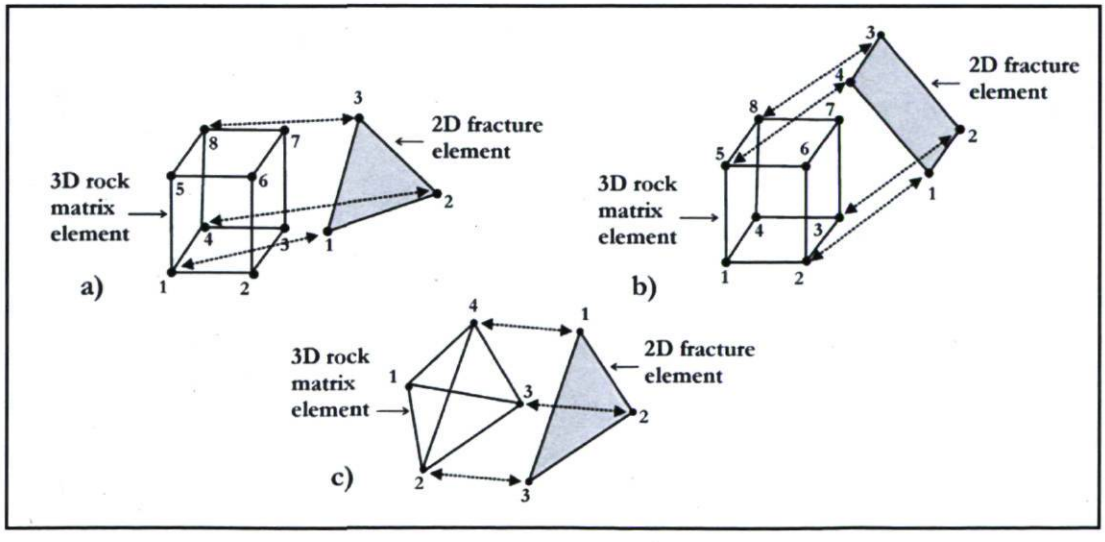

Figure 3.7 - Examples of relations between 2D and 3D finite elements: a) and b) fracture faces defined in blocks and c) fracture face defined in tetrahedra

Major code modifications are described in the following paragraphs to highlight new features and their implementation. A logical variable called *tetramesh* has been added to the numerical code to distinguish between the use of a 3D fully tetrahedral mesh created by the modeling approach proposed here and other mesh generation techniques already available. Therefore, the variable *tetramesh* is switched to true to use the new mesh type and related instructions. An overview of instructions generally used in combination with a tetrahedral mesh are presented and explained in Appendix B.

3.3.1 Calculation of segments and faces

The calculation of the number of faces and segments is the first and essential computation executed by the GROK pre-processor after reading the nodal coordinates and connectivity list of a mesh. A careful analysis of tetrahedral meshes was necessary to find out what parameters should be modified and how to modify them. In particular, to compute faces and segments, HydroGeoSphere uses the maximum number of connections to a single node. This number can be easily determined in structured and regular meshes. For example, it is constant and equal to 27 for block-based meshes. In contrast, it varies greatly in tetrahedral meshes, depending on the complexity of the mesh. Figure 3.8 illustrates this difference, by showing all segments that can be traced from a node. In block-based meshes, internal and face diagonals are also considered as segments (Figure 3.8a), while in tetrahedral meshes no diagonal can be traced and segments are restricted to the external edges of tetrahedra. For a simple 8-node configuration, where nodes are placed at the vertices of a hexahedron and are connected to 6 tetrahedra, the maximum number of segments connected to a node is equal to 7 (Figure 3.8b). In contrast, if nodes are irregularly distributed in space, this number increases without following a specific rule and it must be calculated every time a mesh is generated (Figure 3.8c). This number is essential for memory allocation to store the stiffness matrix, as shown in Section 3.1.2.

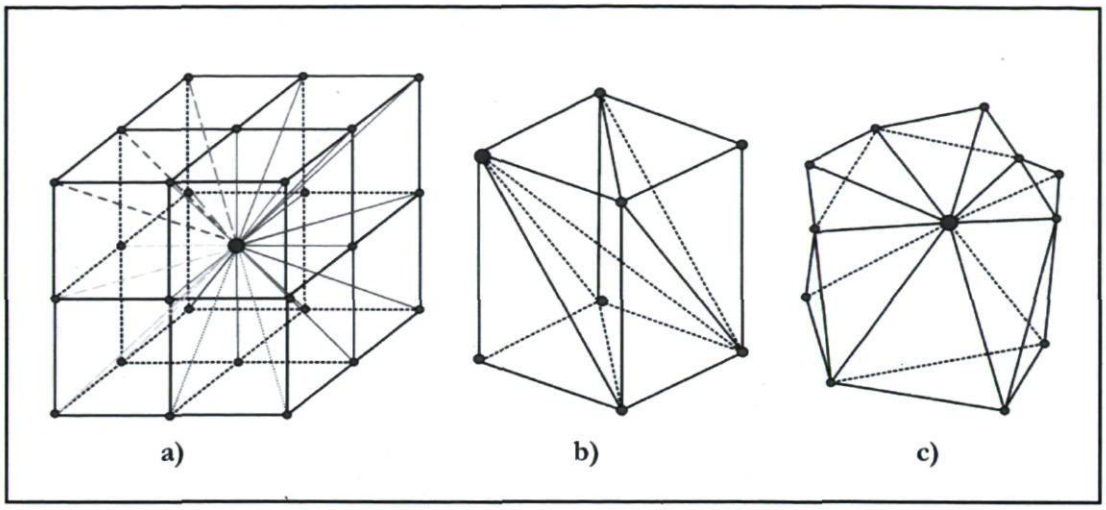

Figure 3.8 - Segments connected to a single node: a) in a block-based mesh, b) in a tetrahedral mesh with regular nodal distribution and c) in a tetrahedral mesh with irregular nodal distribution

The mesh generator LaGriT provides the maximum number of connections to a single node in the entire mesh. Therefore, this number has been incorporated as a new parameter into the HydroGeoSphere numerical code and is used by the subroutines that calculate the number of faces and segments in the mesh. During the calculation, it is necessary to look for segments and faces which are shared between adjacent elements, to avoid storing them twice. Faces and segments are identified by their nodes, listed in ascending order. When a new face is read, it is compared to others formerly written to check if it has already been stored in memory. Otherwise, a new face will be added to the faces list. Simple meshes were used to verify the correct implementation of this new parameter.

3.3.2 Identification of 2D fracture elements

To identify which faces of tetrahedra lie on fractures, the connectivity of the fracture triangular meshes and their global nodal numbering are required, as mentioned in Chapter 2. In particular, each triangulated fracture extracted from the tetrahedral mesh has nodes numbered from 1 to N, which is the maximum number of nodes for that specific fracture. Thus, each

fracture is a mesh object independent from the tetrahedral mesh, as it is characterized by its own, or local, nodal numbering. To select triangular elements that should act like fractures, it is necessary to identify to what tetrahedral face each triangle corresponds to. This identification is made by knowing the global nodal numbering of the fracture triangular mesh. Otherwise it would be impossible to select the right tetrahedral faces. Looking up all faces in the tetrahedral mesh, when the face defined by each series of three nodes of fracture triangles is found, the face is chosen and defined as a fracture. For example, in reference to Table 3.2, if a tetrahedral face defined by nodes 2793, 3103, 3105 exists in the mesh, this face will act as a fracture.

Table 3.2 - Example of nodal coordinates for a discrete fracture

Local numbering 2D triangular mesh	Node X coordinate	Node Y coordinate	Node Z coordinate	Global numbering 3D tetrahedral mesh
1	2.074	0.281	1.744	2793
2	2.016	0.375	1.700	3103
3	2.172	0.375	1.812	3105

The time required for the identification of fracture faces increases if the number of elements in the mesh increases, because the total number of faces will increase as well and consequently, more time is required to find the tetrahedral face that matches each triangle belonging to the fracture surfaces. For example, in a mesh of 235000 tetrahedra, a fracture characterized by 4500 triangular elements is identified in less than 20 seconds. In bigger meshes, constituted by 1500000 elements for example, the time required for the identification of each discrete fracture increases up to a few minutes, depending on the number of triangles in the fracture.

If the top of the simulation domain does not have a constant elevation, the same procedure developed for fractures is used to select top faces. This is the case when real topography data are included in the Geomodel. In fact, with geomodeling tools a triangulated surface representing the topography of the simulation domain can be easily generated and then integrated in the mesh as done for fractures (Section 2.2.1.2). A *.txt file contains nodal coordinates and connectivity of this triangular mesh which is read by the pre-processor

GROK, which will identify the faces on the top of the domain. Selecting these faces is useful, for example, to assign a Neumann boundary condition.

3.3.3 Discretization of wells

Suitable discretization of wells is a challenging task. In fact, a typical borehole diameter is at the centimeter scale, while the flow around wells affects the overall hydraulic head distribution in the domain over hundreds of meters. Thus, a proper grid generation technique should allow additional points to be concentrated near well locations. However, accurate representation of the path of a real well can be difficult, because the well is not always vertical (Cherry et al., 1996). In this work, wells are discretized using 1D linear elements, which are represented by edges of tetrahedra. With block or prism finite elements, a staircase representation of inclined wells is obtained. In contrast, the use of tetrahedra in combination with the mesh procedure presented in Chapter 2 allows for a more realistic discretization of wells, which will be represented by a perfect straight line. The difference between a block-based mesh and a tetrahedral mesh in the discretization of inclined wells will be clearly shown by an example in the next chapter.

The mesh procedure adopted here creates an optimal distribution of nodes around well axes and connects them to tetrahedra, such that the real path of the well is reproduced, even if it is inclined. However, the standard HydroGeoSphere method to make a well is based on the definition of the shortest line between top and bottom nodes, which are entered by the user. Then, the mesh segments nearest to this line are selected and defined as well elements. Unfortunately, as mesh segments are generally not aligned along the well axis, the axis will be characterized by a staircase path (Figure 3.9a). In contrast, thanks to the coupling of GOCAD-LaGriT, it is possible to choose the nodes that will describe the well axis before they are connected to tetrahedra. Nodes are chosen knowing the real drilled borehole path. The mesh generation procedure described in Chapter 2 ensures that the chosen nodes are connected by the edges of tetrahedra. Then, chosen nodes are listed in a *.txt file. The GROK pre-processor simply reads in this file and defines as well elements the segments having those nodes as

extremities. With this technique, the "staircase" profile of a well axis is replaced by a straight line, which corresponds to the inclined axis of the drilled borehole (Figure 3.9b).

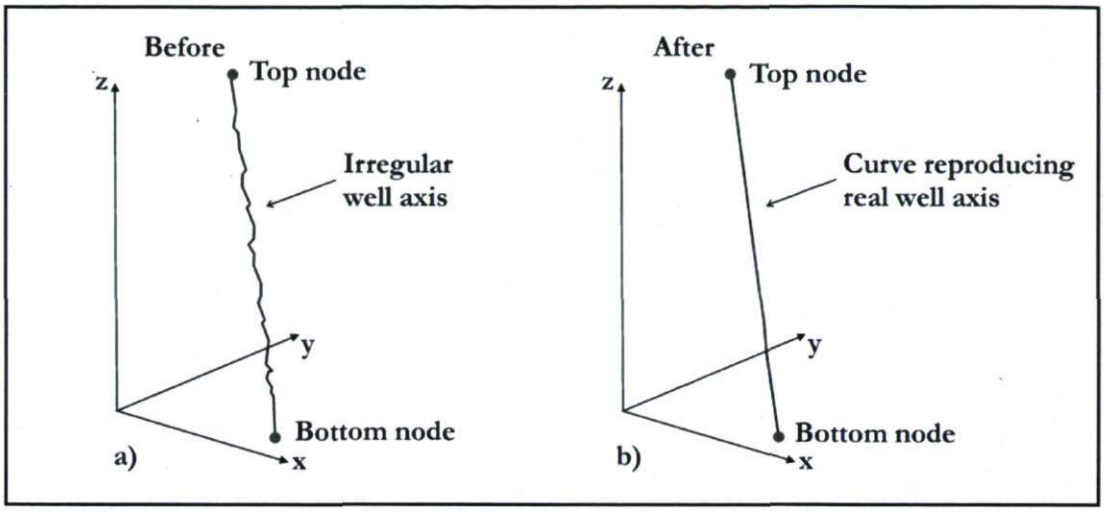

Figure 3.9 - Discretization of inclined wells: a) standard method and b) new method

Moreover, this discretization technique allows the user to better define the mesh resolution, as nodal spacing along well axes should be chosen at the beginning of the mesh generation phase. This nodal spacing determines the local refinement around the well (Section 2.2.1.2). Finally, as well nodes are known before executing the pre-processor GROK, the node that will act as the discharge point of the well during pumping or extraction is more easily chosen at the required location along the well axis.

3.3.4 Output files

Output files are required to visualize and analyze simulation results. File format depends on the type of finite element used in the mesh, as variable values are printed out and visualized for each node or element. Thus, it is essential to generate output files adapted to the new combination of finite element used here, tetrahedra and triangles. Subroutines that create Tecplot and GMS output files have been adapted to the new geometry. A specific header for tetrahedral elements has been added in Tecplot output file. Likewise, modifications have been

made to generate GMS formatted output: GMS *.2dm file contains fracture triangular mesh information, while GMS *.3dm file is formatted for 4-nodes tetrahedral elements. New format file options are active only if the switch *tetramesh* is true, which is the case when a tetrahedral mesh built by LaGriT is used.

3.3.5 Implementation of the Orthogonal Subdomain Collocation (OSC) method

Major code development has focused on the OSC method as an alternative to the standard Galerkin method to evaluate transmissibilities. Implementation of the OSC method required adding a code subroutine that evaluates Eq.(3.44). For example, if the first expression of Eq.(3.44) is considered here:

$$\gamma_{ij} = -\frac{K}{48V}\left[2\left(r_{ik}\cdot r_{jk}\right)\left(r_{il}\cdot r_{jl}\right) + A_k \cdot A_l\left(\frac{\left(r_{ik}\cdot r_{jk}\right)^2}{A_l \cdot A_l} + \frac{\left(r_{il}\cdot r_{jl}\right)^2}{A_k \cdot A_k}\right)\right] \tag{3.47}$$

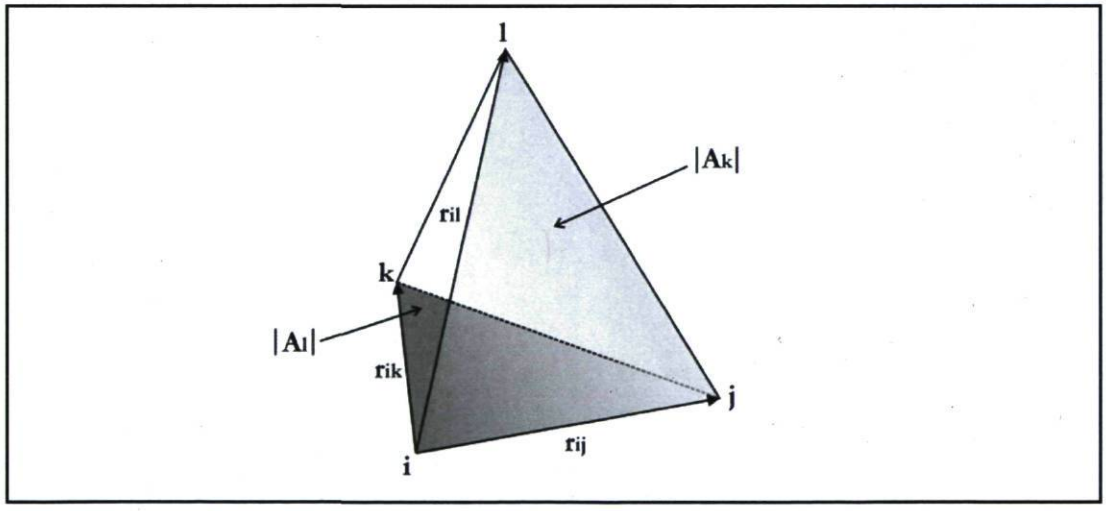

Figure 3.10 - Tetrahedral face areas used to evaluate transmissibility γ_{ij}

Tetrahedral face areas are calculated by the cross product between vectors *r*, which correspond to tetrahedral edges (Figure 3.10):

$$A_k = \frac{1}{2} r_{il} \times r_{ij} \qquad A_l = \frac{1}{2} r_{ij} \times r_{ik} \tag{3.48}$$

where, for example:

$$A_k = \frac{1}{2}\left(r_{il} \times r_{ij}\right) = \frac{1}{2}\begin{vmatrix} \hat{i} & \hat{j} & \hat{k} \\ x_l - x_i & y_l - y_i & z_l - z_i \\ x_j - x_i & y_j - y_i & z_j - z_i \end{vmatrix} \tag{3.49}$$

Moreover, the following quantity is calculated by the dot product between tetrahedral edges:

$$\left(r_{ik} \cdot r_{jk}\right) = \left[\left(x_k - x_i\right)\cdot\left(x_k - x_j\right) + \left(y_k - y_i\right)\cdot\left(y_k - y_j\right) + \left(z_k - z_i\right)\cdot\left(z_k - z_j\right)\right] \tag{3.50}$$

Eq.(3.47) evaluates the scalar value of transmissibility γ_{ij}. In anisotropic media, the hydraulic conductivity tensor has different components in the three spatial directions. Thus, Eq.(3.47) can be applied as presented only if $K_x = K_y = K_z = K$. To overcome this limitation in analyzing anisotropic porous media, Putti and Cordes (1998) proposed to use an isotropic equivalent system. A relationship exists between solutions of flow problems in isotropic and anisotropic systems (Bear and Dagan, 1965; Bear, 2007). This relationship is based on the solution of equations on a distorted frame of reference (x_{eq}, y_{eq}, z_{eq}) and on the definition of an equivalent hydraulic conductivity K_{eq}:

$$K_{eq} = \sqrt[3]{K_x K_y K_z} \tag{3.51a}$$

$$x_{eq} = x\sqrt{\frac{K_{eq}}{K_x}}, \qquad y_{eq} = y\sqrt{\frac{K_{eq}}{K_y}}, \qquad z_{eq} = z\sqrt{\frac{K_{eq}}{K_z}} \tag{3.51b}$$

Using these distorted scales, the original problem is first transformed into an equivalent isotropic system, solved in that system and then transformed by the same relationships back to the original, anisotropic system (Bear, 2007). However, it is not practical to integrate this procedure in HydroGeoSphere, especially because of the distortion of the frame of reference. Moreover, the transport equation would require an analogous procedure, but in this case the extension of Eqs.(3.51a-3.51b) to the hydrodynamic dispersion tensor is not as straightforward as it may seem. In fact, even for an isotropic medium, dispersion is related to the longitudinal and transversal dispersivities and to the velocity field, as shown by Eq.(3.19). Thus Eq.(3.47) cannot be applied because it is not possible to define an equivalent dispersion coefficient as it is done for the hydraulic conductivity (Eq. 3.51a).

Thus, a different strategy from that proposed by Putti and Cordes (1998) is developed to apply Eq.(3.47) to anisotropic flow fields and transport problems in HydroGeoSphere. The fluid conductance matrix can be thought as split into three distinct contributions, as done with the Galerkin method in Eqs.(3.34) and (3.35). It should be observed that the scalar value of transmissibility γ_{ij} is given by the ratio $F_{ij}/|r_{ij}|$, where the numerator represents the area of Voronoi face orthogonal to edge r_{ij}. As F_{ij} is a vector (Figure 3.11a), its components can be used to express the fluid conductance matrix as a sum of three contributions corresponding to the three Cartesian directions. These components are shown in Figure 3.11b.

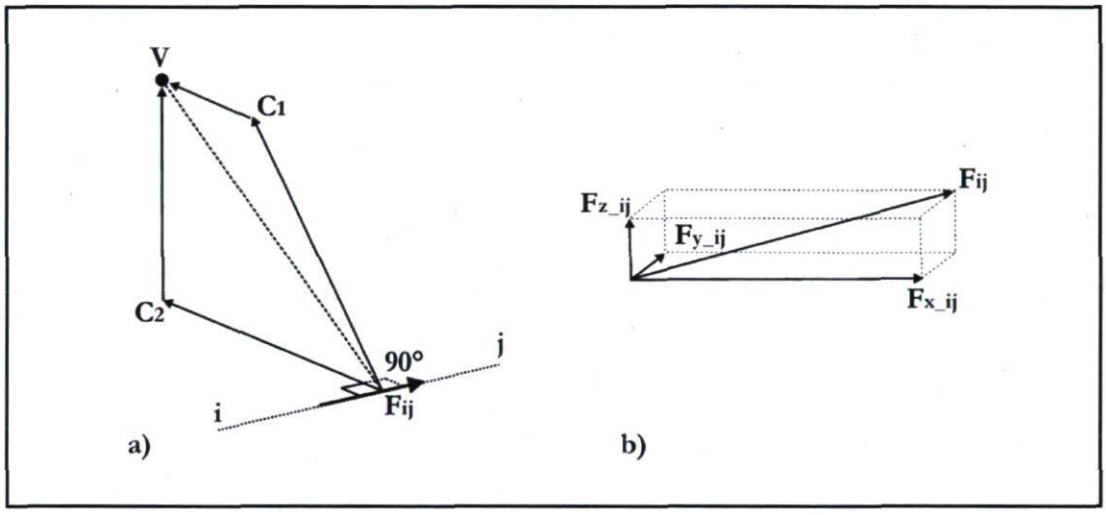

Figure 3.11 - a) Voronoi face vector F_{ij} and b) its components

To obtain an expression for the OSC method analogous to Eq.(3.33), which is used for the Galerkin method, F_{ij} is multiplied by the unit vector components corresponding to the tetrahedral edge r_{ij}. This computation is justified by the fact that Voronoi face F_{ij} is associated with edge r_{ij}. The unit vector, denoted by $\hat{r}_{ij}$, is written as:

$$\hat{r}_{ij} = \left(\frac{x_j - x_i}{|r_{ij}|}, \frac{y_j - y_i}{|r_{ij}|}, \frac{z_j - z_i}{|r_{ij}|} \right) \tag{3.52}$$

By knowing that:

$$\left|\hat{r}_{ij}\right| = 1 \tag{3.53}$$

The following components are determined:

$$F_{x\_ij} = F_{ij}\frac{\left(x_j - x_i\right)}{\left|r_{ij}\right|}$$

$$F_{y\_ij} = F_{ij}\frac{\left(y_j - y_i\right)}{\left|r_{ij}\right|} \tag{3.54}$$

$$F_{z\_ij} = F_{ij}\frac{\left(z_j - z_i\right)}{\left|r_{ij}\right|}$$

As $\left|r_{ij}\right|$ is a scalar value, it is possible to define transmissibility using just the components of F_{ij}. Therefore, by using Eqs.(3.54) and (3.41) it is possible to write:

$$\gamma_{x\_ij} = \frac{F_{x\_ij}}{\left|r_{ij}\right|} = \frac{F_{ij}}{\left|r_{ij}\right|}\frac{\left(x_j - x_i\right)}{\left|r_{ij}\right|} = \gamma_{ij}\frac{\left(x_j - x_i\right)}{\left|r_{ij}\right|}$$

$$\gamma_{y\_ij} = \frac{F_{y\_ij}}{\left|r_{ij}\right|} = \frac{F_{ij}}{\left|r_{ij}\right|}\frac{\left(y_j - y_i\right)}{\left|r_{ij}\right|} = \gamma_{ij}\frac{\left(y_j - y_i\right)}{\left|r_{ij}\right|} \tag{3.55}$$

$$\gamma_{z\_ij} = \frac{F_{z\_ij}}{\left|r_{ij}\right|} = \frac{F_{ij}}{\left|r_{ij}\right|}\frac{\left(z_j - z_i\right)}{\left|r_{ij}\right|} = \gamma_{ij}\frac{\left(z_j - z_i\right)}{\left|r_{ij}\right|}$$

Then, similarly to Eq.(3.33), coefficients of matrices A_{xx}, A_{yy}, and A_{zz} for the OSC method can now be introduced. They are calculated as follows:

$$A_{xx\_ij} = \gamma_{ij}\left[\frac{\left(x_j - x_i\right)}{\left|r_{ij}\right|}\right]^2$$

$$A_{yy\_ij} = \gamma_{ij}\left[\frac{\left(y_j - y_i\right)}{\left|r_{ij}\right|}\right]^2 \tag{3.56}$$

$$A_{zz\_ij} = \gamma_{ij}\left[\frac{\left(z_j - z_i\right)}{\left|r_{ij}\right|}\right]^2$$

The sum of the expressions presented above is equal to the scalar value calculated with Eq.(3.47). In fact, it is possible to write:

$$A_{xx\_ij} + A_{yy\_ij} + A_{zz\_ij} = \gamma_{ij}\left[\left(\frac{x_j - x_i}{|r_{ij}|}\right)^2 + \left(\frac{y_j - y_i}{|r_{ij}|}\right)^2 + \left(\frac{z_j - z_i}{|r_{ij}|}\right)^2\right] \tag{3.57}$$

Since from Eq.(3.53) the quantity in square brackets on the right-hand side of Eq.(3.57) is equal to 1, it is easily verified that:

$$A_{xx\_ij} + A_{yy\_ij} + A_{zz\_ij} = \gamma_{ij} \tag{3.58}$$

Thus, it is possible to use Eq.(3.56) to evaluate the fluid conductance matrix, such that subsurface flow in anisotropic media and solute transport equations are properly evaluated with the OSC method. For example, matrix $\left[A_{xx} \right]_{OSC}$ is calculated as:

$$\left[A_{xx} \right]_{OSC} = \begin{bmatrix} \gamma_{ii} & \gamma_{ij}\left[\frac{(x_j - x_i)}{|r_{ij}|}\right]^2 & \gamma_{ik}\left[\frac{(x_k - x_i)}{|r_{ik}|}\right]^2 & \gamma_{il}\left[\frac{(x_l - x_i)}{|r_{il}|}\right]^2 \\ & \gamma_{jj} & \gamma_{jk}\left[\frac{(x_k - x_j)}{|r_{kj}|}\right]^2 & \gamma_{jl}\left[\frac{(x_l - x_j)}{|r_{jl}|}\right]^2 \\ & & \gamma_{kk} & \gamma_{kl}\left[\frac{(x_k - x_l)}{|r_{kl}|}\right]^2 \\ & & & \gamma_{ll} \end{bmatrix} \tag{3.59}$$

Matrices $\left[A_{yy} \right]_{OSC}$ and $\left[A_{zz} \right]_{OSC}$ will have a similar expression, but calculated using coordinates y and z. Finally, it is possible to write:

$$A^e_{OSC} = K_{xx}\left[A_{xx} \right]_{OSC} + K_{yy}\left[A_{yy} \right]_{OSC} + K_{zz}\left[A_{zz} \right]_{OSC} \tag{3.60}$$

Eq.(3.60) is also used to solve the transport equation by replacing the hydraulic conductivity with the hydrodynamic dispersion coefficient as follows:

$$A^e_{OSC} = D_{xx}\left[A_{xx} \right]_{OSC} + D_{yy}\left[A_{yy} \right]_{OSC} + D_{zz}\left[A_{zz} \right]_{OSC} \tag{3.61}$$

The OSC evaluation of fluid conductance matrix coefficients has been implemented in HydroGeoSphere following the procedure just presented. Implementation verification is presented in the next paragraph by comparison with previous studies and known matrix coefficient values for simple meshes.

3.3.5.1 Implementation verification

Two test cases have been designed to verify the implementation of the OSC method and to show the difference between Galerkin and OSC methods in the evaluation of the fluid conductance matrix. In the first test, a unit cubic nodal distribution has been used and six Delaunay tetrahedra (Figure 3.2) have been created with LaGriT and then imported into HydroGeoSphere. With the Galerkin method, the global fluid conductance matrix has three positive off-diagonal entries (Figure 3.12a), violating the M-matrix definition. Positive off-diagonal entries correspond to edges (2,3), (4,5), and (6,7). These positive values demonstrate, as stated earlier, that in three-dimensions a Delaunay tetrahedralization may not lead to an M-matrix (Forsyth, 1991; Letniowski and Forsyth, 1991; Letniowski, 1992; Putti and Cordes, 1998; Cordes and Putti, 2001).

$$\begin{bmatrix} 3/6 & -1/6 & -1/6 & 0 & -1/6 & 0 & 0 & 0 \\ & 5/6 & 1/6 & -3/6 & -1/6 & -1/6 & 0 & 0 \\ & & 5/6 & -3/6 & -1/6 & 0 & -1/6 & 0 \\ & & & 7/6 & 2/6 & -1/6 & -1/6 & -1/6 \\ & & & & 7/6 & -3/6 & -3/6 & 0 \\ & & & & & 5/6 & 1/6 & -1/6 \\ & & & & & & 5/6 & -1/6 \\ & & & & & & & 3/6 \end{bmatrix}$$

a) Galerkin

$$\begin{bmatrix} 3/4 & -1/4 & -1/4 & 0 & -1/4 & 0 & 0 & 0 \\ & 3/4 & 0 & -1/4 & 0 & -1/4 & 0 & 0 \\ & & 3/4 & -1/4 & 0 & 0 & -1/4 & 0 \\ & & & 3/4 & 0 & 0 & 0 & -1/4 \\ & & & & 3/4 & -1/4 & -1/4 & 0 \\ & & & & & 3/4 & 0 & -1/4 \\ & & & & & & 3/4 & -1/4 \\ & & & & & & & 3/4 \end{bmatrix}$$

b) OSC

Figure 3.12 - Global matrix for 8-node tetrahedral mesh

In contrast, with the OSC method, off-diagonal coefficients are either zero or negative (Figure 3.12b). Moreover, they are equal to those given by the LaGriT mesh generator, which is based on the Delaunay algorithm and which guarantees that the fluid conductance matrix is a semi-positive definite matrix, such that flux calculations do not have negative transmissibilities (Gable et al., 1996b). In fact, in addition to the generation of tetrahedral meshes, LaGriT also provides matrix coefficients, which are calculated considering the Voronoi dual mesh

associated with the tetrahedral Delaunay mesh. In Figure 3.12a, a zero coefficient at position (i, j) means that there is no segment in the mesh joining nodes i and j. Furthermore, in Figure 3.12b, zero coefficients appear either when the Galerkin method gives a positive off-diagonal entry or when contributions to γ_{ij} from distinct elements are of opposite sign. The only exact zero connection value corresponds to the diagonal segment joining nodes 4 and 5.

A second test case is based on the example presented by Letniowski (1992), who considered a mesh created by Delaunay triangulation containing five tetrahedra. He applied the Galerkin method and showed that Delaunay triangulation does not ensure that an M-matrix is obtained. Letniowski's example is also mentioned by Putti and Cordes (1998), who illustrated the difference between the Galerkin and OSC methods. These two studies are used here to verify the results obtained with the new enhanced HydroGeoSphere version. The mesh considered by Letniowski is composed of five tetrahedra (Figure 3.13). Nodal coordinates and the connectivity list are shown in Tables 3.3a and 3.3b.

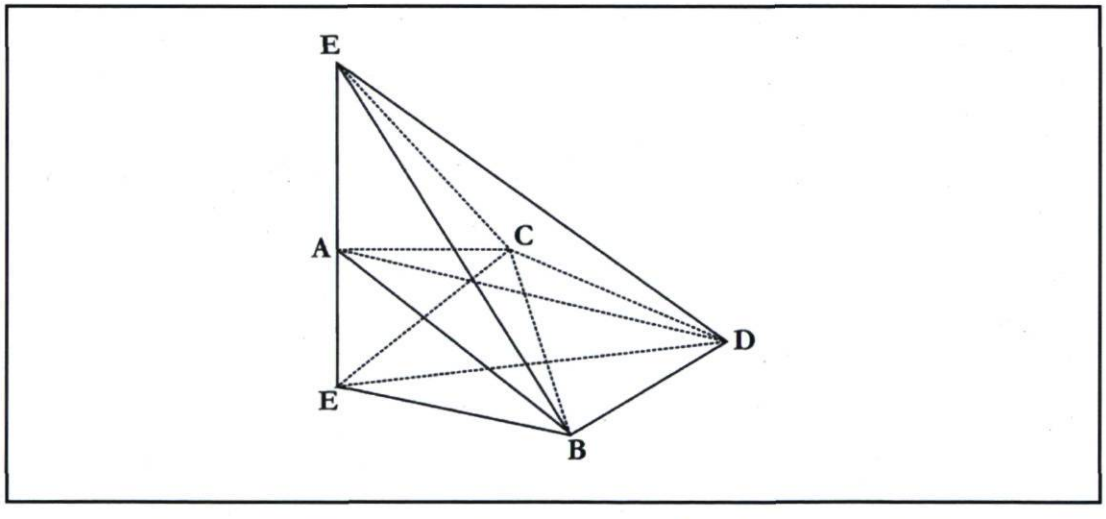

Figure 3.13 - Tetrahedral discretization used by Letniowski (1992)

Table 3.3a - Nodal coordinates (Letniowski, 1992)

Nodes	x	y	z
A	-2	-2	0.5
B	0	-2	0.1
C	-2	0	0.1
D	0	0.1	0
E	-2	-2	-0.25
F	-2	-2	1.5

Table 3.3b - Connectivity list for Letniowski's example

Tetrahedron	Node1	Node2	Node3	Node4
1: ABDF	1	2	4	6
2: ACDF	1	3	4	6
3: ABCE	1	2	3	5
4: BCDE	2	3	4	5
5: ABCD	1	2	3	4

Transmissibilities associated with edges AD and BC are presented in Tables 3.4a and 3.4b, respectively. The Galerkin method gives a value equal to 2.208 for edge connection AD and 3.695 for edge connection BC. In contrast, with the OSC method, negative values equal to -3.287 x 10^{-3} and -2.168 x 10^{-2} are calculated, respectively, for edges AD and BC. These negative values coincide with those calculated by Putti and Cordes (1998), providing a verification of the correct implementation of the OSC method in HydroGeoSphere. It can be observed that the global γ_{ij} coefficients calculated with the OSC method are always negative or zero, such that an M-matrix is obtained. Although some elemental contributions can be positive, like γ_{ACDF} in Table 3.4a, the global coefficient is never positive if the OSC method is applied. Therefore, the OSC method ensures that an M-matrix is obtained.

Table 3.4a - Transmissibility values for segment AD

Tetrahedron	γ_{AD} Galerkin method	γ_{AD} OSC method
ABDF	-0.0159	-7.293 x 10^{-3}
ACDF	-0.005	1.1796 x 10^{-2}
ABCD	2.229	-7.790 x 10^{-3}
	$\gamma_{AD}^{G} = \gamma_{AD}^{ABDF} + \gamma_{AD}^{ACDF} + \gamma_{AD}^{ABCD}$	
GLOBAL γ_{AD}^{G}	2.208	-3.287 x 10^{-3}

Table 3.4b - Transmissibility values for segment BC

Tetrahedron	γ_{BC} Galerkin method	γ_{BC} OSC method
ABCE	0	-1.669 x 10^{-4}
BCDE	1.469	-7.595 x 10^{-3}
ABCD	2.226	-1.392 x 10^{-2}
	$\gamma_{BC}^{G} = \gamma_{BC}^{ABCE} + \gamma_{BC}^{BCDE} + \gamma_{BC}^{ABCD}$	
GLOBAL γ_{BC}^{G}	3.695	-2.168 x 10^{-2}

The two test cases just presented demonstrate the correct implementation of tetrahedral meshes and the OSC method in HydroGeoSphere. In the first example, fluid conductance matrix coefficients computed with HydroGeoSphere are compared to those computed by LaGriT, while in the second example they are compared with those presented by previous studies (Letniowski, 1992; Putti and Cordes, 1998). Both examples demonstrate that coefficients are correctly calculated by the enhanced numerical code. Moreover, these examples highlight that a Delaunay mesh produces an M-matrix only if the OSC approach is applied. In contrast, with the standard Galerkin method, positive off-diagonal matrix coefficients arise.

Chapter 4

Verification and illustrative examples

The purpose of this chapter is to show the correct numerical solution of subsurface flow and mass transport equations on a fully 3D tetrahedral mesh with the enhanced HydroGeoSphere version. Simple domain geometries and simulation scenarios are chosen to verify the modeling approach that combines the three software tools (GOCAD, LagriT, and HydroGeoSphere). In fact, it is preferable to use simple cases to check mesh information, compatibility of input/output files between different software tools, and simulation results. This chapter focuses on a clear presentation and verification of the modeling approach presented in Chapters 2 and 3. Analytical solutions and numerical results obtained with block-based finite element meshes are employed to verify simulation results obtained with tetrahedral meshes. These results are presented in Section 4.1. Then, illustrative examples are presented in Section 4.2 to illustrate the modeling capabilities of the enhanced numerical code version, especially in relation to mesh refinement and representation of fracture-well intersections. These verifications are necessary before applying the modeling approach to real case studies, which are generally much more complex. An application to a real site will be presented in Chapter 5.

4.1 Verification examples

The enhanced HydroGeoSphere numerical code is verified by comparing numerical results obtained with tetrahedral and block-based meshes. The term "block" refers to the same element cited in Chapter 2 as a hexahedron, which is an eight-node element with six quadrilateral faces. Moreover, analytical solutions, when they can be applied, are also used as comparative tools. Simple domain geometries characterized by only one discrete fracture are chosen here, to facilitate the verification of simulation results. A pumping well is considered in test case 1. Because fractures and wells are included in the various simulation scenarios, it should be mentioned how the hydraulic conductivity of these elements is evaluated by the numerical code. The saturated hydraulic conductivity of a fracture having a uniform aperture 2b is calculated by HydroGeoSphere as follows:

$$K_f = \frac{\rho g}{12\mu}(2b)^2 \tag{4.1}$$

where ρ and μ are the water density and viscosity, respectively. The hydraulic conductivity of wells with screen radius r is obtained from a similar formula:

$$K_w = r^2 \frac{\rho g}{8\mu} \tag{4.2}$$

Before presenting the solute transport simulations, the first test case focuses only on a subsurface flow simulation. As the groundwater flow field is always calculated by HydroGeoSphere at the beginning of every simulation, it is important to verify its computation as a first verification step. In this way, possible errors in the fluid conductance matrix evaluation can be detected and fixed before they affect the solute transport solution. Once the groundwater flow solution is shown to be correct, other test cases are designed to simulate the temporal variation of solute concentration. Unless mentioned otherwise, mass transport refers to a general solute component, which, for example, may represent a contaminant or a tracer. Only the transport simulation results are presented, except when the hydraulic head distribution is of special interest. In general, for the test cases presented, unidirectional flow is imposed and a simple hydraulic head distribution is obtained. Implicit transport time weighting and upstream weighting of velocities are adopted, as both options have a positive effect on the computation of solute concentration, reducing numerical oscillations. The Peclet number is kept as small as possible, depending on mesh element size. The comparison between the OSC

and Galerkin methods is presented by analyzing the simulation results. The aspect ratio of the simulation domains considered in this section always exceeds ratio limits considered by Tecplot, which automatically adjusts this ratio to visualize the domain with reasonable and convenient shape and size.

The following test cases are presented in this section:

1. Test case 1:
   Pumping well in an anisotropic aquifer with a single horizontal fracture
2. Test case 2:
   Horizontal fracture
3. Test case 3:
   Inclined fracture in a low permeability porous rock
4. Test case 4:
   Inclined fracture in an impermeable rock

4.1.1 Test case 1 - pumping well in an anisotropic aquifer with a single horizontal fracture

The purpose of this example is to show the correct implementation of the OSC method if an anisotropic hydraulic conductivity tensor is considered. As explained in Chapter 3, the OSC method presented by Putti and Cordes (1998) has been adapted here to anisotropic porous media assuming a similar computation to that used with the Galerkin method. Although Cordes and Putti (2001) presented a strategy for solving the anisotropic tensor, they did not present a numerical example for an anisotropic aquifer. Moreover they considered only groundwater flow problems. In contrast, one of the objectives of this study is to extend the application of the OSC method to transport problems. Fluid conductance matrix coefficients, or transmissibilities, are evaluated just once during the numerical solution, but are used to solve both subsurface flow and transport equations. The calculation of transmissibilities is first verified for the solution of subsurface flow in an anisotropic aquifer.

The simulation domain has dimensions of 500 m x 500 m x 20 m and represents a homogeneous anisotropic aquifer with a vertical pumping well placed at its center and crossing the entire aquifer thickness. Moreover, a fracture cuts the whole domain horizontally and intersects the well axis at z = 10 m (Figure 4.1). The hydraulic conductivity K_x is two orders of magnitude lower than K_y (Table 4.1). Specified heads equal to 35 m are imposed at all boundaries and drawdown at the pumping well is observed. No mesh refinement is performed.

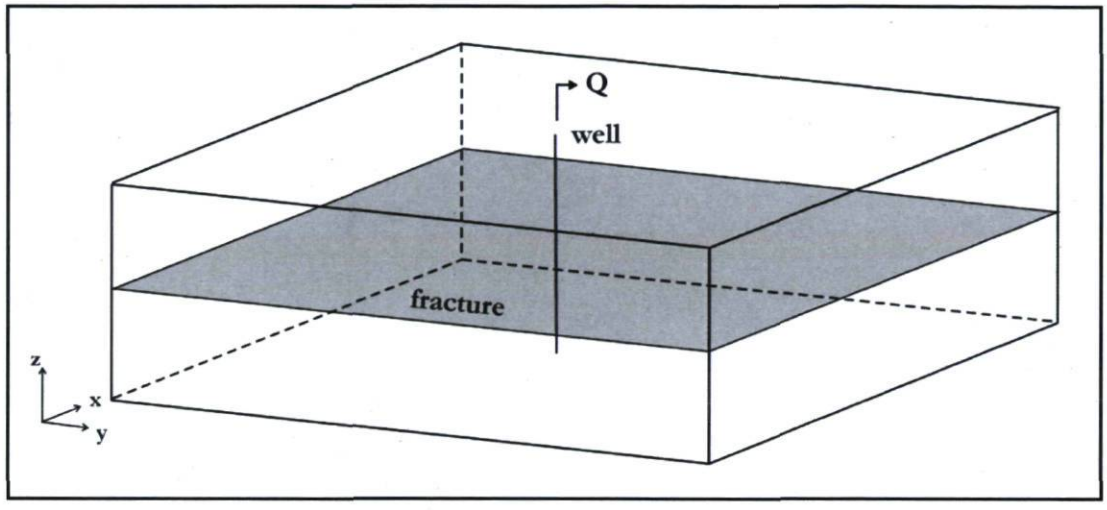

Figure 4.1 - Simulation design for test case 1

Table 4.1 - Simulation parameters for test case 1

Parameter definition	Value
Matrix hydraulic conductivity $K_x = K_z$ [m/y]	5
Matrix hydraulic conductivity K_y [m/y]	100
Fracture aperture 2b [m]	4×10^{-4}
Specific storage S_S [m^{-1}]	1×10^{-5}
Pumping rate Q [m^3/y]	5000
Well casing and screen radius r [m]	0.01

The simulation is executed with both Galerkin and OSC methods to compare steady-state hydraulic head values. As the Galerkin method was already implemented in previous

HydroGeoSphere versions, it is used to confirm the implementation of the OSC method. Steady-state hydraulic head isocontours are shown in Figure 4.2. Simulation results confirm the aquifer anisotropy; since hydraulic conductivity K_y is smaller, head isocontours have an elliptical shape instead of being perfectly circular as is the case for an isotropic aquifer (Figure 4.2). Hydraulic head isocontours in Figure 4.2a and Figure 4.2b are identical, demonstrating the correct evaluation of the fluid conductance matrix with the OSC method. Thus, the development described in Section 3.3.5 and, particularly, Eq.(3.59), are verified by this simple example, which demonstrates that the anisotropic hydraulic tensor is properly integrated in the numerical solution.

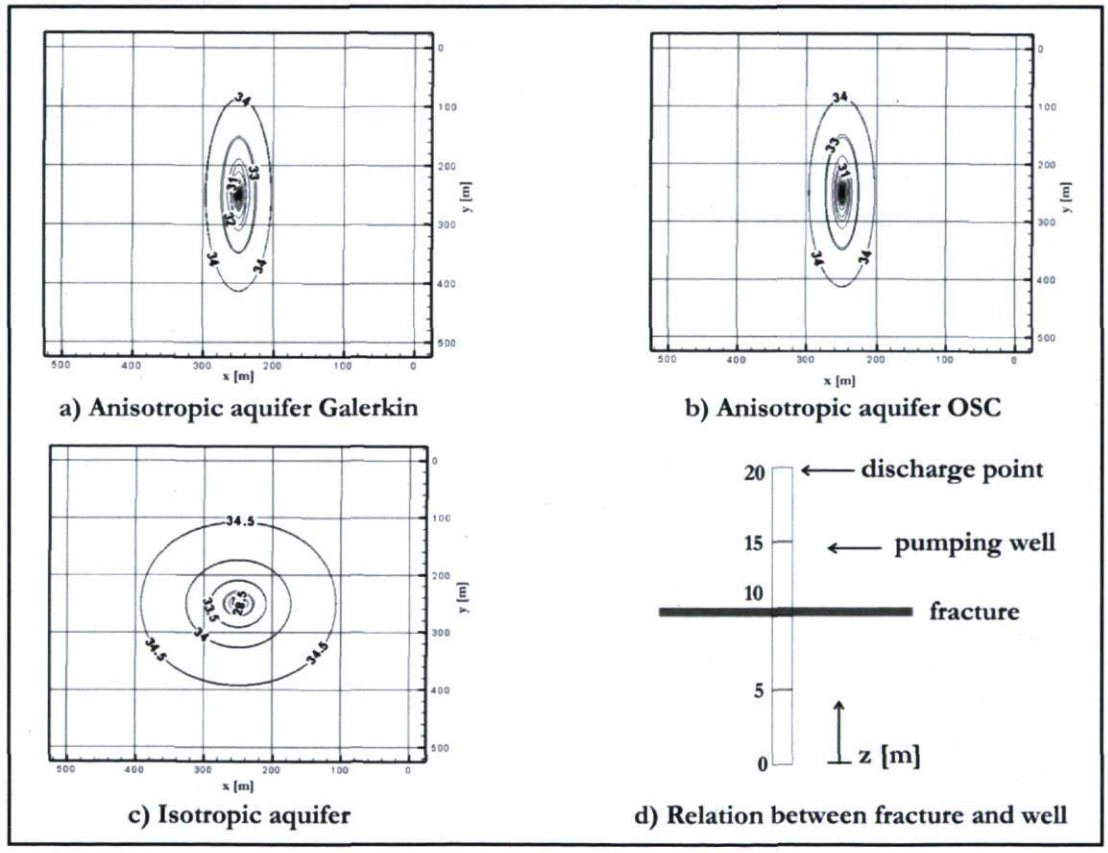

Figure 4.2 - Hydraulic head steady-state isocontours

The minimum steady-state hydraulic head at the pumping well is presented in Table 4.2, which shows that the two methods give comparable results. It is reasonable to obtain a small difference in hydraulic heads because fluid conductance coefficients, or transmissibilities, are

evaluated on the basis of a different control volume dual mesh. As already shown in Putti and Cordes (1998) and explained in Chapter 3, the Galerkin method uses the median dual mesh, while the OSC method considers the Voronoi dual mesh.

Table 4.2 - Minimum hydraulic head at the pumping well

Numerical method	H_{MIN} [m]
Galerkin	20.6
OSC	20.2

To analyze the effect of the fracture on the groundwater field, hydraulic conductivity values of the rock are reduced by an order of magnitude. If the aquifer is characterized by a lower permeability and the pumping rate is kept the same, a bigger volume of water is extracted from the fracture. Table 4.3 presents hydraulic heads and flow rates at well nodes, whose coordinates are listed in the last three columns on the right. Even if the discharge point is placed at the top of the domain, z = 20 m, the bigger inflow is at the intersection between the vertical well and the horizontal fracture. The negative value indicates flow from the fracture to the well, as is expected since water is extracted from the aquifer by pumping. Hydraulic heads are lower than the values shown in Table 4.2 because the hydraulic conductivity of the porous matrix has been reduced, as mentioned above. Thus, this simulation also demonstrates that the representation of the intersection between the pumping well and fracture is properly reproduced in the tetrahedral mesh.

Table 4.3 - Hydraulic heads and flow rates at pumping well nodes

Head [m]	Flux [m^3/y]	x [m]	y [m]	z [m]
-31.3	-478.6	250	250	0
-32.1	-994.2	250	250	5
-34.6	-1586.2	250	250	10
-39.7	-1194.6	250	250	15
-46.9	-746.3	250	250	20

Now that the evaluation of the groundwater flow field has been verified, transport simulations can also be considered, as done in the next test cases.

4.1.2 Test case 2 - horizontal fracture

The new modeling approach is verified here with an example previously solved both analytically and numerically with the block-based mesh. In this test case, the propagation of uranium isotope U^{234} along a horizontal fracture embedded in a porous rock matrix is simulated. The horizontal fracture was created in GOCAD and then imported into LaGriT to build the 3D tetrahedral mesh. Although the use of GOCAD is not necessary to represent a single horizontal fracture, it is employed here to verify the coupling between software tools. Once the simulation domain is discretized, LagriT files containing tetrahedral and triangular mesh information become input files for HydroGeoSphere. Now the numerical code selects fracture faces with the new approach described in Section 3.3.2. Nevertheless, in this simple case, fracture faces could also be selected using the existing HydroGeoSphere commands, as the fracture is horizontal and the faces to chose lie on a horizontal plane. Considering a very simple geometry represents the first step to verify the proposed modeling approach.

The simulation scenario comes from the numerical example already treated in Therrien et al. (2007). The fracture is defined by the xy plane located at $z = 0.05$ m and cuts through the whole domain. A first-type solute source is imposed at the right extremity of the fracture, at $x = 0$ m. A hydraulic head gradient equal to 1.305×10^{-2} is imposed along the x-axis reproducing unidirectional flow (Figure 4.3). The domain contains 3025 nodes (respectively 121, 5 and 5 in the x, y, and z directions), it has a unit thickness in the y-direction, a length of 30 m in the x-direction and a length of 0.1 m in the z-direction. Thus, nodal spacing orthogonal to the fracture is equal to 0.025 m. Domain dimensions have high aspect ratio and no refinement is done to avoid obtaining badly-shaped tetrahedra. The nodal distribution described above is also used to build block elements to execute the same simulation in a different finite element mesh and to compare these numerical results with those obtained with the tetrahedral mesh.

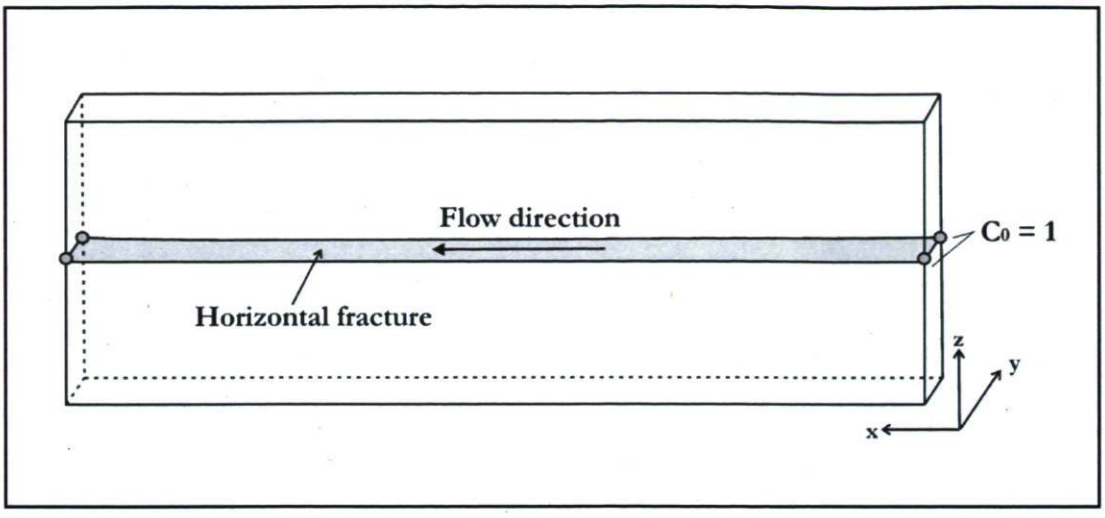

Figure 4.3 - Simulation design for test case 2

The same problem is also solved with the analytical solution CRAFLUSH (Sudicky, 1988), which solves the transport equation in a system of parallel fractures with matrix diffusion and longitudinal dispersion along the fracture. CRAFLUSH numerically inverts the Laplace transformed solution that is presented in the studies of Tang et al. (1981) and Sudicky and Frind (1982). The solution takes into account advection and longitudinal mechanical dispersion in the fracture, molecular diffusion along the fracture and from the fracture into the matrix, adsorption and radioactive decay of solutes. All these processes are also simulated by the numerical code HydroGeoSphere.

Simulation parameters are listed in Table 4.4. Mechanical dispersion through the porous rock matrix is neglected by setting the dispersivity to zero. Several observation points are placed along the fracture to visualize the concentration profile, which is presented in Figure 4.5. A maximum concentration variation of 0.01 is imposed for each time-step. Final simulation time is set to 10000 years.

Table 4.4 - Simulation parameters for test case 2

Parameter definition	Value
Matrix hydraulic conductivity K [m/y]	8.6×10^{-6}
Matrix porosity θ [-]	0.01
Tortuosity τ [-]	0.1
Fracture aperture 2b [m]	1×10^{-4}
Fracture spacing B [m]	0.1
Fracture longitudinal dispersivity α_L [m]	1
Free solution diffusion coefficient D_0 [m^2/y]	3.1×10^{-2}
Volumetric distribution coefficient K_d [kg/m^3]	7.1×10^{-2}
Solute half-life $T_{1/2}$ [y]	245000

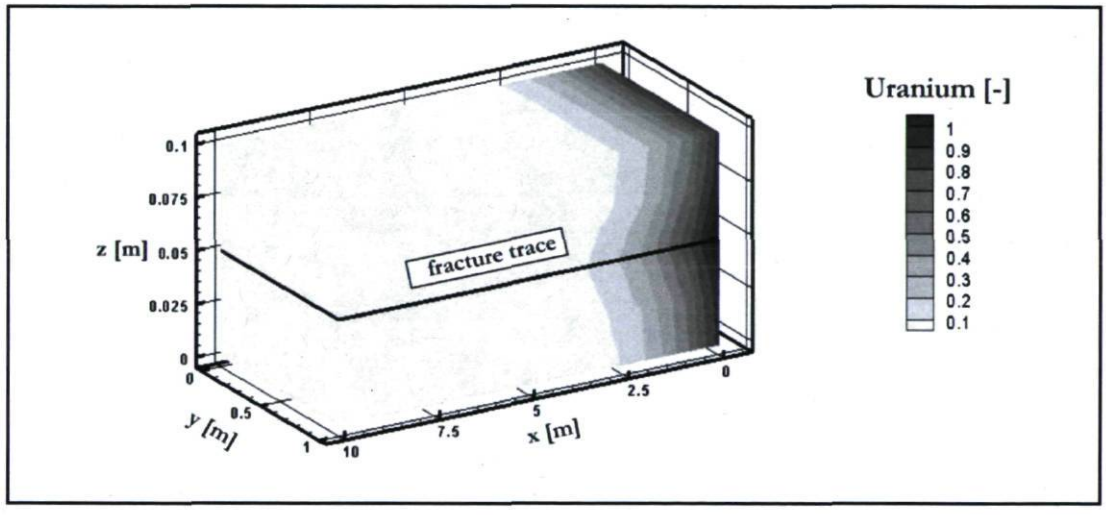

Figure 4.4 - Concentration isocontours for test case 2 after 10000 years

Concentration isocontours indicate the preferential propagation along the fracture (Figure 4.4). The decay and sorption of U^{234}, represented by its large retardation factor, slows down its migration; after 10000 years, the contamination plume has only traveled 2.5 m. Because the concentration rapidly decreases to zero away from the fracture, Figures 4.4 and 4.5 present simulation results only for the first 10 m from the contamination source

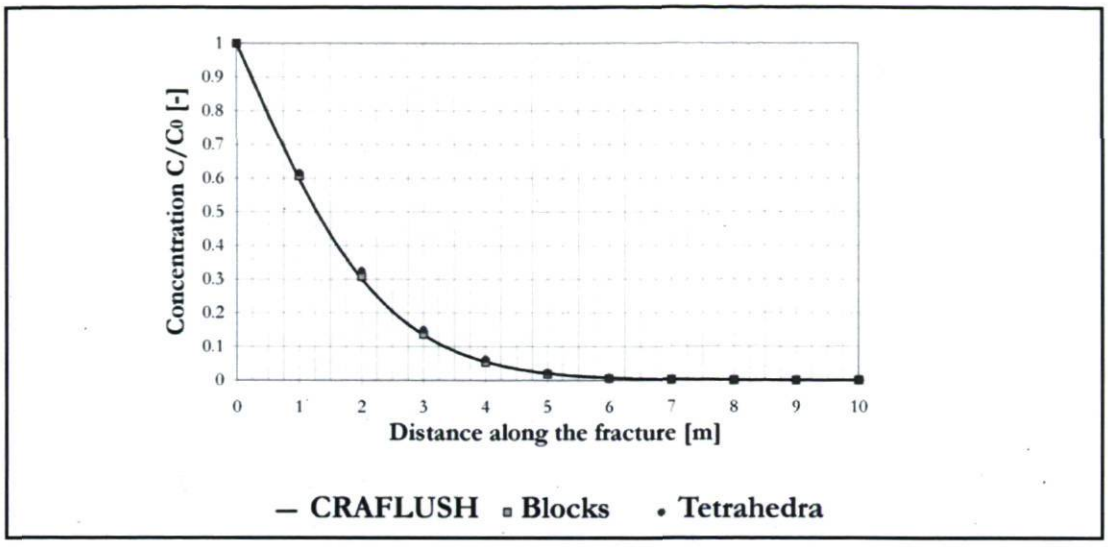

Figure 4.5 - Breakthrough curves for test case 2

Results obtained using HydroGeoSphere with the newly-implemented tetrahedral mesh agree very well with results obtained with the analytical solution CRAFLUSH and with the block-based mesh (Figure 4.5). Because the fracture is horizontal, the use of blocks or tetrahedra does not affect the geometry of the discretized fracture and numerical results match the analytical solution, which assumes that the fracture is planar.

4.1.3 Test case 3 - inclined fracture in a low permeability porous rock

The simulation domain has a length of 10 m and 12 m in the vertical and horizontal directions, respectively, with a unit thickness in the third direction. An inclined fracture (about 40°) crosses the whole domain. A hydraulic head difference equal to 0.5 m is imposed along the x-axis. A constant concentration of solute equal to 1.0 is imposed on the top of the domain, at z = 10 m (Figure 4.6, test case 3). All other boundaries are assigned zero dispersive flux for transport. Simulation parameters are listed in Table 4.5.

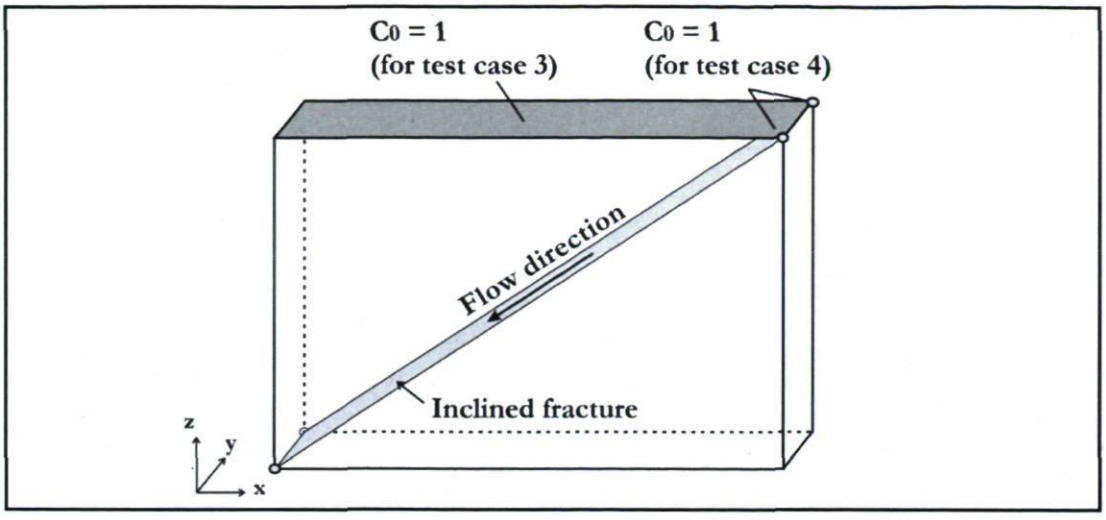

Figure 4.6 - Simulation design for test cases 3 and 4

Table 4.5 - Simulation parameters for test case 3

Parameter definition	Value
Matrix hydraulic conductivity K [m/y]	0.86
Matrix porosity θ [-]	0.35
Tortuosity τ [-]	0.1
Fracture aperture 2b [m]	0.0002
Fracture and matrix longitudinal dispersivity α_L [m]	0.1
Free solution diffusion coefficient D_0 [m^2/y]	0.16

Three different fracture configurations are considered here: two are based on a block-based mesh (Figures 4.7a and 4.7b), while the third configuration is obtained with the tetrahedral mesh (Figure 4.7c). Only the tetrahedral mesh exactly reproduces the inclined plane of the fracture. In contrast, fracture configurations obtained with a block-based mesh generate a staircase path for the fracture, which lengthens the solute travel distance. Therefore, solute breakthrough curves will be influenced by the discretization of the inclined fracture, as will be shown later.

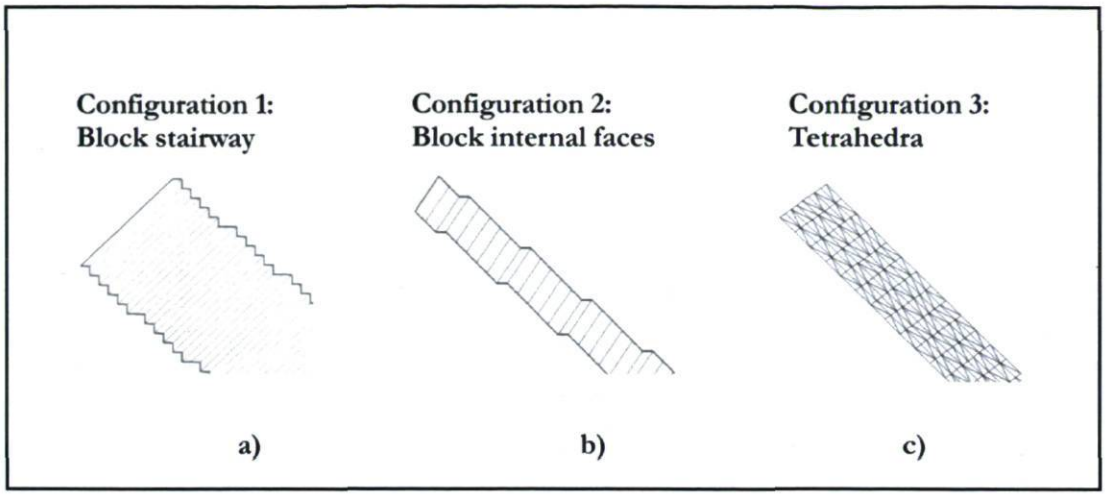

Figure 4.7 - Different discretizations for inclined fractures

The block-based mesh contains 1612 nodes, with 31 nodes along the x-axis, 26 along the z-axis, and 2 along the y-axis. From this nodal distribution, 750 block elements are generated. The tetrahedral mesh was generated from the same nodal distribution resulting in a nodal spacing equal to 0.4 m far from the fracture. Then, two successive refinement steps produced a finer mesh near the fracture, where nodal spacing is now 0.1 m (Figure 4.8). Nodal spacing on the fracture surface is equal to 0.125 m. The refined tetrahedral mesh contains 11105 nodes and 51223 elements. To obtain the same resolution near the fracture, with a block-based mesh, the whole domain has to be finely discretized with blocks 0.1 m long, resulting in a mesh containing 24442 elements and 12000 nodes.

An observation point is located at coordinates (6,0,5), where the solute breakthrough curve is computed. The maximum concentration change for a time-step is set to 0.1 and the final simulation time is 5 years. By observing concentration isocontours (Figure 4.9), it is clear that the fracture strongly controls the solute migration. Isocontours are shown only for the tetrahedral mesh, but there is no visible difference in their shape if the block-based mesh, the OSC or the Galerkin methods are used.

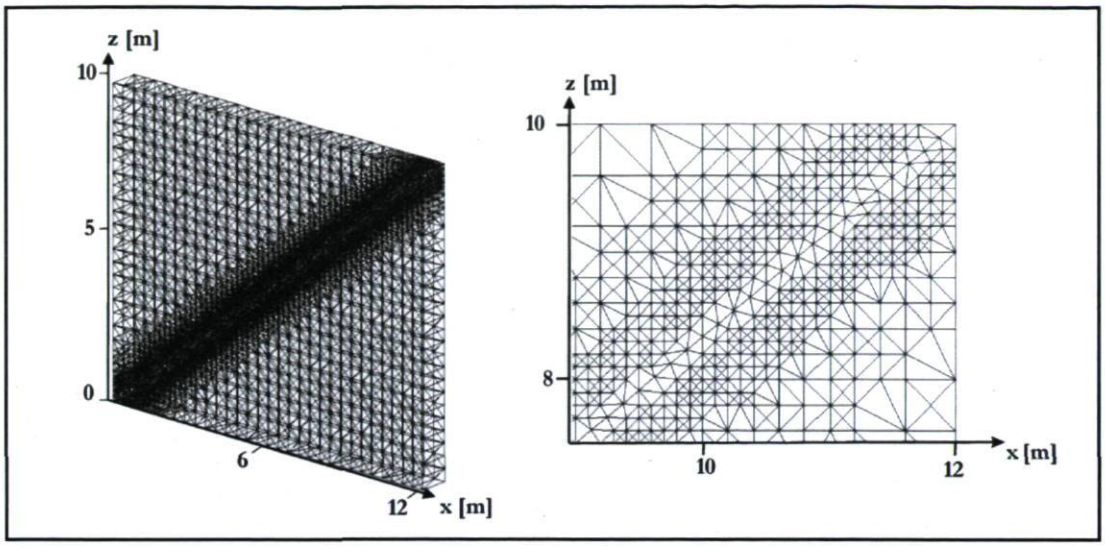

Figure 4.8 - Tetrahedral mesh with refinement around fracture

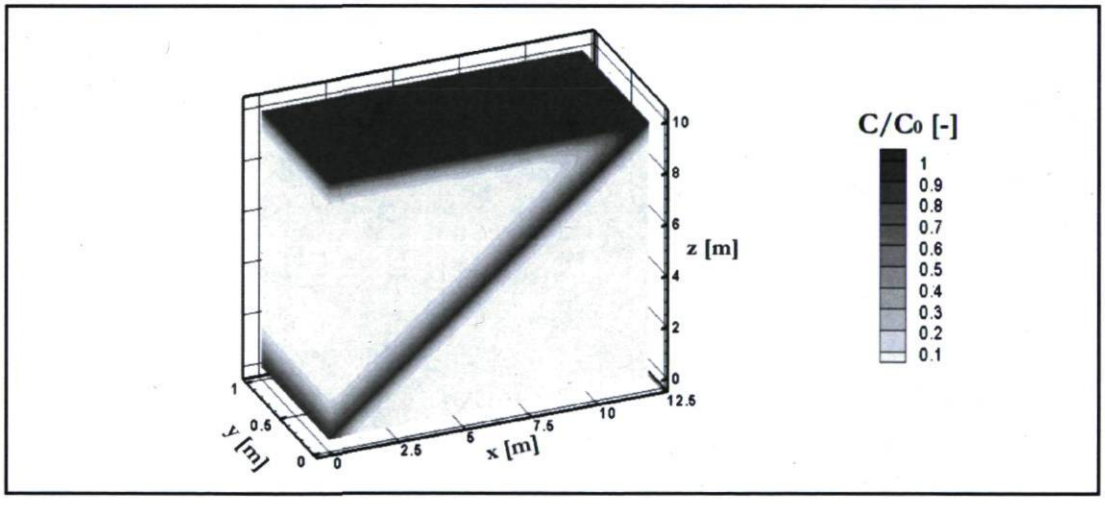

Figure 4.9 - Concentration isocontours for test case 3 after 5 years

Differences can be observed if single concentration values are observed. In particular, it is interesting to observe the difference between Galerkin and OSC methods by considering relative concentration minimum values C/C_0, which should be zero and never negative. The smallest concentration value obtained with the Galerkin method is equal to -9×10^{-6}, while the OSC method gives exactly 0, which is equal to the initial concentration set for the simulation. Although the value obtained with the Galerkin method is almost zero and it is acceptable, it is

obvious that the OSC method seems to be a better solution procedure. Other examples, in the next paragraphs, will show the same tendency, suggesting that the OSC method is more accurate than the Galerkin method to solve the mass transport equation.

Other differences in numerical results arise if breakthrough curves computed at the observation point are considered. In reference to the fracture configurations shown in Figure 4.7, the corresponding curves are presented (Figure 4.10). A distinction between simulations made on tetrahedral mesh solved with the Galerkin or OSC method is made. Curve shapes reflect the difference in the fracture path length. With the tetrahedral mesh, the fracture is represented by an inclined plane joining the domain extremities, without lengthening the solute pathway. As a result, the solute breakthrough curve for the tetrahedral mesh is the first one from the left (Figure 4.10). In contrast, the fracture path is the longest with the Block Stairway configuration and the corresponding curve moves to the right. Finally, the Block Internal Faces configuration produces a curve that is halfway between the previous ones, as the fracture path length is shorter than the Block Stairway but longer than the Tetrahedra configuration. Furthermore, a small difference in the shape of the breakthrough curve can be observed between the Galerkin and OSC methods for concentration values between 0.8 and 0.9.

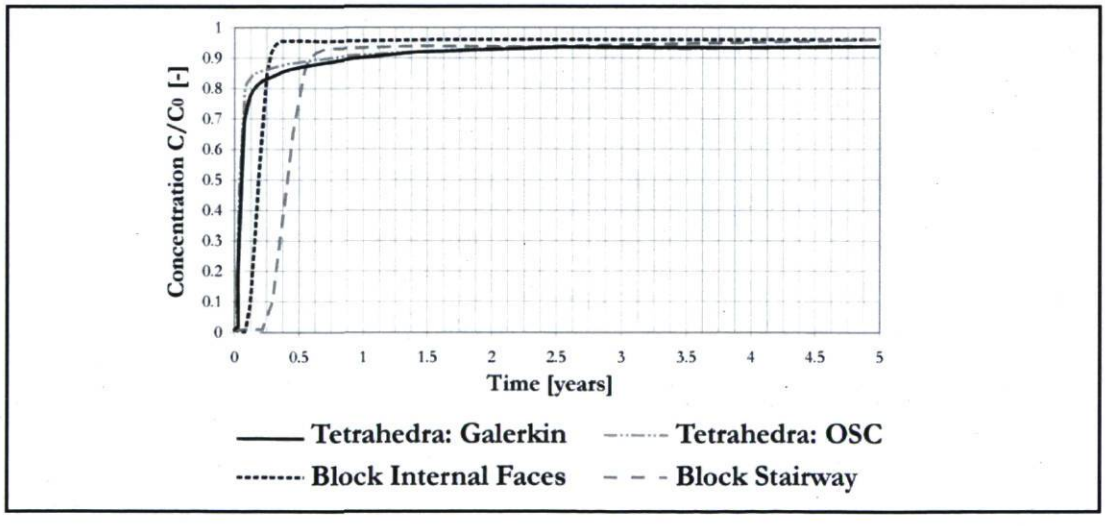

Figure 4.10 - Breakthrough curves for test case 3

Only with the tetrahedral mesh it is possible to refine the mesh locally around the fracture. Refinement orthogonal to a fracture plays a major role in the case of low matrix diffusion (Weatherill et al., 2008). Thus, a tetrahedral mesh offers more flexibility and it is more suitable than a structured mesh to discretize discretely-fractured media, especially if irregular fractures have to be represented. Furthermore, fractures are discretized with the path length attributed during the geomodeling phase, no matter if they are planar or not. In conclusion, the greatest advantage is that the mesh generation procedure adopted here allows for easy refinement around fractures, representing a great asset for the accuracy of the numerical solution. For example, Weatherill et al. (2008) stated that spatial grids have to be fine at the fracture-matrix interface and in cases of low matrix diffusion they need to be on the scale of the fracture aperture to accurately simulate solute transport.

4.1.4 Test case 4 - inclined fracture in an impermeable porous rock

The next simulation, test case 4, verifies the fracture behavior. The geometry is the same used in the previous example, but now the source of concentration is imposed at the extremity of the fracture (Figure 4.6, test case 4). In contrast to the previous example, the porous rock matrix is now considered impermeable. As a result, flow and solute propagation are restricted to the fracture. Fracture parameters are the same as those listed in Table 4.5. As the surrounding rock matrix is considered impermeable, solute propagation along the fracture can be evaluated with the simplified Ogata-Banks analytical solution, which is applicable when the observation point is far from the source, such as considered in this case. In fact, the observation point is located at half-way along the fracture, at the node with coordinates (6,0,5), which is 8 m far from the top of the fracture, where the concentration c_0 is imposed. The simplified Ogata-Banks solution expresses concentration as:

$$c(x,t) = \frac{c_0}{2} \cdot erfc\left(\frac{x - v \cdot t}{2 \cdot \sqrt{D \cdot t}}\right) \tag{4.3}$$

where D is the hydrodynamic dispersion coefficient, v is the velocity along the fracture, x is the distance between the observation point and the source, and t is the time. Simulation results are shown in Figure 4.11. The difference from Figure 4.9 is clear, where propagation

also took place orthogonally to the fracture, due to diffusion and dispersion through the porous rock matrix. In contrast, in this case, the propagation occurs only along the plane of fracture and, therefore, is much faster.

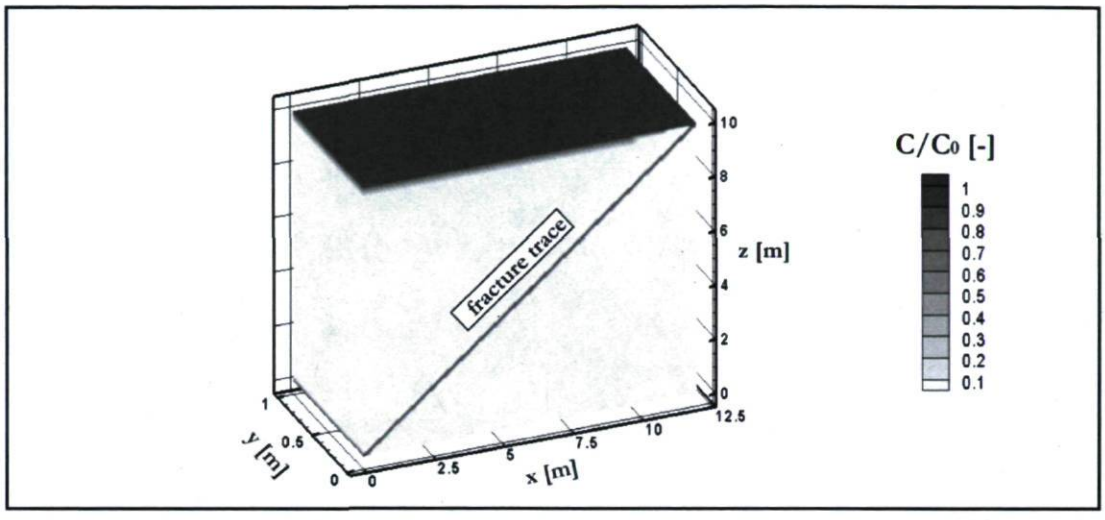

Figure 4.11 - Concentration isocontours for test case 4 after 5 years

The three fracture configurations presented above (Figure 4.7) are considered again here. Breakthrough curves computed at the observation point of coordinates (6,0,5) are shown in Figure 4.12, to highlight the influence of the fracture path length on solute migration.

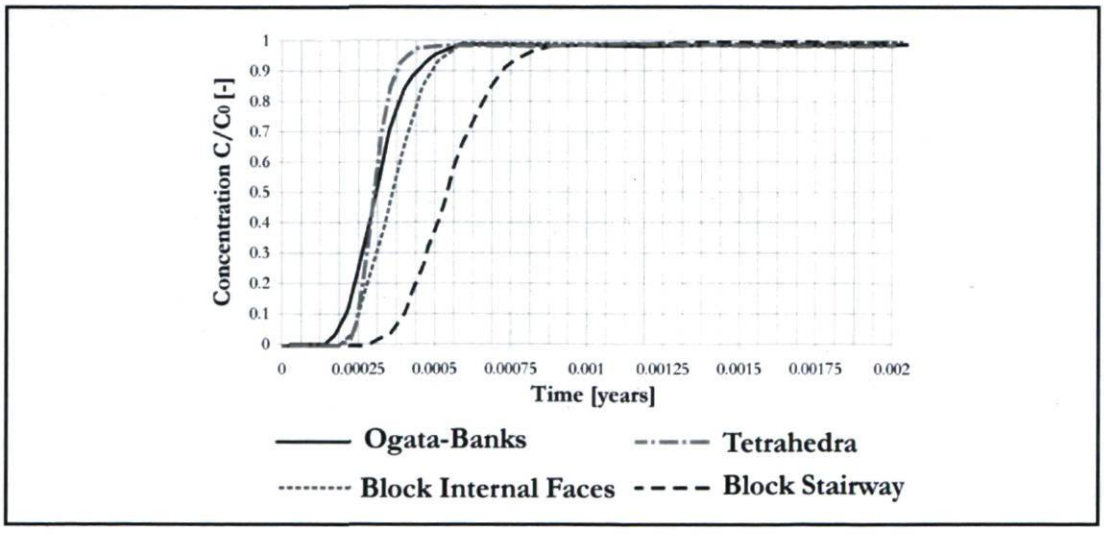

Figure 4.12 - Breakthrough curves for test case 4

The tetrahedral mesh gives a good approximation of the Ogata-Banks analytical solution, better than the Block Internal Faces configuration. If the analytical solution and the tetrahedral mesh configuration are considered, it can be observed that the advective front reaches the observation point at the same time, while there is a slight difference in the spreading of solute around the advective front. The Block Stairway configuration is obviously the worst, as the solute travel distance is lengthened compared to that for a planar fracture. Thus, the mesh generation process adopted here leads to a representation of inclined fractures that is the closest one to the analytical solution.

4.2 Illustrative examples

Illustrative examples show the capabilities of the new modeling approach for cases closer to real field situations. Simulation scenarios have been designed to check specific modeling aspects of special interest for the application to a real site that will be shown in Chapter 5. The complexity of the scenarios increases gradually. At first, in test case 5, an inclined pumping well is considered to illustrate the advantage of using a tetrahedral mesh. Then, a discrete fracture is incorporated in test cases 6 and 7, to confirm the representation of intersections between the fracture and well. Finally, in the last illustrative example, a network of three irregular fractures is considered to verify the correct representation of their intersections.

The Galerkin and OSC methods will be compared by observing simulation results. Moreover, it should be noted that, contrary to the test cases presented in Section 4.1, discrete fractures no longer extend to the external boundary of the simulation domain. Thus, the test cases presented in this section demonstrate that there is no limitation to represent fractures that do not extend to the external domain boundary, as explained in Chapter 1 in relation to previous studies in discretely-fractured media, which often had this limitation.

In summary, the following test cases are presented in this section:

1. Test case 5:
   Discretization of an inclined well
2. Test case 6:

Contamination propagation: fracture and open borehole

3. Test case 7:

   Contamination propagation: fracture and pumping wells

4. Test case 8:

   Contamination propagation: network of irregular fractures

4.2.1 Test case 5 - discretization of an inclined pumping well

This illustrative example is designed to show the advantage of using tetrahedra to discretize inclined wells. An inclined well is first discretized for a mesh made of blocks and then for another mesh made of tetrahedra. Mesh refinement and hydraulic head isocontours are compared to show the influence of different mesh types on numerical results. The domain is 1000 m long in each spatial direction. The pumping well crosses the whole aquifer thickness: the well top and bottom nodes are placed, respectively, at coordinates (500,500,1000) and (500, 350,0). The transient flow option is chosen: the well is pumping during the first 73 days and then recovery is simulated and, after 145 days, the initial head distribution is naturally reestablished. A hydraulic head equal to 15 m is specified at the boundaries. The same head value is used as the initial head. Other simulation parameters are listed in Table 4.6.

Table 4.6 - Simulation parameters for test case 5

Parameter definition	Value
Pumping rate [m^3/y]	5000
Well casing radius [m]	0.076
Specific storage [m^{-1}]	1×10^{-5}
Hydraulic conductivity [m/y]	3.16

As mentioned above, different mesh types are employed here. Two meshes are based on uniform size blocks, while the third one on variable size blocks. The fourth and fifth meshes are based on the same refined tetrahedral mesh, but the two different numerical methods, Galerkin and OSC, are used (Table 4.7). In the refined meshes presented, the shortest edge is 6

m long. Although to obtain this resolution around the well about 59000 tetrahedra are enough, more than the double number of blocks is required. Simulations are executed on the same computer to compare CPU time. If values listed in Table 4.7 are observed, it can be observed that CPU time for the refined tetrahedral meshes is significantly shorter than the meshes with fine block elements. In fact, with the tetrahedral mesh it is possible to refine the mesh just locally around the well, ensuring optimal resolution and avoiding large CPU times. Finally, the CPU time difference between OSC and Galerkin methods is not relevant for this test case.

Table 4.7 - Inclined well discretizations

Mesh type	Edge lengths	Nodes	Elements	H_{MIN}	Well nodes	CPU time
Uniform coarse blocks	50 m	9261	8000	13.92	21	8 s
Uniform fine blocks	20 m	132651	125000	13.68	51	136 s
Refined blocks	6 -100 m	134064	123246	13.4	168	169 s
Refined tetrahedra OSC	6 -100 m	10431	58915	13.65	201	33 s
Refined tetrahedra Galerkin	6 -100 m	10431	58915	13.66	201	30 s

It is interesting to observe the well axis after its discretization (Figure 4.13). If the block-based mesh is used, the resulting well axis has a stairway shape. In contrast, it is possible to reproduce the real well geometry with the tetrahedral unstructured mesh. In that case, the discretization technique does not affect the axis geometry, as presented in Figure 4.13d, where only the boundary elements are shown to highlight the shape of the discretized well axis, which is perfectly linear.

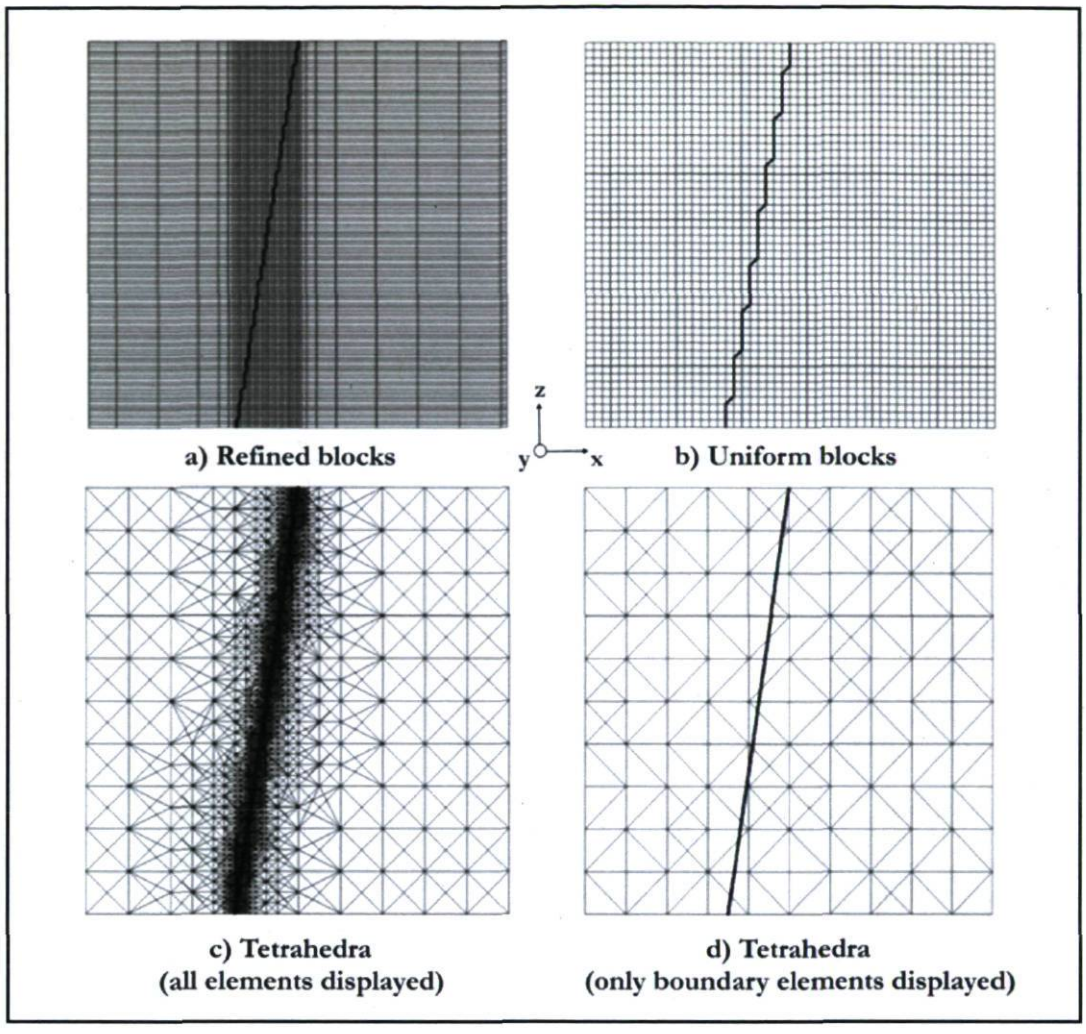

Figure 4.13 - Different discretizations of the same inclined well

Numerical results are shown for a slice inside the domain, at x = 400 m (Figure 4.14). Head isocontours are influenced by the discretization of the well axis: coarse elements around the well cause the shape of the isocontours to be irregular and almost unrealistic, as three marked discontinuities are visible (Figure 4.14a). If block elements around the well are smaller, the discretized well is closer to the real inclined axis (Figure 4.14b). Thus, with a properly refined block-based mesh, hydraulic head isocontours will not be affected by the discretization, but the CPU time will be much longer (Table 4.7). Thus, the unstructured tetrahedral mesh is the best solution to discretize inclined wells, because it offers the best resolution with the lowest computing time.

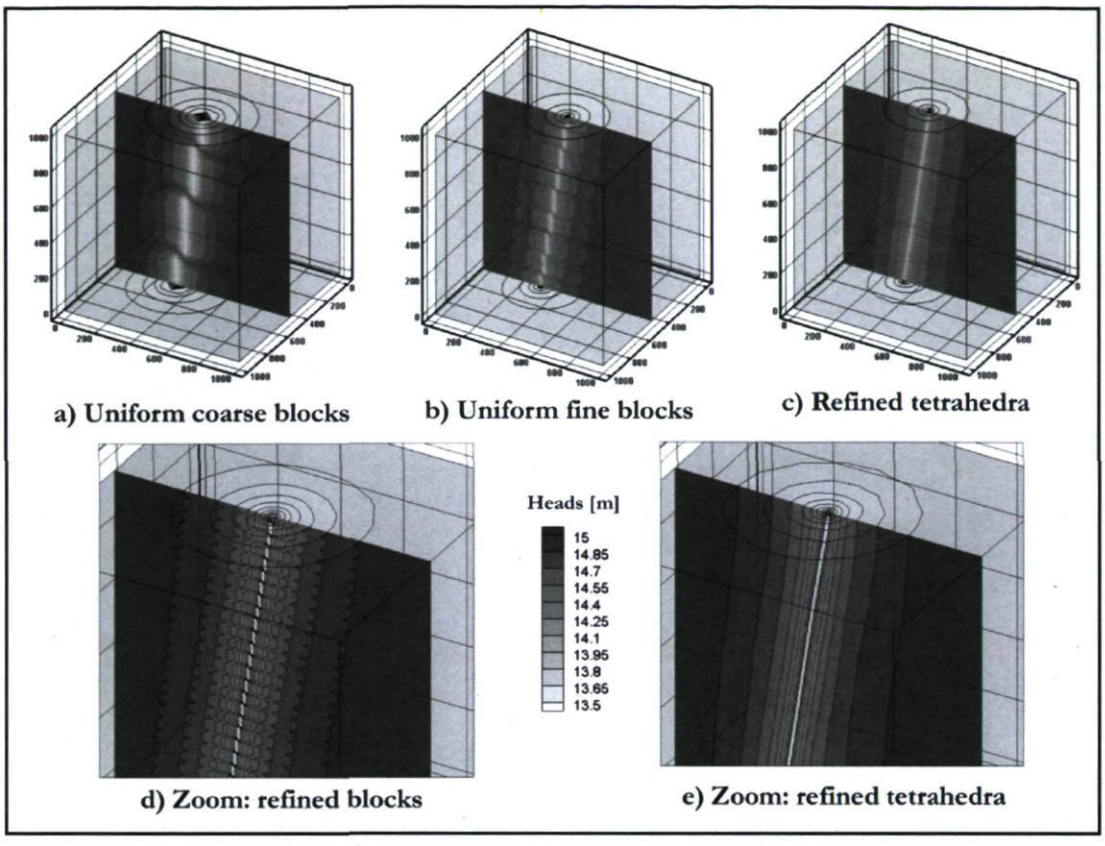

Figure 4.14 - Hydraulic heads around the inclined well at the end of pumping after 73 days

In conclusion, the new approach developed and explained in Section 3.3.3 represents an interesting and suitable technique to reproduce inclined wells in simulation scenarios. This technique is based on the identification of mesh segments joining the well nodes listed in the HydroGeoSphere input file. These nodes describe the real well axis thanks to the modeling approach that couples HydroGeoSphere with GOCAD. Therefore, this technique provides accurate resolution with reasonable computing effort.

4.2.2 Test case 6 - contaminant propagation: fracture and open borehole

This illustrative example is designed to show the effects of open boreholes and fractures on solute propagation. The borehole is represented by a discretized well with zero flowrate. The borehole intersects a discrete fracture embedded in a low permeability porous rock matrix. A

unit concentration is imposed on a block of nodes around the fracture, at a depth of about 600 meters. A hydraulic gradient equal to 0.036 is imposed along the y direction (Figure 4.15). The hydraulic conductivity difference between the porous rock matrix and fracture is seven orders of magnitude (see Table 4.8).

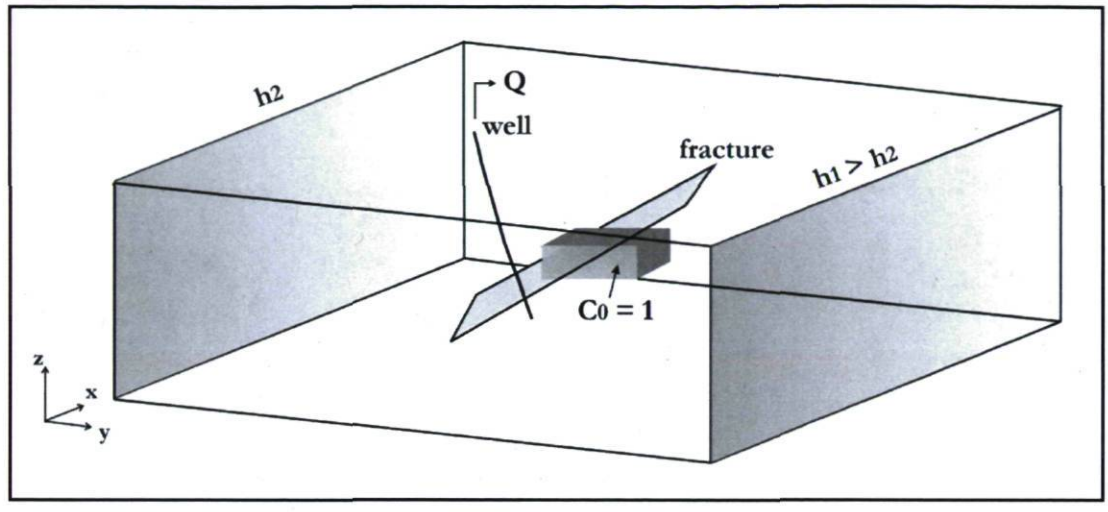

Figure 4.15 - Simulation design for test case 6

The tetrahedral mesh contains about 237000 tetrahedra. Local mesh refinement is performed around the well and near the fracture and the nodal spacing along the well axis is about 6 m, while far from the well and the fracture the nodal spacing is 100 m. The fracture has 4544 triangular elements and 2365 nodes, while the well axis is discretized with 151 nodes. The intersection between the well and the fracture is located at node 143, while the withdrawal node is chosen at the bottom of the well, node 151, as printed in the *.eco file by the preprocessor GROK (Figure 4.16).

The time-step length is modified as the solution proceeds using adaptive time-steps based on a maximum absolute change in nodal concentration equal to 0.15. Simulation parameters are listed in Table 4.8.

```
Data for pumping/injection well: 1
 ----------------------------------
   Well is fluid filled
   Well name:              Pumping well
   Well radius:            0.10000E-01
   Casing radius:          0.10000E-01
   Well conductivity:      0.34393E+10
   Well storage coefficient: 0.43149E-05
   Pumping/injection schedule
       Time on     Time off     Flowrate
     0.00000    0.100000E+31  0.00000

   Number of well nodes: 151
   Well nodes      x-y-z location

     143          1525819   6792240     -822  ---> fracture

     151          1525814   6792255     -868  ---> Injection/withdrawal node
```

Figure 4.16 - Open borehole description (from GROK *.eco file)

Table 4.8 - Simulation parameters for test case 6

Parameter definition	Value
Matrix hydraulic conductivity K [m/y]	0.864
Porosity θ [-]	0.38
Tortuosity τ [-]	0.35
Matrix longitudinal dispersivity α_L [m]	50
Matrix transverse dispersivities α_T [m]	10
Fracture aperture $2b$ [m]	4×10^{-6}
Fracture longitudinal dispersivity α_L [m]	20
Fracture transverse dispersivity α_T [m]	5
Free solution diffusion coefficient D_0 [m²/y]	0.16
Well casing and screen radius r [m]	0.01

The open borehole constitutes a preferential path for solute transport, as does the fracture. It is possible to observe this behavior in Figure 4.17, where the solute plume follows the fracture trace, moves up the borehole, and reaches the surface.

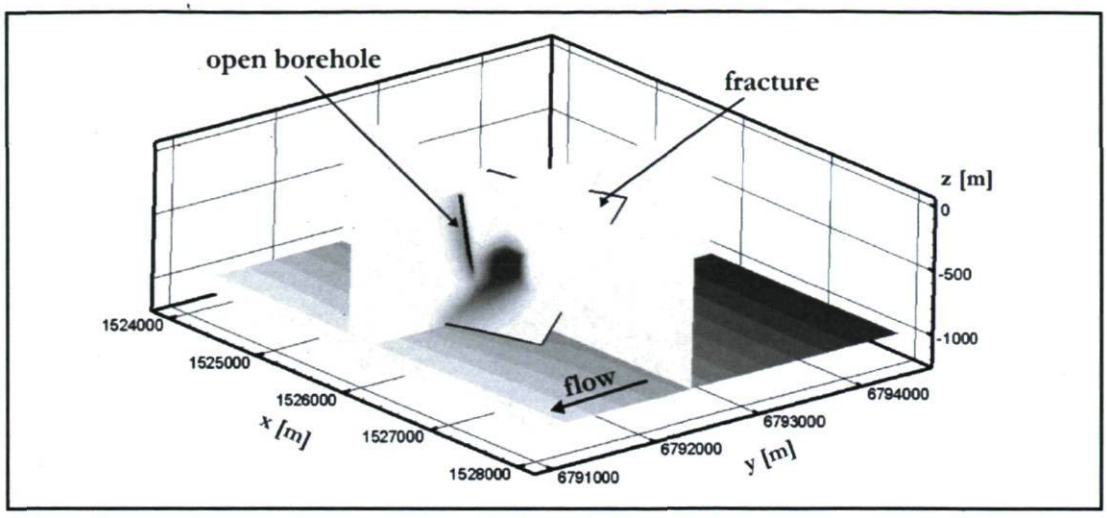

Figure 4.17 - Hydraulic heads (slice orthogonal to the z-plane) and concentration isocontours (along the fracture and the borehole) shown after 1000 years

A close-up of Figure 4.17 is provided in Figure 4.18, to highlight the solute plume along the fracture and borehole. A comparison of the Galerkin and OSC methods shows that the isocontours are almost identical.

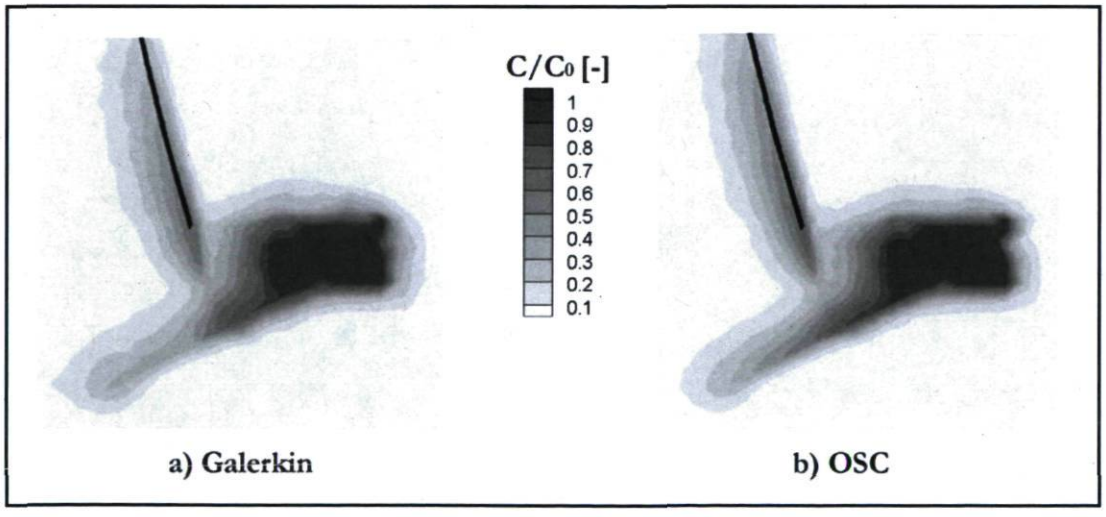

Figure 4.18 - Concentration isocontours at slice x = 1525800 m after 1000 years

If minimum relative concentration values are considered, a small difference can be observed between the Galerkin and OSC methods, as presented in Table 4.9. The minimum relative

concentration value should be zero, which is the initial concentration value imposed at the beginning of the simulation. Furthermore, negative concentrations are unreal and non-physical, simply representing numerical errors. It can be observed that the OSC method gives a value nearer to zero than the Galerkin method, even if any error in the visualization of concentration isocontours arises.

Table 4.9 - Minimum relative concentration values for test case 6

Mesh type	C_{MAX}	C_{MIN}
Galerkin	1	-0.004
OSC	1	-1.7×10^{-7}

If this test case is simulated using smaller rock matrix dispersivities (25 m and 2.5 m for longitudinal and transverse dispersivity, respectively) and higher hydraulic conductivity (10 m/y), but keeping the same mesh, numerical errors appear if the Galerkin method is applied. In fact, when concentration results are visualized, the isocontour of concentration equal to zero, normally not present, is now shown. In contrast, with the OSC method no errors are visualized, even if concentrations are slightly negative (Table 4.10).

Table 4.10 - Minimum relative concentration values for test case 6 modified

Mesh type	C_{MAX}	C_{MIN}
Galerkin	1	-0.0503
OSC	1	-0.0094

4.2.3 Test case 7 - contaminant propagation: fracture and pumping wells

A simulation scenario similar to the previous one is considered here. The main difference is that the open borehole is replaced by three vertical pumping wells located upstream of the fracture. Moreover, the concentration source is moved upstream of the fracture (Figure 4.19). This simulation scenario has been designed to reproduce solute propagation with and without pumping. The specific goal is to verify that the numerical solution based on the tetrahedral

mesh correctly simulates solute transport when pumping wells and discrete fractures are concomitant. Again, time-step length is modified as the solution proceeds using adaptive time-steps based on a maximum absolute change in nodal concentration equal to 0.15. Simulation parameters are listed in Table 4.11.

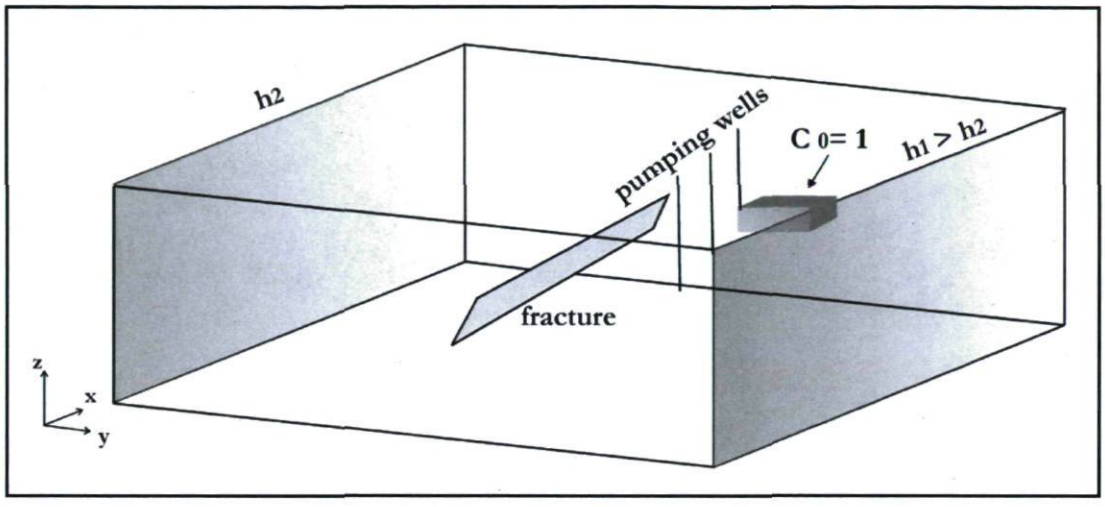

Figure 4.19 - Simulation design for test case 7

Table 4.11 - Simulation parameters for test case 7

Parameter definition	Value
Hydraulic conductivity rock K [m/y]	10
Fracture aperture $2b$ [m]	5 x 10^{-6}
Porous rock and fracture longitudinal dispersivity α_L [m]	25
Porous rock and fracture transverse dispersivities α_T [m]	2.5
Free solution diffusion coefficient D_0 [m^2/y]	0.16
Porosity θ [-]	0.38
Tortuosity τ [-]	0.35
Well casing and screen radius r [m]	0.01

Concentration isocontours at x=1525800 m are presented in Figure 4.20. Both wells and fracture traces are visible. As wells intersect the fracture, it is clear that with a proper pumping rate solute propagation is slowed down and migration along the fracture is stopped (Figure

4.20c and 4.20d). As the rock matrix is characterized by a low permeability, the propagation takes place mainly by molecular diffusion through the porous rock matrix. In contrast, solute moves preferentially by advection along the discrete fracture of aperture 500 μm when there are no wells in the simulation scenario. If the Galerkin and OSC results are compared, it can be observed that propagation along the z direction is reduced with the OSC method, even if dispersivity values are the same. This effect may be due to the different definition of control volumes, as already mentioned.

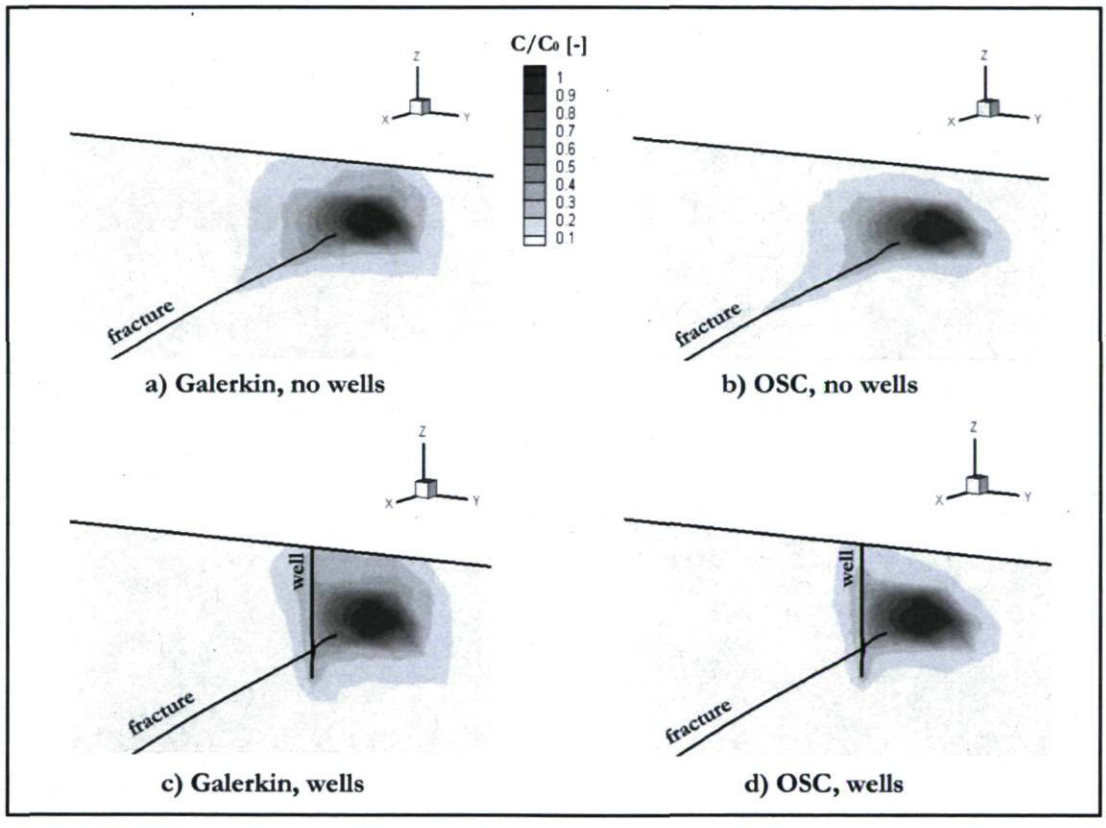

Figure 4.20 - Concentration isocontours after 500 years: fracture and well traces are shown

If minimum relative concentration values are observed, it is possible to note that with the OSC method, concentrations are nearer to zero than with the Galerkin method, regardless of whether pumping wells are included in the simulation or not (Table 4.12).

Table 4.12 - Minimum relative concentration values for test case 7

Mesh type	C_{MAX}	C_{MIN}
Galerkin, no wells	1	-0.0014
OSC, no wells	1	-6.0×10^{-8}
Galerkin, pumping wells	1	-0.0017
OSC, pumping wells	1	-2.8×10^{-8}

4.2.4 Test case 8 - contaminant propagation: network of irregular fractures

The purpose of this test case is to verify the solute propagation along intersecting fractures. Fracture intersections have been modeled in GOCAD, as explained in Chapter 2. Simulation results presented here verify the proper topology of fracture intersections. In particular, the commonality of nodes at intersecting lines is properly considered by the numerical solution if plume propagation follows the intersection line patterns. Otherwise, if fractures have no mutual nodes, solute will propagate independently along each fracture.

The simulation domain covers an area of 3 km x 4 km and has a thickness of 1.4 km. Three fractures are placed at its center (Figure 4.21). The porous rock is characterized by a very low permeability, while the fractures have a high hydraulic conductivity due to their apertures. A difference in hydraulic heads is imposed along the y direction. A specified unit concentration is imposed within the xz plane located at y = 6791100 m, while the inflow boundary at the xz plane located at y = 6791000 m is set to zero concentration. Porous rock and fracture dispersivity values are chosen in relation to the mesh element size to keep the Peclet number small and, consequently, to avoid numerical errors. Time-step length is modified as the solution proceeds using adaptive time-steps based on a maximum absolute change in nodal concentration equal to 0.1. Simulation parameters are listed in Table 4.13.

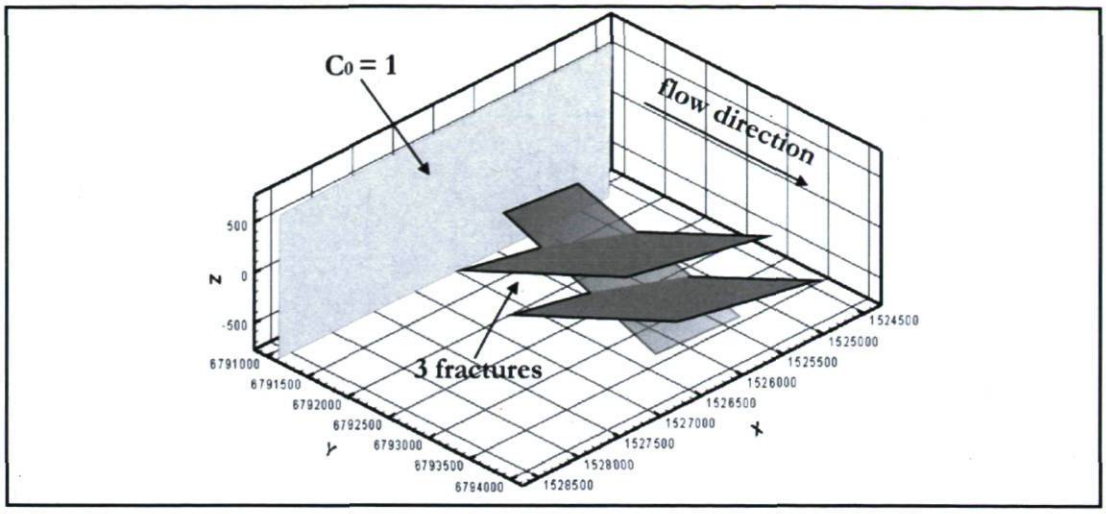

Figure 4.21 - Simulation design for test case 8

Table 4.13 - Simulation parameters for test case 8

Parameter definition	Value
Hydraulic conductivity rock K [m/y]	0.031
Rock matrix longitudinal dispersivity α_L [m]	100
Rock matrix transverse dispersivities α_T [m]	10
Free solution diffusion coefficient D_0 [m²/y]	0.16
Porosity θ [-]	0.38
Tortuosity τ [-]	0.35
Fracture apertures $2b$ [m]	100×10^{-6} 200×10^{-6} 300×10^{-6}
Fracture longitudinal dispersivities α_L [m]	50 30 40
Fracture transverse dispersivities α_T [m]	5 3 4

The fracture triangular mesh is shown in Figure 4.22. The number of triangles for each fracture is 4344, 6205, and 6254, respectively, for a total of 16803 triangular tetrahedral faces selected and defined as fracture elements. The mesh contains 435526 tetrahedra, which are refined

around the fractures applying the procedure explained in Chapter 2 (Figure 4.23). Two successive refinement steps allow to obtain tetrahedral edges 25 m long near fractures. In contrast, away from the fractures, the nodal spacing is equal to 100 m.

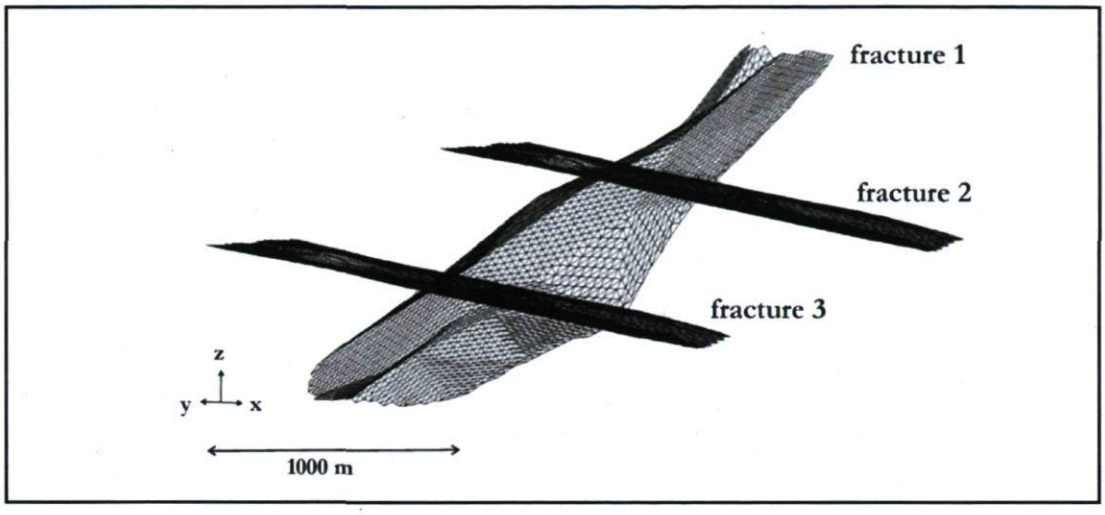

Figure 4.22 - Discrete fractures: triangular mesh

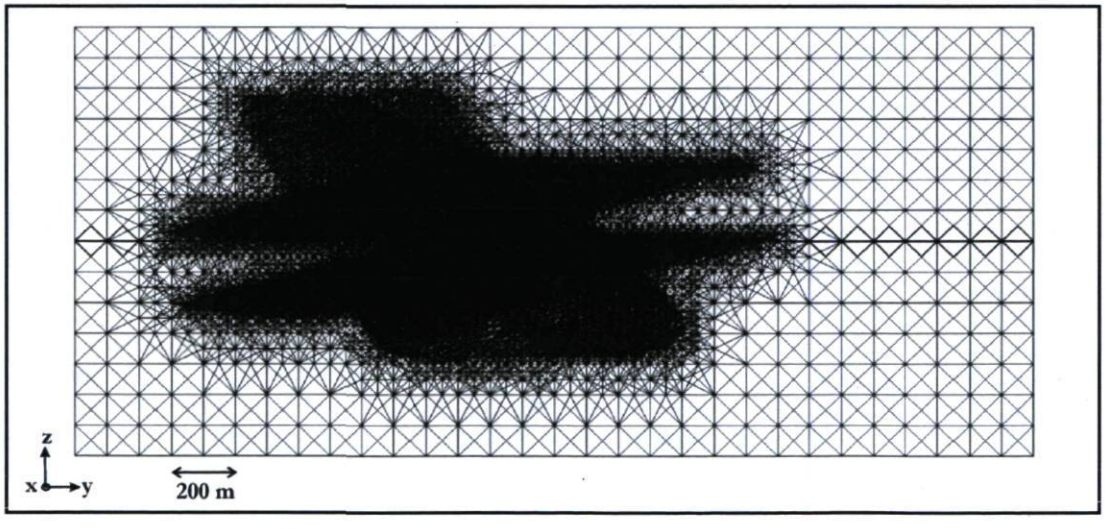

Figure 4.23 - Tetrahedral mesh: refinement around fractures

The groundwater flow field is shown in Figure 4.24, with a focus on a vertical slice located at x = 1526400 m. The fractures clearly influence the shape of the hydraulic head isocontours. The

porous rock matrix can be considered as impermeable (hydraulic conductivity of the order of 10^{-9} m/s), while the fractures are the major flow conductors in the domain.

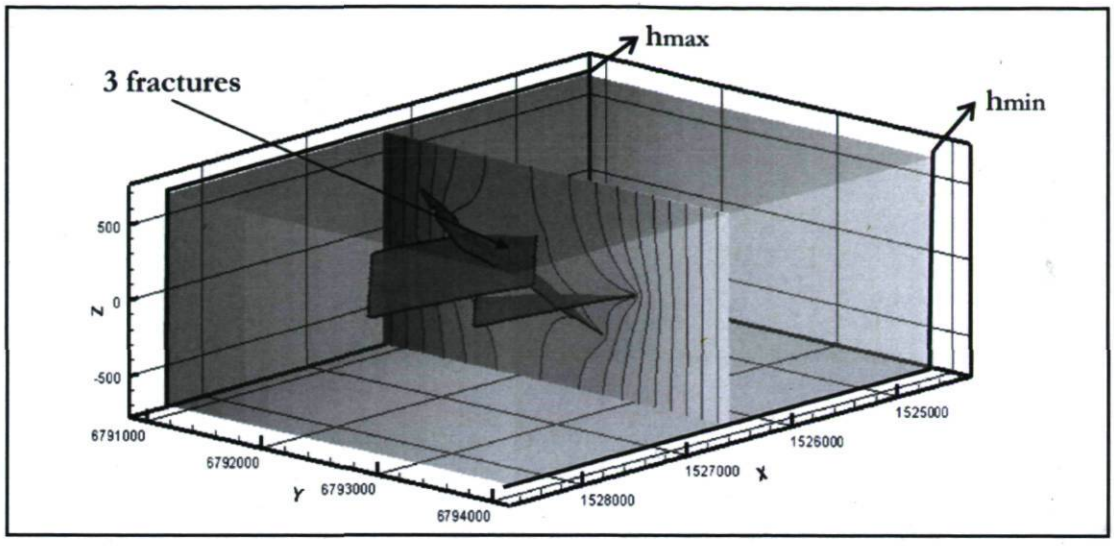

Figure 4.24 - Hydraulic heads: influence of fracture on groundwater flow

Figure 4.25 shows the same vertical slice at x = 1526400 m with fracture traces, which should be kept in mind before analyzing solute transport results.

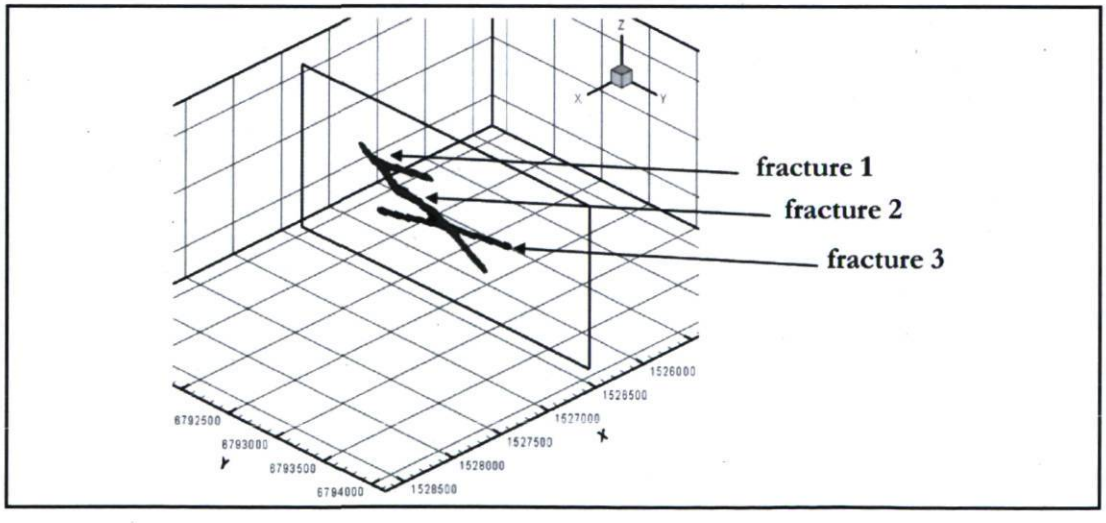

Figure 4.25 - Fracture traces at slice x = 1526400 m

Transport simulation results are shown in Figure 4.26, for different output times. Solute propagation follows exactly the fracture traces, demonstrating that their intersections are properly considered by the numerical code. As soon as the contamination plume reaches a fracture intersection, it migrates along both the intersecting fractures, demonstrating that the mesh provides the connection between the surfaces, with common nodes at intersection lines. It is therefore possible to observe how the solute propagation is clearly influenced by the presence of the fractures, which strongly control solute migration. The diffusion through the rock matrix perpendicular to the fractures is also visible. The minimum relative concentration value is equal to 0, if the OSC method is applied. Comparing once again the two methods, the Galerkin method gives a minimum value for relative concentration equal to -1.95×10^{-22}, which is with good approximation near to zero (Table 4.14).

Table 4.14 - Minimum relative concentration values for test case 8

Mesh type	C_{MAX}	C_{MIN}
Galerkin	1	-1.95×10^{-22}
OSC	1	0

An observation point is located at coordinates (1526400,6792000,0) near intersecting fractures, as shown in Figure 4.26. As soon as the solute plume reaches the first fracture, the migration becomes much faster, covering more than 1 km (Figure 4.26b and 4.26c). Moreover, concentration isocontours match fracture traces presented in Figure 4.25, demonstrating that the network of these three fractures is properly discretized.

Breakthrough curves computed at the observation point with the two different methods, OSC and Galerkin, are similar (Figure 4.27). A minor difference is visible, but this is expected because matrix coefficients are evaluated in a different way, as already mentioned.

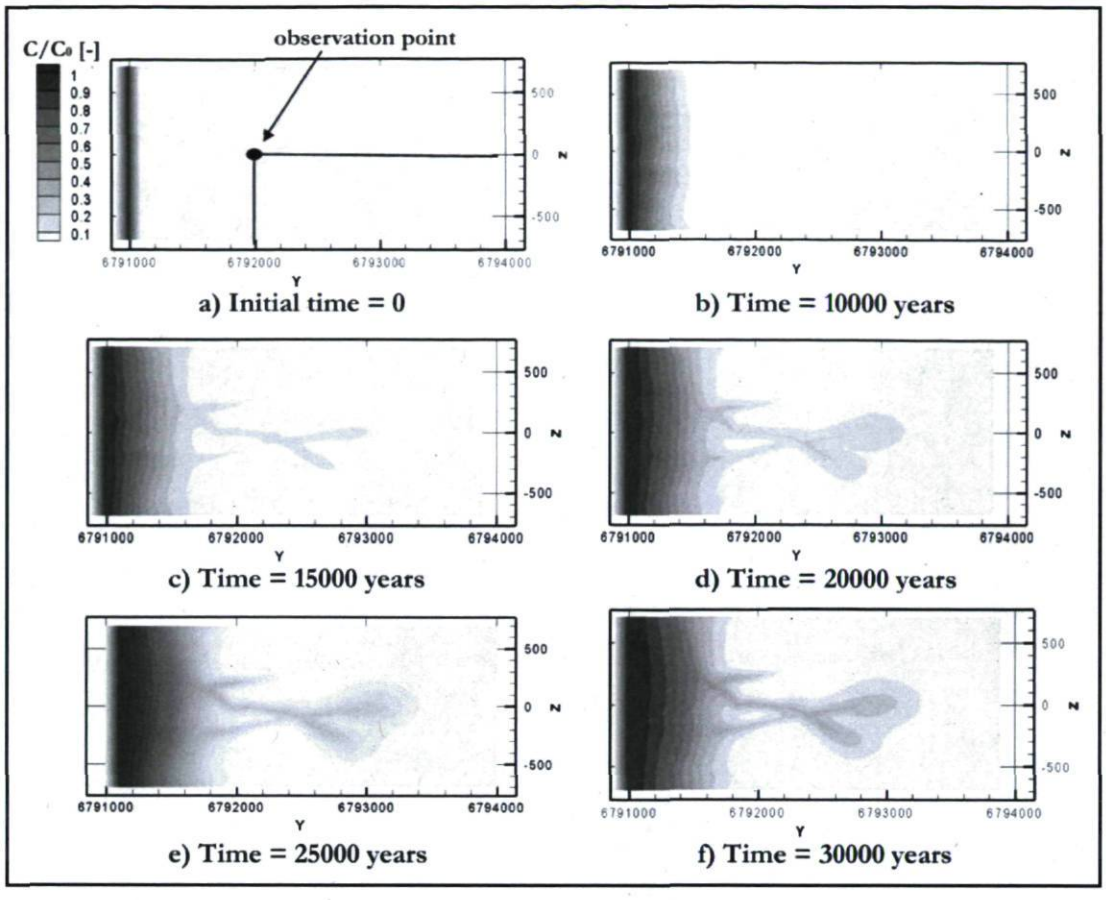

Figure 4.26 - Plume propagation for the slice at x =1526400 m

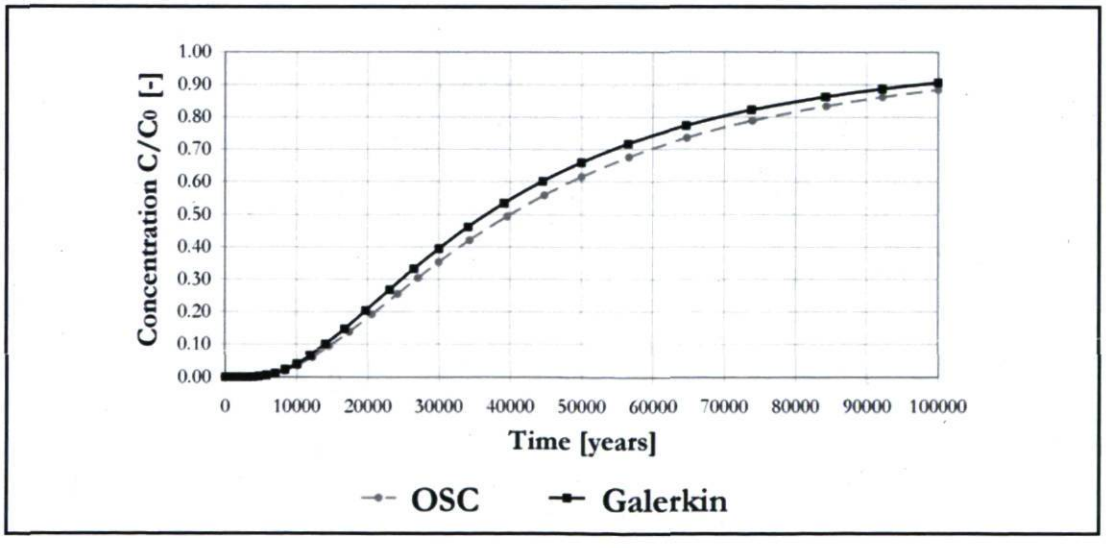

Figure 4.27 - Breakthrough curves for test case 8

4.3 Modeling approach verification: concluding remarks

All test cases analyzed in this chapter allow to draw some conclusions on the modeling approach developed during this thesis. It has been shown that mesh element type and size have a large influence on the discretization of specific elements, like inclined wells or fractures. Moreover, as numerical accuracy and CPU time also depend on mesh characteristics, tetrahedral meshes have shown more flexibility and suitability to discretize complex geometries without requiring excessive CPU time. To ensure that realistic results are obtained with transport simulations, suitable dispersivity values should also be chosen. In fact, dispersivity values and mesh element size directly influence the Peclet number, as mentioned in Chapter 3.

In conclusion, although no errors appear in the visualization of concentration isocontours if values are slightly negative, these values are always nearer to zero when the OSC method is applied to evaluate transmissibilities. This demonstrates that the OSC method is more appropriate for the numerical solution, because nonphysical results are more easily reduced. This behavior can be explained by the different dual meshes adopted for the Galerkin and OSC methods, using the median and Voronoi mesh, respectively. In fact, the physical interpretation of transmissibility γ_{ij} as a flux from node i to node j requires that dual mesh cells be orthogonal to the tetrahedral edge joining nodes i and j (Cordes and Putti, 2001). As a result, only the OSC method satisfies this relation between finite element and dual meshes.

An additional and very interesting observation that arises from the analysis of simulation results relates to the number of solver iterations required for steady-state and transport simulations. For all test cases, flow and transport solver convergence criteria are set to 1×10^{-10}. The number of iterations required by the solver to converge is smaller with the OSC method than with the Galerkin method. This difference is observed for both flow and mass transport simulations and is larger when negative concentrations are encountered in simulation results. Marked differences are observed for test cases 6 and 7, as shown in Tables 4.15 and 4.16. In particular, for test case 7, the Galerkin method requires about twice the number of iterations compared to the OSC method. In contrast, other test cases do not show a large difference, although the number of solver iterations required by the Galerkin method is always greater

than that required by the OSC method. This behavior can be explained by the different global matrix obtained with the two methods. As stated earlier, if the OSC method is applied to a Delaunay mesh, an M-matrix is obtained. This type of matrix is desirable for iterative solvers as it ensures accuracy and stability of the numerical solution (Letniowski and Forsyth, 1991; Murphy and Gable, 1998) and reduces the number of iterations required for convergence.

Table 4.15 - Number of flow solver iterations

Mesh type	Test case 6	Test case 7 No wells	Test case 7 Pumping wells
Galerkin	116	154	158
OSC	86	80	85

Table 4.16 - Number of transport solver iterations for the last time-step

Mesh type	Test case 6	Test case 7 No wells	Test case 7 Pumping wells
Galerkin	61	37	43
OSC	40	15	18

Chapter 5

Case study

The purpose of this chapter is to describe the application of the developed modeling approach to a real site. This case study extends the application of the modeling approach presented in the previous chapters to a complex domain geometry. Moreover, available field data are used to calibrate the hydrogeological model and the numerical results are compared to previous studies conducted at the same site.

The subject of this study is Olkiluoto Island, which is located off the west coast of Finland. In 1999, Posiva Oy, the Finnish organization responsible for the disposal of spent nuclear fuel, proposed Olkiluoto Island as the site for building a final disposal facility. The suitability of the Olkiluoto crystalline bedrock to host a spent fuel repository has been investigated over a period of fifteen years by means of ground and airborne methods and from shallow and deep boreholes (Posiva Oy, 2005). An underground research facility, ONKALO, is being built for characterization of the Olkiluoto bedrock, which is characterized by low permeability, and crossed by a few major fracture zones that control groundwater flow. A goal of the current investigations is to delineate existing or potential paths of groundwater flow and their influence on radionuclide migration. It is therefore necessary to locate the hydraulically active fractures, to define their geometry and to provide a proper spatial discretization to integrate these fractures in a numerical model that will be used to simulate the groundwater flow system. The

deep boreholes, which are characterized by inclined axes with lengths between 300 and 1000 m, should also be integrated in the model. The main objectives of the hydrogeological modeling are to quantify the impact of the hydraulically active fractures and open boreholes on groundwater flow, to simulate the response of the geological system to long term pumping, and to investigate the disturbances caused by construction and operation of ONKALO.

The Olkiluoto site well suited for the modeling approach developed in this thesis, which is particularly amenable to the representation of inclined boreholes and irregular discrete fractures with a refined tetrahedral mesh. After a short description of the Olkiluoto site and an overview of some issues related to the deep geological disposal of nuclear waste, the three modeling phases, Geomodeling, mesh generation and numerical simulations, are described in this chapter.

5.1 Site description

Olkiluoto Island (12 km^2) is located on the Bothnian Sea and is part of the Eurajoki municipality, 13 km north of the town of Rauma, in the south-west part of Finland (Figure 5.1). In this area, the coast is characterized by shallow bays surrounded by small archipelagos. The average annual temperature is 5.8 °C, the annual precipitation is 555 mm, and the snow thickness in winter is usually less than 20 cm. Seawater around Olkiluoto is a brackish Na-Cl type water with a TDS of about 6 g/l and a maximum depth of 30 m (Posiva Oy, 2003). The average island topographic height is about 5 m above sea level (a.s.l.), with the highest point being at 18 m a.s.l. The soil, mainly stony moraine, is no more than 1.5 m thick and usually less than 0.8 m. An overburden layer made of till, sand, and silt is found between the organic soil and the bedrock. The overburden has an average thickness of 3 m, with a maximum value of 10 m. The crystalline bedrock, which is part of the Precambrian Fennoscandian Shield, lies underneath.

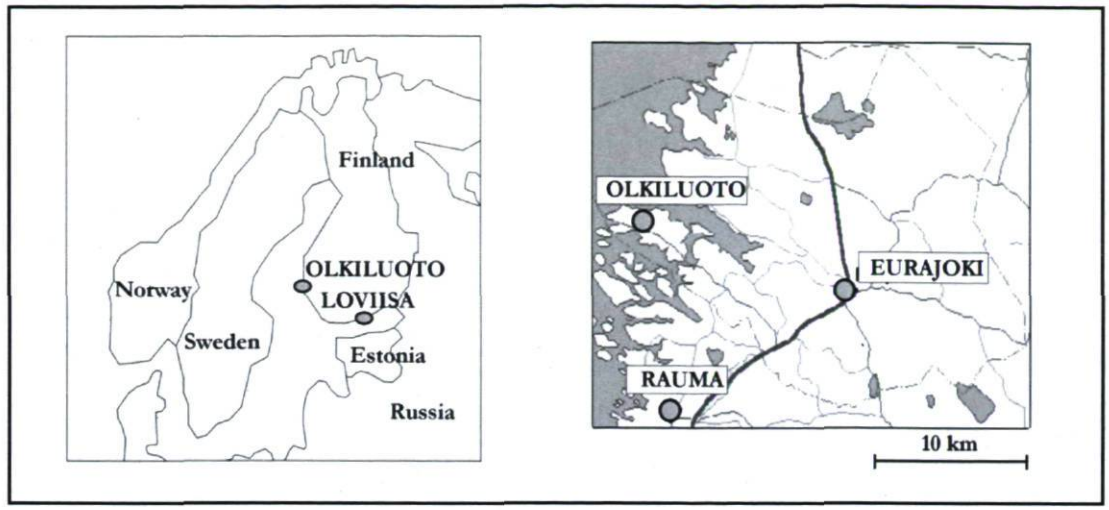

Figure 5.1 - Location of Olkiluoto (adapted from Posiva Oy, 2005)

The present knowledge of the bedrock at Olkiluoto is based both on geological and geophysical characterization and interpretation. Geophysical studies were required because rock outcrops cover only 4% of the island (Posiva Oy, 2003). Rocks have undergone several episodes of metamorphism and tectonic deformations and are mainly represented by metasedimentary migmatic mica gneisses. Other lithologies are found, including grey gneiss, granite pegmatite, diabase dykes and amphibolite. Forests cover most of Olkiluoto Island and small-scale agriculture is practiced in its southeastern part. A small harbor for transportation of bulk materials is located on the northern side. The most dominant infrastructure is a nuclear power plant, which is characterized by two commercial reactors with auxiliary facilities. Another Finnish power plant is located in Loviisa (Figure 5.1). An artificial reservoir is located in the middle of the island to provide fresh water for the power plant. The construction of the ONKALO underground research laboratory started in 2004. ONKALO is an acronym based on the Finnish language expression for Olkiluoto Rock Characterization for Final Disposal. In fact, ONKALO is planned to be used to dispose of waste generated by the Finnish nuclear power plants.

5.1.1 Geological disposal of nuclear waste

Without entering into specific details, a general overview of the current knowledge on disposal of nuclear waste is presented below to better define the context of this case study. Geological disposal is a scientifically and technically credible long-term solution available to meet the need for safety without reliance on active management. A well-designed repository represents, after closure, a passive system containing a succession of potentially robust safety barriers. Our present civilization designs, builds, and lives with technological facilities of much greater complexity and higher hazard potential (National Research Council, 2001). Deep geological disposal relies on a multi-barrier system that isolates the waste from the biosphere. The multi-barrier system typically comprises the natural barrier provided by the host rock and the Engineered Barrier System, EBS, whose purpose is to prevent and/or delay the eventual release of radionuclides from the waste to the host rock, at least during the first several hundred years after repository closure (OECD, 2003). An EBS is composed of a variety of components, such as the waste form, canister, buffer, backfill, seals, and plugs (Figure 5.2a). For example, the disposal concept proposed by the SKB (Swedish Nuclear Fuel and Waste Management Company) is based on copper canisters with a cast iron insert, where the spent fuel assemblies are placed (Figure 5.2b).

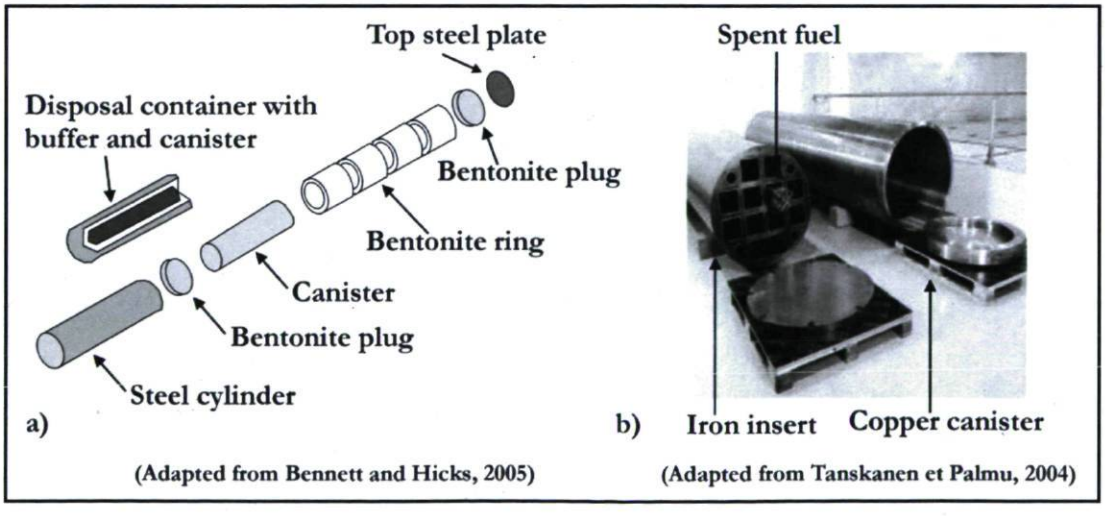

Figure 5.2 - a) The components of the supercontainer in the KBS-3H repository system and b) spent fuel canister manufacturing

The preferred, and internationally recommended, option for the long term management of long lived and high level radioactive wastes consists of their disposal in deep geological repositories (IAEA, 2001). Four host geological formations are being widely considered for disposal: crystalline rocks, salt formations, argillaceous formations and tuff (IAEA, 1999). As ONKALO is excavated in crystalline rocks, only the characteristics of that type of geological formation are discussed. Crystalline rocks have high mechanical strength, such that stable shafts, tunnel and gallery openings can be excavated at depths appropriate for geological disposal (about 500 m). In general, they are poorly transmissive and flow predominantly takes place through interconnected networks of fractures. They frequently have low matrix permeability and matrix porosity, as well as very low solubility. Finally, crystalline rocks normally have good thermal conductivity, such that any heat generated by the waste can be dissipated so that thermal effects on both the engineered barriers and the surrounding rock will be minimized (IAEA, 1999).

Characterization work performed in Underground Research Laboratories (URLs) plays an important role in the development of deep geological repository systems (IAEA, 2001). URLs are used to perform generic-type experiments of interest to deep disposal. The first URLs were already developed in the 1960s and 1970s in order to assess the suitability of rock as the repository host formation, such as the Lyons (Kansas) and Asse (German) salt mines. URLs can be developed from existing underground facilities, such as mines, tunnels for railways, dams and highways or constructed in undeveloped sites. A complete list of past and operating Underground Research Laboratories is given in IAEA (2001). URLs are located in twelve different countries: Belgium, Canada, Czech Republic, Finland, France, Germany, Hungary, Japan, Sweden, Switzerland, UK, and USA. Just to cite a few examples, the Mol site (Belgium) is characterized by a clay formation, the Äspö Hard Rock Laboratory (Sweden) by granite, the Yucca Mountain site (Nevada) by tuff, and the Gorleben site (German) by a domed salt formation. In Canada, an Underground Research Laboratory was built in the 1980s at the Lac du Bonnet site (Manitoba), in a granitic formation, but is now closed.

5.1.2 Äspö Modeling Task Force

The ONKALO Underground Research Laboratory is planned to become a final deep geological repository for high-level nuclear waste. To accomplish this goal, several research projects and investigations are presently active. The Swedish company SKB is hosting the secretariat of the Äspö Task Force, which is a forum of international organizations with the objective to interact in the area of conceptual and numerical modeling of groundwater flow and solute transport in fractured rock. Originally, the Task Force focused on the Äspö Hard Rock Laboratory (Sweden). Since 2005 the Task Force has initiated its Task 7, which focuses on the Olkiluoto site and modeling teams from Finland, Sweden, Canada, France, and Japan are participating. The Canadian modeling team is represented by the Nuclear Waste Management Organization (NWMO). The Nuclear Waste Management Organization (NWMO) was established in 2002, in accordance with the Nuclear Fuel Waste Act (NFWA) to assume responsibility for the long-term management of Canada's used nuclear fuel, a by-product of electricity generation in a nuclear power plant (NWMO, 2007).

The Äspö Modeling Task Force, AMTF, has been set up for integrating the results and the modeling work in the different disciplines. The AMTF will conduct site understanding modeling to provide the necessary input to the safety analysis predictions (Posiva Oy, 2005). Different discipline-specific models have been developed by the AMTF, such as a geological model, a rock mechanics model, a hydrogeological model, and a hydrogeochemical model. Numerical modeling of fluid flow and solute transport becomes the fundamental tool for site characterization and performance assessment, which is based on the definition of a system that fulfils the safety requirements set for disposal. In particular, Task 7A focuses on modeling a pumping test conducted at ONKALO in 2004, to understand the major features of the groundwater system at Olkiluoto. Specific goals are to determine proper means of incorporating the open boreholes in the hydrogeological model to simulate flowrates between fractures and boreholes, which are the main flow conductors. Available information related to Task 7A is used here to setup the simulation scenarios. In particular, the Task7A Report presented by the NWMO modeling team (Therrien, 2008) is one of the main references for this chapter, since the simulation results were obtained with the HydroGeoSphere numerical code.

5.1.3 The underground research facility ONKALO

Established in 1995, Posiva Oy is an expert organization responsible for the final disposal of spent nuclear fuel, for research into final disposal and for other expert nuclear waste management tasks. Posiva Oy has been conducting field investigations for the disposal of spent nuclear fuel in the crystalline bedrock at the Olkiluoto site since 1988 (Cosgrove et al., 2003). Legislation requires nuclear waste generated in Finland to be processed, stored and finally disposed of in Finland. The underground research facility, ONKALO, is being built on the site for detailed characterization of the planned repository host rock as well as for testing and demonstration purposes (Vaittinen et al., 2003). The underground rock facility construction started in July 2004 and consists of a system of exploratory tunnels accessed by a spiraling tunnel and a ventilation shaft (Figure 5.3). The final disposal facility will be excavated at a depth of about 500 meters in the Olkiluoto bedrock. The total underground volume of ONKALO is approximately 330000 m^3 and the combined length of tunnels and the shaft is 8500 m.

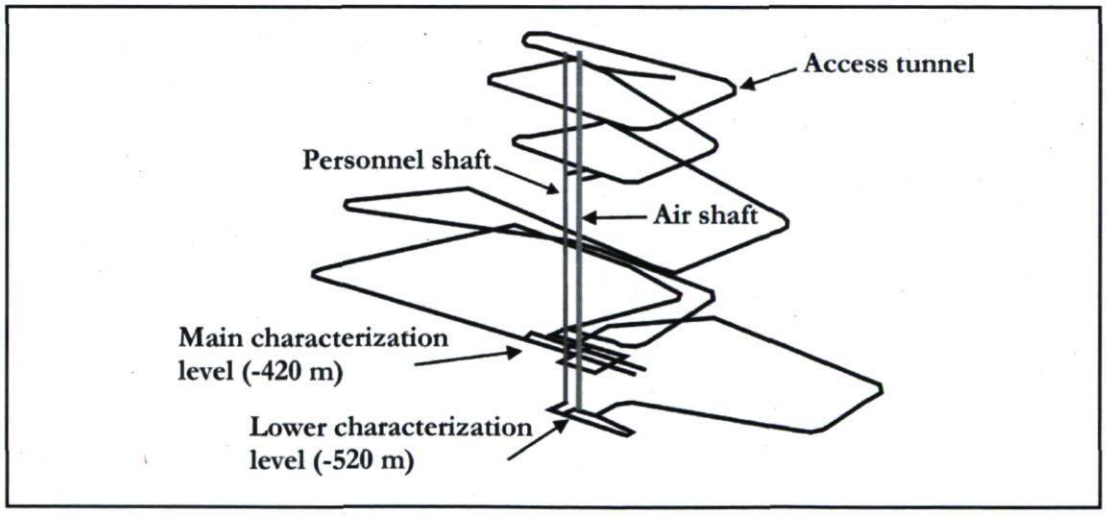

Figure 5.3 - Layout of ONKALO (adapted from Taskanen and Palmu, 2004)

The construction of ONKALO requires a detailed knowledge of the bedrock of Olkiluoto, which includes the hydrogeological, hydrogeochemical, rock mechanical, tectonic and seismic conditions of the site (Posiva Oy, 2003). From all available data collected since the beginning

of site investigations, only those relevant to the work presented in this chapter will be described.

To model the discrete fractures as surfaces, the definition of structural intersection given by Vaittinen et al. (2003) is adopted. In this chapter, the discrete fractures are referred to as fracture zones, fracture surfaces, structures or simply fractures. Vaittinen et al. (2003) defined polygonal fracture surfaces by observing borehole cores and identifying the borehole intersections belonging to each structure. A borehole intersection is a fixed point that represents a core interval having properties that are important from a rock engineering and/or hydrogeological point of view and that differ from the average borehole properties. The core sample from the borehole KR09 constitutes an example of these intersections (Figure 5.4).

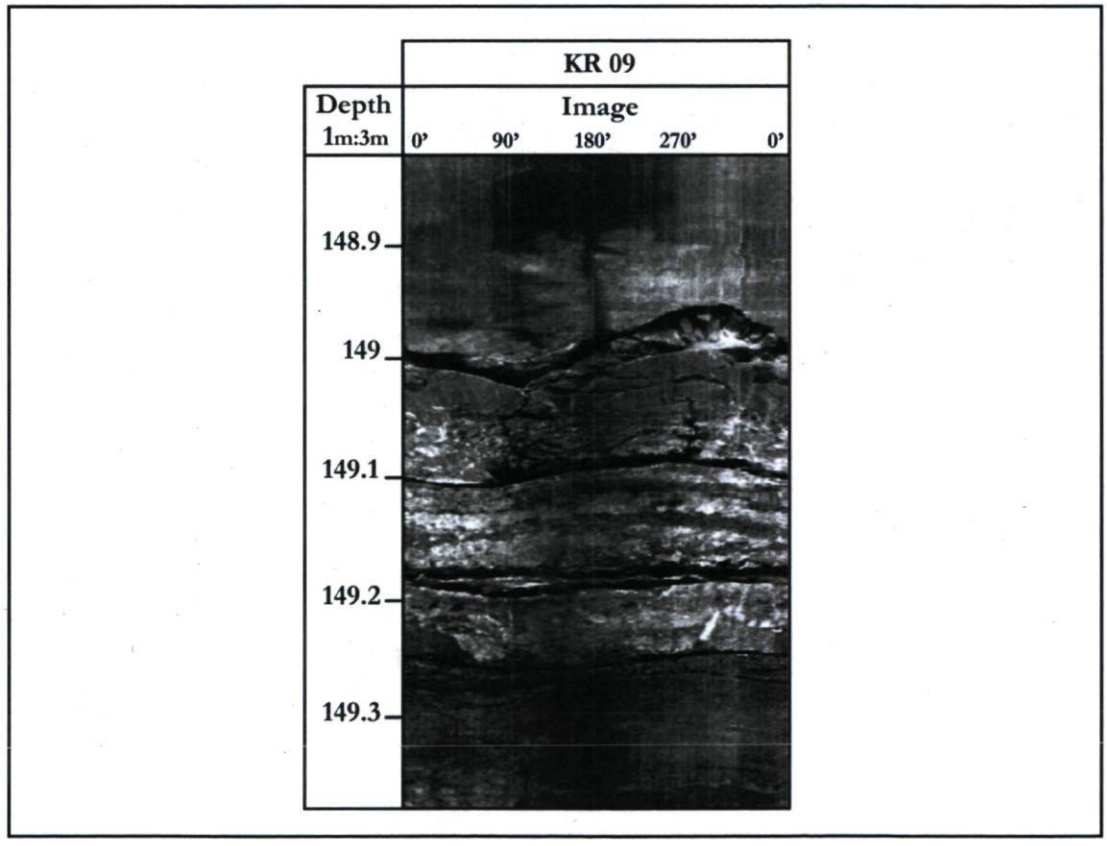

Figure 5.4 - Example of a conductive section, from KR09 borehole wall image (adapted from Hella et al., 2004)

The structural intersections identified in the boreholes have been oriented according to the mean orientation of fractures measured in the borehole intersection. The intersection lengths for such structures are set to 2 m, even if the real intersection length is only some tens of centimeters (Vaittinen et al., 2003). The basic assumption used is that the mean orientation of the individual fractures reflects the orientation of the whole structure. The continuity of structures is estimated on the basis of the observed responses in long-term pumping tests, the geological and hydraulic properties of borehole intersections, and the compatible orientations of VSP-reflectors. An intersection is identified when fracture frequency is more than 10 fractures/m or when the hydraulic conductivity is equal to or higher than $K_{2m} = 5 \cdot 10^{-7}$ m/s, where the subscript "2m" indicates the structural intersection length. These intersections are then correlated between boreholes, assuming that they represent parts of quasi-planar structures in 3D. When a structure intersects several boreholes, it is extended halfway between a borehole intersecting the structure and a borehole with no intersection.

5.2 Geomodel of ONKALO

The first bedrock model of Olkiluoto was compiled on the basis of the results of the preliminary site characterization in 1992, using the data from five deep boreholes (Posiva Oy, 2003). During the detailed site characterization stage, the bedrock model was regularly updated. One of the first flow models included 30 distinct structural units covering 26 km^2 (Löfman, 1999). For modeling purposes the geometry had to be simplified and modified to give a transparent and understandable framework while retaining all the important features at the site scale (Posiva Oy, 2003). The volume modeled in this case study covers 17.5 km^2 (3.5 km x 5 km) and its limiting coordinates are 6791000 - 6794500 Northing and 1523000 - 1528000 Easting (Figure 5.5). The domain is 1200 m deep.

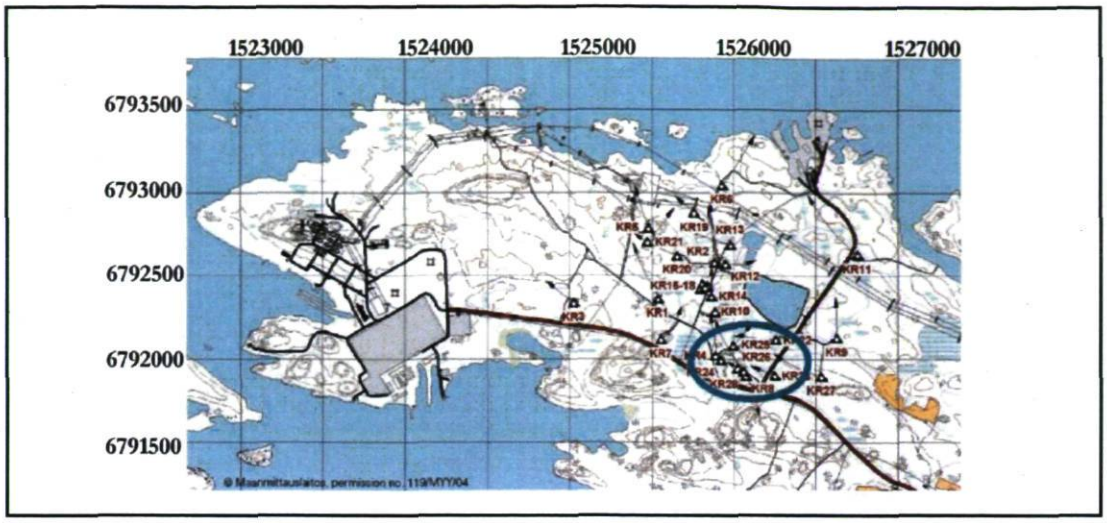

Figure 5.5 - Plan view of Olkiluoto Island, where the location of ONKALO is circled (adapted from Ahokas and Koskinen, 2005)

The geological model considered here contains 13 fractures and 14 boreholes. The fractures integrated in this model are HZ1, HZ2, HZ3, HZ4, HZ8, HZ19A, HZ19C, HZ20A, HZ20AE, HZ20B_ALT, HZ21, HZ21B, and BFZ99, where HZ is the acronym for Hydrogeological Zone and BFZ for Brittle Fault Zone (Andersson et al., 2007). Fracture HZ8 does not intersect any borehole but it has been included in the model as suggested in Vidstrand et al. (2006). Moreover, this fracture was considered by Therrien (2008), whose work forms the basis to compare and validate numerical results obtained here. A global view of the Geomodel is shown in Figure 5.6, where the extent of the simulation domain is also indicated. The fractures and boreholes integrated in the Geomodel are located in the center of the domain. For the sake of clarity, only the names of fractures HZ8, HZ21, HZ19A, HZ4, and borehole KR24 are indicated. With reference to the Geomodel orientation shown in Figure 5.6, three additional views are presented to highlight fracture and borehole geometries, spatial locations, and intersections (Figure 5.7). Some boreholes are characterized by a significantly inclined axis (Figure 5.7a). Local refinement is visible on fracture HZ19A, which is intersected by twelve boreholes (Figure 5.7b). Fracture HZ8 has no intersections with other fractures or with boreholes, while subvertical fracture HZ4 intersects subhorizontal fractures HZ21, HZ20B_alt, HZ20A, HZ19C, and HZ19A (Figure 5.7c).

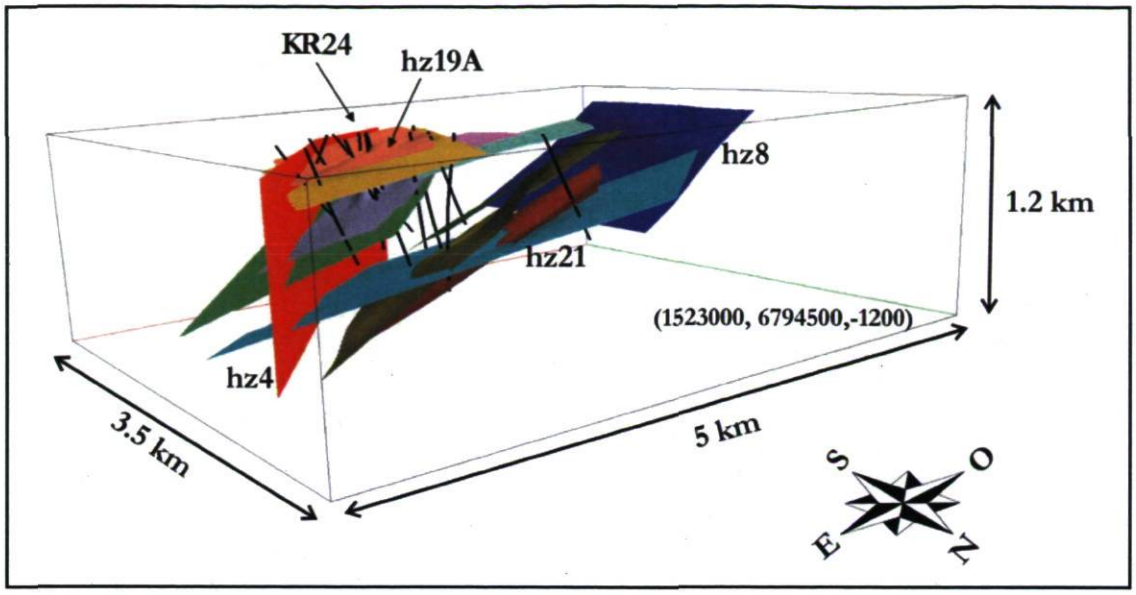

Figure 5.6 - Geomodel built with GOCAD: global view with simulation domain boundary

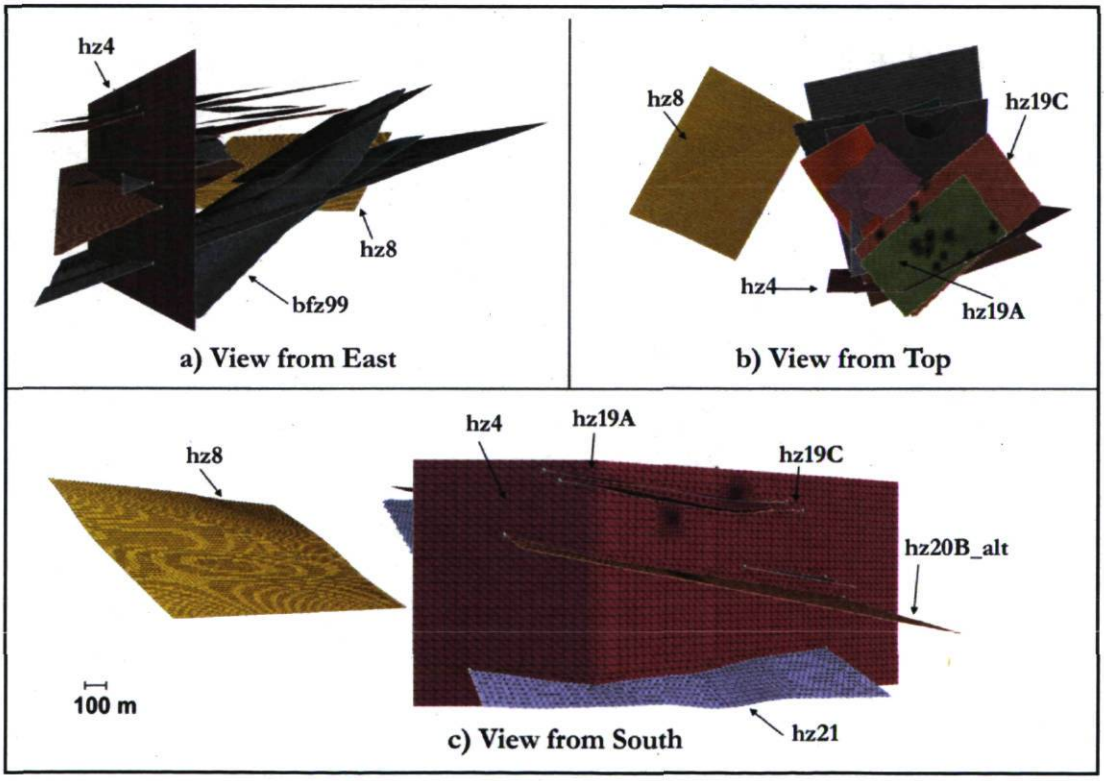

Figure 5.7 - Geomodel built with GOCAD: view of fractures

Each fracture is built independently, from raw fracture geometries available as *.dxf files. These files contain triangulated surfaces, made up of coarse and heterogeneous triangles. For numerical modeling purposes, fractures should be represented by a higher resolution triangular mesh. Thus, as explained in Section 2.1.2.2, their geometry and their triangular mesh are modeled using the *Pset*, *2DGrid* and *Surface* GOCAD tools, as well as the *Fit Surface to Pset* option. The objective is to obtain a homogeneous triangulation for all the fractures. The length of triangular edges should be selected at the beginning of the modeling phase based on the level of resolution envisioned for the 3D tetrahedral mesh. For this specific application, triangular edges are about 25 m long. The edge length should be chosen equal to the desired nodal distribution around the fractures. If the edge length is greater than the nodal hexahedral spacing around fractures, the connection into tetrahedra will not respect the fracture surface, which will be characterized by tetrahedra that extend beyond the fracture surface. This unsuitable mesh characteristic is clearly illustrated in the close-up detail of Figure 5.8a, which shows the portion of the mesh around fracture HZ8 obtained with the *Extract* LaGriT command. In contrast, when triangular edges of the fracture surface have almost the same length as the nodal spacing around the fracture, a regular fracture surface is obtained (Figure 5.8b). Triangular surfaces are refined around borehole intersections. The boreholes included in the Geomodel are all deep boreholes drilled at the Olkiluoto site and are listed in Table 5.1, where the number of nodes used to discretize their axis is also shown. The boreholes are all characterized by inclined axes, except KR24, and are discretized by tetrahedral edges 6 m long.

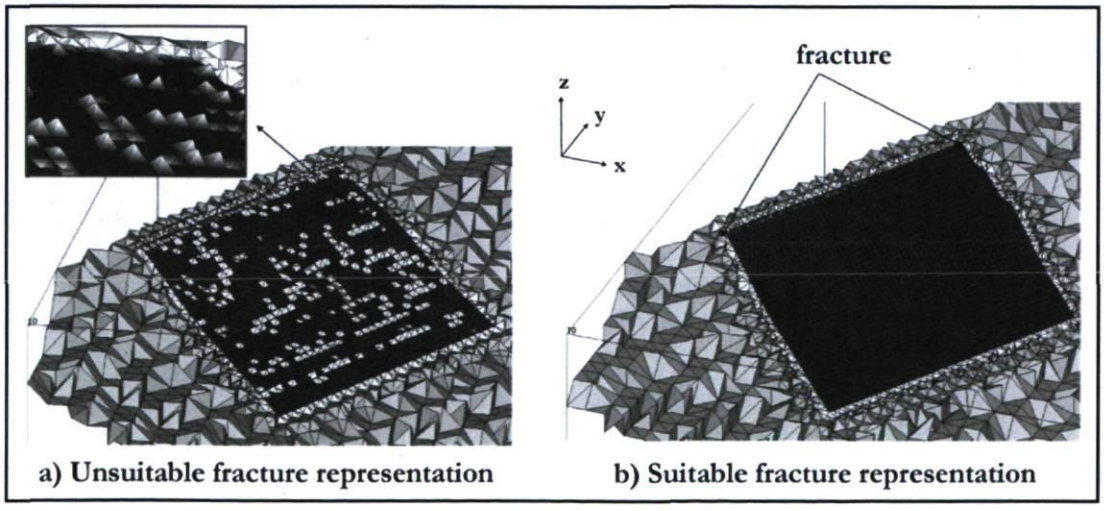

Figure 5.8 - Fracture HZ8 extracted from the tetrahedral mesh with LaGriT

Table 5.1 - List of boreholes included in the Geomodel of ONKALO

Borehole	KR4	KR6	KR7	KR8	KR9	KR10	KR12
Nodes	151	100	136	101	100	103	135
Depth [m]	-870	-466	-750	-530	-530	-602	-761
Azimuth [degrees]	0	36	43	155	360	0	90
Inclination [degrees]	77	50	70	64	70	85	70
Borehole	KR14	KR22	KR23	KR24	KR25	KR27	KR28
Nodes	85	84	52	93	102	93	110
Depth [m]	-462	-410	-250	-540	-567	-430	-515
Azimuth [degrees]	0	270	290	140	43	285	325
Inclination [degrees]	70	60	60	90	70	55	55

Regions are defined on the fracture surfaces by drawing a polygonal *Curve* around each intersecting borehole. The *Split* algorithm is executed twice on these regions to obtain triangular edges 6 m long around the borehole intersections. Intersecting fractures are then selected and the *Mutual Cut Among Surfaces* tool is executed to create the intersection lines. It should be noted that all intersecting fractures must be selected together and only one global *Cut* is executed. Otherwise, if each couple of intersecting fractures is selected separately, successive *Cut* operations will affect previous intersecting lines, where a nonconforming triangular mesh will be obtained. Finally, the *Simplify All Surface Borders* command is used to improve the triangulation at intersection lines and to create a conforming triangular mesh, as explained in Chapter 2. The final Geomodel is constructed by intersecting boreholes and fractures (Figure 5.9a). The complexity of the simulation domain is particularly visible where multiple intersections between boreholes and fractures occur (Figure 5.9b). The fracture network covers a volume of 4.2 km x 2.4 km x 1 km, in the x, y, and z directions respectively.

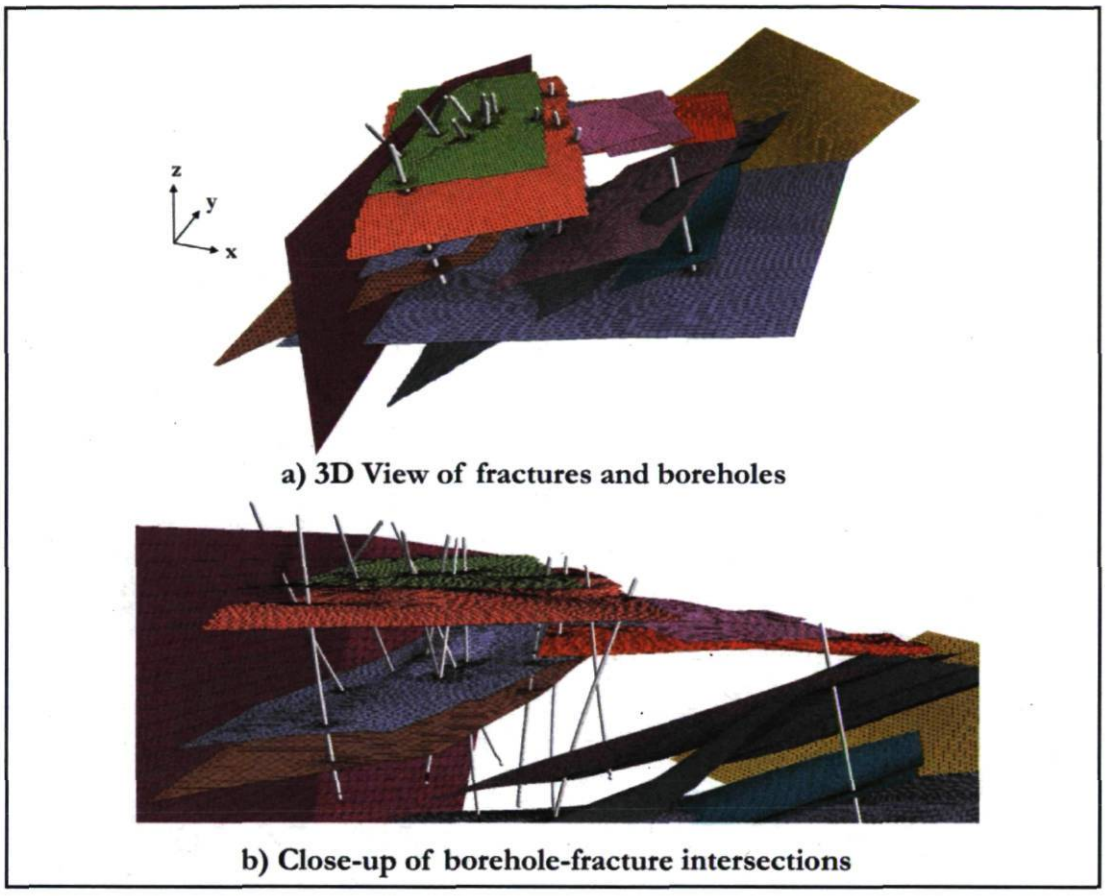

Figure 5.9 - Geomodel built with GOCAD: fractures and boreholes

5.3 Geomodel discretization

The purpose of this section is to describe the Geomodel discretization, which is performed with the mesh generator LaGriT. Since a detailed description of the mesh generation procedure has already been presented in Section 2.2.1.2, only the features specific to this case study are mentioned here.

The GOCAD *.ts files, which contain triangular mesh information, and *.avs files, which contain borehole nodal coordinates, are imported into LaGriT. As a result, 14 triangular Mesh Objects, which describe the 13 fractures and the topography of the domain, and 14 linear Mesh Objects, which represent the boreholes, become the current Mesh Objects of a LaGriT session.

A hexahedral Mesh Object is generated to create the background nodal distribution for the simulation domain, with a nodal spacing of 100 m. Hexahedral elements are selected for refinement near fractures and boreholes using the *dfield* tool mentioned in Chapter 2. Elements located within 50 m of each fracture are selected for the first refinement step, while elements within a distance of only 20 m are selected for the second refinement step. These two refinement steps produce hexahedral edges that are 25 m long around fractures. The same two-step procedure is used to refine near boreholes and obtain a nodal spacing of 6 m around the boreholes. The same element can be refined more than required and may therefore become too small if it is selected by the *dfield* tool in successive refinement steps. Therefore, to avoid obtaining hexahedra that are too small, only the elements whose volume is greater than a user-defined minimum value are selected for refinement.

Once the mesh is properly refined, the hexahedra that are close to fractures and boreholes are removed. Moreover, the triangles of fracture surfaces that are close to the borehole intersections are also removed, as shown by the holes around boreholes in Figure 5.10. If they are not removed, these triangular elements can complicate the connection into tetrahedra, especially because fracture and borehole nodes may be very close.

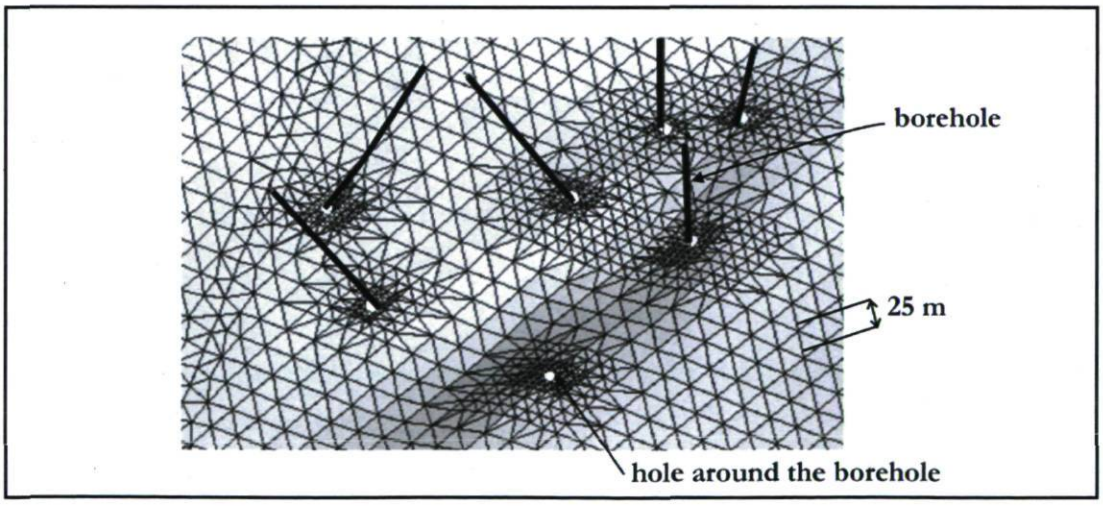

Figure 5.10 - Example of intersection between boreholes and fracture HZ19A

Once the hexahedral mesh is refined around fractures, boreholes, and topography, all its nodes are copied to a tetrahedral Mesh Object, where they are connected using a Delaunay algorithm. Fracture surfaces are then extracted from the tetrahedral mesh just created. Finally, indexes of the tetrahedral nodes that correspond to fractures and borehole nodes are identified. These tetrahedral node indexes will be used by the numerical code HydroGeoSphere to define the fracture and well elements.

The topography of ground surface can be integrated in the mesh, as a ground surface model of the Olkiluoto site is available. However, instead of including the real topography into the mesh, a constant elevation top boundary can also be considered, as groundwater table elevations can be interpolated on the constant elevation top boundary to provide a suitable boundary condition.

In the geological system considered, fractures and boreholes conduct the most of the flow and they have mutual intersections. It is important, although rather challenging, to represent these intersections with a finite element mesh. In fact, wells are important elements in numerical simulations of groundwater flow, since rapid changes in hydraulic head occur near wells because of pumping. Therefore, in these regions the finite element mesh should be refined and should reproduce the real well axis geometry such that the solution has the required accuracy. Multiple well-fracture intersections generate a larger connectivity and increase the global hydraulic conductivity. When pumping a well, multiple intersections increase the efficiency in extracting water from the surrounding rock and the withdrawal is split into all the intersections influencing flowrates and hydraulic head computation at the well. The block-based mesh used by Therrien (2008) is considered here to compare the discretization of these intersections. For this mesh, multiple intersections of borehole KR06 with fractures HZ21 and HZ21B occurred because of the staircase shape of the discretized borehole that is obtained when a block-based mesh is used (Figure 5.11b). In contrast, for the tetrahedral mesh, the inclined borehole intersects the two fractures just once (Figure 5.11a).

Node	x	y	z	Fracture
11165	1526065	6793248	-303	
11166	1526067	6793251	-308	---> hz21b
11167	1526069	6793254	-312	
11168	1526071	6793257	-317	
.....	.....	.....	.....	
11177	1526088	6793285	-360	
11178	1526090	6793288	-365	
11179	1526092	6793291	-370	---> hz21
11180	1526093	6793294	-375	

a) Tetrahedral mesh

Node	x	y	z	Fracture
257961	1526064	6793246	-300	--->hz21b
248719	1526064	6793246	-320	--->hz21b
239478	1526084	6793246	-340	--->hz21b
239477	1526064	6793246	-340	
230236	1526084	6793246	-360	
220994	1526084	6793246	-380	--->hz21
220995	1526107	6793246	-380	--->hz21
211752	1526084	6793246	-400	--->hz21
202619	1526107	6793346	-420	

b) Block-based mesh

Figure 5.11 - Example of intersection between borehole KR06 and fractures HZ21B and HZ21

Information on the created tetrahedral mesh is listed in the Summary of Final Data Set generated by the pre-processor GROK and written to the *.eco (Table 5.2).

Table 5.2 - Tetrahedral mesh information

Parameter	Value
Number of nodes	237775
Number of segments	1643088
Number of faces	2795944
Number of elements	1390630
Number of 3D elements with well nodes	30041
Number of fracture elements with well/fracture nodes	309

The local refinement of the tetrahedral mesh is clearly visible in the center of the domain, where the fractures and boreholes are located (Figure 5.12a). The refinement in the right portion of the domain corresponds to fracture HZ8, which does not intersect the other fractures, as mentioned in Section 5.2.

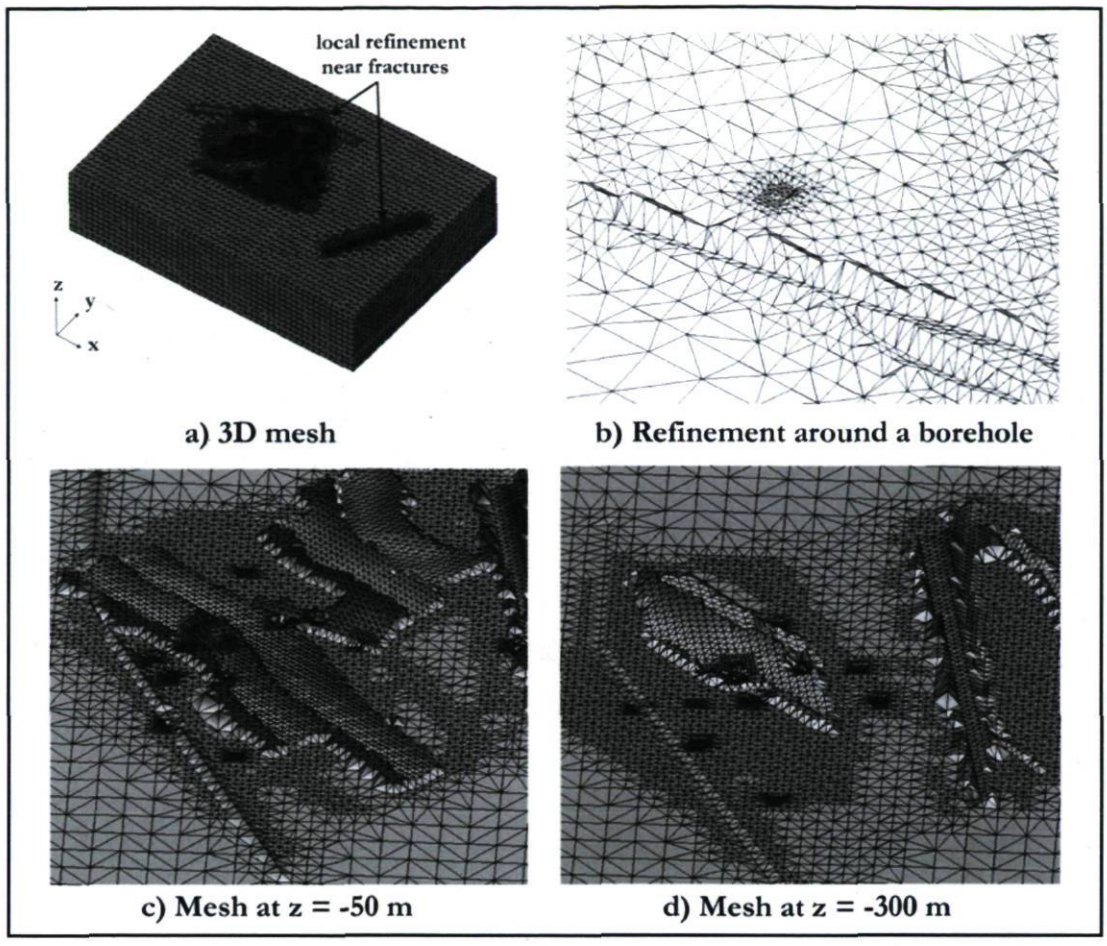

Figure 5.12 - Tetrahedral mesh built with LaGriT

A close-up of the central portion of the mesh highlights the refinement around one of the 14 boreholes included in the Geomodel (Figure 5.12b). Finally, two portions of the discretized domain are shown in Figures 5.12c and 5.12d, where only tetrahedra located deeper than 50 m and 300 m are shown, respectively.

5.4 Numerical simulations

The main geological formation at the Olkiluoto site is a low permeability composite gneiss crossed by major fracture zones. The use of the discrete fracture conceptual model is justified by the fact that these fracture zones conduct the majority of groundwater flow in the lower

parts of the bedrock (Vidstrand and Ahokas, 2005a). These fracture zones are intersected by the open boreholes, which create a complex network of conductive features. Hydrogeological modeling aims at understanding the role of these major hydraulic conductors on the groundwater flow field. An essential part of the groundwater flow analysis is calibration, whose goal is to ensure that the flow model reproduces the hydrogeological observations of the real system as well as possible. The steady state and transient flow fields at Olkiluoto are simulated. Moreover, illustrative scenarios are designed to present transport simulation results for the test site.

5.4.1 Flow simulations: KR24 pumping test

Construction of the underground facilities of ONKALO will affect both the groundwater table and hydraulic head in the vicinity of the access tunnel and shafts. To predict the effects of construction on the groundwater flow system and to characterize hydraulic connections at the scale of 100 m - 1 km, a long-term pumping test was carried out in deep borehole KR24 in 2004 (Vaittinen and Ahokas, 2005). Information and data collected during this pumping test are used to set up the simulation scenarios presented in the following sections. The pumping test started on March 25, 2004 and finished on June 2, 2004. Groundwater was pumped at a constant rate of 18 l/min with a submersible pump. When the pumping test started, there was still snow cover and frost on the ground. Snow started to melt in early March and had entirely melted by April 15. After that period, head values decreased due to natural outflow of groundwater from the island into the sea and increasing evapo-transpiration (Vaittinen and Ahokas, 2005). Hydraulic heads were measured in shallow boreholes, multilevel piezometers, open deep boreholes, and packed-off boreholes. Shallow observation points are more sensitive to precipitation, topography, presence of wetland, location either on overburden or outcrops, and construction work at the site. Moreover, they do not intersect the fracture zones identified at the site. Since the focus of the simulation presented here is on the deep bedrock, where the repository for nuclear waste should be built, shallow boreholes and piezometers are not considered in the mesh design and the mesh resolution has been adapted to discretize only the deep boreholes.

The annual precipitation at Olkiluoto Island is approximately 550 mm of which 60-70 % returns to the atmosphere by evapotranspiration. The potential recharge at the site is approximately 100-150 mm/y and the most likely deep groundwater recharge to bedrock during natural conditions is approximately 5-20 mm/y (Vidstrand and Ahokas, 2005b). Since mean long-term groundwater table elevations are available for the site, they are interpolated on the top boundary of the simulation domain and the resulting values are used to define a first-type boundary condition, as done in Therrien (2008). This boundary condition mimics a recharge that depends on the hydraulic conductivity of the geological medium and is adopted here for both steady-state and transient simulations of KR24 pumping test.

Borehole KR24 had a casing section down to 20.13 m. A one meter packer with a bypass tube was installed at the borehole depth of 80.60-81.60 m (Figure 5.13). As a result, the lower part of KR24, partially isolated by the packer, experienced a smaller drawdown than the upper section during the pumping (Vidstrand et al., 2006).

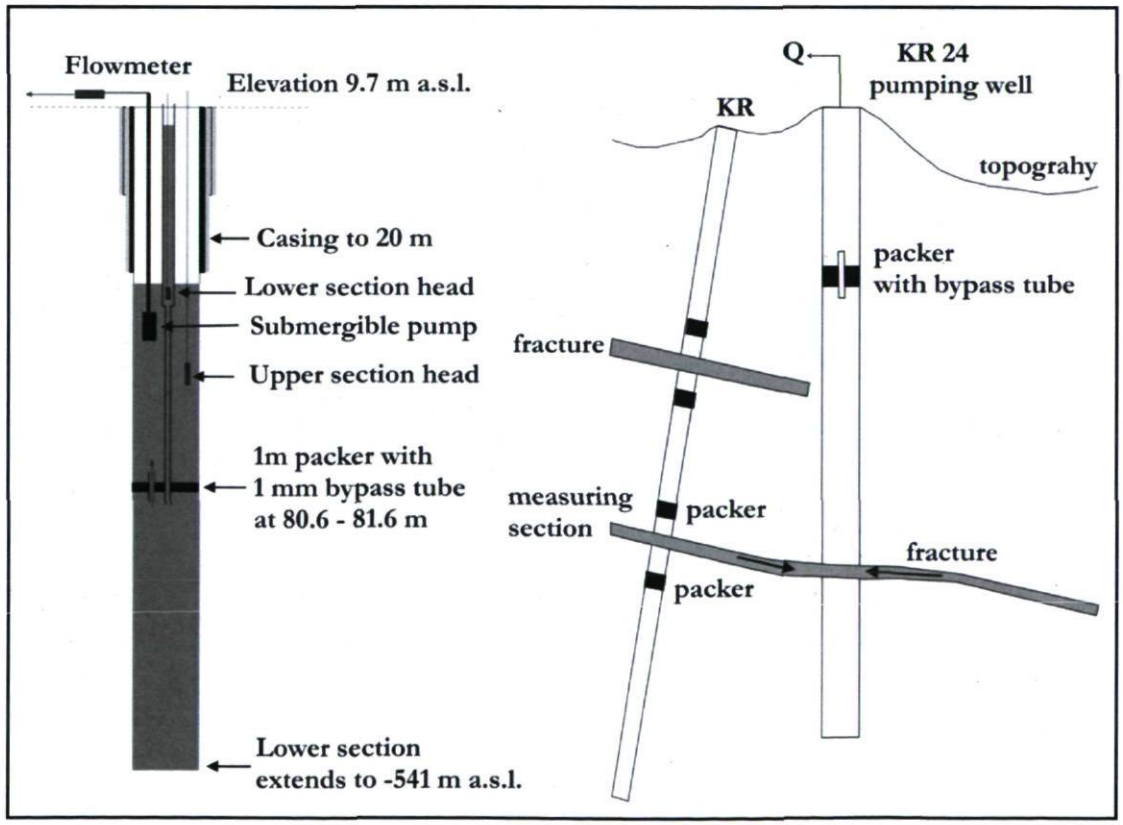

Figure 5.13 - Pumping well KR24

(adapted from Vidstrand et al., 2006 and Vaittinen and Ahokas, 2005)

The following three modeling options for borehole KR24 are suggested in decreasing order of "realism" by Vidstrand et al. (2006):

1. Withdrawal from the upper section at a total constant rate outflow from the two sections of KR24 of 18 l/min. This option requires that the flow through the by-pass packer is simulated within the numerical model. The packer partially isolates the lower section of borehole KR24, such that a different drawdown is observed in the two sections of the borehole. The bedrock experiences a larger drawdown than the upper portion of the rock, which is more permeable.
2. A constant rate outflow of 12.5 l/min (6570 m^3/y) from the upper section and constant rate outflow of 5.5 l/min (2891 m^3/y) from the lower section of KR24. This option allows for the simulation of two different drawdowns by selecting two distinct withdrawal points along borehole KR24.
3. A constant rate outflow of 5.5 l/min from the lower section of the borehole only. This option assumes that the responses to extraction in the lower section are unaffected by the extraction from the upper section.

Since the flow through the by-pass packer cannot be represented with the simulation options available in HydroGeoSphere, the second option is adopted here. Two separate sections are defined for borehole KR24 and pumping rates equal to 6570 m^3/y and 2891 m^3/y are assigned to the upper and lower section, respectively. Borehole KR24 is intersected by fractures HZ19A, HZ19C, HZ20A, and HZ20B_alt. All boreholes are assigned a radius equal to 0.01 (Therrien, 2008).

5.4.1.1 Steady state flow simulation with open boreholes

A first type boundary condition is imposed at the top boundary of the domain, as mentioned above. Prescribed hydraulic heads are determined from interpolation of groundwater table measurements, which vary from 0 (sea level) to 9 m (maximum head levels in the center of Olkiluoto Island). Open boreholes are disconnected from the surface, by locating their top node 10 m below the topographic surface, otherwise the hydraulic head would not change in the boreholes, since constant heads are imposed on the top boundary. This choice is justified by the fact that all boreholes have a casing section that prevents groundwater at the surface

from flowing to the boreholes (Vidstrand and Ahokas, 2005b). Heads on the lateral boundaries are all equal to sea elevation, while the bottom boundary is assumed impermeable. The porous rock is divided into two sections characterized by different hydraulic conductivities. This division is supported by measured transmissivity values, by calibration during subsurface flow modeling, and by comparison with previous modeling tasks conducted by the OMTF teams. A hydraulic conductivity equal to 7.8×10^{-8} m/s is attributed to the top 70 m of the bedrock, while the deeper bedrock is assigned a lower conductivity equal to 1×10^{-12} m/s. Fracture apertures calculated from the geometric mean transmissivity values given by Vidstrand et al. (2006) are listed in the third column of Table 5.3. These apertures are referred to as "series 1" and correspond to the apertures used by Therrien (2008).

Table 5.3 - Fracture apertures calculated from transmissivity (series 1) and calibrated (series 2)

Fracture	Transmissivity (log10) [m^2/s]	Aperture [m] series 1	Aperture [m] series 2
HZ1	-7.9	2.60×10^{-5}	2.60×10^{-5}
HZ2	-6.0	1.12×10^{-4}	1.12×10^{-4}
HZ3	-6.2	9.60×10^{-5}	9.60×10^{-5}
HZ4	-6.8	6.06×10^{-5}	6.06×10^{-5}
HZ8	-5.0	1.31×10^{-4}	1.31×10^{-4}
HZ19A	-5.8	2.41×10^{-4}	1.0×10^{-5}
HZ19C	-5.5	1.64×10^{-4}	1.64×10^{-4}
HZ20A	-5.1	2.23×10^{-4}	3.9×10^{-4}
HZ20AE	-6.0	1.12×10^{-4}	1.12×10^{-4}
HZ20B_ALT	-5.5	1.64×10^{-4}	5.0×10^{-4}
HZ21	-7.8	2.81×10^{-5}	2.81×10^{-5}
HZ21B	-6.1	1.04×10^{-4}	1.04×10^{-4}
BFZ99	-7.8	2.81×10^{-5}	2.81×10^{-5}

Although the apertures of "series 1" provide an acceptable reproduction of observed hydraulic heads for natural conditions, they are not appropriate to reproduce the drawdown at KR24. Therefore, fracture apertures have been modified to better calibrate the model. A steady state

simulation is executed to reproduce the maximum drawdown at pumping well KR24. The apertures of the four intersecting fractures are adjusted to match the minimum head reached during pumping. In particular, the aperture of fracture HZ19A has been reduced by one order of magnitude to simulate a greater drawdown in the upper section of the well. In contrast, the apertures of HZ20A and HZ20B_ALT have been slightly increased to reduce the drawdown in the lower section of the borehole. This second series of fracture apertures is referred to as "series 2" and is listed in the fourth column of Table 5.3.

Observation points are located in open deep boreholes KR04, KR07, KR08, KR10, KR14, KR22, KR27, and KR28. Heads measured at those boreholes are listed in Table 5.4 together with corresponding simulated heads. Observed heads are calculated as the average between March 16th and March 24th measurements. This choice is motivated by two main reasons. First of all, no values are available at KR4 on March 24th. Moreover, the average is intended to balance water table fluctuations during the ten days separating the measurements, since the heads imposed on the top boundary are the long term groundwater table mean values.

Table 5.4 - Simulated and observed average head values at open deep boreholes

Borehole	Observed head [m]	Simulated head [m]	Absolute difference [m]
KR4	6.03	6.00	0.03
KR7	5.31	6.04	0.73
KR8	6.28	6.06	0.215
KR10	5.98	6.16	0.185
KR14	6.82	6.7	0.115
KR22	6.17	6.02	0.15
KR27	6.72	5.85	0.87
KR28	5.69	6.00	0.11

Simulated hydraulic heads on the domain boundary are shown in Figure 5.14. Since a first-type boundary condition is imposed, the top and lateral boundaries show, respectively, the

interpolated groundwater table elevation and sea elevation. The flow is directed from the topographic high areas of the island toward the sea, where the hydraulic head is equal to zero.

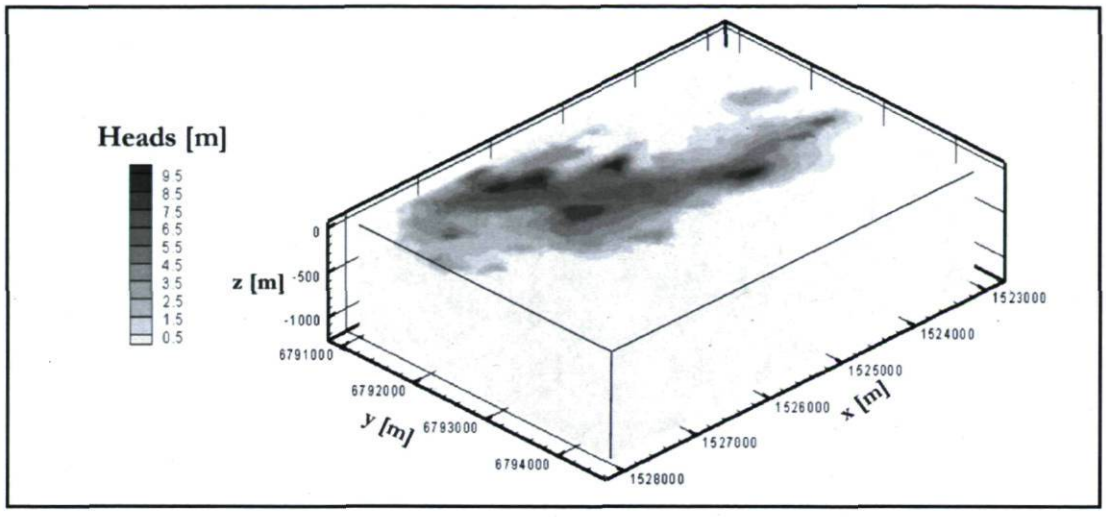

Figure 5.14 - Simulated hydraulic heads on Olkiluoto Island

Simulated hydraulic heads at the observation points are compared to those obtained by Therrien (2008) with a block-based mesh. A difference between the two series of results is noticed (Figure 5.15). The model proposed here provides a better match between observed and simulated heads, especially at boreholes KR8, KR10, and KR14. In contrast, simulated heads at boreholes KR7 and KR27 maintain almost the same difference from the observed values with the two models. The maximum absolute difference between observed and simulated heads obtained here is less than 0.9 m (Table 5.4). This difference can be due to the influence of the hydraulic head distribution imposed on the top boundary.

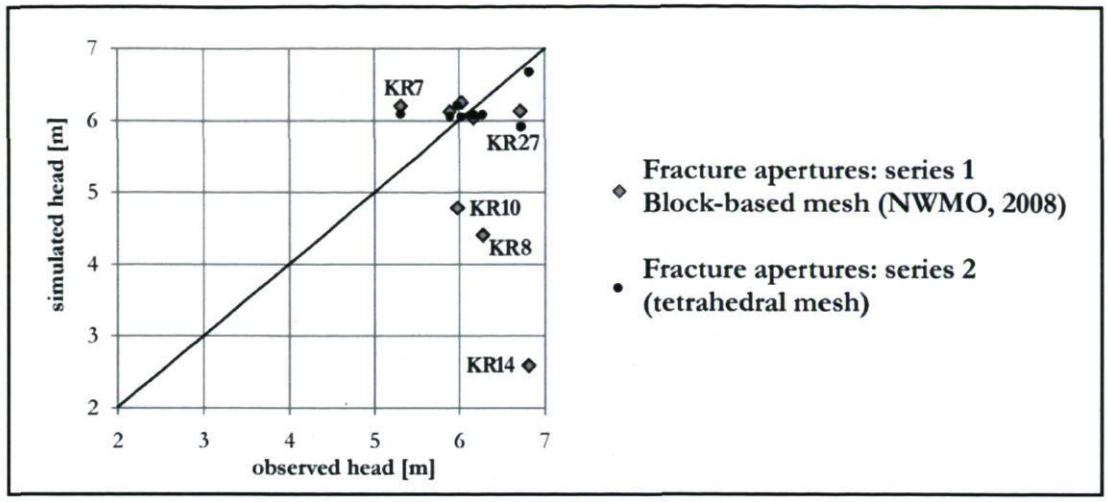

Figure 5.15 - Hydraulic heads at deep observation boreholes

To analyze the effects of different simulation parameters on hydraulic heads, three additional simulations (a,b,c) were conducted. In simulation "a", the hydraulic conductivity of the top rock is increased to 1.3 x 10^{-7} m/s. In simulation "b", the apertures of the fractures that do not intersect borehole KR24 are reduced to 10^{-6} m. In simulation "c", the aperture of fracture HZ19C, which intersects the lower section of KR24, is reduced to 1 x 10^{-5} m, which is the same for HZ19A. These three distinct scenarios produce approximately the same hydraulic heads at observation boreholes and don't improve calibration of head values at boreholes KR7 and KR27 (Figure 5.16)

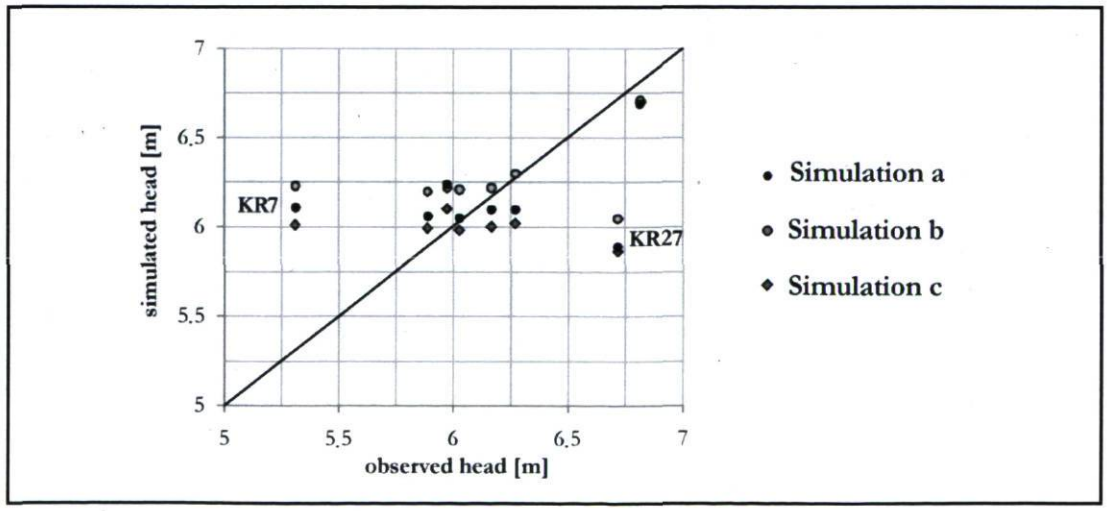

Figure 5.16 - Hydraulic heads at deep observation boreholes: sensitivity analysis

5.4.1.2 Steady state flow simulation without boreholes

The impact of the open boreholes on the groundwater flow field is analyzed by simulating flow and comparing the hydraulic head distribution with and without the boreholes. The differences in the flow field are clearly shown for three vertical sections inside the simulation domain in Figure 5.17. Since the open boreholes intersect the fractures, a complex network of major flow conductors is created. As a result, when the open boreholes are included, the global hydraulic conductivity of the domain increases and hydraulic heads are higher at greater depths. The difference in hydraulic heads is particularly noticeable toward the north, in the direction of increasing y coordinates, around borehole KR6, which intersects fractures HZ1, HZ21B, and HZ21. In particular, the top and bottom nodes of this borehole are located at coordinates y=6793050 m and y=6793350 m, generating greater hydraulic heads in this portion of the domain. Thus, the boreholes drilled at the site have a considerable influence on the groundwater flow field in the discretely-fractured medium.

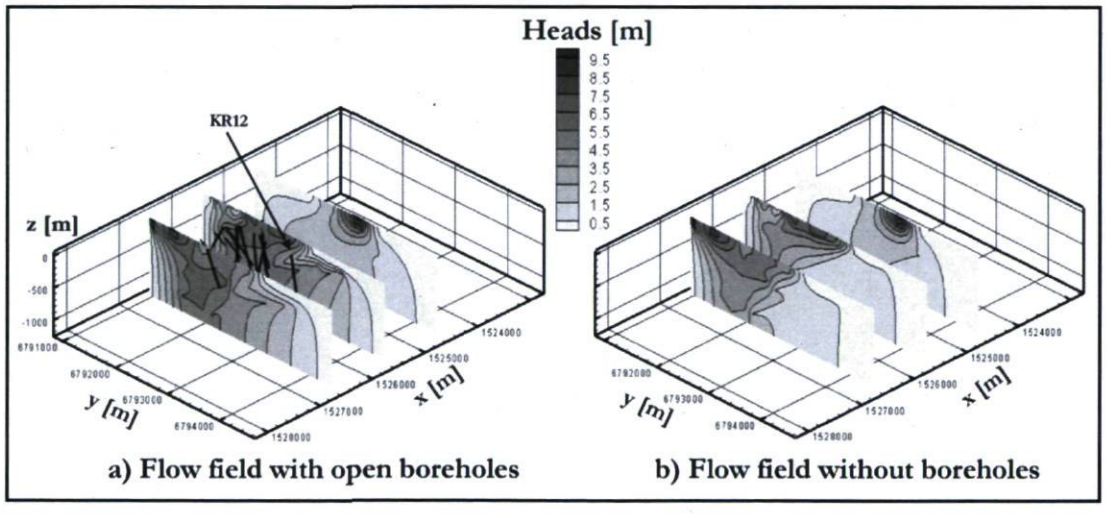

Figure 5.17 - Steady state simulation results: view inside the domain

5.4.1.3 Transient flow simulation: pumping at borehole KR24

The purpose of this section is to simulate the pumping test conducted at borehole KR24. The packer is represented in the model by splitting the borehole into two separated sections: the

upper section extends from ground surface to -86 m, while the lower starts at -92 m from the surface and extends down to -540 m. The upper section only intersects fracture HZ19A and it is discretized by 15 nodes. This intersection with HZ19A also coincides with the withdrawal node, where a pumping rate equal to 6570 m^3/y is prescribed. In contrast, the lower section is discretized by 76 nodes and intersects fractures HZ19C, HZ20A, and HZ20B_alt at depths of about -105 m, -296, and -390 m, respectively. A pumping rate equal to 2891 m^3/y is imposed at the top of this lower section. Few manual head measurements are available above and below the packer, while automatic measurements, taken every 15 minutes, are conducted from March 26 to July 22. The maximum drawdown observed in the upper section of KR24 is 19.25 m, while it is 1.94 m in the lower section. A difference between water levels before and after pumping is observed and is assumed to be caused by the natural decrease of groundwater surface in the island (Ahokas and Vidstrand, 2005). Simulation results presented in this section have two main objectives. A validation of the enhanced HydroGeoSphere version is first provided by comparison with the numerical results obtained on the same site with a block-based mesh (Therrien, 2008). Then, the model is calibrated by adjusting hydraulic parameters of the discretely-fractured medium to match observed and simulated drawdown at both observation points and pumping well.

For the first simulation scenario, the hydraulic parameters assigned to the fractures and to the porous rock matrix are identical to those used by Therrien (2008). Fractures are assumed non-deformable and fluid-filled, such that there is no contribution to the storage term from fracture compressibility (Therrien et al., 2007). Fracture apertures are those listed in Table 5.4 as "series 1". Specific storage is set to 4.4×10^{-6} m^{-1} for the fractures and to 1.0×10^{-6} m^{-1} for the rock matrix. The geological medium is assumed isotropic. The hydraulic conductivity of the first 70 m of the porous rock is equal to 2×10^{-7} m/s, while the deeper rock has a lower conductivity equal to 1×10^{-10} m/s. Initial heads are obtained by a steady-state simulation using the same geometry and parameters. A first-type boundary condition is imposed at the top of the domain and the open boreholes and pumping well are disconnected from the topographic surface, as done for the steady state flow simulations. Simulated drawdown at observation wells KR4, KR7, KR8, KR10, KR22, KR27, and KR28 are presented for both the NWMO model (Therrien, 2008) and the model proposed here, based on the tetrahedral mesh (Figures 5.18 and 5.19). Comparison to observed drawdown will be provided later (Figures 5.23 and 5.24).

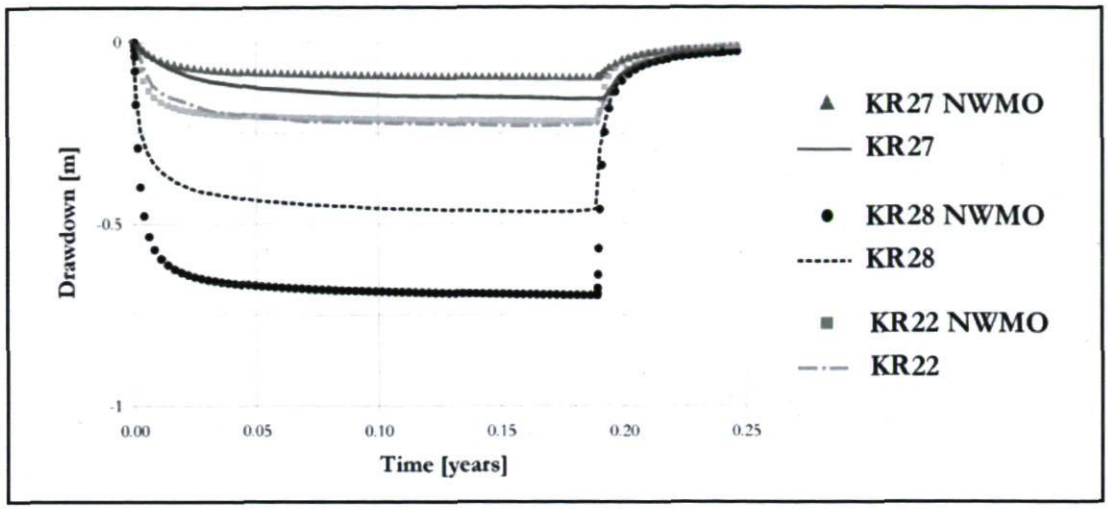

Figure 5.18 - Simulated drawdown at observation boreholes: comparison with results presented by NWMO in Therrien (2008) - part 1

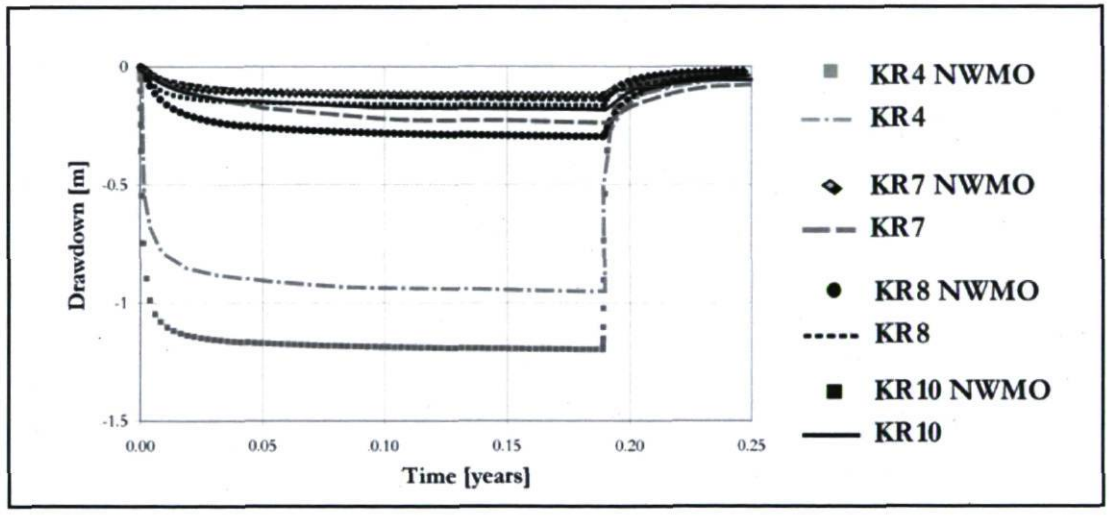

Figure 5.19 - Simulated drawdown at observation boreholes: comparison with results presented by NWMO in Therrien (2008) - part 2

It can be observed that all curves have the same shape, showing that the steady state condition is reached almost at the same time at the open boreholes for the two models. A difference is noticed in the maximum drawdown simulated, especially for KR4 and KR28, which are the boreholes nearest to pumping well KR24, at a distance of 60 and 100 m, respectively. This difference may be explained by the proximity of boreholes KR4 and KR28 to the pumping

well and, as a consequence, by the mesh resolution in this area, where large changes in hydraulic head occur. The local refinement and the representation of the fracture-well intersection affect the numerical results in this region. As mentioned in Section 5.3, the staircase approach is used to discretize fractures and boreholes with a block-based mesh (Therrien, 2008), such that multiple fracture-borehole intersections may occur. In fact, borehole KR28 is characterized by multiple intersections with fractures HZ19A and HZ19C, which intersect pumping well KR24. Concerning borehole KR4, no multiple intersections are observed with the block-based mesh. The difference in the simulated drawdown (Figure 5.18) may be due to the fact that borehole KR4 is the nearest to the pumping well and, therefore, the drawdown is computed differently because of the local tetrahedral refinement. The maximum observed drawdown in borehole KR4 is 0.62 m (Figure 5.23), while the drawdown simulated with the tetrahedral and block-based mesh is 0.92 m and 1.19 m, respectively (Figure 5.18). Thus, the result obtained with the tetrahedral mesh is nearer to the observed value than that obtained with the block-based mesh, although the difference is still quite significant. Uncertainty in the geometry and location of fractures may also be a cause of the differences between observed and simulated hydraulic heads. An additional reason for the difference between tetrahedral and block-based mesh simulation results may be found in the mesh resolution of borehole axes, which are discretized by 1D linear finite elements that are 6 m and 20 m long in the tetrahedral and block-based mesh, respectively. Since fractures and boreholes are the major flow conductors of the Olkiluoto groundwater system, their spatial discretization and the local refinement play a major role in the numerical results.

The drawdown at pumping well KR24, simulated with the tetrahedral mesh and the hydraulic parameters adopted by Therrien (2008), is far from the observed values. In the lower section the simulated drawdown is 4 m greater than the observed value, while it is 12 m lower in the upper section. To test the impact of fracture aperture on drawdown at borehole KR24, a second simulation is performed with the fracture apertures of "series 2". The hydraulic head values around well KR24 without and with pumping are presented in Figure 5.20 for this second simulation. The triangular discretization of fractures is also shown (Figure 5.20a).

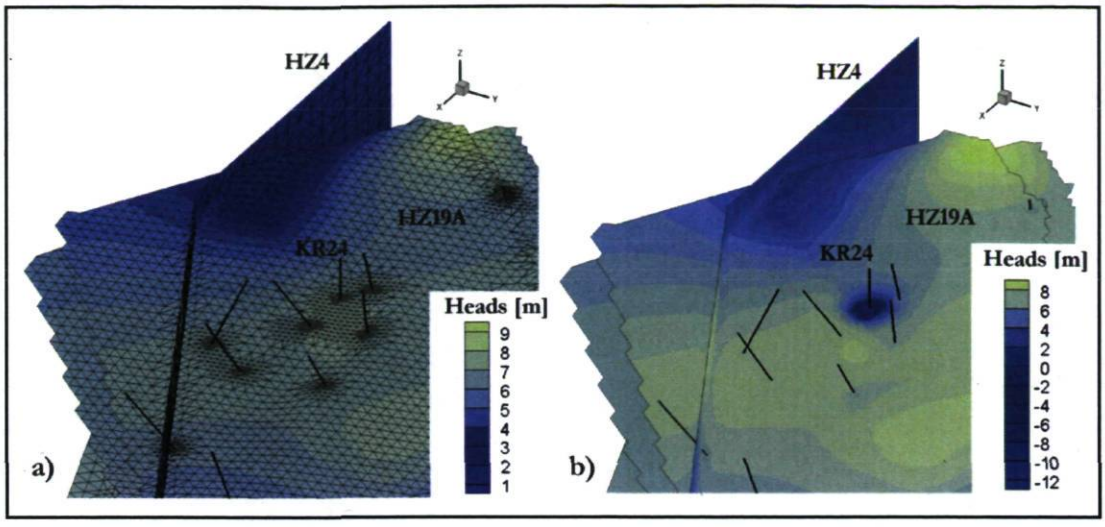

Figure 5.20 - Hydraulic heads on fracture HZ19A: a) without pumping and b) with pumping

Compared to the model with the "series 1" apertures, a much improved match between measurements and simulated heads at the pumping well is obtained using the apertures referred to as "series 2". The porous rock hydraulic conductivities are the same as those used for the steady state simulations. The quick recovery at the end of pumping is accurately reproduced as well as the minimum hydraulic head reached during pumping (Figure 5.21).

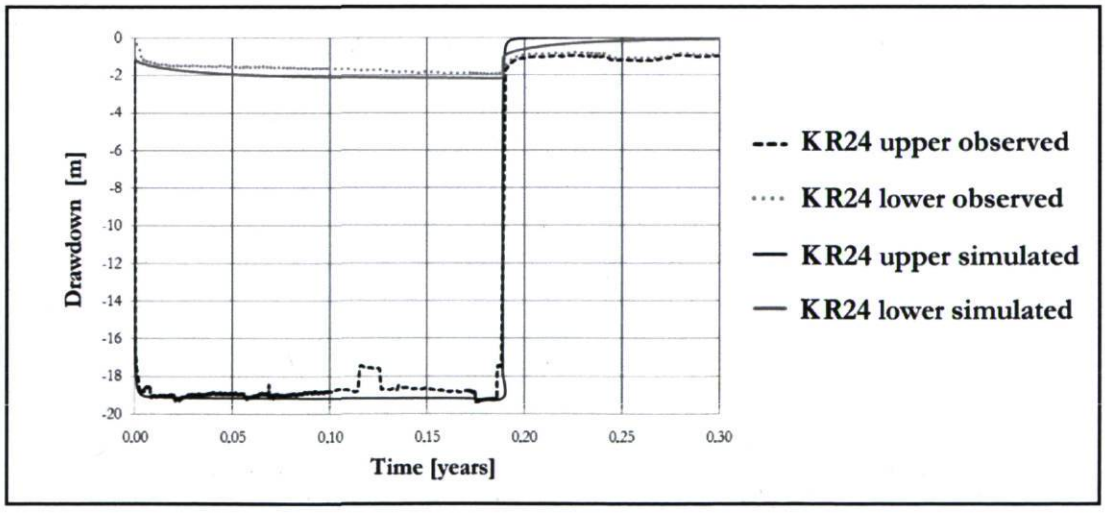

Figure 5.21 - Calibrated drawdown at pumping well KR24

A slight difference can be noticed at the end of the simulation, after 110 days, when the observed heads are lower than the simulated heads. This difference is explained by a natural decreasing trend in hydraulic head caused by seasonal water-table variations, which has been observed on Olkiluoto Island (Ahokas, 2007).

Additional simulations investigated the impact of the hydraulic parameters of the porous rock matrix on the drawdown curve. For these simulations, the fracture aperture and specific storage remain unchanged and the properties of the porous rock matrix and the boundary condition on the top of the domain are changed. These modifications are shown in Table 5.5, where K_{top} is the hydraulic conductivity of the first 70 m of the porous rock, and $K_{bedrock}$ is that of the lower bedrock.

Table 5.5 - Simulation parameters

Simulation	S_S [m^{-1}]	K_{top} [m/s]	$K_{bedrock}$ [m/s]	Top boundary
Base case	1×10^{-6}	7.8×10^{-8}	1×10^{-12}	Specified head
Sim_K	1×10^{-6}	5×10^{-8}	1×10^{-10}	Specified head
Sim_S_S	5×10^{-6}	7.8×10^{-8}	1×10^{-12}	Specified head
Sim_h	5×10^{-6}	7.8×10^{-8}	1×10^{-12}	No flow

The simulated drawdown curves demonstrate that, for the variations considered, the hydraulic conductivity has a stronger influence on drawdown than the specific storage (Figure 5.22). In particular, the lower value of K_{top} for Sim_K increases the drawdown in the upper section of the well by about 10 m. In contrast, even if the hydraulic conductivity of the lower bedrock is increased by two orders of magnitude, from 1×10^{-12} m/s to 1×10^{-10} m/s, the drawdown in the lower section does not change significantly. A larger specific storage coefficient (Sim_S_S) slightly reduces the drawdown in the lower section and modifies to some extent the shape of the curve in the upper section at the beginning of pumping. If the top of the domain is a no-flow boundary (Sim_h), the shape of the curve changes, especially for the upper section of KR24 where steady-state is reached more gradually than what was observed. Moreover, the initial head is not recovered. Finally, a better fit of the drawdown in the lower section is obtained with a larger storage coefficient. In that case, however, the drawdown at the

observation wells would be more difficult to calibrate. Thus, the "base case" parameters listed in Table 5.5 and the apertures "series 2" are the combination of parameters that give the best calibration of the flow model.

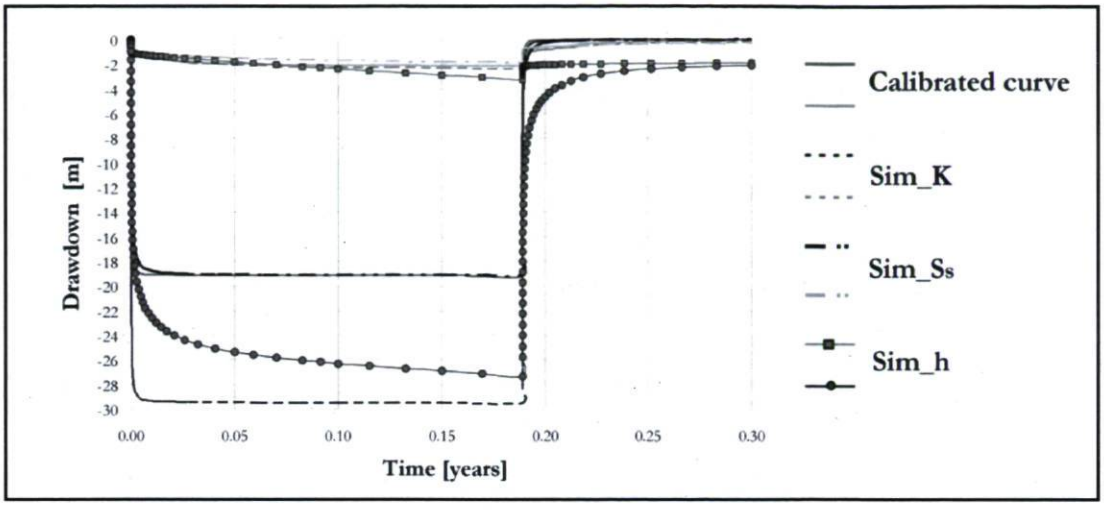

Figure 5.22 - Drawdown curve at pumping well KR24: sensitivity analysis

For the same calibrated flow model, the simulated drawdown at observation points is compared to that observed. However, the observed drawdown contains not only the decrease in hydraulic heads due to pumping at borehole KR24, but also the natural decreasing trend observed on Olkiluoto Island. Ahokas (2007) described some historical relationships between observed heads near surface and deeper in the bedrock. Decreasing trends have been analyzed for summers 1991, 1994, 1996 and for the longer period January 2002 - May 2003. An average trend of 1 cm/day is observed between mid-July and mid-September 1991. This natural decreasing trend is considered here to correct the observed drawdown at boreholes KR04, KR07, KR08, KR10, KR22, KR27, and KR28, which are chosen as observation points. The resulting observed "detrended" drawdown is compared to the drawdown simulated at observation boreholes (Figures 5.23 and 5.24). The corresponding drawdown at borehole KR24 has been presented in Figure 5.21.

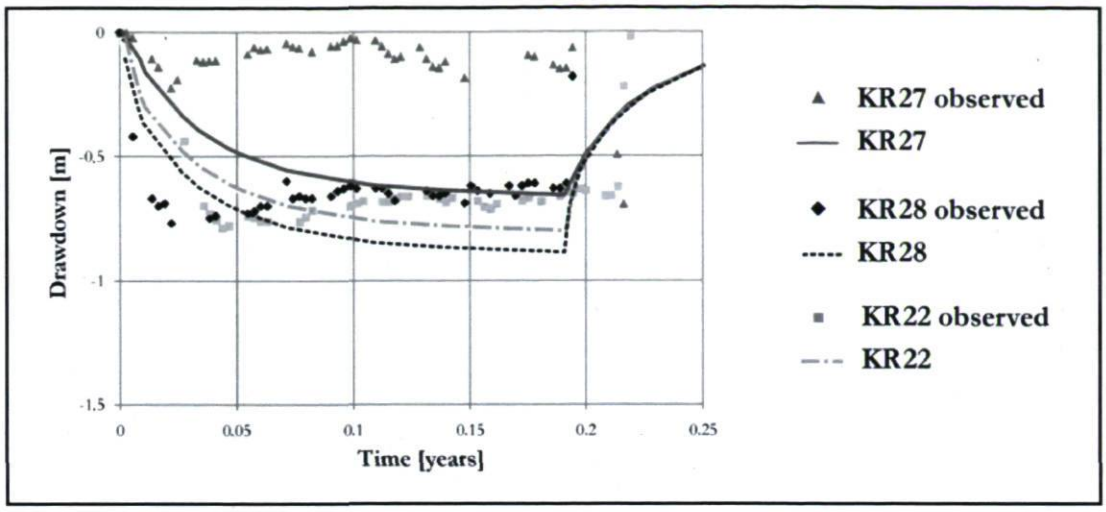

Figure 5.23 - Simulated and observed "detrended" drawdown at observation boreholes - part 1

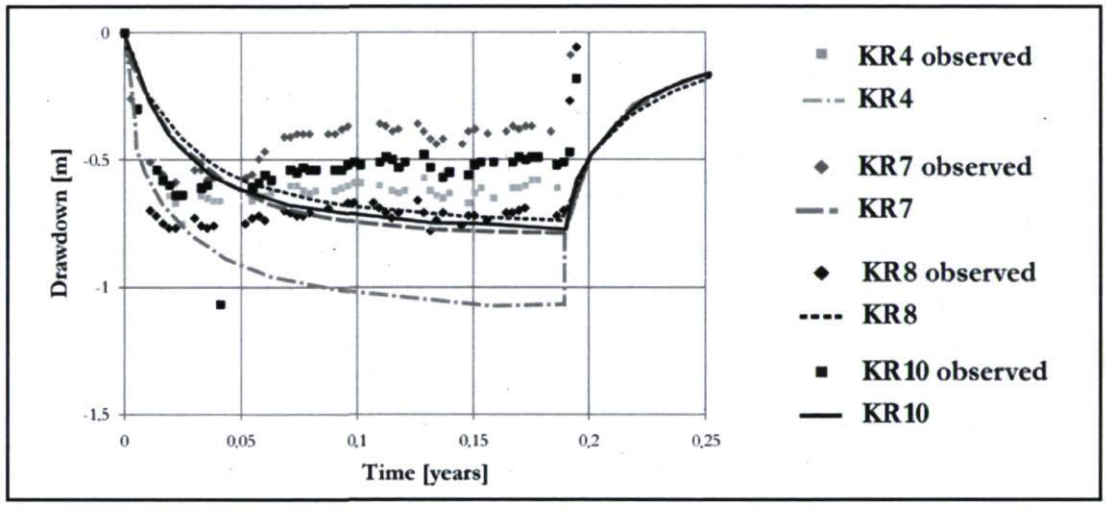

Figure 5.24 - Simulated and observed "detrended" drawdown at observation boreholes - part 2

Boreholes KR4, KR7 and KR27 show the largest difference between observed and simulated drawdown. For borehole KR4 this difference is probably due to the fact that KR4 is the nearest borehole to pumping well KR24 (about 60 m) and, therefore, the effect of pumping may be greater than the natural decreasing trend. Concerning boreholes KR7 and KR27, the differences have already been observed with the poor calibration in the steady-state simulation described in Section 5.4.1.1. Since the hydraulic head distribution evaluated in that steady-state simulation is used here as the initial condition for the transient flow simulation, the imprecise

evaluation of the hydraulic heads at boreholes KR7 and KR27 also influences the computation of their drawdown.

In Figures 5.18 and 5.19, which presented the simulated hydraulic heads with the simulation parameters of Therrien (2008), the simulated drawdown is generally smaller than the observed "detrended" drawdown. In particular, the simulated drawdown at boreholes KR7, KR8, and KR10 is less than 0.25 m. Borehole KR4 still shows the largest difference between simulated and observed drawdown. In contrast, the simulated drawdown at borehole KR27 (Figure 5.19) is closer to the observed "detrended" drawdown.

The rate of decrease in head depends on local properties, such as topography, location either on an outcrop or on overburden, and porosity (Vaittinen and Ahokas, 2005). Thus, it may be too simplistic to correct all observed heads by the same amount. Tidal effects are an additional component in the natural variation. In several cases, observed drawdowns are on the order of a few centimeters and are highly uncertain due to the unknown effect of infiltration on measured heads (Vaittinen and Ahokas, 2005). Given the complexity of the site, the available data, and the uncertainty in the knowledge of the trend in heads, simulation results reproduce quite well the in situ subsurface flow conditions.

5.4.2 Transport simulations

The purpose of this section is to present examples of solute transport applied to the Olkiluoto site. To keep the amount of work within reasonable limits, two representative simulation scenarios are considered. These simulations extend the application of the enhanced HydroGeoSphere version to solute transport in complex geological media and demonstrate the potential of the modeling approach developed. Numerical modeling focuses on the impact of open boreholes and fractures on solute transport at the Olkiluoto site, with specific interest on salinity distribution and on radionuclide migration.

The simulation parameters are those of the base case for the flow model presented in the previous sections (Tables 5.3 and 5.5). The transport simulations require the definition of

additional parameters, such as porosity, tortuosity, and dispersivity of the fractured geological medium, as well as solute properties. Dispersivity is a critical parameter for the transport simulations because its value has a direct influence on numerical results. It depends on the spatial scale and on the heterogeneity of the geological formations (Gelhar et al., 1992). Site-specific values for the Olkiluoto site were not available and have therefore been assigned on the basis of information found in the literature. The references considered here are summarized in Table 5.6. Unfortunately, no site specific information exists on the longitudinal or transverse dispersion lengths (Andersson et al., 2007). Thus, dispersivity constitutes a source of uncertainty from the point of view of solute transport, as there are no experimental data available for these parameters (Posiva Oy, 2005). Andersson et al. (2007) presented two sensitivity cases, where they adopted a weaker and a stronger value, respectively 25 m and 100 m for the longitudinal dispersivity and 6 m and 25 m for the transverse dispersivity. The sensitivity of transport simulation results to the dispersion length was also studied by Löfman and Mészáros (2005), who increased the longitudinal dispersion length to 75 m and 100 m. In general, the longitudinal dispersion was selected as small as possible in order to decrease the spreading of solutes and the transverse dispersion length was taken to be one-quarter of the longitudinal dispersion length (Löfman and Mészáros, 2005; Posiva Oy, 2005). Where the Darcy velocities are strong, dispersivity values shorter than 50 m caused numerical problems associated with a too large Peclet number when solving the transport equation.

Table 5.6 - Dispersivity values for the Olkiluoto site found in the literature

Source	Longitudinal dispersivity [m]	Horizontal and vertical transverse dispersivity [m]
Kattilakoski et al., 2000	200	50
Posiva Oy, 2005a	50	12.5
Löfman and Mészáros, 2005	50	12.5
Andersson et al., 2007	50	13

Longitudinal and transverse dispersivities equal to 50 m and 12.5 m, respectively, are considered for the illustrative simulations presented here. They correspond to the published values and also result in Peclet numbers that are not too large for the tetrahedral mesh, with

the computed Darcy velocities. The tortuosity of the porous rock matrix is set to 0.1 and the porosity to 0.05, as in Therrien (2008).

Simulation results presented in Section 5.4.2.2 are for a transient flow field, while those presented in the Section 5.4.2.1 are based on a steady state flow field. Implicit transport time weighting and upstream weighting of velocities are always used as simulation options. Concentration control is adopted to generate adaptive time-steps. Unless mentioned otherwise, the Orthogonal Subdomain Collocation method is employed.

5.4.2.1 Simulation of the evolution of salinity distribution

The evolution of the salinity distribution is one of the hydrogeological modeling aspects of particular interest at the Olkiluoto site. This topic is largely covered in Posiva Oy reports (Riekkola et al., 2003; Löfman, 2005; Löfman and Mészáros, 2005). Although a variable-density flow and transport simulation would be the most appropriate option to simulate the evolution of the salinity distribution, a simplified scenario is considered here, where density effects on fluid flow are neglected. Therefore, an initial concentration distribution of TDS (Total Dissolved Solid) is assigned to the simulation domain and the density of water is assumed to be constant. The dependence of the density of water on the salinity is neglected and the salt is considered as a conservative solute.

A first scenario considers the effect of pumping on the salinity distribution. The following depth-dependent salinity profile $s(z)$ is adopted as the initial conditions for the solute (Löfman, 1999):

$$s(z)=\begin{cases}-0.04982z & 0\ m \le z \le -100\ m \\ 3.582e^{-0.0033z} & -100\ m \le z \le -900\ m \\ 72 & -900\ m \le z \le -1200\ m\end{cases} \tag{5.1}$$

A linear model for salinity is used from the surface to the depth of 100 m. From 100 m to 900 m, an exponential increase in salinity is applied, whereas a constant value 72 g/l is used for depths greater than 900 m. The curve obtained with Eq.(5.1) follows the trend of salinity values measured in boreholes at the site (Figure 5.25). The water is generally defined as saline

at concentrations of about 30 g/l, which are found at a depth of about 600 m, according to the profile given by Eq.(5.1). In the numerical model, the initial salinity values are attributed to horizontal layers 100 m thick, such that salinity values change every 100 m, which is the length of the edges of the largest tetrahedral elements in the mesh. The horizontal initial salinity distribution was also adopted by Löfman and Mészáros (2005). Salinity values are expressed as relative concentrations, based on a fraction of the maximum salinity value. Thus, the maximum salinity of 72 g/l corresponds to a relative concentration equal to 1 and, for example, the relative concentration at the depth of 500 m is equal to 0.26.

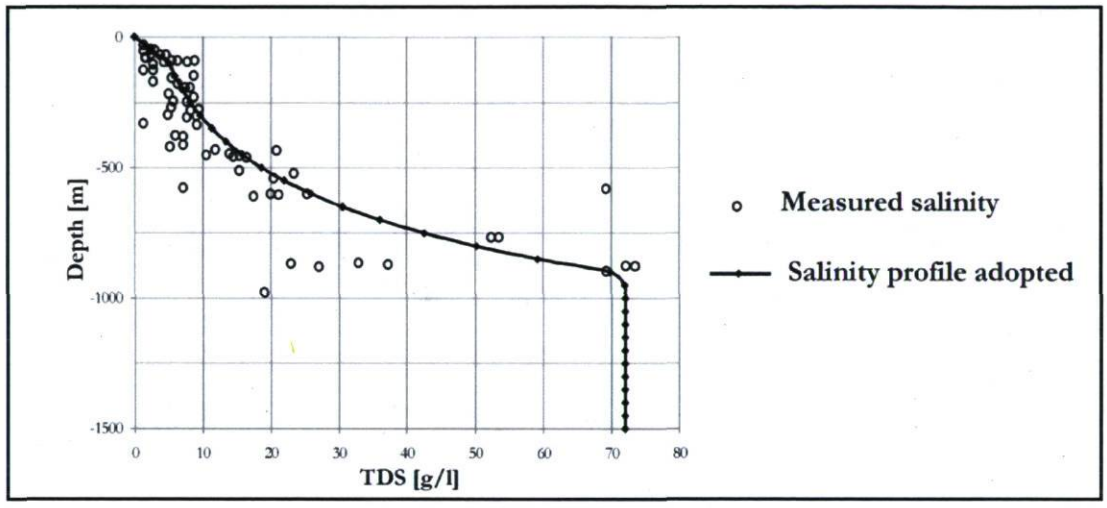

Figure 5.25 - Salinity profile of groundwater (TDS)
(adapted from Löfman and Mészáros, 2005)

For this hypothetical simulation scenario, boreholes KR4, KR7, KR12, and KR24 are considered as pumping wells. A flowrate equal to 10000 m^3/y, which is the same value of the pumping test conducted in 2004 at borehole KR24, is imposed at the bottom node of the well axes. The computed salinities, shown in Figure 5.26, indicate that salinity decreases at the bottom node of the wells, which is the discharge point. In contrast, the concentration in the middle of the well axis slightly increases. Thus, the location of the well withdrawal point controls the mixing of groundwater characterized by different salinity values. The curves shown in Figure 5.26 have the tendency to converge to the same value, which is explained by the fact that the deep well pumps groundwater that has a different TDS concentration.

Borehole KR24 is the shortest pumping well considered, thus its concentration at the bottom node is the smallest one, equal to 0.33, or 24 g/l of TDS. In contrast, inclined well KR4 reaches a depth of 870 m, thus it is characterized by an initial relative concentration at its bottom node equal to 1. Because of pumping, this value decreases to about 0.3, which corresponds to 22 g/l of TDS. Regardless of the initial difference of salinity along the well axis, at the end of pumping the TDS concentration is almost the same along the well axis. These simulation results demonstrate that open boreholes tend to homogenize the salinity concentration.

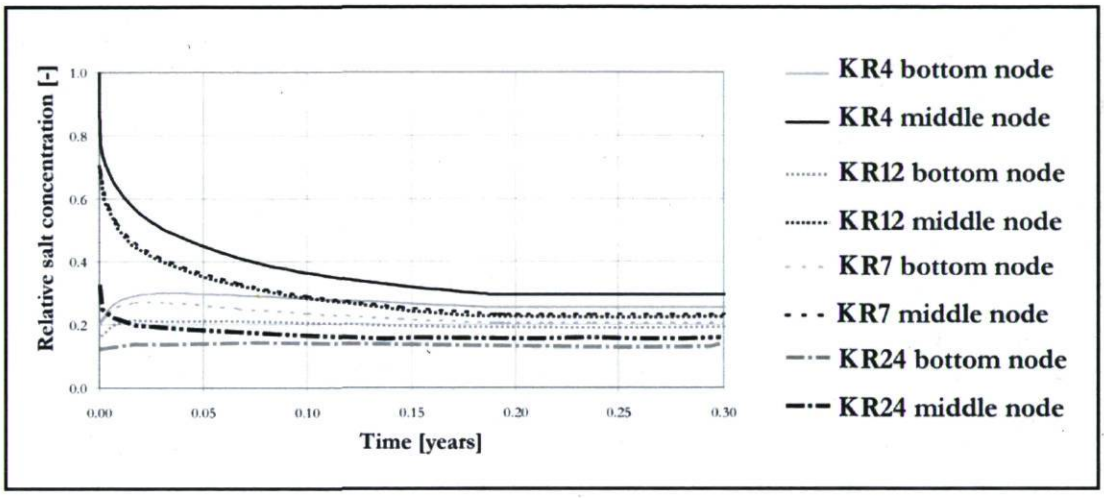

Figure 5.26 - Simulated evolution of TDS relative concentration at pumping wells

Another topic related to the salinity distribution is the analysis of the inflow into ONKALO. The open tunnel will constitute a major hydraulic disturbance for the site's natural groundwater system (Löfman and Mészáros, 2005). Inflow can be limited by a careful selection of the locations of the underground facilities and their surface connections and by forming a watertight zone in the rock around tunnels and shafts. This is normally completed by engineering measures, such as grouting the rock before or after excavation (Riekkola et al., 2003). The open ONKALO can be thus thought as a major sink that draws groundwater from all directions in the bedrock. Most of the inflow would come from the conductive subhorizontal fracture zones intersected by the access tunnel and the shaft during excavation. Riekkola et al. (2003) estimated with analytical methods the total groundwater ingress into ONKALO. They obtained an inflow of about 3000 l/min in the absence of any engineering

measures, while they estimated that inflow declined to about 450 l/min after grouting. ONKALO was modeled by a set of nodes in the finite element mesh by Löfman and Mészáros (2005), treating each tunnel node as a sink and using for each node a prescribed outflow rate. This effect is reproduced here by assigning the equivalent total outflow rate to borehole KR4, as the ONKALO tunnel geometry was not included in the Geomodel. The real inflow into ONKALO is thus reproduced in the numerical model as outflow from borehole KR4, which represents the whole open ONKALO. An average inflow equal to 1100 l/min is used here, which is equal to the inflow into the access tunnel calculated by Löfman (2005). Other boreholes are not included in the simulation. This simulation aims at reproducing the general direction of the subsurface flow and the change in salinity distribution presented in Löfman and Mészáros (2005), who, however, simulated a variable-density flow.

The initial salinity distribution obtained by applying Eq.(5.1) is shown in Figure 5.27a. The open ONKALO is considered hydraulically active at the beginning of the simulation, which covers 200 years. It is clear that the simplified approach used here cannot lead to the same results obtained by Löfman and Mészáros (2005). However, the purpose here is to offer an illustrative example to draw some conclusion on the validity of the proposed modeling approach.

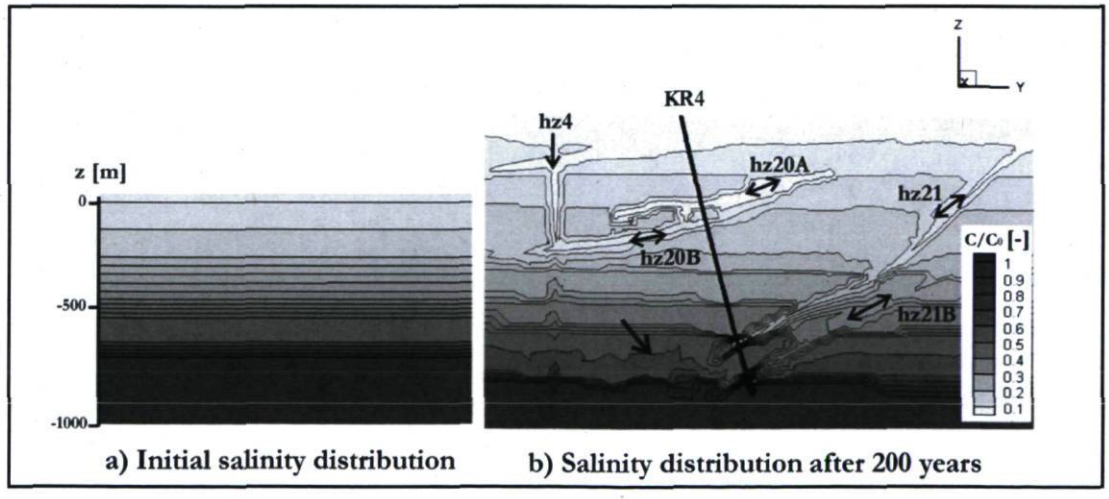

Figure 5.27 - Effect of inflow into ONKALO on the salinity distribution for a vertical section at x = 1525815 m

The effect of inflow is clearly visible in Figure 5.27b, where the groundwater migrating from the surface through the fracture network determines the migration of brackish water deep into the bedrock. Saline water moves along fracture HZ4, although this behavior is more evident in Figure 5.28b. An increase in TDS concentration at depths of 700-800 m is also observed, as indicated by the black arrow (Figure 5.27b).

The effect of the porous rock hydraulic conductivity on the evolution of the salinity profile is also investigated. If the hydraulic conductivity is increased by two orders of magnitudes, from 1×10^{-12} m/s to 1×10^{-10} m/s, which is the value used by Therrien (2008), groundwater mixing increases (Figure 5.28b). In particular, the rise of brine water along fracture HZ4 is more evident. The salinity evolution presented by Löfman and Mészáros (2005) is comparable to that obtained here, although changes in the salinity distribution are greater in Löfman and Mészáros (2005), probably because of the use of a variable-density flow solution and the discretization of the real geometry of ONKALO.

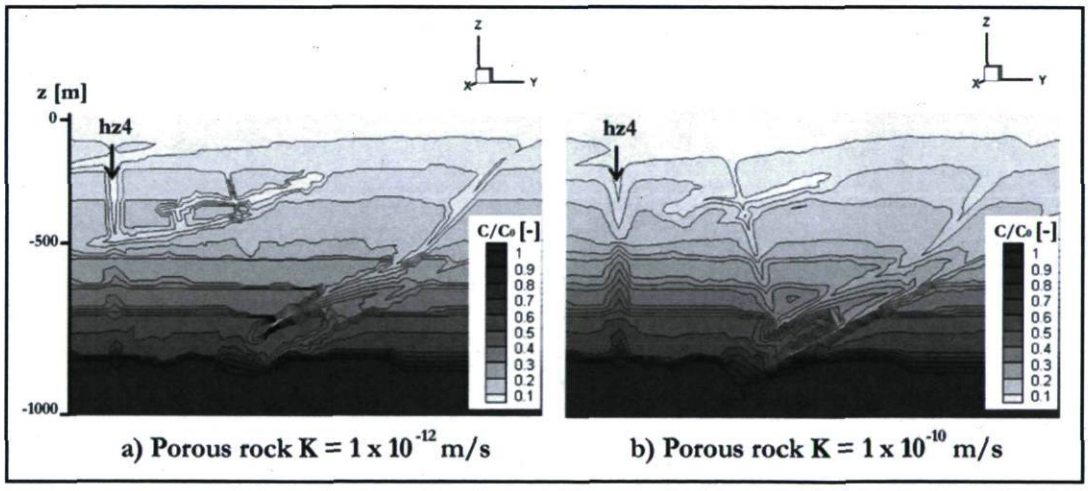

Figure 5.28 - Influence of the porous rock hydraulic conductivity on the salinity distribution for a vertical section at x = 1525875 m

Darcy velocities simulated here are also compared to those presented by Löfman and Mészáros (2005). Inflow into ONKALO creates a flow field convergent toward the center of the simulation domain, where the outflow rate is applied (Figure 5.29). The natural groundwater flow without the underground rock laboratory is characterized by a discharge toward the sea

(Figures 5.14 and 5.17). In contrast, the inflow reverses the main direction of groundwater flow, which now is directed from the lateral boundaries towards the open ONKALO, as expected. Although Löfman and Mészáros (2005) included in their model the geometrical representation of the access tunnel and shaft, and used a slightly different fracture network configuration, the two images presented in Figure 5.29 are comparable.

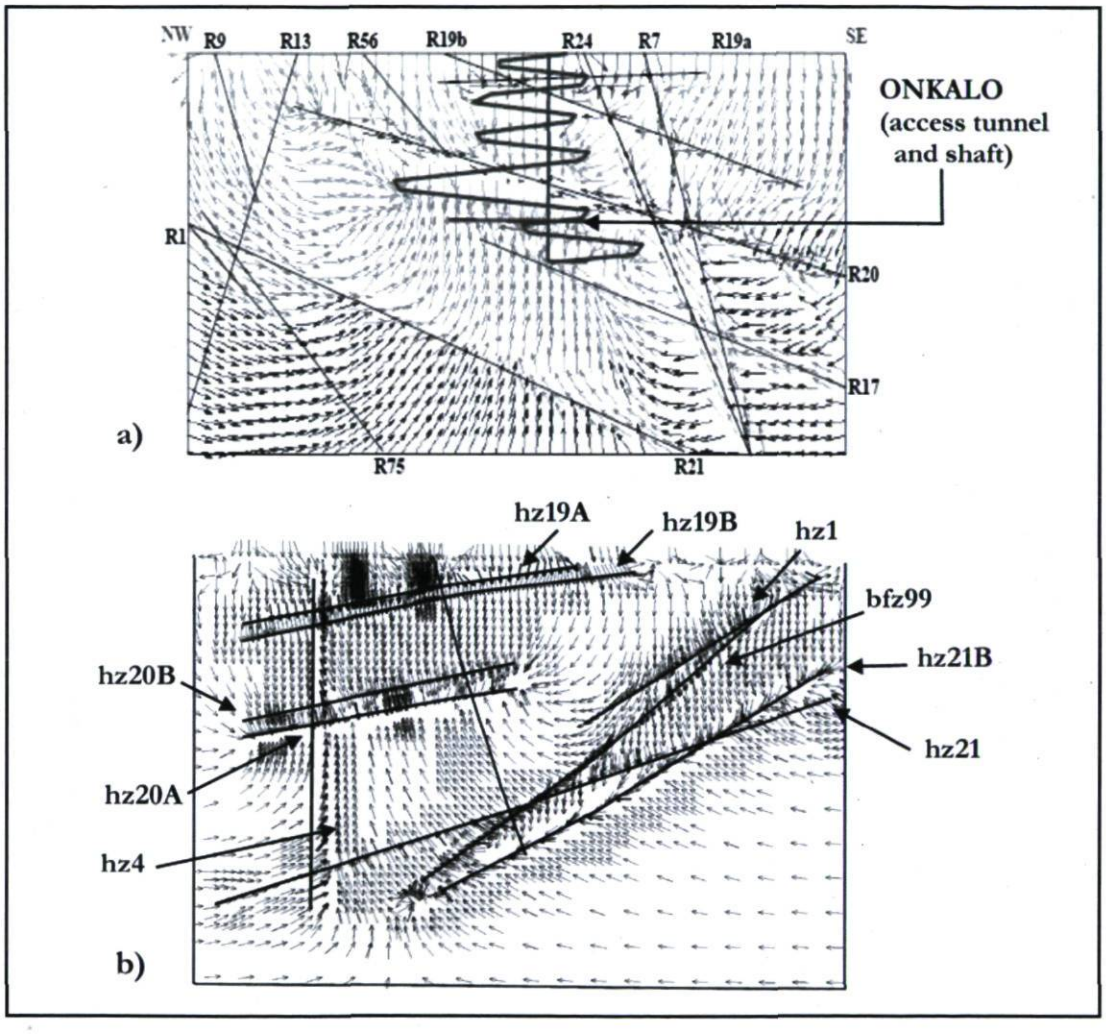

Figure 5.29 - Inflow into ONKALO: a) Darcy velocities within porous matrix presented by Löfman and Mészáros (2005) and b) Darcy velocities simulated

5.4.2.2 Simulation of radionuclide migration

The performance assessment of a repository requires a detailed understanding of the processes that can affect contaminant transport. The purpose of this section is to present an illustrative example representing a base case for radionuclide transport modeling. Two main reactive processes can be considered to simulate the movement of radionuclides in groundwater. Radionuclides undergo radioactive decay according to their half-life, and they can also be adsorbed on mineral surfaces. Both processes are important mechanisms for retarding the potential radionuclide migration from a geological nuclear fuel repository to the biosphere. Sorption is highly dependent on the particular combination of mineral and radionuclide. Sorption is described through the retardation factor, which, in saturated conditions, is defined as:

$$R = 1 + \frac{\rho K_d}{n} \tag{5.2}$$

where K_d is the volumetric distribution coefficient, ρ and n the bulk density and the porosity of the porous rock, respectively. The coefficient K_d describes the distribution between two phases, in this case the solid porous rock and the water, and it is calculated as the ratio of the concentration of the solute in one phase to the concentration of the solute in the other phase under equilibrium conditions. Dissolved radionuclides are then transported by diffusion and advection, with mechanical dispersion. In general, radionuclide transport in low permeability formations is dominated by diffusion.

Two radionuclides are considered here, the anion ^{129}I and the cation ^{133}Ba. They have been chosen on the basis of radionuclide studies found in the literature (Kosakowski, 2004; Andersson et al., 2002; Dershowitz et al., 2003). The bulk density of the most abundant lithology, the mica gneiss, is equal to 2800 kg/m^3 (Hudson and Johansson, 2006), which has been assigned to the whole porous rock. ^{129}I is long-lived and relatively mobile in the environment. In a deep geological repository for unreprocessed used fuel, it is likely to be the radionuclide of most potential impact at long times. It is considered as a conservative tracer and its K_d is set to 0. In contrast, ^{133}Ba undergoes adsorption. Its distribution coefficient is given by Dershowitz et al. (2003), who estimated the distribution coefficients for several

sorbing tracers in the context of the Äspö Hard Rock Laboratory modeling Task Force. Dershowitz et al. (2003) presented the information required to construct a fractured granite hydrostructural model for Performance Assessment modeling. As the Olkiluoto site is a similar geological environment, the study of Dershowitz et al. (2003) has been considered as one of the main references for this section. Radionuclides are assumed to be sorbed on the fracture walls because of the presence of mineral coating. The HydroGeoSphere input parameter for sorption on the fracture walls is the fracture retardation factor, which is calculated as:

$$R_f = 1 + \frac{2K_a}{2b} \tag{5.3}$$

where the surface sorption coefficient K_a can be evaluated from the K_d for the fracture coating (Dershowitz et al., 2003) and $2b$ is the fracture aperture. The average aperture of the 13 fractures is considered, to simplify the simulation scenario by attributing the same retardation factor to all the fractures.

Radionuclide parameters are listed in Table 5.7. Note that hydraulic parameters are those used to calibrate the flow model and longitudinal and transverse dispersivities are 50 m and 12.5 m, as mentioned in Section 5.4.2. For the porous rock matrix, it is assumed that horizontal and vertical transverse dispersivities have the same value equal to 12.5 m.

Table 5.7 - HydroGeoSphere input parameters to simulate radionuclide migration

Parameter		Value
^{129}I	Volumetric distribution coefficient K_d [m^3/kg]	0
^{133}Ba	Volumetric distribution coefficient K_d [m^3/kg]	1 x 10^{-3}
^{129}I	Fracture retardation factor R_f [m]	1
^{133}Ba	Fracture retardation factor R_f [m]	106
^{129}I	Decay constant λ [y^{-1}]	4.4 x 10^{-8}
^{133}Ba	Decay constant λ [y^{-1}]	6.6 x 10^{-2}
^{129}I	Free diffusion coefficient D_0 [m^2/y]	1.9 x 10^{-2}
^{133}Ba	Free diffusion coefficient D_0 [m^2/y]	2.7 x 10^{-2}

Figure 5.30 illustrates the simulation design for the radionuclide transport simulation. A unit radionuclide concentration is imposed at nodes located between depths of -500 m and -550 m, which is the approximate depth where the spent fuel should be placed according to the preliminary design of the repository. The first-type concentration source is located in the porous rock at the center of the fracture network, between coordinates 1526000 - 1526050 m and 6792000 - 6792050 m in the x and y directions, respectively. The purpose is to investigate if the contaminant reaches the nearest fracture HZ21 and then migrates through the fracture network. Boreholes have not been included in this scenario because the simulation is assumed to start once the repository is closed and that all open borehole have been backfilled. The potential source of contamination corresponds to either an initially defective canister or a subsequently breached canister.

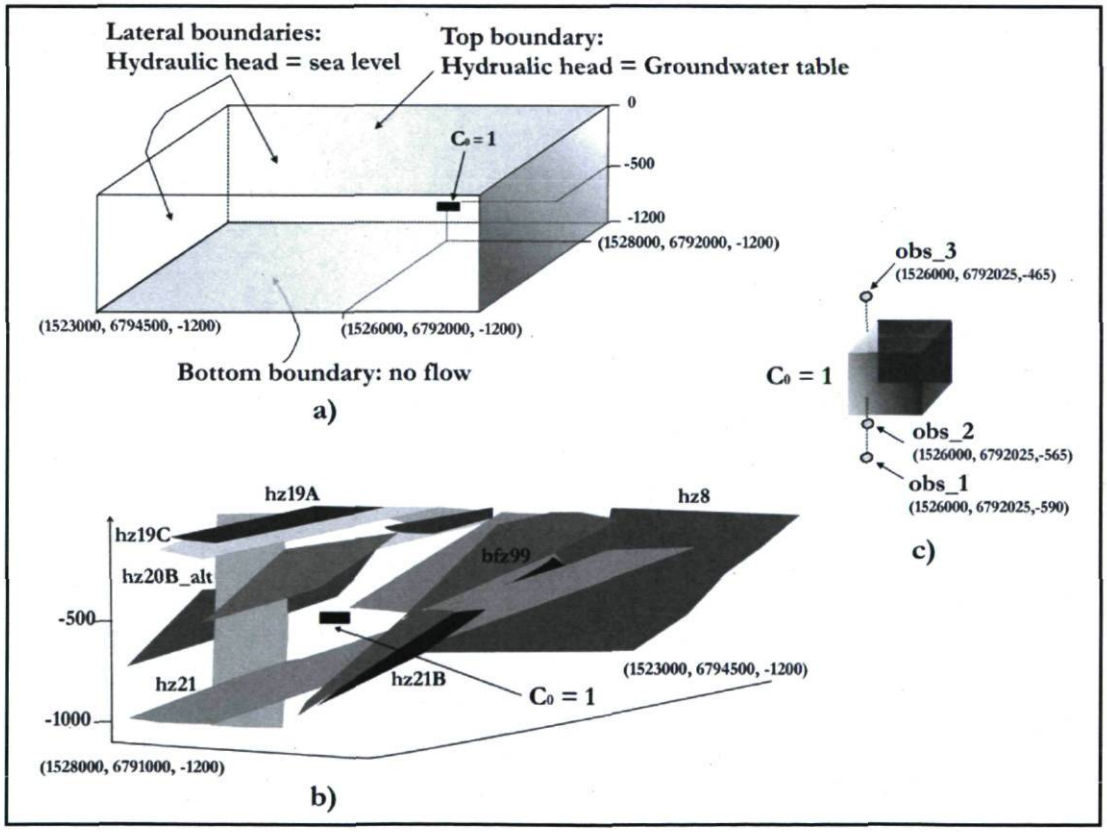

Figure 5.30 - Model design for radionuclide transport simulations: a) boundary conditions, b) location of the concentration source and c) position of the observation points above and below the concentration source C_0

Two observation points obs_1 and obs_2 are located below the source of contamination at coordinates (1526000, 6792025, -590) and (1526000, 6792025, -565), respectively. A third observation point, obs_3, is located above the source of contamination, at coordinates (1526000, 6792025, -465). This simulation scenario considers a steady state flow field.

The difference in the migration of the two species can be seen in their corresponding breakthrough curves (Figure 5.31). Barium, which decays faster than ^{129}I and also undergoes sorption, is not found at any observation point. In contrast, ^{129}I is found at the three observation points, but at different concentrations. Since obs_1 is further from the contamination source than obs_2, the relative concentration is smaller. The lowest relative concentration is found at obs_3, which is located above the contamination source.

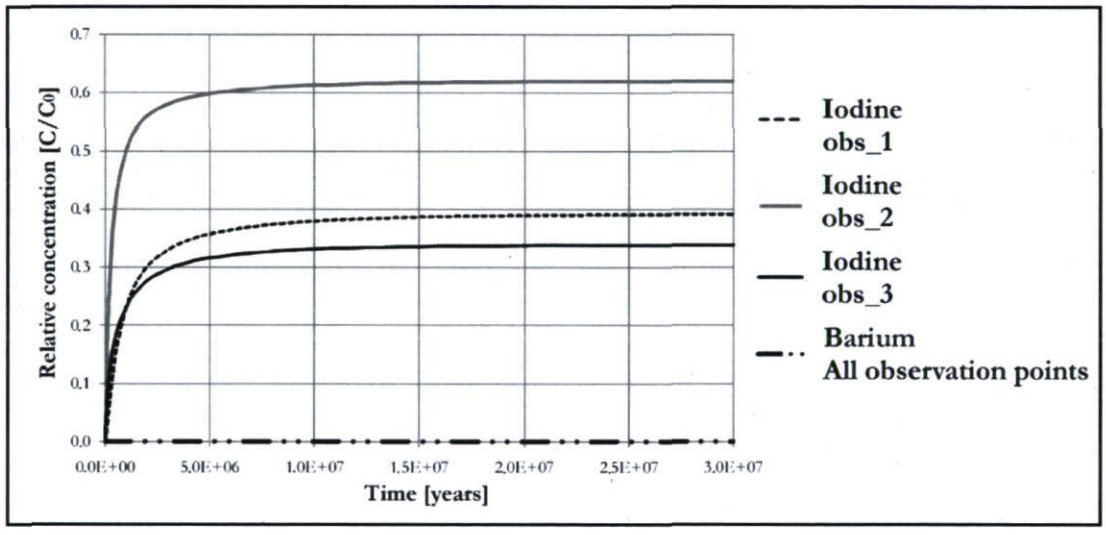

Figure 5.31 - Breakthrough curves for ^{129}I and ^{133}Ba at the observation points

The Iodine migrates through the rock matrix and does not reach the nearest fractures in this specific simulation scenario. To better investigate Iodine propagation, dispersive and advective fluxes through the porous rock matrix are computed for a slice of nodes around the concentration source (Table 5.8).

Table 5.8 - Mass fluxes computed at nodes near the concentration source

Flux	Below the source	Above the source	To the right of the source
Advective flux [MT^{-1}]	5.6×10^{-4}	3.1×10^{-4}	5.0×10^{-4}
Dispersive flux [MT^{-1}]	1.1×10^{-2}	6.9×10^{-3}	6.0×10^{-3}

The concentration isocontours are not perfectly symmetric around the Iodine source, with a slightly larger migration in the direction of the groundwater flow (Figure 5.32). The dispersive flux is larger than the advective flux at all three locations, as hydrodynamic dispersion is the dominant transport process in the low permeability porous rock matrix. The advective flux is at least one order of magnitude smaller at all locations and the largest value is found below the contamination source, where the largest dispersive flux is also computed.

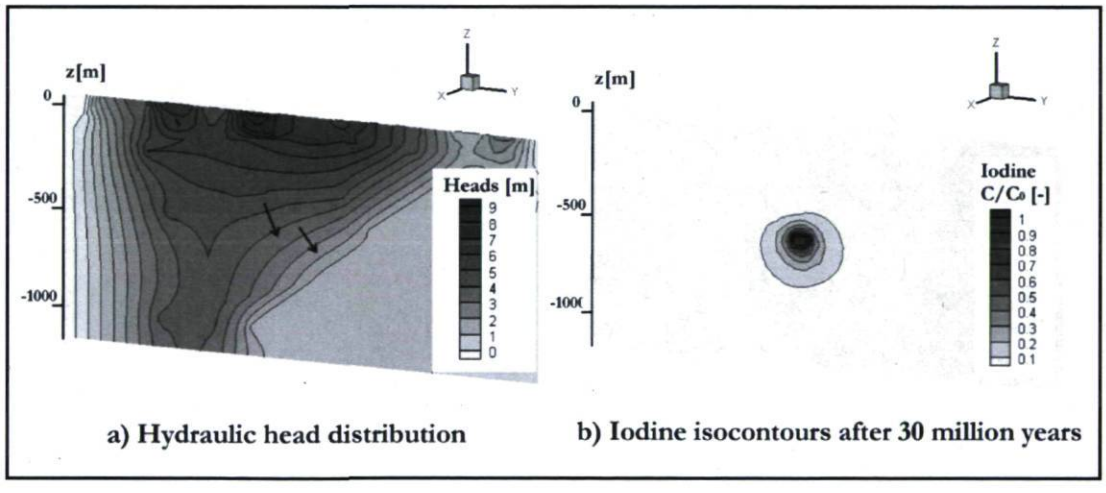

Figure 5.32 - Vertical section at x = 1526000 m: a) groundwater field and b) ^{129}I concentration isocontours

The sensitivity of the porous rock permeability on the contaminant plume migration has also been tested by increasing the hydraulic conductivity from 1×10^{-12} m/s to 1×10^{-8} m/s. For this new scenario, the ^{129}I plume is larger and reaches fractures HZ21, HZ4, and BFZ99, where the relative concentration is less than 0.2 (Figure 5.33a). ^{129}I reaches HZ4 because it intersects

fracture HZ21, which is attained by the contamination plume. Fractures HZ20A and HZ20B_alt are located above the concentration source and the plume does not reach them.

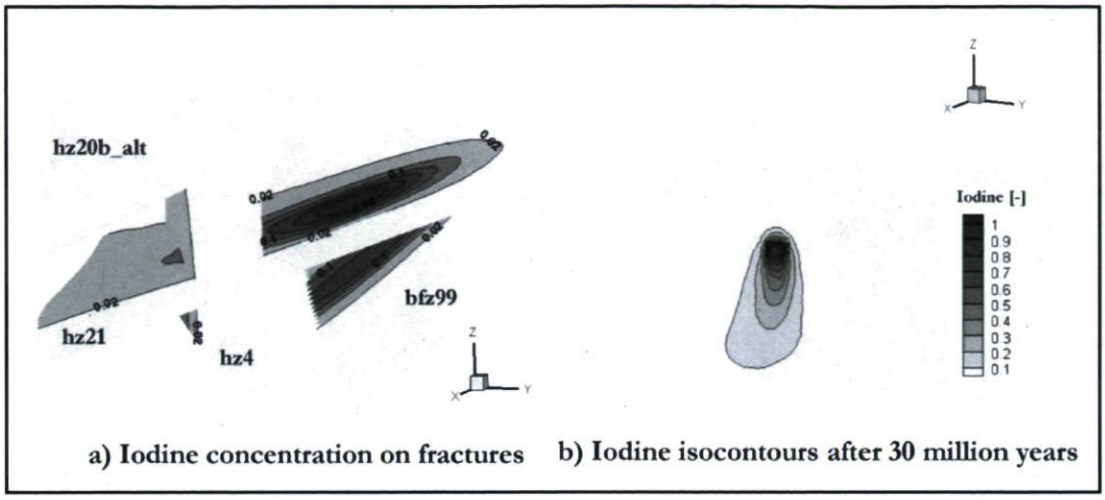

Figure 5.33 - ^{129}I concentration isocontours for K_{rock} = 1 x 10^{-8} m/s:
a) concentration in the fractures and b) concentration for a vertical section at x = 1526000 m

A final comparison between the Galerkin and OSC methods is based on the simulation of the Iodine propagation. Implicit transport weighting and upstream weighting of velocities are used for both simulations. With the Galerkin method negative concentrations occur, which significantly affect the visualization of the concentration contours (Figure 5.34). In particular, a minimum concentration equal to -0.042 is obtained. In contrast, with the Orthogonal Subdomain Collocation method, the largest negative concentration value is -3.9 x 10^{-10}, which is nearer to zero, and no visualization errors appear. Moreover, the difference in the number of solver iterations follows the trend mentioned in Chapter 4. The number of flow solver iterations is 346 and 283 for the Galerkin and OSC methods, respectively. Likewise, the mass transport solver iterations are 200 and 150 for the Galerkin and OSC methods, respectively.

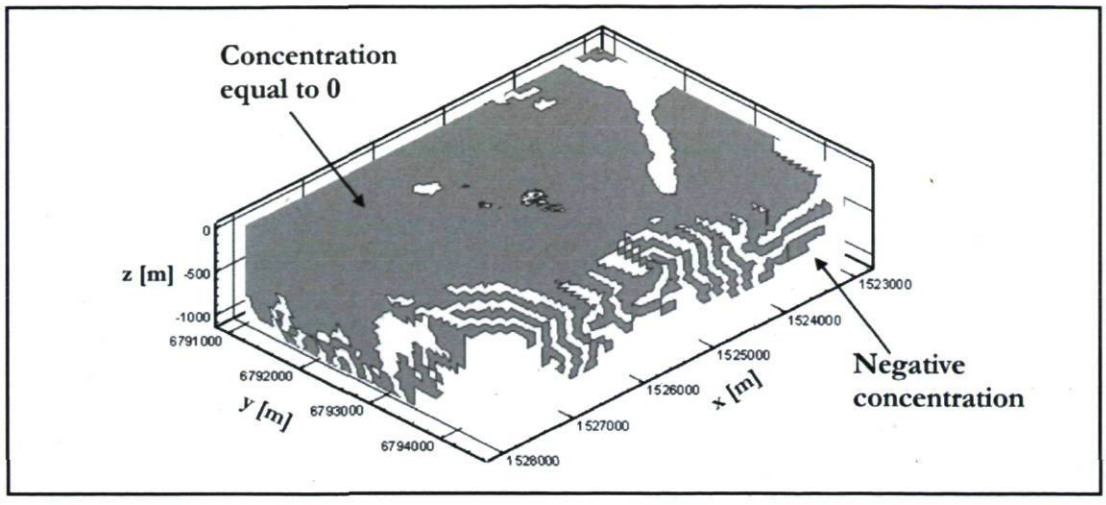

Figure 5.34 - Galerkin method: errors in numerical results

5.5 Concluding remarks on case study simulations

This case study demonstrates that the modeling approach developed here is a suitable tool for hydrogeological modeling of complex fractured media. The geological modeling platform GOCAD is particularly suitable to create the 3D fracture network. Then, the tetrahedral mesh is the most appropriate way to discretize this complex domain, if compared to simpler structured meshes, and it constitutes a good compromise between high mesh resolution and computational time.

Flow simulations aim at reproducing the pumping test conducted at the Olkiluoto site in 2004. A satisfactory agreement between the simulated and observed hydraulic head is obtained. Moreover, illustrative transport simulation scenarios are designed to show the numerical capabilities of the enhanced numerical model. The evolution of the salinity distribution and the propagation of two representative radionuclides are considered. Simulations provide expected results and, in particular, similar differences between the Galerkin and the Orthogonal Subdomain Collocation methods highlighted in Chapter 4 are observed here. With the OSC method, negative concentration values are more easily avoided and a smaller number of solver iterations is required.

Other modeling aspects that may be considered for this case study are density dependent flow and heat transfer. Saline water is a major concern for performance of the tunnel backfill after the closure of the repository, and it may significantly decrease the swelling pressure and increase the hydraulic conductivity of such a backfill (Löfman and Mészáros, 2005). Thus, accurate simulations of variable-density flow may provide useful information. Moreover, high thermal gradients will be caused by the repository, since the decay heat of spent nuclear fuel raises the temperature of the repository and the surrounding bedrock several tens of degrees for many centuries (Löfman, 2005). As a result, it may be interesting to investigate how these variations of temperature will affect the groundwater flow conditions. Other phenomena may affect the subsurface flow over a long time scale, such as land up-lift and glaciations. For example, the land at Olkiluoto is still expected to rise relative to sea level by approximately 10 m during the next 2000 years (Löfman, 2005) and elevated hydrostatic pressure during glaciation may be considered (Raiko, 2005; Vieno and Ikonen, 2005)

Chapter 6

Conclusion

The main objective of this work was to develop a workflow to couple 3D geological modeling techniques with numerical modeling tools, represented, in this specific case, by the geological modeling platform GOCAD and the numerical code HydroGeoSphere, respectively. This objective was defined in the context of the GEOIDE project GeoTopo3D, which represented the basis of this work. As defined in Kirkwood et al. (2003), one of the goals of the GeoTopo3D project was to create an efficient link between Geomodels and numerical models, such that the knowledge gained in constructing Geomodels can benefit numerical modeling. Advanced geomodeling techniques aim to create a detailed 3D representation of geological systems, which can be used for numerical modeling of various physical processes. This work addressed the 3D geological modeling of discretely-fractured geological media as well as numerical simulations of groundwater flow and solute transport.

The work was organized in several successive phases. At first, different options and modeling tools available in GOCAD were tested to find the most suitable procedure to represent a network of discrete fractures. Fractures were represented by triangulated irregular surfaces whose shape was attributed on the basis of field observations. Mutual cuts between intersecting fracture surfaces were executed and a conforming triangular mesh at intersection

lines, which is the essential requirement to satisfy to represent the connectivity between the fractures, was guaranteed.

Spatial discretization of the simulation domain was then required to represent the porous rock matrix surrounding the fractures and to numerically solve the partial differential equations of groundwater flow and mass transport. Unstructured meshes provide multiscale resolution and conformity to complex geometries (Shewchuck, 1999). As a result, an unstructured tetrahedral mesh was chosen to discretize the discretely-fractured media considered here. However, the open problem was how to build tetrahedral elements that satisfy a specific topological relation with triangles that discretize the fractures. In fact, the envisioned relation between tetrahedra and triangles requires that every triangle lying on a fracture surface matches a face of the surrounding tetrahedra. After a survey of available tools, the mesh generator LaGriT was selected as the best tool for 3D discretization of the Geomodel. A particular mesh generation procedure was adopted to discretize the 3D space around the network of fractures. This procedure preserves the fracture network geometry defined with GOCAD, includes a local refinement around the fractures and the boreholes, and provides the required information to identify the tetrahedral faces matching the triangles that lie on the fracture surfaces.

In the next step, the focus shifted to the numerical code HydroGeoSphere. The essential part of this work was actually the modification of HydroGeoSphere, such that the fully 3D tetrahedral mesh could be read by the code. A new procedure was also developed to select the tetrahedral faces representing the fractures. Although the main objective was to import the fully 3D tetrahedral mesh into HydroGeoSphere, an additional aspect was included in the code development. The Orthogonal Subdomain Collocation method was integrated in the numerical code as an alternative to the standard Galerkin method to evaluate the coefficients of the fluid conductance matrix.

To prove the correct numerical solution of subsurface flow and mass transport equations on fully 3D tetrahedral mesh with the enhanced HydroGeoSphere version, some verification examples were designed. Simple simulation scenarios were preferred, in order to check more easily mesh information, compatibility of input/output files between different software tools, and simulation results. Analytical solution and numerical results obtained with block-based

mesh were used as comparative tools. Moreover, some illustrative examples characterized by a gradual increase in the complexity of the simulation scenarios were presented. Furthermore, the difference between Galerkin and Orthogonal Subdomain Collocation methods was analyzed. The matrix arising form the discretization of the governing equations with the Control Volume Finite Element numerical method reflects the connectivity of the mesh used to discretize the simulation domain. The CVFE method is actually based on the definition of two meshes, a finite element mesh, which is the tetrahedral mesh in this case, and a dual mesh. The basic difference between the OSC and Galerkin methods is in the definition of this dual mesh. The OSC method considers the Voronoi mesh as the dual mesh, while the Galerkin method uses the median dual mesh. If the OSC method is adopted together with a tetrahedral Delaunay mesh, the fluid conductance matrix will be an M-matrix. As a result, oscillations in numerical results are more easily avoided. Moreover, a direct link exists between the matrix type and the evaluation of flow between two adjacent nodes. If the matrix is not an M-matrix, up-gradient flow can be simulated, which is unphysical.

Finally, the last part of the work was the application of the modeling approach to Olkiluoto Island (Finland). The purpose was the validation of the modeling approach by analyzing groundwater flow at a real site. Olkiluoto Island has been selected for long-term disposal of spent nuclear fuel. The granitic bedrock of the island is characterized by low permeability, but it is crossed by major fracture zones that control groundwater flow. Thus, hydrogeological modeling becomes essential for site characterization and performance assessment. The three phases of the modeling approach, Geomodeling, mesh generation, and numerical modeling are described in detail with reference to this case study. The model input was represented by the location and the connectivity of the fractures, as well as the coordinates of the boreholes drilled at the site. The Geomodeling phase has shown that the geological modeling platform is suitable and practical to give a realistic representation of the geological system, as spatial data are easily managed and various tools are available to model the geological features, like fracture surfaces and boreholes in this case. Then, the mesh generation procedure applied to this case study has revealed its advantages, such as the local refinement, the representation of intersecting fractures with arbitrary geometry, and the discretization of inclined boreholes. Finally, the numerical code has provided proper simulation results, which have been compared to previous hydrogeological modeling conducted on the same site. Through model calibration,

the hydrogeological properties of the flow model were modified until an acceptable agreement with field observations was achieved. Moreover, solute transport simulations have been executed as illustrative scenarios for the site.

Unlike the previous HydroGeoSphere versions, it is now possible to directly import a fully 3D mesh. This new mesh allows for more flexibility in the choice of the simulation domain geometry. The use of a fully 3D mesh represents the main novelty of the enhanced version of the numerical code. In fact, it is a common practice to simplify the geometry of the simulation domain for modeling purpose. In contrast, with this new modeling approach, complex geometries can be adopted, thus avoiding excessive simplifications. The simultaneous discretization of irregular fractures, inclined wells, and porous rock matrix with a refined tetrahedral mesh, represents another novelty of this work. In fact, in previous work found in the literature, simplifications were often necessary. For example, either the fractures (Mancini, 2004) or the porous rock matrix (Kalbacher et al., 2005) were neglected. If the fractures were considered, they were generally assumed to be planar (Taniguchi and Fillion, 1996; Kalbacher et al., 2005). Moreover, the Geomodel was often created as an ensemble of volume bounded regions (Taniguchi and Fillion, 1996; Andenmatten-Berthoud and Kohl, 2003; Prevost et al., 2004) restraining the domain geometry that can be represented. All these simplifications are no longer required with this modeling approach. An additional innovation that should be highlighted is the advantage of using the geological modeling platform GOCAD as the first step of the modeling phase in which 2D triangulated fracture surfaces are modeled and visualized before building the 3D mesh. 3D modeling allows to create fracture surfaces that fit field observations. 3D visualization allows to validate the geometrical consistency of the fracture network. Boreholes can also be easily integrated in the Geomodel enabling a better modeling of intersections with the fractures. Therefore, the Geomodel gives a detailed reproduction of the subsurface geological structures. Thanks to the link developed here between GOCAD and HydroGeoSphere, it is now possible to execute numerical simulations on a domain that is a more detailed reproduction of the real geological system.

The main outcome of this work is an enhanced version of the HydroGeoSphere numerical code. This new version is based on the coupling between GOCAD and LaGriT. Compared to previous releases, the advantage of this version is that it is better suited for hydrogeological

investigations of complex fractured systems, where irregular fractures and inclined wells must be discretized. This work extends the development done by Graf (2005), as a more flexible mesh is used to fit complex geometries. The tetrahedral mesh can be locally refined and it provides a more suitable representation of the intersections between wells and fractures. In contrast, with the previous versions of the numerical code, block and prism meshes had refinement limitations and were generally built by stacking 2D slices composed of triangular or quadrilateral elements generated by other compatible mesh generators. The resulting 3D mesh was a layered system not suitable to represent discretely-fractured geological media. An additional and very important contribution of this work is that the proposed tetrahedral discretization is suitable not only for reproducing complex geometries, but it also satisfies strict numerical criteria when the Orthogonal Subdomain Collocation method is used. This method ensures that the fluid conductance matrix is an M-matrix and, as a consequence, that the positive transmissibility condition is respected. These two aspects guarantee that the numerical model produces physically realistic results.

Future development may be envisioned to continue with the research direction proposed with this work. It may be interesting to extend the application of this modeling approach to the other existing simulation options in HydroGeoSphere, such as unsaturated flow conditions, variably-density flow and heat transfer. In particular, the application of the Orthogonal Subdomain Collocation method to nonlinear systems may improve the convergence of the Newton iterations because of the presence of an M-matrix, which has excellent properties for iterative solvers (Letniowski and Forsyth, 1991). In contrast, discretizations generating a large number of negative transmissibilities, which are represented by positive off-diagonal entries in the fluid conductance matrix, require a greatly increased number of Newton iterations (Forsyth, 1991).

In conclusion, this work not only led to the development of a software coupling framework between GOCAD, LaGriT and HydroGeoSphere, but it also presented the implementation of an alternative technique to evaluate the coefficients of the fluid conductance matrix as well as the application of the modeling approach to a real test site. The software coupling framework leads to an enhancement of the modeling capabilities for discretely-fractured media, the OSC

method improves the numerical solution, and, finally, the Olkiluoto case study provides a real-world validation of the overall modeling approach.

References

[1] Aagaard BT, 2000. Finite-element simulations of earthquakes. Ph.D. Dissertation, California Institute of Technology, Pasadena, California.

[2] Adler PM and Thovert J-F, 1999. Fractures and Fracture Networks. Dordrecht, The Netherlands: Kluwer Academic Publishers; 444pp.

[3] Ahokas H, 2007. Preliminary analysis on the effect of natural trend of groundwater table on head below the packer during long-term pumping test in KR24 in 2004. Vantaa, Finland: Pöyry Environment Oy.

[4] Ahokas H and Koskinen L, 2005. Task 7: Modelling the KR24 long-term pumping test at Olkiluoto.

[5] Ahokas H and Vidstrand P, 2005. Task 7: Test cases for September 2005.

[6] Allaire PE, 1985. Basis of the Finite Element Method Solid Mechanics Heat Transfer and Fluid Mechanics. Dubuque, Iowa: Wm. C. Brown Publishers; 691pp.

[7] Andenmatten-Berthoud N and Kohl T, 2003. Assessment and evaluation of geothermal potential in Switzerland (Atlas des ressources géothermiques suisses). Commission Suisse de Géophysique, Zurich, Switzerland.

[8] Andersson J, Ahokas H, Hudson JA, Koskinen L, Luukkonen A, Löfman J, Keto V, Pitkänen P, Mattila J, Ikonen ATK, Ylä-Mella M, 2007. Report 2007-03, Olkiluoto site description 2006. Olkiluoto, Finland: Posiva Oy.

[9] Andersson J and Dverstorp B, 1987 Conditional simulations of fluid flow in three-dimensional networks of discrete fractures. Water Resource Research 23 (10): 1876-1886.

[10] Andersson P, Byegård J, Tullborgb E-L, Doe T, Hermanson J, Winberg A, 2004. In situ tracer tests to determine retention properties of a block scale fracture network in granitic rock at the Äspö Hard Rock Laboratory, Sweden. Journal of Contaminant Hydrology 70: 271-297.

[11] ANDRA, 2005. Dossier 2005 granite - Tome évolution phénoménologique du stockage géologique. France, Agence Nationale pour la gestion des déchets radioactifs, Collection Les Rapports.

[12] Barenblatt GI, Zheltov IP, Kochina IN, 1960. Basic concepts in the theory of seepage of homogeneous liquids in fissured rocks. Journal of Applied Mathematics and Mechanics (English Translation) 24 (5): 1286-1303.

[13] Bear J, 1988. Dynamics of Fluids in Porous Media. Mineola, NY: Dover Publications, Inc.; 764pp.

[14] Bear J, 2007. Hydraulics of Groundwater. Mineola, NY: Dover Publications, Inc.; 569pp.

[15] Bear J and Dagan J, 1965. The relationship between solutions of flow problems in isotropic and anisotropic soils. Journal of Hydrology 3: 88-96.

[16] Bennett DG and Hicks TW, 2005. SKI Report, The Swedish concept for disposal of spent nuclear fuel: differences between vertical and horizontal waste canister emplacement. Sweden: the Swedish Nuclear Power Inspectorate.

[17] Beinhorn M and Kolditz O, 2003. Triangular prismatic elements PART II: analytical integration, GeoSys - Preprint. Center for Applied Geosciences, University of Tübingen, Tübingen, Germany.

[18] Berkowitz B, 2002. Characterizing flow and transport in fractured geological media: a review. Advances in Water Resources 25: 861-884.

[19] Bern M and Eppstein D, 1995. Mesh generation and optimal triangulation. In: Du D-Z and Hwang F (Eds.) Computing in Euclidean Geometry, 2nd edition. Farrer Road, Singapore: World Scientific; 47-123.

[20] Bern M and Plassmann P, 1999. Mesh Generation. In: Sack J-R and Urrutia J (Eds.) Handbook of Computational Geometry. Ottawa, Ontario, Canada: North-Holland; 291-333.

[21] Bodin J, Delay F, De Marsily G, 2003. Solute transport in a single fracture with negligible matrix permeability: 2. mathematical formalism. Hydrogeology Journal 11 (4): 434-454.

[22] Bogdanov II, Mourzenko VV, Thovert JF, Adler PM., 2007. Effective permeability of fractured porous media with power-law distribution of fracture sizes. Physical Review E 76, 036309 1-15.

[23] Bower KM, Gable CW, Zyvoloski GA, 2005. Grid resolution study of ground water flow and transport. Ground Water 43 (1): 122-132.

[24] Cacas MC, Ledoux E, De Marsily G, Tillie B, Barbreau A, Durand E, Feuga B, Peaudecerf P, 1990. Modelling fracture flow with a stochastic discrete fracture network:

calibration and validation. 1. The flow model. Water Resources Research 26 (3): 479-489.

[25] Charbeneau RJ, 2000. Groundwater Hydraulics and Pollutant Transport. Upper Saddle River, NJ: Prentice Hall; 593pp.

[26] Cherry TA, Gable CW, Trease H, 1996. 3-Dimensional wells and tunnels for finite element grids. In: Soni BK, Thompson, JF, Hausser, H, Eiseman PR (Eds.) Proceedings of 5th International Conference on Numerical Grid Generation in Computational Fluid Dynamics and Related Fields. Mississippi State University, MS; 12pp.

[27] Cordes C and Putti M, 2001. Accuracy of Galerkin finite-element for groundwater flow simulations in two and three dimensional triangulations. International Journal for Numerical Methods in Engineering 52 (4): 371-387.

[28] Cosgrove J, Jokinen J, Siivola J, Tirén S, 2003. IMGS 2002 Report: The geological and structural characterization of the Olkiluoto site in a critical perspective, STUK-YTO-TR 196. Dark Oy, Vantaa/Finland.

[29] Dershowitz W, Winberg A, Hermanson J, Byegård J, Tullborg E-L, Andersson P, Mazurek M, 2003. Äspö Task Force on modelling of groundwater flow and transport of solutes - task 6c: a semi-synthetic model of block scale conductive structures at the Äspö HRL. International progress report IPR-03-13. Swedish Nuclear Fuel and Waste Management Co, Stockholm, Sweden.

[30] Diodato DM, 1994. A compendium of fracture flow models. Center for Environmental Restoration Systems, Energy Systems Division, Argonne National Laboratory, IL.

[31] Earth Decision, 2006. Earth decision suite 2.1 User guide part I, base module. Houston, TX: Earth Decision Sciences.

[32] Euler N, Sword CH Jr, Dulac JC, 1999. Editing and rapidly updating a 3D Earth Model. In: Proceedings of Society of Exploration Geophysicists International Exposition and 69th Annual Meeting, Houston, TX; 950-953.

[33] Forsyth PA, 1991. A control volume finite element approach to NAPL groundwater contamination. SIAM Journal on Scientific and Statistical Computing 12 (5): 1029-1057.

[34] Gable CW, 2000. Mesh generation for Yucca Mountain. Los Alamos Science Number 26; 472-473.

[35] Gable CW, Trease HE, Cherry TA, 1996a. Automated grid generation from models of complex geologic structure and stratigraphy. In: Proceedings of 3rd International Conference/Workshop on Integrating GIS and Environmental Modeling, Santa Fe, NM; 10pp.

[36] Gable CW, Trease HE, Cherry TA, 1996b. Geological applications of automatic grid generation tools for finite elements applied to porous flow modeling, In: Soni BK, Thompson JF, Hausser H, Eiseman PR (Eds.) Proceedings of 5th International Conference on Numerical Grid Generation in Computational Fluid Dynamics and Related Fields, Mississippi State University, MS; 9pp.

[37] Geiger S, Roberts S, Matthai SK, Zoppou C, Burri A, 2004. Combining finite element and finite volume methods for efficient multiphase flow simulations in highly heterogeneous and structurally complex geologic media. Geofluids 4 (4): 284-299.

[38] Gelhar LW, Welty C, Rehfeldt KR, 1992. A critical review of data on field-scale dispersion in aquifers. Water Resources Research 28 (7): 1955-1974.

[39] Gleeson T and Novakowski K, 2009. Identifying watershed-scale barriers to groundwater flow: lineaments in the Canadian Shield. Geological Society of America Bulletin 121: 333-347.

[40] Graf T, 2005. Modeling coupled thermohaline flow and reactive solute transport in discretely-fractured porous media. Ph.D. Dissertation, Université Laval, Québec, Canada.

[41] Graf T and Therrien R, 2008. A method to discretize non-planar fractures for 3D subsurface flow and transport simulations. International Journal for Numerical Methods in Fluids 56 (11): 2069-2090.

[42] Hellä P, Tammisto E, Ahokas H, 2004. Working report 2004-21, Hydraulically conductive fractures and their properties in boreholes KR4 and KR7-KR10 at Olkiluoto site. Olkiluoto, Finland: Posiva Oy.

[43] Huyakorn PS, Andersen PF, Mercer JW, White HO, 1987. Saltwater intrusion in aquifers: development and testing of a three-dimensional finite-element model. Water Resources Research 23 (2): 293-312.

[44] Huyakorn PS, Springer EP, Guvanasen V, Wadsworth TD, 1986. A three-dimensional finite-element model for simulating water flow in variably saturated porous media. Water Resources Research 22 (13): 1790-1808.

[45] Huyakorn PS, Thomas SD, Thompson BM, 1984. Techniques for making finite-element competitive in modeling flow in variably saturated porous media. Water Resources Research 20 (8): 1099-1115.

[46] IAEA, 1999. Hydrogeological investigation of sites for the geological disposal of radioactive waste. Technical reports Series No. 391. International Atomic Energy Agency, Vienna, Austria.

[47] IAEA, 2001. TECDOC - 1243 - The use of scientific and technical results from underground research laboratory investigations for the geological disposal of radioactive waste. International Atomic Energy Agency, Vienna, Austria.

[48] Kalbacher T, Wang W, McDermott C, Kolditz O, Taniguchi T, 2005. Development and application of a CAD interface for fractured rock. Environmental Geology 47 (7): 1017-1027.

[49] Kattilakoski E, Suolanen V, 2000. Groundwater flow analysis and dose rate estimates from releases to wells at a coastal site, STUK - YTO - TR169. Oy Edita Ab, Helsinki, Finland.

[50] Kirkwood D, Pouliot J, Therrien R, MacQuarrie K, Li S, 2003. GeoTopo3D project proposal. Université Laval, Québec, Canada.

[51] Kosakowski G, 2004. Time-dependent flow and transport calculations for project Opalinus Clay (Entsorgungsnachweis). Nuclear Energy and Safety Research Department Laboratory for Waste Management, Paul Scherrer Institute, Switzerland.

[52] Kosik R, Fleischmann P, Haindl B, Pietra P, Selberherr S, 2000. On the interplay between meshing and discretization in three-dimensional diffusion simulation. IEEE Transactions on Computer-Aided Design of Integrated Circuits and Systems 19 (11): 1233-1240.

[53] Lattuada R and Raper J, 1996. Applications of 3D Delaunay triangulation algorithms in geoscientific modelling. In: Proceedings of 3rd International Conference/Workshop Integrating GIS and Environmental Modeling, Santa Fe, NM; 16pp.

[54] Lepage F and Mallet J-L, 2001. Filling 3-dimensional geological models with nice tetrahedra honoring boundaries. In: Proceedings of 21th GOCAD Meeting, Nancy, France; 15pp.

[55] Letniowski FW, 1992. Three-dimensional Delaunay triangulations for finite-element approximations to a second-order diffusion operator. SIAM Journal on Scientific and Statistical Computing 13 (3): 765-770.

[56] Letniowski FW and Forsyth PA, 1991. A control volume finite-element method for three dimensional NAPL groundwater contamination. International Journal for Numerical Methods in Fluids 13 (8): 955-970.

[57] Löfman J, 1999. Report 99-03, Site scale groundwater flow in Olkiluoto. Olkiluoto, Finland: Posiva Oy.

[58] Löfman J and Mészáros F, 2005. Report 2005-08, Simulation of hydraulic disturbances caused by the underground rock characterisation facility in Olkiluoto. Olkiluoto, Finland: Posiva Oy.

[59] Mallet J-L, 2002. Geomodeling. New York, NY: Oxford University Press; 599pp.

[60] Mancini P, 2004. Geometric modelling of engineered barrier system for waste isolation. M.Sc. Thesis, Eberhard-Karls University, Tübingen, Germany.

[61] Murphy M and Gable CW, 1998. Strategies for nonobtuse boundary Delaunay triangulations. In: Proceedings of 7th International Meshing Roundtable, Dearborn, MI; 309-320.

[62] National Research Council, Committee on disposition of high-level radioactive waste through geological isolation, Board on radioactive waste management, 2001. Disposition of high-level waste and spent nuclear fuel: the continuing societal and technical challenges. Washington, D.C.: National Academy Press; 212 pp.

[63] Neuman SP, 1981. A Eulerian-Lagrangian numerical scheme for the dispersion-convection equation using conjugate space-time grids. Journal of Computational Physics 41 (2): 270-294.

[64] Neuman SP, 1990. Universal scaling of hydraulic conductivities and dispersivities in geologic media. Water Resources Research 26 (8): 1749-1758.

[65] Neuman SP, 2005. Trends, prospects and challenges in quantifying flow and transport through fractured rocks. Hydrogeology Journal 13 (1): 124-147.

[66] Nordqvist AW, Tsang YM, Tsang CF, Dverstorp B, Andersson J, 1992. A variable aperture fracture network model for flow and transport in fractured rocks. Water Resources Research 28 (6): 1703-1713.

[67] NWMO, 2005. Annual report: From dialogue to decision, managing Canada's nuclear fuel waste. Toronto, Canada: Nuclear Waste Management Organization.

[68] OECD, 1999. Progress towards geologic disposal of radioactive waste: where do we stand? An international assessment. Nuclear Energy Agency, Organization for Economic Co-operation and Development.

[69] OECD, 2003. Radioactive waste management. Engineered Barrier Systems (EBS) in the context of the entire safety case. Workshop Proceedings, Oxford, United Kingdom: Nuclear Energy Agency, Organization for Economic Co-operation and Development.

[70] Posiva Oy, 2003. Report 2003-02, Baseline conditions at Olkiluoto. Olkiluoto, Finland: Posiva Oy.

[71] Posiva Oy, 2005. Report 2005-03, Olkiluoto site description 2004. Olkiluoto, Finland: Posiva Oy.

[72] Posiva Oy, 2003. Report 2003-03, ONKALO Underground Characterization and Research Program (UCRP). Olkiluoto, Finland: Posiva Oy.

[73] Prevost M, Lepage F, Durlosfky LJ, Mallet J-L, 2004. Unstructured 3D gridding and upscaling for coarse modeling of geometrically complex reservoirs. In: Proceedings of the 9th European Conference on the Mathematics of Oil Recovery, Cannes, France; 8 pp.

[74] Putti M and Cordes C, 1998. Finite-element approximation of the diffusion operator on tetrahedra. SIAM Journal on Scientific Computing 19 (4): 1154-1168.

[75] Raiko H, 2005. Report 2005-02, Disposal canister for spent nuclear fuel - design report. Olkiluoto, Finland: Posiva Oy.

[76] Rausch R, Schäfer W, Therrien R, Wagner C, 2005. Introduction to Solute Transport Modelling. Berlin, Germany: Gebrüder Borntraeger; 205 pp.

[77] Riekkola R, Sievänen U, Vieno T, 2003. Working Report 2003-46, Controlling of disturbances due to groundwater inflow into ONKALO and the deep repository. Olkiluoto, Finland: Posiva Oy.

[78] Saad Y, 1996. Iterative Methods for Sparse Linear Systems. Boston, MA: PWS Publishing Company; 447pp.

[79] Selroos J, Walker DD, Strom A, Gylling B, Follin A, 2002. Comparison of alternative modeling approaches for groundwater flow in fractured rock. Journal of Hydrology 257: 174-188.

[80] Shewchuk JR, 1999. Lecture notes on Delaunay mesh generation. Department of Electrical Engineering and Computer Science, University of California at Berkeley.

[81] Shewchuk JR, 2005. Theoretically guaranteed Delaunay mesh generation - In practice. Short Course, 14th International Meshing Roundtable, UC Berkeley, San Diego, CA.

[82] Sudicky EA and Frind EO, 1982. Contaminant transport in fractured porous media: analytical solutions for a system of parallel fractures. Water Resources Research 18 (6): 1634-1642.

[83] Sudicky EA, 1988. CRAFLUSH, Programmer's Guide. Waterloo Centre for Groundwater Research, University of Waterloo, Waterloo, Canada.

[84] Tang DH, Frind EO, Sudicky EA, 1981. Contaminant transport in fractured porous media: analytical solution for a single fracture. Water Resources Research 17 (3): 555-564.

[85] Taniguchi T and Fillion E, 1996. Numerical experiments for 3-dimensional flow analysis in a fractured rock with porous matrix. Advances in Water Resources 19 (2): 97-107.

[86] Tanskanen J and Palmu M, 2004. Working Report 2004-26, Facility description 2003. Olkiluoto, Finland: Posiva Oy.

[87] Therrien R, 2008. DRAFT - Äspö Modelling Task Force - Modelling the KR24 pumping test at Onkalo Task 7A. Université Laval, Québec, Canada.

[88] Therrien R, McLaren RG, Sudicky EA, Panday SM, 2007. HydroGeoSphere - A three-dimensional numerical model describing fully-integrated subsurface and surface flow and solute transport. Université Laval and University of Waterloo, Canada, 379pp.

[89] Therrien R and Sudicky EA, 1996. A three-dimensional analysis of variably-saturated flow and solute transport in discretely-fractured porous media. Journal of Contaminant Hydrology 23: l-44.

[90] Thompson JF, Soni BK, Weatherill NP, 1999. Handbook of Grid Generation. Boca Raton, FL: CRC Press; 1136pp.

[91] Vaittinen T and Ahokas H, 2005. Working report 2005-40, Long-term pumping test in borehole KR24 and pressure observations at Olkiluoto, Eurajoki in 2004. Olkiluoto, Finland: Posiva Oy.

[92] Vaittinen T, Ahokas H, Heikkinen E, Hellä P, Nummela J, Saksa P, Tammisto E, Paulamäki S, Pananen M, Front K, Kärki A, 2003. Bedrock model of the Olkiluoto site, version 2003/1. Finland: Posiva Oy.

[93] Vieno T, Lehikoinen J, Löfman J, Nordma H, Mészáros F, 2003. Report 2003-06, Assessment of disturbances caused by construction and operation of ONKALO. Olkiluoto, Finland: Posiva Oy.

[94] Vieno T and Ikonen ATK, 2005. Report 2005-01, Plan for safety case of spent fuel repository at Olkiluoto. Olkiluoto, Finland: Posiva Oy.

[95] Vidstrand P and Ahokas H, 2005a. TASK 7A, Version 1.2.

[96] Vidstrand P and Ahokas H, 2005b. TASK 7A, Version 2.2b: Task description for sub-task 7A.

[97] Vidstrand P, Lanyon W, Ahokas H, 2006. Task 7A, part 1, version 3.0: task description for Task 7A specifications for task 7A1 & task 7A2. Reduction of performance assessment uncertainty through site scale modelling of long-term pumping in KR24 at Olkiluoto, Finland.

[98] Warren JE and Root PJ, 1963. The behavior of naturally fractured reservoirs. Transactions of the Society of Petroleum Engineers of AIME 228 (3): 245–255.

[99] Weatherill D, Graf T, Simmons CT, Cook PG, Therrien R, Reynolds DA, 2008. Discretizing the fracture–matrix interface to simulate solute transport. Ground Water 46 (4): 606-615.

[100] Xu M and Eckstein Y, 1995. Use of weighted least-squares method in evaluation of the relationship between dispersivity and field scale. Ground Water 33 (6): 905-908.

Appendix A

Basic LaGriT commands

cmo

* Current mesh object

infile file_name.lgi

* Instruct LaGriT to begin processing commands from a *lgi text file

read/gocad/frac_name.ts/cmo_name

* Read a GOCAD *.ts surface file

read/avs/well_name.avs/ cmo_name

* Read a *.avs text file that contains well nodes

cmo/create/hexfrac///hex

createpts/brick/xyz/NX,NY,NZ/XMIN,YMIN,ZMIN/XMAX,YMAX,ZMAX/1,1,1

* Create a hexahedral mesh

compute/distance_field/hex_mesh /cmo_name/dfield

* Compute the distance between the hexahedral mesh (hex_mesh) and another Mesh Object

* (cmo_name), such as a fracture or a well

pset/prefine/attribute/dfield/1,0,0/dist_ref/lt

* Select the nodes within a specific distance dist_ref

eltset/erefine/inclusive/pset,get,prefine

* Select the elements that correspond to the nodes selected above

refine/eltset/eltset,get,erefine

* Refine the elements in eltset

cmo/DELATT/hexfrac/dfield

* Delete the dfield attribute

intersect_elements/hex_mesh/cmo_name/if_cmo_name

eltset/e_if_cmo_name/if_cmo_name/gt/0

rmpoint/element/eltset get e_if_cmo_name

rmpoint/compress

* Select and remove the hexahedral elements that intersect the Mesh Object cmo_name

compute/distance_field/hex_mesh/cmo_name/dfield

pset/pfield/attribute/dfield/1 0 0/dist_rem/lt

eltset/efield/inclusive/pset get pfield

rmpoint/element/eltset get efield

rmpoint/compress

* Remove the hexahedral elements included within the distance dist_rem from the Mesh

* Object cmo_name

cmo/create/tetra_mesh///tet

* Create a tetrahedral Mesh Object

copypts/tetra_mesh/hexfrac

copypts/tetra_mesh/wellmesh

copypts/tetra_mesh/fracmesh

* Copy all nodes from hexfrac, wellmesh, and fracmesh to the tetrahedral Mesh

```
* Object tetra_mesh
connect/noadd
* Connect all nodes into tetrahedra

cmo/select/tetra_mesh
surface/surf1/reflect/sheet/frac_name
region/rabove/ge surf1
region/rbelow/lt surf1
mregion/mrabove/ge surf1
mregion/mrbelow/lt surf1
* Define two distinct regions around the fracture frac_name according to the direction of
* the surface normal vector
settets/geometry
extract/intrfac2/mrabove/mrbelow/1,0,0/frac_extracted/tetra_mesh
* Extract the tetrahedral faces aligned along the fracture surface. The resulting extracted
* Mesh Object is frac_extracted

cmo/set_id/tetra_mesh/node/nodenumber
cmo/set_id/frac_extracted/node/node_frac
interpolate/voronoi/frac_extracted node_frac/1,0,0/tetra_mesh nodenumber
cmo/printatt/frac_extracted/node_frac/
* Print on the screen the global nodal numbering for fractures

cmo/addatt/tetra_mesh/edge_connections/nconnect
* Create the attribute edge_connections that contains the maximum number of segment
* connections to a single node in the mesh
dump/coord/file_name/cmo_name
* Create a *.txt file that contains nodal coordinates and connectivity of cmo_name
```

Appendix B

New HydroGeoSphere commands

```
read 3d tetra                  ! Read a file containing the tetrahedral mesh information
tetra_file_name                ! *.txt file name
nb_tetra                       ! Maximum number of connection in the mesh
solution method                ! OSC or Galerkin
end

make fractures from faces file ! Define an irregular fracture in a tetrahedral mesh
fracture_file                  ! *.txt file name containing the triangular mesh information
label                          ! Fracture name

make well from nodes           ! Define an inclined well in a tetrahedral mesh
well_name                      ! Well name
number_of_nodes                ! Total number of nodes discretizing the well axis
well_file_name                 ! *.txt file name containing the nodal numbering of the well axis
npanel                         ! Number of time panels for which a well flowrate is specified
```

```
t_on flowrate                ! Time on and flowrate
discharge_node_number        ! Nodal index of the discharge point of the well
screen radius                ! Screen radius
casing radius                ! Casing radius

choose nodes top tetra       ! If top boundary has constant elevation

choose faces top tetra       ! If top boundary has constant elevation

choose nodes bottom tetra    ! If bottom boundary has constant elevation

make node observation point  ! Define an observation point by using its node index
name                         ! Observation point name
node_index                   ! Node index
```